The jets in radio galaxies

Martin John Hardcastle
Churchill College

September 1996

A dissertation submitted in candidature for the degree of Doctor of Philosophy in the University of Cambridge

‘*Glaucon*: “…But how did you mean the study of astronomy to be reformed, so as to serve our purposes?”

Socrates: “In this way. These intricate traceries on the sky are, no doubt, the loveliest and most perfect of material things, but still part of the visible world, and therefore they fall far short of the true realities — the real relative velocities, in the world of pure number and all geometrical figures, of the movements which carry round the bodies involved in them. These, you will agree, can be conceived by reason and thought, not by the eye.”

Glaucon: “Exactly.”

Socrates: “Accordingly, we must use the embroidered heaven as a model to illustrate our study of these realities, just as one might use diagrams exquisitely drawn by some consummate artist like Daedalus. An expert in geometry, meeting with such designs, would admire their finished workmanship, but he would think it absurd to study them in all earnest with the expectation of finding in their proportions the exact ratio of any one number to another…” ’

— Plato (429–347 BC), *The Republic*, trans. F.M. Cornford.

Contents

Chapter 1

Introduction

1.1 This thesis

This thesis describes two studies of extragalactic radio sources at high resolution and sensitivity. Most of the well-known facts about radio sources come from low-resolution imaging, despite the fact that much of the interesting physics (that of the jets and hotspots) occurs on scales that are small compared to the overall source size. This thesis is an attempt to redress the balance and to extract some physical information on the energy transport in these sources from their small-scale radio structure.

In this chapter I introduce extragalactic radio sources and briefly describe the current state of knowledge about them and the physics we might hope to extract from observations. In chapter 2 the instruments and techniques used to image sources with the required sensitivity and resolution are described.

Chapter 3 is concerned with observations of a small 'representative' sample of FRI sources. The features seen in the radio structures of the jets are discussed and used to estimate the physical parameters in the beams. I compare the structures seen in the jets with existing models.

In chapter 4 I describe observations of a large sample of FRII sources, and discuss some trends in the features observed. In chapter 5, techniques are developed for extracting quantitative information from the resulting images and from data from previous work by others, and the results are tabulated. In chapter 6 I use these results to try to constrain some physical parameters of the sources.

The conclusions of the whole thesis are summed up in chapter 7.

1.2 A brief history

In the early days of radio astronomy large numbers of bright unresolved radio sources ('radio stars') were discovered. It was soon found that many of these were associated with external galaxies, and others with star-like objects of high redshift known as quasars (Schmidt 1963). The radiation was found to be synchrotron in origin, an inference made from its spectrum and polarization (see below, section 1.3). Jennison and Das Gupta (1953) were the first to note (in Cygnus A) the double structure characteristic of many of these sources; understanding of the basic physical processes going on in them came with the large-scale development of interferometry (see chapter 2) at Cambridge and elsewhere. Interferometry made systematic cataloguing of radio sources possible, leading to source catalogues (particularly, from the point of view of this thesis, the 3C and 4C catalogues) still in use today. Subsequently it allowed sub-arcsecond resolution images to be made and began a process of complicated morphological classification which has continued until the present day. One classification that has remained useful is that of Fanaroff and Riley (1974: FR) who noticed that centre-brightened sources (class I) and edge-brightened sources (class II) were separated in luminosity with a dividing luminosity at 178 MHz of around 2×10^{25} W Hz^{-1} sr^{-1}. Their two classes are now known as FRI and FRII.

Meanwhile Miley and Wade (1971) and Hargrave and Ryle (1974) had discovered the hot spots (see section 1.4.3) in Cygnus A; these regions of high brightness embedded in more diffuse lobes were soon found to be ubiquitous in FRIIs, leading to a picture of the prototypical 'classical double' which is not too different from today's (see figure 1.1). The synchrotron lifetime in the hot spots was less than the light travel time from the central object to the hot spots, ruling out simple models of the sources involving a single explosion. Jets (by Bridle and Perley (1984)'s definition: see below, section 1.4.1) were also beginning to be discovered in a variety of different types of source (e.g. Northover 1973). These linked with the 'beam models' being proposed by Blandford and Rees (1974) and Scheuer (1974), in which the outer lobes of the source were supplied with energetic electrons by twin beams or exhausts from the central source. In this thesis, the term 'beam' will be retained (following Hughes and Miller 1991) to refer to the inferred pipe of particles from the central source, and 'jet' will refer to the observed linear features in the radio sources.

The subject was transformed again at the beginning of the 1980s by the NRAO Very Large Array (VLA: see chapter 2) which allowed high-sensitivity and high-resolution maps of radio sources to be made routinely and which did not suffer from the problems of long integration times and declination-dependent resolution experienced at the existing east-west interferometers (notably the Cambridge 5-km and One-mile telescopes and the Westerbork array). By 1984 Perley, Dreher and Cowan had imaged Cygnus A with sufficient dynamic range to discover a faint jet in the western lobe. In the meantime, advances in Very Long Baseline Interferometry (VLBI) had allowed the discovery of parsec-scale jets and apparent faster-than-light motions in the regions close to the central sources of some objects. Jets, interpreted as

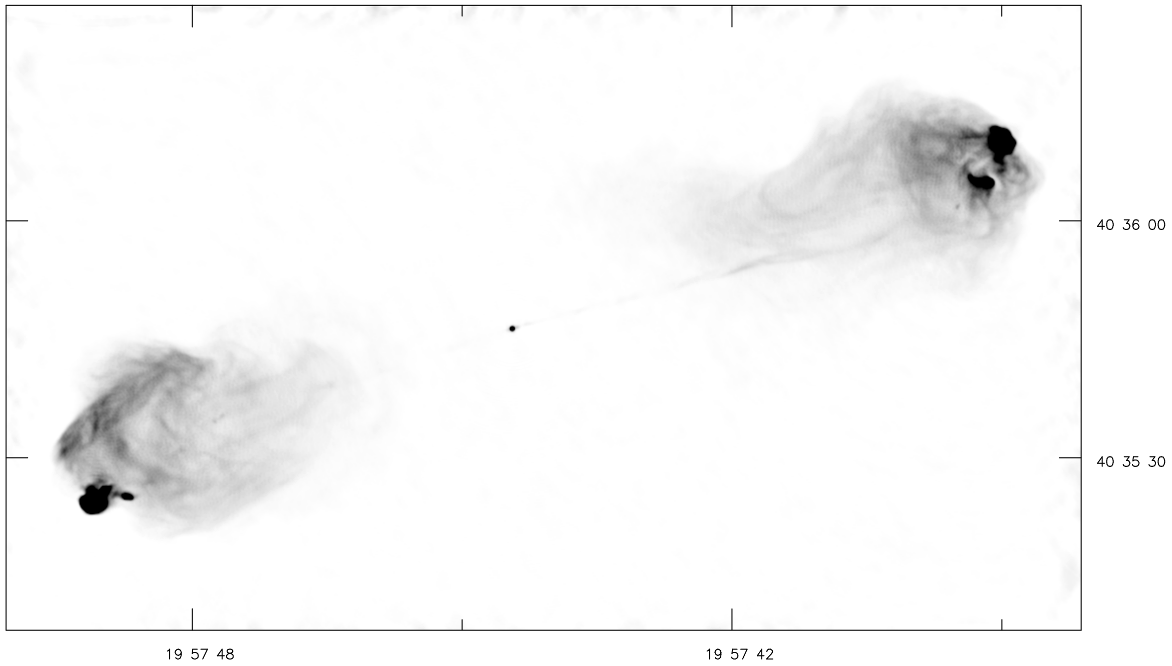

Figure 1.1: The ‘prototypical’ classical double radio source Cygnus A (3C 405). Note the jets, multiple hot spots and filaments in the lobes. Figure taken from Perley, Dreher and Cowan (1984).

evidence of outflow from the central source, seemed to be the common feature linking a range of quite disparate phenomena.

1.3 Synchrotron physics

It will be useful to consider briefly the physics of synchrotron emission[1]. This is the term for radiation from a highly relativistic charged particle in the presence of magnetic field; energy is radiated because of the centripetal acceleration of the charge. An individual electron — the particle of astrophysical interest — radiates at a range of frequencies with the central frequency determined by its Lorentz factor, the cyclotron frequency and the angle between the net velocity and the magnetic field direction. The behaviour of an ensemble of electrons is then obtained by integrating the spectrum of one electron over an appropriate distribution function. The electrons in sources of interest are found to have a power-law distribution in energy, that is

$$n(E)\mathrm{d}E \propto E^{-\delta}\mathrm{d}E$$

and this leads to an emissivity which varies with the observing frequency ν as $\nu^{-\alpha}$ with $\alpha = (\delta - 1)/2$. The quantity α is known as the spectral index and can be measured if maps at two or more frequencies are available.

The polarization of ideal synchrotron emission with a homogeneous magnetic field is independent of frequency and determined only by the spectral index,

$$\pi_L = \frac{3\alpha + 3}{3\alpha + 5}$$

where π_L is the fractional linear polarization. Typical observed values of the spectral index α are between 0.5 and 1, implying fractional polarization of between 70 and 75%. In fact, the fractional polarizations of real sources are often much lower, and can be frequency-dependent. Several effects contribute to this. Firstly, the magnetic field need not be homogeneous; unresolved cellular structure in the field can dramatically reduce the polarization at all frequencies (e.g. Burn 1966). A high degree of polarization is therefore often taken as an indicator that there is considerable order in the magnetic field, though (as shown by Laing 1980) it does not necessarily imply that the field is uniform. More interesting are effects which produce a frequency-dependent depolarization. These depend on the effect known as Faraday rotation, in which the plane of polarization of a linearly polarized light wave rotates as it passes through a magnetoionic medium; the angle of Faraday rotation at a frequency ν is given by

---

[1] For an introduction, see e.g. Hughes and Miller 1991.

$$\phi(s) = \frac{c^2}{\nu^2} K \int_0^s n_{th} \mathbf{B}.\mathbf{ds}$$

where K is a constant, s is the distance from the observer and $\mathbf{B}$ and n_{th} are the magnetic field and the density of thermal electrons, respectively, both functions of position; the integral is known as the Faraday depth. In practice the Faraday depth to different parts of the source within the same telescope beam may be different, but there is usually a straight-line relationship between the rotation angle ϕ and the wavelength squared ($\lambda^2 = c^2/\nu^2$); the slope of this relationship, $\mathrm{d}\phi/\mathrm{d}(\lambda^2)$, is known as the rotation measure, RM, an emission-weighted average of the Faraday depth. Significant depolarization arises when the different lines of sight (or points along a line of sight) seen by a telescope beam have significantly different Faraday depths.

Different effects on the fractional polarization and rotation measure arise depending on whether the magnetoionic medium between us and a radio source is resolved or unresolved and whether it is external to the source or mixed with it; these are discussed in detail elsewhere (e.g. Burn 1966; Laing 1984; Leahy 1985). Here I will only point out that the major component of the Faraday depth to most extragalactic sources is the interstellar medium of our own galaxy; this contribution is resolved, and so should not cause significant differential rotation across the source. The current consensus is that a medium *outside* the radio-emitting material is responsible for the observed depolarization in most radio sources; this is probably the hot halo of the host galaxy.

Inferring physical quantities from radio emissivity is difficult to do with any degree of certainty. The energy in radiating electrons for a given region whose geometry is known depends on its brightness, its spectral index and the local magnetic field. The first two are observables, but the magnetic field is not. A minimum value can be found for the energy density, however, and this is frequently used to estimate physical parameters, as are similar variants such as assuming equipartition between energy in particles and magnetic fields. There is no evidence that even the basic assumptions of these methods are correct, and their application requires further guesses (about, for example, the filling factor of emitting particles and the ratio of the energy density in emitting to non-emitting particles). As strict lower limits, these quantities are valid; as measurements, they are dubious at best. Apart from a brief venture into equipartition calculations in section 3.4.3, I will avoid using such diagnostics.

1.4 Current observational knowledge in the radio

A number of different (and differently applied) morphological classification schemes have been used to describe radio sources. In what follows it will be important to be clear about what these mean, so a summary of the terms as used in the thesis follows (similar in structure and content to that in Muxlow and Garrington 1991).

1.4.1 Jets

Bridle and Perley (1984: BP) provided a widely used operational definition of a jet: it should be a feature of a radio source at least four times as long as it is wide, separable at high resolution from other extended structures, and aligned with the radio core where it is closest to it. Jets often contain compact features (‘knots’) and BP extended their definition to trains of knots with more than two knots or with elongated knots. It is often tempting to identify a single strategically-placed knot or pair of knots as a tracer of the beam (and therefore a part of a jet) — where I have succumbed to this temptation warnings have been placed in the text. As described above, jets are identified with the beams carrying energetic particles from the central core (q.v.) to the outer regions of the source. Jets typically have lower spectral index than the surrounding lobe material ($0.5 \lesssim \alpha \lesssim 1.0$).

BP and subsequent workers have divided jets into two types or ‘flavours’. As first discussed by Bridle (1982, 1984), type I jets have large opening angles ($5^\circ - 30^\circ$) and projected B-fields predominantly perpendicular to the jet; they typically start off bright (often in a knot at the base) and decrease smoothly in brightness with distance from the nucleus. These jets are almost always two-sided (brightness asymmetry between the jet and counterjet no more than a factor 4). A source containing this type of jet is always an FRI, but the converse is not true (Leahy 1993). These jets will be discussed in detail in chapter 3. Type II jets, in contrast, have small or zero opening angles, typically have a B-field predominantly parallel to the jet, are knotty and show no systematic variation of brightness along their length and are usually one-sided; where a counterjet is detected at all, the brightness asymmetry between it and the jet is greater than a factor 4. The generally accepted physical model for these differences is discussed in section 1.6.

1.4.2 Cores or nuclei

Most radio sources have an inverted- or flat-spectrum component at GHz frequencies ($\alpha \lesssim 0$) which is unresolved on arcsecond scales and coincident in position with the host galaxy when this is identified. These are described in this thesis as *cores* or (when the term ‘core’ is being used for something else) as *nuclei*. They are believed (as a result of VLBI imaging) to be the synchrotron self-absorbed bases of jets, and so the terminology used is not entirely appropriate (Bridle *et al.* 1994a, hereafter B94, prefer ‘central feature’) but will be retained for consistency with earlier work.

1.4.3 Hot spots

These are compact (linear size often less than 1 kpc) flat-spectrum ($0.5 \lesssim \alpha \lesssim 0.7$) bright regions associated with the termination of the beam (the 'working surface'; Blandford and Rees 1974). The term is usually used in the context of classical double sources, in which the hot spots typically lie at or near the ends of the source. At high resolution, the hot spots of classical doubles are often (perhaps even mostly) resolved into multiple components, and this presents a problem, as we would expect that there can be only one termination of the beam at any given time; the physics of one of these components should be different from that of all the others. This is discussed further in section 1.6.4. Laing (1989) classifies hot spots as 'primary' (compact) and 'secondary' (more diffuse), noting that the jet, where detected, always enters a primary hot spot. The problem with this classification is that it is subjective and to some extent resolution-dependent; some workers (e.g. Black 1992) have been unable to apply it to certain classes of source at all. This is discussed further in section 4.1. B94, in their study of quasars at high resolution, adopt a stringent definition of hot spots in terms of size and contrast (their hot spots are the brightest points in the lobe, have FWHM $<$ 5% of the source diameter, have a surface brightness at least four times that of the surrounding emission and are further from the nucleus than the end of the jet if one is detected). This unfortunately has the effect that some features that are clearly hot spots according to the qualitative definition given above are not included in their analysis. I shall adopt a less exclusive definition of hot spots in chapter 4 and shall attempt to isolate a beam-termination hot spot in each lobe (using compactness and jet direction as the main criteria) from the remaining features of the source.

1.4.4 Large scale structure

All the other features of a radio source are typically extended (with scale sizes of several arcseconds to arcminutes). The catch-all term for these extended features is 'lobes'; in physical terms, these contain all the radio-emitting plasma which has been ejected through the beams and passed through the hot spot if one is present. Lobes typically have steep spectra ($\alpha > 0.7$) and may be highly polarized, particularly at their edges if these are well defined. In well-studied sources the lobes are often strongly filamented (e.g. Cygnus A, Perley *et al*. 1984; 3C 353, Swain, Bridle and Baum 1996) suggesting that complicated processes introducing large-scale order are present. The spectra steepen away from the hot spots (e.g. Alexander and Leahy 1987) and fits of theoretical synchrotron spectra with minimum-energy assumptions have been used to assign lifetimes of the order 10^7 years to radio sources.

Other terms are used to describe particular lobe structures; these include *plumes* (extended diffuse linear regions in FRI radio sources, probably still representing outflow and therefore observationally difficult to separate from the jet), *tails* (lobe structures, similar to plumes, which are substantially curved away from the original outflow axis, leading to a non-linear source structure), *bridges* (the low-surface-brightness regions in the central regions of radio sources, particularly classical doubles) and *haloes* (diffuse and poorly-defined regions of low-surface-brightness material). The term *wings* is used for those parts of the lobes of classical doubles which curve significantly away from the axis of the source; the different types of symmetry for these distortions in the bridges and their origins are discussed in Leahy and Williams (1984). These appear to be a phenomenon of low-luminosity sources (Leahy and Parma 1992).

1.4.5 The radio source menagerie

This section briefly lists the names given to the different types of radio source that will be discussed in this thesis and the characteristics that distinguish them. This scheme is based on that of Leahy (1993).

- **Classical doubles**. These show a more or less symmetrical double lobe structure with hot spots at the end of each lobe. Jets, where present, are type II and one-sided. Most FRIIs and all radio sources of high luminosity are classical doubles. 3C 405 (figure 1.1) is a classical double, as are most of the sources shown in chapter 4. Spectral index in the lobes steepens away from the hot spot (e.g. Myers and Spangler 1985; Alexander and Leahy 1987; Liu, Pooley and Riley 1992). The host objects may be elliptical galaxies or quasars.
- **Tailed twin jets and narrow-angle tails**. These sources have type I jets leading into plumes, but no hot spots (though there may be a knot at the base of one or both jets, and type II jets close to the nucleus; see chapter 3). Narrow-angle tails have bent jets and swept-back plumes — the natural interpretation of this is in terms of motion in the cluster environment and bending due to ram pressure. These sources often have large linear sizes and ill-defined boundaries. 3C 31 and 3C 449 are the classical examples of tailed twin jets; 3C 83.1B is a well-known narrow-angle tail, and 3C 75N and S probably fall into this category (chapter 3). Spectral index in the jets and plumes steepens with distance from the core. These sources are almost always classed as FRIs and their hosts are elliptical galaxies.
- **Bridged twin jets**. These are similar to the tailed twin jets but the jets form bridges or lobes rather than plumes; in some cases the edges of the source are almost as well-defined as those of a classical double. 3C 296 (chapter 3) is a good example. They are FRIs lying in elliptical galaxies.
- **Wide-angle tails**. These always have well-defined knots (often described as hot spots) at the bases of plumes which may (but do not necessarily) bend with increasing distance from the host galaxy. With high sensitivity, a one- or two-sided type II jet is seen. 3C 465 (Leahy 1984) is the prototype of this class; 3C 130 (chapter 3) is another good example. These sources are always found in central cluster galaxies and are intermediate in radio luminosity (lying around or above the FRI/FRII break) but are generally classed as FRIs.

- **BL Lac objects**. These are identified in the optical by their nearly stellar appearance, line-free spectrum, strongly variable optical flux and high and variable optical polarization. There do not appear to be any radio-quiet BL Lacs. In the radio they are compact but high-dynamic-range images usually reveal extended haloes and jet-like features (e.g. Antonucci and Ulvestad 1985, Murphy, Browne and Perley 1993, Perlman and Stocke 1994). A related class of objects, the optically violently variable quasars, have similar optical properties but also show broad lines; together these two classes are sometimes referred to as **blazars**. 3C 66A (chapter 3) is a BL Lac object.
- **Core-dominated quasars**. These are optically identified as quasars and have a compact radio structure similar to BL Lac objects.

1.4.6 Observational trends

A number of 'facts' about extragalactic radio sources can be adduced from the study of comparatively large samples.

... in FRIIs

Historically FRIIs have tended to attract more interest because of their higher luminosity and their greater numbers in well-studied samples such as the 3CR catalogue. Among the observational facts that will be relevant to this thesis are the following:

- **Jets**. Jets in these sources are one-sided. They are much more one-sided and had until recently been believed to be much more prevalent in sources whose hosts are quasars rather than radio galaxies (but see section 4.1). A recent review (Muxlow & Garrington 1991) puts the jet detection fraction for quasars at around 70% and for radio galaxies at around 10%. These differences are normally explained in terms of unified models for the two classes of object (section 1.6.6).
- **Hot spots**. Laing (1989) reviews the radio observations of hot spots. He suggests that there is a strong tendency for the brighter hot spot to lie on the side with the jet, where one is present. Black (1992) in his sample of low-luminosity objects fails to find this trend, however.
- **Lobe length/lobe brightness**. Mackay (1971) was the first to note a weak tendency for the brighter lobe of a double radio source to be the shorter, later also observed by Macklin (1981) and McCarthy, van Breugel and Kapahi (1991). This is generally explained in terms of an asymmetrical environment.

- **Lobe length/spectral index**. Pedelty *et al*. (1989a) found in a sample of high-redshift radio galaxies without prominent jets that the longer lobe tended to have the flatter spectral index.

- **Lobe brightness/spectral index**. Liu and Pooley (1991b) and Mackay (1971) both seem to see a trend for the brighter lobe to have the steeper spectral index; this is in agreement with the previous two observations.

- **Depolarization/spectral index**. Liu and Pooley (1991a) find a tendency for the lobe which is more depolarized to have the steeper spectral index, in a sample of radio galaxies. This trend is also found by Garrington and Conway (1991). This tendency can be explained in terms of an asymmetric galactic environment.

- **Lobe length/depolarization**. Pedelty *et al*. (1989a) find a trend for the shorter lobe to be the more depolarized in a sample of radio galaxies, in agreement with the previous observations.

- **Jet side/depolarization**. Laing (1988) and Garrington *et al*. (1988) found a strong trend in samples mostly containing quasars for the lobe containing the (brighter) jet to be the less depolarized. This effect, known as the 'Laing-Garrington effect', was later confirmed with larger samples by Garrington, Conway and Leahy (1991) and Garrington and Conway (1991). The trend is strongest in small, high-redshift sources. This is generally regarded as good evidence for beaming and orientation models, but causes some problems when combined with the other effects spectral index and depolarization effects described above (Bridle *et al*. 1994b; Dennett-Thorpe, in prep.).

- **Jet side/lobe length**. Garrington *et al*. (1988) claim a weak tendency for the lobe containing the jet to be the longer. Black (1992) finds no such effect in his low-luminosity sample, however. Scheuer (1995) analyses a large sample of high-power sources with detected jets and again finds a tendency for the jet side to be the longer. In the context of unified models (see below, section 1.6.6), it might be expected that the samples of Scheuer and of Garrington *et al*. would show a stronger effect due to light travel time, since they are preferentially oriented at small angles to the line of sight (being largely quasars).

- **'Compactness'/luminosity**. Jenkins and McEllin (1977) find a relationship between the compactness of a source, defined as the fraction of the flux in the hotspots rather than the lobes, and its radio power; more powerful sources are more compact. Rossiter (1987) expands this work and appears to confirm the result.

... and in FRIs

Systematic work on FRIs is mainly based on the B2 sample of low-luminosity objects.

- **Jets**. Jets in these sources are usually two-sided on kiloparsec scales. The magnetic field configuration changes from longitudinal to transverse to the jet (Laing 1993). In at least one source (3C 31) the jet-counterjet asymmetry is more pronounced in the centre of the jet than at its edges (Laing 1996; see chapter 3).

- **Laing-Garrington effect**. FRI sources often exhibit considerable brightness asymmetry at the bases of jets. Parma *et al*. (1993) found that the brighter jet tends to be more polarized at 1.4 GHz; this could be taken as evidence for asymmetric depolarization. Parma *et al*. (1996) have confirmed this effect with a multi-frequency study.

- **'Gap'/power correlation**. The spatial extent of the gap between the core and the first bright emission from the jet in FRIs correlates with the power of the source; the more powerful the source, the larger the gap (Birkinshaw *et al*. 1978; Parma *et al*. 1987).

1.4.7 VLBI

Very Long Baseline Interferometry (VLBI) is used to investigate the unresolved cores of radio sources on parsec scales. Jets, mostly one-sided, are detected on these scales and in both FRIs and FRIIs are directed towards the brighter kiloparsec-scale jet. Proper motions in these jets can be used to constrain the outflow pattern velocities on these scales. Motions with apparent velocities faster than the speed of light (superluminal motion) can be explained if the true motion is highly relativistic and the source is aligned towards the observer. The general trend is for the parsec-scale jet to be more one-sided than the kiloparsec-scale one. On these scales there is little discernible difference between the jets in FRIs and FRIIs (Pearson 1996) and this ties in with suggestions that the core/total flux ratio is similar for FRIs and FRIIs at similar radio powers (Zirbel and Baum 1995).

1.5 Observational knowledge in other wavebands

1.5.1 Optical synchrotron radiation

In a small number of powerful radio sources optical counterparts of the radio synchrotron emission have been detected. A small number of FRIs show optical jets (3C 66B, discussed in chapter 3, is an example) and some FRIIs have optical counterparts to their radio hot spots (including 3C 20, chapter 4). Optical synchrotron radiation from a source allows strong constraints to be placed on the acceleration mechanisms in the sources, because of the very short particle lifetimes at these energies.

1.5.2 Host galaxies in optical and infra-red

Optically, the hosts of powerful radio sources are classed as elliptical or giant elliptical galaxies (sometimes cluster dominant galaxies), as N-galaxies (galaxies with a point-like nucleus) or as quasars. In the infra-red, the galaxies behave similarly to ordinary ellipticals and are dominated by an old stellar population (Lilly and Longair 1984). At low redshift, FRI radio sources seem to lie preferentially in clusters (Longair and Seldner 1979; Prestage and Peacock 1988) and the brightest inhabit first-ranked ellipticals (Owen and Laing 1988; Owen and White 1991; but cf. Ledlow and Owen 1996 — not all FRIs inhabit first-ranked ellipticals, but at low redshift an object in a first-ranked elliptical is almost certain to be an FRI). They show a correlation between radio power and host magnitude (Owen and White 1991). FRIIs, on the other hand, are usually found in smaller and less luminous hosts which avoid clusters (e.g. Lilly, McLean and Longair 1984; Prestage and Peacock 1988) though they may be the dominant galaxies of small groups. Their environments are similar to those of ‘average’ radio-quiet ellipticals although they have a tendency to have brighter close companions (Smith and Heckman 1990). There is some evidence that FRII hosts may be more disturbed than those of FRIs (Heckman *et al*. 1986), and that both are more likely to be disturbed than ordinary field ellipticals. These differences have been used to infer that sources cannot evolve between FRI and FRII morphology on the time scales of radio source lifetime (10^7 yr). However, at higher redshift ($z \sim 0.5$), powerful sources are much more likely to lie in rich clusters (Yates, Miller and Peacock 1989), the differences in environment between low-power and high-power radio galaxies seem to be less pronounced (Hill and Lilly 1991) and a large fraction of the quasar population also seems to lie in rich clusters (Yee and Green 1987); this implies either that the host galaxy population has evolved between $z \sim 0.5$ and $z \sim 0$ or that clustering studies at low or high redshift are incorrect. It is worth noting in this context that the luminosity functions of FRI radio sources are similar inside and outside clusters; this suggests that the environments are not as different as might be supposed, and that to first order most or all radio sources might really inhabit reasonably dense environments (e.g. Owen *et al*. 1996).

It has been suggested that the host galaxies of quasars may differ from those of radio galaxies (e.g. Hutchings 1987; Smith and Heckman 1990) but the environments seem similar (Smith and Heckman 1990) and the problems involved in deconvolving the nuclear point source from the stellar emission are severe. If correct, this observation presents a problem for unified models (section 1.6.6).

Several studies have looked at the tendency for host galaxy axes to be aligned with the radio lobes. At low redshifts (and therefore lower powers) there is a slight tendency for the *minor* axis of the elliptical to be aligned with the radio axis (e.g. Guthrie 1979; Palimaka *et al*. 1979; McCarthy and van Breugel 1989). At high redshifts there is a much stronger tendency for the *major* axis of the galaxy to be aligned with the radio axis (McCarthy *et al*. 1987; Chambers, Miley and van Breugel 1987); the host galaxies of these objects appear knotty and quite unlike low-z ellipticals in the rest-frame UV, but the alignment effect is much less significant in the rest-frame IR (Best, in preparation) although Dunlop and Peacock (1993) suggest that it is still present in the most powerful objects. Cimatti and di Serego Alighieri (1995) claim to have seen a UV alignment effect in a particular object at low redshift, and more examples of such objects may turn up.

Optical polarization is often seen in radio galaxies, with the E-vector either parallel or perpendicular to the source axis at low redshift but exclusively perpendicular at $z > 0.6$; the degree of polarization at high redshift correlates with source asymmetry (Tadhunter *et al*. 1992; Cimatti *et al*. 1993). This is used as a strong argument for the mechanism of the alignment effect being the scattering of a nuclear continuum in the high-z objects. The mechanism for polarization in lower-redshift objects is less clear.

1.5.3 Nuclear and extended emission lines

Emission in the form of lines from excited atomic species can come from three size scales of the host galaxy. Broad lines are seen in the spectra of quasars; these are velocity-broadened and from variability timescales and ionization energetics we know that they come from a region about 1 pc from the active nucleus. Broad-line radio galaxies (BLRG) also exhibit broad lines, and in fact are spectroscopically indistinguishable from quasars (Sandage 1973a). Most radio galaxies do not show broad lines. The broad lines are photoionized by the quasar continuum.

Further from the nucleus, many host galaxies of powerful radio sources show strong high-excitation narrow emission lines. Observation can spatially resolve these and puts their extent on the order of 1 kpc about the nucleus. Whereas the mean detection rate of emission lines is around 16% in ellipticals as a whole (Gisler 1978) it is considerably higher in 3CR radio sources (Laing, Riley and Longair 1983 [LRL]). In the nearby elliptical population as a whole, line detection is strongly anti-correlated with cluster membership (Gisler 1978) and this is also true of radio sources (Longair and Seldner 1979, Guthrie 1981); this may be because of the gas-poor nature of cluster galaxies. In a sample of nearby radio galaxies (mainly FRIs) lying in rich clusters, Owen, Ledlow and Keel (1995) find that the line luminosity of the radio sources is not significantly different from that of the radio-quiet cluster ellipticals of the same magnitude.

Hine and Longair (1979) divide a sample of 3CR sources into two classes, class A having strong [OII]-λ3727 and class B having no or very weak emission at that line. They find that weak galaxies are almost all class B while at the highest luminosities in their sample over 70% are class A; the dividing line is such that most FRI objects in their sample are class B and most FRIIs are class A. This division is made quantitative by Laing *et al*. (1994), using high-quality spectra; they define high-excitation objects as having [OIII]/H$\alpha > 0.2$ and equivalent widths of [OIII] > 3 Å, and in their sample of LRL sources with $z < 0.88$ and $0^h <$RA$< 13^h$ all the FRI objects were low-excitation or ‘dull’. Smith and Heckman (1989) claim that high-excitation galaxies at low redshift are more likely to be optically disturbed. As described above, FRI sources are much more likely to lie in clusters than FRIIs, and FRIIs are more likely to be optically disturbed; we therefore see a multi-way correlation between line strength, cluster environment and radio and optical morphology. (It is important to emphasise, in view of what will follow, that the correlations are not tight; in particular, not all 'dull' radio galaxies are FRIs.) The source of energy for these nuclear narrow lines is probably photoionization from the AGN. (Since these narrow lines appear in ellipticals without radio sources, the radio source or the associated outflow is unlikely to be responsible for them in general.)

In addition to these nuclear emission lines, many radio sources have extended emission-line regions (EELR). Typically 90% of the line emission is found in the nuclear regions (Baum and Heckman 1989b) but the remainder can be seen on scales of tens of kpc, extending up to 100 kpc or so in some cases (Baum and Heckman 1989a; McCarthy, Spinrad and van Breugel 1995). They are filamentary and often preferentially distributed along the radio axis (McCarthy 1993); the sizes, luminosities and degree of alignment of the EELRs increase with redshift (McCarthy and van Breugel 1989). Their ionization parameters are similar to those of the nuclear emission lines, and are consistent with photoionization from the nuclear continuum (Baum and Heckman 1989) although there is evidence in particular sources for direct interaction between the radio source and the narrow-line emitting gas (e.g. 3C 171; section 4.5.10) which might be better explained in terms of shock excitation of the cold gas. Some EELR are significantly larger than the associated radio galaxy. The different possible mechanisms for the alignment between EELR and radio source direction (and the optical continuum/radio source alignment discussed above), particularly important at high redshifts, have been discussed extensively in the literature but are outside the scope of this thesis. A result which is relevant is that the extended line emission in FRII radio galaxies is brighter on the side of the *shorter* of the two radio lobes (McCarthy, van Breugel and Kapahi 1991).

A number of workers have attempted to relate the luminosity of the nuclear narrow lines to the radio luminosity or another measure of the power of the radio source. Rawlings (1987) and subsequently Rawlings and Saunders (1991) relate the luminosity in narrow lines to the beam power of the source (called by them 'jet power' and calculated from the source luminosity and age), arguing that the narrow-line luminosity is a measure of the total power of the AGN. More recently Zirbel and Baum (1995) have looked at the correlations between line luminosity and total source power and core power for a large sample of disparate objects, finding significant differences between the correlations which exist for FRIs and FRIIs.

Jackson and Browne (1990) find that FRII radio galaxies have dimmer [OIII]λ5007 line luminosities than quasars of similar radio luminosity by a factor of 5-10, a fact which bears on unified models (see section 1.6.6) and which makes [OIII] lines less useful than they might be as a measure of AGN power. Some suggestion that this is true of the BLRG as well as the quasars can be found in the results of Antonucci (1984). However, Hes, Barthel and Fosbury (1993) have shown that quasar [OII] line luminosities are very similar to those of radio galaxies at the same radio power. This will be discussed in chapter 6.

1.5.4 X-ray

X-ray emission can come from radio sources in several ways (e.g. Birkinshaw and Worrall 1996). It has been suggested in a few exceptional cases (e.g. M87, Biretta, Stern and Harris 1991; 3C 273, Harris and Stern 1987) that synchrotron radiation is responsible for the X-ray emission from jets. In other cases the radiation identifiable with a component of the radio source appears to come from the hot spots or lobes; the most definite example is Cygnus A (Harris, Carilli and Perley 1994) and the most likely explanation is synchrotron self-Compton radiation. In more normal sources, X-rays are often detected from an unresolved core, although it is not clear (in the absence of X-ray spectra) whether this is central hot gas or more directly related to the radio source. Extended emission in general comes from the hot gas surrounding the host galaxy or cluster (striking evidence that this is true for Cygnus A comes from the observation of X-ray deficits coincident with the radio lobes: Carilli, Perley and Harris 1994), and physical diagnostics from this have been used to investigate whether the gas is dense enough to confine the lobes by thermal pressure; since these estimates generally rely on equipartition calculations, I shall not discuss them here. In this thesis X-ray evidence is mainly used in the last sense, as an indication of hot gas surrounding the radio lobes.

1.6 Current theories of radio sources

1.6.1 The central engine

The suggestion (Lynden-Bell 1969) that the energy sources for active galactic nuclei in general are super-massive black holes is now almost universally accepted. As Begelman, Blandford and Rees wrote in 1984

> No other entity can convert mass to energy with such a high efficiency, or within such a small volume.

Recent observations have shown beyond reasonable doubt that a great deal of mass is indeed concentrated in a small volume in the centre of active galaxies (e.g. Miyoshi *et al.*1995) and there is also some evidence from X-ray observations that these objects are indeed black holes (Tanaka *et al.* 1995). However, the mechanisms for producing the highly collimated beam necessary in the Scheuer/Blandford and

Rees model of powerful radio sources from a black hole are not well known, primarily because of a lack of observational evidence on these scales. It seems likely that the black hole has to rotate to provide a well-defined and stable axis, and that magnetic fields are involved. There are numerous theoretical models in the literature, all currently untestable.

1.6.2 Beams and the production of radio sources

The beam model seems secure given the observations of jets, and will be assumed as a basis throughout this thesis. In the simplest versions, energy leaves the AGN in two oppositely directed and symmetrical beams of highly energetic particles, either positrons and electrons or protons and electrons. All the various types of structure seen in the radio are then the results of the interaction of this beam with the interstellar, intergalactic and intra-cluster media. The hot spots in powerful sources are explained as the sites of beam termination, where the bulk kinetic energy is converted to random energy of charged particles; a shock forms when the beam leaves the under-dense cocoon it has made for itself and encounters the ISM or IGM, and particle acceleration occurs by a first-order Fermi process. The spectra of hot spots are consistent with this model (Meisenheimer *et al.*1989). Material expands out from the hot spots (provided the jet is less dense than the external medium, Williams 1991) and the advance of the hot spots, possibly together with backflow (shock-processed material moving back towards the central source in the shock frame) then produces the lobes. In the less powerful sources the beam is presumed to be disrupted before it can form a strong shock, and a plausible and widely adopted hypothesis is that the beams in the type I jets of FRI sources have sub-sonic or trans-sonic bulk velocities whereas those in FRII sources are supersonic. Particle acceleration in FRIs might then occur at a reconfinement shock (which could be identified with the bright base knot seen in some FRIs) but must also occur throughout the jet to account for the observed sub-adiabatic brightness decay (chapter 3). A plausible model for this acceleration is to allow the beams to be turbulent and to entrain material from the ISM; second-order Fermi acceleration can then take place in the turbulent regions. The details of this model are not fully agreed, however (e.g. Leahy 1991). It is known that the FRI/FRII transition depends not just on the luminosity of the radio galaxy, but also on the magnitude of the host galaxy (e.g. Owen and Ledlow 1994), in the sense that near the nominal FRI/FRII break an object in a brighter (and therefore larger, more massive) galaxy is more likely to be an FRI (and thus more likely to have a jet that disrupts). Bicknell (1996) has used his entrainment model to fit the slope of this relationship successfully.

1.6.3 Cores and jets

The cores (considered as the unresolved bases of self-absorbed jets) and jets in this class of model are indicators of the presence of the beam. What they can tell us quantitatively about the beam is less clear.

In the lower-power sources most of the beam power evidently goes into jets. But in the high-power sources, a large fraction of the power in the beam must reach the hotspots, with the remainder being dissipated in the jet. It is not clear what controls the efficiency of the beam; this will be discussed in chapter 6.

The one-sidedness of the jets in powerful sources is normally interpreted in terms of relativistic bulk velocities of the emitting material, giving rise to relativistic beaming; the jetted side in this model would be the one pointing towards us. Strong evidence for this comes from the Laing-Garrington effect. If there is a uniform depolarizing halo around radio sources, then the lobe pointing away from us would be seen through a greater depth and would be more depolarized, as is observed. If the jet one-sidedness is indeed due to relativistic beaming, then a ‘typical’ bulk velocity for the emitting material may be derived; this would represent a lower limit on the bulk velocity in the beam, and might be compared to the limits on hot spot advance speed set from lobe length asymmetries (e.g. Longair and Riley 1979; Best *et al*. 1995; Scheuer 1995).

The geometry of cores is limited quite strongly by the fact that their spectra are flat. The reasons for this are discussed in Phinney (1985). It seems likely (given the VLBI observations of superluminal motion discussed above) that there is relativistic beaming in the cores, and this is frequently assumed in the literature so as to allow the use of cores as orientation indicators.

1.6.4 Hot spots and after

As discussed above, many FRII sources have multiple hot spots. This was first noticed in a few very striking sources (e.g. 3C 20, Laing 1982; see also section 4.5.2). There are several related classes of model for this type of hot spot structure. In the first, usually known as the ‘dentist’s drill’ model (following Scheuer 1982) the beam moves about in the cocoon on comparatively short timescales and impinges on different parts of the external medium at different times. This model would generate primary and secondary hotspots. The primary hot spot would be the site of the beam impact, and the jet, if any, should be seen leading into it. The secondary hotspots would be sites of previous beam impact; with the energy supply of the beam withdrawn they would have a steeper spectrum (no ongoing particle acceleration) and would be more diffuse (hotspots are overpressured with respect to the rest of the lobe, and so would expand rapidly).

In alternatives to this model, the secondary hot spots are still being fed by the beam in some fashion, although the primary remains the point of beam termination. This is motivated by observations suggesting that the secondaries are edge-brightened away from the primaries (e.g. Laing 1982), by observations of features linking them, and by the fact that particle acceleration appears still to be going on in some secondaries. Versions of this model include beam-deflection models (e.g. Lonsdale and Barthel 1986), in which the beam strikes a cloud and is deflected, and the ‘splatter-spot’ model of Williams and Gull (1985) in which a jet changes its direction and ‘bounces’ off the wall of a previously formed cocoon. In both this latter model and the ‘dentist’s drill’ model some mechanism is needed to deflect the beam — it may be possible to do this with asymmetric backflow (e.g. Hardee and Norman 1989). Numerical simulations (Cox, Gull and Scheuer 1991) have shown that both disconnected secondaries (dentist’s drill) and connected ones (splatter-spot) can be generated in the same general conditions; they point out that a disconnected hot spot can continue to be fed for some time if the disconnection occurs some way up the beam. On the other hand, other simulations (Higgins, O’Brien and Dunlop 1996) have shown that interactions with clouds of plausible densities can generate multiple hotspots. It has been suggested (e.g. Lonsdale and Barthel 1986) that the secondaries in the splatter-spot model should always lie ahead of the primaries, and that this is not observed; it seems likely, however, that the pressure gradient responsible for backflow can also bend collimated outflow from the primary, as seen in the simulations of Cox *et al.* (1991). In chapter 4 I will discuss some observational constraints on these models.

Backflow is expected if the excited particles from the hot spot(s) have some net momentum when they leave the shock regions. As described by Williams (1991), the fluid is bent back along the cocoon by the pressure gradient between the shocked IGM and the cocoon material. If this process is significant, its result is to produce a net velocity of the hot spot-processed material back along the cocoon in the frame of the AGN. This clearly has implications for large-scale source structure, and Leahy and Williams (1984) attribute the distortions in the bridges of their sample to non-axisymmetric backflow. As discussed by Alexander and Leahy (1987) spectral-ageing methods of speed determination in classical doubles measure the sum of the hot spot advance speed and the backflow speed, so a correct assessment of the contribution of backflow to source properties is also important here. In different ways Liu, Pooley and Riley (1992) and Scheuer (1995) have argued that backflow velocities are significant compared to hot spot advance speeds. Backflow throughout a source with velocities greater than that of the hot spot advance will lead to a central bulge of aged material; there are certainly sources where it is plausible that this has happened, but it is also likely that backflow will slow with distance from the hot spot. Later I will discuss observations of sources in which backflow appears to be an important process.

1.6.5 Environment

Because the radio sources are made visible by the interaction of the beam with the environment, it is not surprising that radio source properties often reflect features of the ISM, IGM and ICM. Obvious examples of this are the narrow-angle tails found on the edges of clusters (the bending is believed to be caused by ram pressure as the AGN (and host galaxy) moves with respect to the cluster gas) and the wide-angle tails found in their centres (in which the mechanism for bending is not clear, but is likely to be related to large-scale motions in the cluster gas and to buoyancy). More subtly, differences in the environment on the two sides of the radio source can affect the behaviours of the jets and the characteristics of any lobes formed. In simple models with symmetrical beams, the environment must be invoked to explain any differences between the lobes (the two lobes of a single source are often strikingly different). Indicators of the gaseous environment around the galaxy are sparse; X-ray instruments, which could provide information on the hot gas component, do not generally have the combination of resolution and sensitivity to study a large sample of radio sources. An important result is that of McCarthy *et al*. (1991) (section 1.5.3) who showed a correlation between the brighter emission-line region and the shorter lobe in powerful (FRII) radio galaxies. It is impossible to explain this other than in terms of an asymmetrical environment producing an asymmetrical radio source, as first discussed by Swarup and Banhatti (1980). The result (discussed above, section 1.4.6) that the shorter lobe tends also to be the brighter lobe can be interpreted as supporting this, since it can be explained in terms of a denser medium providing better confinement and thus reducing losses by adiabatic expansion.

The environment of radio galaxies may well be clumpy on a range of scales. Pedelty *et al*. (1989a,b) have shown evidence for this derived from the size scales in rotation measure variations; there is evidence in individual sources (see Wilson 1993 for a review) for interaction between the jets and the extended emission-line regions. This would help to explain the observed bends and knots in jets (Bridle and Perley 1984 note that jets may bend through very large angles without disrupting) and the wide variety of structures observed in hot spots (see section 1.6.4). Numerical simulations (e.g. Higgins, O'Brien and Dunlop 1996) involving dense clouds reproduce the observations (knotty jets and multiple hot spot structure) well.

1.6.6 Unified models

There are many schemes which seek to unify apparently distinct classes of sources by considering them as the same class of source at different angles to the line of sight. Differences in the source properties are then explained by anisotropic extinction or by relativistic beaming. In this thesis I will only be concerned with models which unify FRII radio galaxies and FRII quasars, and FRI radio sources and BL Lac objects. Reviews of the current status of unified models in general can be found in Antonucci (1993) and Barthel (1994).

FRII radio galaxies and quasars

FRII quasars exhibit superluminal motion in their cores, have very one-sided jets and generally show a pronounced Laing-Garrington effect. It seems likely (as discussed above) that this can be attributed to relativistic beaming, which prompts the question 'what are the unbeamed counterparts of quasars?'. In a sample such as that of LRL, where objects are selected on the basis of low-frequency flux (predominantly from the lobes, which cannot be strongly beamed; Mackay 1973) there are no selection effects which could exclude the unbeamed counterparts of lobe-dominated quasars; therefore they must be present in the sample, and the only possible candidates are the FRII radio galaxies. This unification, first suggested in Bridle and Perley (1984) and put forward again in Barthel (1987) and Scheuer (1987), is now widely thought to be true to first order. Barthel (1989) shows that this simple unified scheme is consistent with the number counts of FRII radio sources in LRL with $0.5 < z < 1$ and with the optical, IR and X-ray data, provided that there is also obscuring material (usually suggested to be in the form of a torus) which prevents us seeing the AGN in the centres of radio galaxies. This model is illustrated in figure 1.2. The torus obscures both the optical continuum and the broad-line region (BLR) of quasars when they are in the plane of the sky. Significant evidence in favour of this model comes from the detection of weak *polarized* broad lines in some radio galaxies (e.g. 3C 234, Antonucci 1982 and chapter 4); this is interpreted as being due to scattering of the emission from the BLR into the line of sight. It now appears that some of the narrow-line region must also be obscured, to explain the differences in high-excitation emission line luminosity between quasars and radio galaxies of similar radio powers (Jackson and Browne 1990, 1991; Hes *et al*. 1993). But care has to be taken to compare like with like in estimating the degree of obscuration (see chapter 6).

A problem with applying these unified models to the low-redshift end of LRL (including the sample discussed in chapter 4 and thereafter) is that there are no FRII quasars in LRL with $z < 0.3$. Since there are plenty of FRII radio galaxies, we expect there to be a low-redshift analogue of quasars, and in simple extensions of the unified models these are taken to be the BLRG. The host galaxies of these are often, though not exclusively, N-galaxies (Grandi and Osterbrock 1978) and so resemble weak quasars in their broad-band optical as well as spectral appearance (Sandage 1973a). However, as discussed above (section 1.5.3) there is a class of FRII objects with no high-excitation line emission. It seems plausible that these would not appear as BLRG even if they were aligned close to the line of sight. Dropping these ‘dull’ sources brings BLRG–NLRG unification at the low-redshift end of LRL into line with the number counts in Barthel (1989) (Laing *et al*. 1994); but there is then the problem of identifying the highly-beamed counterparts of the dull objects. This will be discussed in chapter 6.

FRI radio sources and BL Lacs

The history of unified models for these objects parallels that of the FRII quasar/radio galaxy schemes. The suggestion that BL Lacs are beamed is not new (e.g. Blandford and Rees 1978), based on their rapid variability, the absence of the synchrotron self-Compton X-rays that would be expected from unbeamed sources of such high brightness temperature, and their superluminal motion when observed with VLBI. Again the essential observation for unifying BL Lacs with a particular class of objects was that the diffuse, and presumably unbeamed, haloes around some BL Lacs were often themselves bright enough to bring the object into the flux-limited sample of interest (Browne 1983). Most BL Lac objects have extended luminosities consistent with being beamed FRI radio galaxies, and their redshift distribution is also consistent with this, together with their luminosity function if a range of beaming factors $5 < \gamma < 35$ is used (Urry, Padovani and Stickel 1991). Beaming factors of this magnitude in BL Lacs are consistent with the limits placed on them by superluminal motion, where observed, and with decelerating jet models (Bicknell 1994). However, a few BL Lacs are too luminous in extended structure to be FRIs, or have FRII-like double structure (Kollgaard *et al*. 1992). It is possible that the parent population of these sources is the ‘dull’ (low-excitation) FRIIs described in section 1.5.3. Alternatively, these BL Lacs may be misclassified quasars (the broad lines may have been missed). A simple sketch of unified models for these objects is shown in figure 1.2.

1.6.7 A ‘standard model’ for radio sources

It will be useful to define a very basic ‘standard model’ for radio sources, abstracted from the results discussed above. This is not intended to be true in all cases, and indeed is clearly not true for a few peculiar objects. However, it is expected to be true to first order for the bulk of the objects to which it applies. The results of the remainder of this thesis can then be considered in the context of the extent to which they bear out or contradict this model.

- Extragalactic double radio sources are formed by the interaction between two symmetrical beams of energetic particles with initially relativistic bulk velocity (emanating from the AGN) and the galactic atmosphere.
- The beams may produce along their length synchrotron-emitting plasma with a bulk velocity comparable to that in the beam as a whole. This is observed as a core and a jet or jets.
- Beams may entrain material and decelerate gradually, dissipating much or all of their energy in jet emission and producing an FRI source; or they may be stopped at the ends of a source in a strong shock, producing an FRII source. Which of these processes actually occurs depends on the power of the jet and the environment of the radio source. Sources with structure intermediate between FRI and FRII exist either on the borderline in jet power or in particularly unusual environments.
- Where strong shocks occur, particle acceleration takes place by a first-order Fermi mechanism. Shocks advance with a velocity given by ram pressure balance between the jet and the external medium. The material left behind after the shocks inflates to form the lobes. Depending on the Mach number and density of the jet, there may be backflow from the hot spots. The large-scale structure of the lobes is determined largely by the environment, though our observations of the source may be dominated by orientation effects if it is close to the line of sight. The total luminosity of a source is a function both of the jet power and of the source age.

- Unified models are correct at some level; orientation effects are important. One-sided jets are produced by beaming, as is the Laing-Garrington effect.
- There is a relationship between the total radio power, the inferred beam power, and the nuclear emission line luminosity; these are all correlated with some measure of the power of the central engine. Scatter is introduced in the correlation by environmental effects.

1.7 Unanswered questions

This review has left a number of questions unanswered. Some require the development of new observational techniques. All the results, true or conjectural, described above would benefit from observations of a large sample of objects. However, there are some questions that can be addressed with a relatively small number of good observations.

Details of the structure and magnetic field configurations in jets and hot spots are necessary to distinguish between the relatively complicated models for source structure now being put forward. The high-frequency imaging work in this thesis will help to provide them.

In spite of the popularity of unified models, there is a lack of direct evidence for the relativistic velocities they require in the jets and beams. In this thesis I will try to test the predictions of unified models and constrain the physical parameters of radio sources. Unbiased samples allow some direct tests which could permit us to reject unified models on the one hand or simple models of side-to-side asymmetry on the other.

The question of what causes jet emission is a fundamental one which has been neglected. In the FRI objects, the turbulent-jet model provides a means for the bulk kinetic energy of the jet to be translated into emission. In FRIIs, in which the beams are selected to be efficient and ‘designed’ to be unaffected by fluid-dynamical instabilities, what are we actually seeing when we see the jet, and why? The theoretical and modelling work necessary to answer this question is outside the scope of this thesis, but observations can provide some constraints on the efficiencies of jets in general and their dependences on particular environments.

1.8 Conventions

Throughout this thesis I use a Friedman cosmology with $H_0 = 50\ \mathrm{km\,s^{-1}\,Mpc^{-1}}$ and $q_0 = 0$. B1950 co-ordinates are used.

Figure 1.2: Cartoon showing the simple unified models

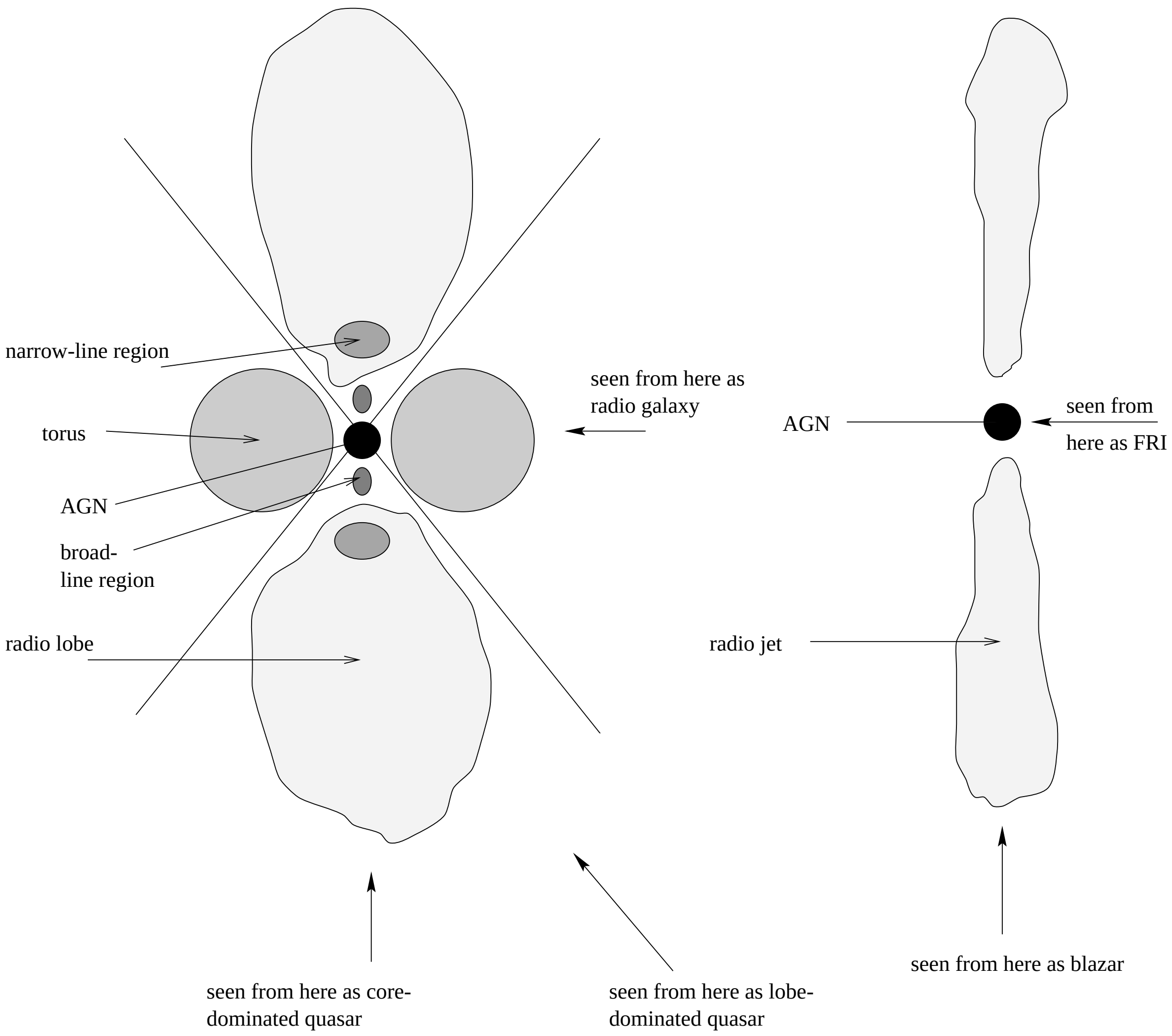

Left: unification of FRII radio galaxies, FRII quasars, and core-dominated quasars. Right: unification of FRI radio galaxies and BL Lac objects. Not to scale.

Chapter 2

The observations

This chapter gives an overview of the technique of aperture synthesis, and describes the details of the observing and reduction procedures, which apply to all the sources I observed and describe in subsequent chapters.

2.1 Aperture synthesis

The principles of aperture synthesis and interferometry have been extensively discussed elsewhere (see Thompson, Moran and Swenson 1986 for a review): here I give a summary only.

In order to achieve sub-arcsecond resolution at radio frequencies apertures many kilometres in diameter are required. This is only possible through aperture synthesis (Ryle & Hewish 1960) in which signals from many distinct antennae are correlated to build up effectively a single though sparsely-sampled large aperture. Each pair of antennae when used as an interferometer samples one point of the Fourier transform of the sky, corresponding to a particular baseline and orientation: in the approximation that the telescope is two-dimensional, these points can be specified by co-ordinates (u,v) whose units are conventionally wavelengths of the observing frequency. The raw data obtained from a synthesis telescope is then the complex amplitude (equivalently, the amplitude and phase) associated with every point sampled in *uv* space: these data points are known as visibilities.

A synthesis telescope has a resolution (θ_r) determined by its longest baseline: unlike conventional telescopes, it also has a largest-scale structure which it can image (θ_m), determined by the shortest baseline. In order to make images containing all the flux from a particular object it is necessary that θ_m be larger than the largest angular size of the object. Otherwise the map will be misleading in its large-scale structure.

The fundamental limit on the field of view of a synthesis telescope is the response of a particular antenna to the sky, known as the primary beam. This is determined by the size of the individual antennae. Often more important in practice are the limits imposed by bandwidth smearing (chromatic aberration: errors introduced by the assumption that radiation is monochromatic), time-averaging smearing (errors introduced by assuming that the visibilities are not time-variable over the integration time used: in fact there is a finite change in the relative phases of different objects as the Earth rotates) and non-coplanar baselines (the breakdown of the two-dimensional approximation).

2.2 The VLA

The Very Large Array is currently the best instrument for detailed imaging of large radio sources. This telescope, operated by the U.S. National Radio Astronomy Observatory, is described in the document ‘Very Large Array Observational Status Summary’ available from the NRAO. Here I give a summary of the main features of the VLA relevant to our project.

The VLA is an aperture synthesis telescope comprising 27 antennae arranged in the form of an inverted Y. The northern arm of the Y is aligned 5 degrees east of north so that there are no purely east-west baselines, and the distance of the *n*th antenna along each arm approximately follows the power-law 1.716^n; these features reduce redundancy in sampling of the *uv* plane. The resolution of the VLA is varied by movement of the antennae; there are four possible configurations, designated A, B, C and D, on size scales in the ratio 32:10:3.2:1. The VLA operates at a large number of different frequencies. For most of the imaging work described in this thesis, we chose 8.4 GHz (X band), whose low-noise receivers allow an excellent compromise to be made between resolution and sensitivity. The other main VLA frequencies that I used were 1.4 GHz (L band) and 15 GHz (U band). Each of these was normally divided into two independent frequency channels which were added together at the imaging stage; the precise frequencies normally used for these two channels, together with the resolutions and maximum size-scales for these frequencies (taken from the 1993 VLA status summary) are shown in table 2.1.

It can be seen from table 2.1 that combining *uv* data from different configurations of the VLA provides (in principle) a ‘spatial dynamic range’ (the ratio between the smallest and the largest scales that can be imaged) of 750: it was this feature that led us to choose the VLA as the main telescope for these projects. In general, we observed the target sources in several or all configurations of the VLA. The resulting databases (*uv* datasets) from each array were then combined and imaged as described in the following sections.

2.2.1 Observations

The observations were made using standard VLA procedure: 3C48 and 3C286 were used as primary flux calibrators, 3C286 or 3C138 were used as polarization position angle calibrators, and point-source phase calibrators within a few degrees of the target sources were observed. All our sources have enough flux in compact features (cores and/or hotspots) for self-calibration to be successful, so the phase calibrators were only observed for short times (typically one minute) and at long intervals (around half an hour), sufficient to allow a first determination of phase corrections to be made. One bright point source was observed at a number of parallactic angles in each observing run to allow polarization calibration; this source was typically also a phase calibrator for one of the target sources to reduce scheduling overheads. Where scheduling allowed, the integration on the target sources was split into two or more runs to improve coverage of the *uv* plane, with observations of the associated phase calibrator before (and, for long runs, after) each run. We required that bandwidth smearing should decrease the peak response of the VLA by less than 5% over the size of the sources we observed; this corresponds to the requirement that bandwidth $\Delta\nu$ satisfy the condition

$$\Delta\nu < \nu\theta_r/\theta_{LAS} \tag{2.1}$$

where ν is the observing frequency, θ_r is the resolution and θ_{LAS} is the largest angular size of the source to be observed.

2.2.2 Data reduction

Calibration

All data reduction was done using the NRAO AIPS software. Calibration of the data followed the standard procedure, described in the AIPS Cookbook and elsewhere. As described above (section 2.2.1), nearby point sources were used as phase references; they were themselves self-calibrated as part of the calibration procedure and their absolute fluxes were determined by reference to the primary flux calibrators. Bad antennae or baselines at this stage showed up as large r.m.s. deviations in amplitude from the mean value or by failing to form part of a solution in phase self-calibration. I flagged any visibilities of this type.

Self-calibration

Once the data had been calibrated, the sources were split out of their original multi-source format and I treated them separately from then on. The data on each source from the different configurations of the VLA were initially also treated separately. For each source and configuration, an initial image was made and lightly CLEANed to produce a model in CLEAN components of the brightest compact features in the source (and of any point confusing sources in the field). This model was then used to phase self-calibrate the *uv* dataset; I took care to ensure that only real features were included in the model, usually by excluding all CLEAN components after the first negative one from the model and by setting a lower limit on the length of baselines included in the solution — this corresponds to ignoring the flux in extended structure, which is not represented in CLEAN components if CLEAN is not run to convergence. (The advantage of this method over using a model from VTESS is that it normally excludes artefacts, such as sidelobes of the dirty beam, which might be caused by phase errors. It might be expected that when CLEAN introduces artefacts such as the ‘rice-pudding’ effect (Black 1992), as it often did when producing a CLEAN component model for self-calibration of a high-resolution dataset, that these would affect the accuracy of the phase solutions; in fact, there were surprisingly few problems of this sort.) Occasionally negative components are necessary to represent a bright point source lying between pixels, as described in B92, and where this appeared to be the case (i.e. where negative CLEAN components were associated with a bright region on the restored map) I included them in my models.

The self-calibrated dataset was then imaged and CLEANed, and a refined model used for further phase (and sometimes amplitude) self-calibration. (It was necessary to use a cell size for the image considerably smaller than the resolution of the array being used, so as to avoid problems due to the pixel binning of the model being used for self-calibration: I typically over-sampled by a factor of 5.) I iterated this procedure until it converged on a solution, usually after two or three runs of self-calibration; convergence entailed the production of a map with no phase or amplitude artefacts (equivalently, no obvious structure in the off-source noise), or a failure to improve the CLEAN model being used, or the corrections to phase or amplitude from self-calibration being consistently small ($< 2^\circ$, 2%), or the r.m.s. noise level approaching the expected thermal noise.

Various strategies are possible for the combination of *uv* datasets (which I did using the AIPS task DBCON, without reweighting) from multiple configurations of the VLA. Self-calibration of the individual datasets tends to make positional information less accurate than the optimum available at the VLA (a consequence, again, of pixel binning of the self-calibration model). It is therefore desirable to make sure that the two datasets to be merged are well aligned, which can be done by self-calibrating one with a CLEAN model made from the other before merging. The question is then whether to calibrate the lower-resolution dataset with a model made from the higher-resolution one or vice versa. In both cases it is necessary to avoid including in the solutions areas of the *uv* plane about which no information is present in the model image. When calibrating a smaller array with an image from a larger one, it was usually possible to do this just by setting a lower limit on the baselines to be included in the solution; when doing the reverse, I found it necessary to set a limit on the baselines used in the *imaging* procedure too.

My usual practice was to use the higher-resolution dataset to self-calibrate the lower before merging. There were some cases where this did not work (for example, a combined B, C and D-configuration dataset cannot be self-calibrated with an image from the A-configuration alone, because there is insufficient information on the shortest baselines — this was a particular problem given that most of the data discussed here became available to me in the order C, D, B, A) or introduced unacceptable errors into the short baselines. Where this happened, I would attempt to self-calibrate the higher-resolution dataset with the lower. If this failed to produce acceptable results, a last resort would be to concatenate the two datasets first, make an image and then use this as a model to self-calibrate the combined dataset. In any case, using the combined dataset to make a model at some resolution for its own self-calibration often resulted in improvement. On some sources I tried more than one of these methods to verify that they converged on similar final maps. These problems resulted in the use of a variety of different strategies for producing the final datasets containing all the observations of a particular object. The intended final result was a *uv* dataset that could be imaged at any sensible resolution without exhibiting significant phase or amplitude artefacts (visible as structure in the off-source noise). This proved surprisingly difficult to achieve but was eventually possible in almost all cases.

Occasionally, it was necessary to correct for the effects of a core source that had varied between the different epochs of observation; this is clearly a problem when combining data from different array configurations, since the dirty map will appear to contain a point source with some intermediate peak value, while the multiple dirty beams with which the source is convolved will produce sidelobes corresponding to the different true values. Where this was the case, I used the AIPS task UVSUB to remove the excess flux from the dataset containing the brighter core — this is noted in the descriptions of individual sources.

Imaging

During the intermediate stages of processing, the AIPS task MX was used to produce dirty maps in total intensity and to deconvolve them, and its output in CLEAN components was used in self-calibration. I chose MX in preference to a combination of HORUS and APCLN because of its multi-field capacity (useful when including confusing sources in the deconvolution) and ability to clean fully smaller maps; its main disadvantage is that it runs more slowly than APCLN, but disc space rather than CPU time was the limiting factor in my case. The AIPS task IMAGR became available at MRAO after I had finished the bulk of the data reduction, but I have used it in preference to MX for the final maps presented in the thesis because of its superior handling of the weighting of the *uv* plane and of residuals. The robust weighting offered by IMAGR allows significant improvement in the signal-to-noise ratio for a small concession in resolution. For final maps at lower resolutions, I normally used IMAGR with robust weighting and heavy tapering of the *uv* plane, as experiment showed that CLEAN was more reliable than VTESS at reproducing the low-surface brightness regions correctly and so obtaining the correct fluxes for components. For final maps using the full resolution of the datasets, I often used a combination of IMAGR and the maximum entropy deconvolution routine VTESS (see Black 1992 for a discussion of this technique) which is computationally less intensive than deep CLEANing and produces acceptable, artefact-free images of the high-surface-brightness regions. Unfortunately VTESS could not be used in cases with distant confusing sources, as it does not have a multi-field capability as yet. Where primary beam corrections were significant, they were applied either with the task PBCOR or through the built-in facilities of VTESS. In the following chapters I shall always state explicitly what deconvolution technique was used to make the maps I present.

Images of polarization are also presented. There was seldom any need to use a maximum entropy technique in making maps of Stokes' parameters Q and U, since these maps rarely have areas of extended emission into which CLEAN can introduce artefacts; unless specified otherwise, therefore, these maps were made using IMAGR. Images of polarized intensity (corrected for Ricean bias) and polarization angle were produced from the Stokes' Q and U maps using the AIPS task COMB, and an image of fractional polarization obtained by dividing polarized by total intensity, clipping both images at a sensible noise value (usually three times the r.m.s. noise).The vectors used in maps of polarization are rotated by 90°, to give the magnetic field direction; this is legitimate provided that Faraday rotation is negligible. (As I will show later, Faraday rotation introduces errors of at most a few degrees in the angle for the majority of the sources we have considered at 8.4 GHz, provided that the integrated rotation measure is a good indicator of the resolved rotation measure across the source.)

In some cases two frequencies were available to me and I was able to make maps of spectral index and depolarization. These were made by imaging the *uv* data sets in Stokes' I, Q and U with matched longest baselines (and, where the source was not well sampled on the shortest baselines of one or both datasets, matched shortest baselines), adjusting the weighting of the two truncated datasets so as to produce similar fitted beams, cleaning to convergence and convolving with identical circular Gaussians larger than the largest axis of a fitted beam to ensure that the effective beam sizes of both maps were the same. Fractional polarization maps were then made as described above. Only points with values larger than three times the r.m.s. noise on both maps were used to compute spectral index and depolarization. Depolarization (DP) was defined as the ratio of fractional polarization at the lower frequency to that at the higher; smaller values of DP thus imply more depolarization between the two.

2.3 MERLIN

MERLIN is the Multi-Element Radio-Linked Interferometer Network, operated by the University of Manchester on behalf of the Particle Physics and Astronomy Research Council in the U.K. Its operation is described in Thomasson *et al*. (1994). It consists of eight antennae (not all of which are typically in use) and has longer baselines than the VLA, leading to higher resolution but worse sensitivity to extended structure. The parameters for the frequencies of interest (1.4 and 5 GHz) are given in table 2.2. These assume that MERLIN is operating in wide-field mode (imaging the 16 MHz bandwidth in 16 distinct channels, to avoid the bandwidth-smearing effect discussed above) and using multi-frequency synthesis (Conway, Cornwell and Wilkinson 1990) to increase the *uv* coverage.

MERLIN data can be combined with VLA data to provide high spatial resolution while retaining sensitivity to extended structure; the VLA supplies the short baselines missing from MERLIN's *uv* plane coverage.

2.3.1 Observations

Observations with MERLIN are planned and carried out by the MERLIN staff. MERLIN observations must be made over a period of at least twelve hours (or as much of this as is possible given the elevation limits of the antennae) to achieve the necessary *uv* plane coverage. Frequent observations of phase calibrators, which must be compact but need not be true point sources, are interleaved with the observations of the target source. 3C286 is used as a polarization angle and flux calibrator; this ensures consistency with the flux standard of the VLA. An additional 'point source calibrator' is also observed.

As described above, *uv* coverage (and so image fidelity) is greatly improved by the technique of multi-frequency synthesis, in which MERLIN observes a given source at frequencies which may differ by up to 10%. Where MERLIN images are presented, the frequencies used will be listed.

2.3.2 Data reduction

MERLIN data start out as files known as 'd-files'. Initial data editing and the first stages of calibration (bootstrapping the point source calibrator flux with the calculated flux from the flux calibrator) are done at this stage. The data can then be written out, with the calibration applied, in FITS format and imported into AIPS using a 'pipeline' process which automatically completes the initial calibration (applying amplitude gain solutions and bandpass calibration derived from the point source calibrator, phase calibration and polarization calibration), splits the required source into single-source format and optionally carries out several iterations of mapping and self-calibration (as described above). The self-calibration and imaging can then proceed essentially in the same way as described above for the VLA, with the exception that the different frequencies of observation are initially different files and must be concatenated (with the AIPS task DBCON) before final maps can be made. MERLIN data are combined with *uv* files from the VLA in the same way as described above for combining different configurations of the VLA, although care is necessary as the MERLIN data are weighted according to the different properties of the array's component antennae.

2.4 The Ryle Telescope

This is the name given to the refurbished Cambridge 5-km telescope, an east-west synthesis array operating at 15 GHz only. It is mainly used for observations of the Sunyaev-Zel'dovich effect towards distant clusters, but is occasionally available for other observations. Its resolution is declination-dependent and low (order of a few seconds of arc, depending on the configuration of the antennae) and so it has only been used in this thesis to provide information which complements results from the VLA. Images are made by an essentially automatic process and may be lightly CLEANed. The Ryle telescope is not capable of measuring polarization at present.

Table 2.1: The primary beam, resolution and maximum structure scale for the VLA at 1.4, 8 and 15 GHz

Band	Frequencies	Primary	A		B		C		D	
	(GHz)	beam[a]	θ_r	θ_m	θ_r	θ_m	θ_r	θ_m	θ_r	θ_m
L	1.465, 1.385	1800	1.40	38.0	3.9	120.0	12.5	420.0	44.0	900.0
X	8.415, 8.465[b]	320	0.24	7.0	0.7	20.0	2.3	60.0	8.4	180.0
U	14.7, 15.2	180	0.14	4.0	0.4	12.0	1.2	40.0	3.9	90.0

---

[a] All angles in arcseconds.

[b] These were the default VLA frequencies at this band until February 1996.

Table 2.2: The number of antennae, resolution, maximum size scale and maximum unaberrated field of view for MERLIN

Band	Frequency (GHz)	Antennae	Resolution (arcsec)	Max. size scale (arcsec)	Max. field of view (arcsec)
L	1.658	7	0.15	8	140
C	5.000	6	0.04	3.5	92

Chapter 3

Jets in FRI radio galaxies

This chapter discusses the comparatively well-studied jets in FRI galaxies and their relation to other types of jet. Observations of four FRI sources are described in detail and their implications for the physics of these jets are discussed.

3.1 A small sample of FRI sources

I observed four FRI sources at high resolution with the aim of investigating the polarization and spectral index variations across the jet and the jet-counterjet asymmetries. The sources are listed in table 3.2. Three of these are twin-jet sources and the fourth (3C 130) is a wide-angled tail.

3.2 Observations

All sources were observed with the VLA in all its configurations, as described in section 2.2.1, at both 8.4 GHz and 1.5 GHz. In addition, 3C 66B was observed at 15 GHz with the VLA and at L-band with MERLIN. The complete observational information is given in tables 3.2 and 3.3. Except where otherwise specified, the two standard observing frequencies (table 2.1) and bandwidths of 50 MHz were used for each array configuration when observing with the VLA. MERLIN observations used the wide-field mode (15 1-MHz channels) at two base frequencies of 1.413 and 1.651 GHz.

Table 3.1: The sample of FRI radio sources

Source	IAU name	z	S_{178} (Jy)	α	P_{178} (10^{24} W Hz^{-1} sr^{-1})	scale (kpc/arcsec)	LAS (arcsec)	Size (kpc)	RM (rad m^{-2})
3C 66B	0220+427	0.0215	26.8	0.50	4	0.61	700.0	424	−67
3C 75	0255+058	0.0240	28.1	0.74	6	0.67	700.0	472	–
3C 130	0449+519	0.109	16.9	0.92	76	2.72	360.0	979	–
3C 296	1414+110	0.0237	14.2	0.67	3	0.67	437.0	291	−3

Data on 3C 66B and 3C 296 were taken from Laing and Riley (in prep.: LR). Data on the other two sources were taken from Spinrad *et al*. (1985). The 178-MHz fluxes were corrected to the scale of Baars *et al*. (1977) and the spectral indices were recalculated from the data of Kellermann, Pauliny-Toth and Williams (1969); see section 5.1 for a discussion of the reasons for this. Largest angular sizes were measured from the VLA maps.

Table 3.2: Observational information for the FRI sample observed with the VLA

Source	Band	A-configuration		B-configuration		C-configuration		D-configuration	
		Date of observation	t_{int} (mins)	Date of observation	t_{int} (mins)	Date of observation	t_{int} (mins)	Date of observation	t_{int} mins
3C 66B	U	19/08/91	600	05/11/91	150	Not observed	–	Not observed	–
	X	19/08/91[4]	120	05/11/91[4]	150	10/11/94	55	06/03/95	20
	L	23/07/95	45	28/11/95	30	10/11/94	26	06/03/95	15
3C 75	X	23/07/95[3]	120	28/11/95	120	10/11/94	55	06/03/95	20
	L	23/07/95[3]	45	28/11/95	30	10/11/94	26	06/03/95	15
3C 130	X	06/08/95[2]	120	28/11/95	120	10/11/95	55	06/03/95	20
	L	23/07/95	45	28/11/95	30	10/11/94	26	06/03/95	15
3C 296	X	24/07/95	120	27/11/95	120	11/11/94	55	06/03/95	30
	L	24/07/95	45	08/12/87[1]	60	10/03/88[1]	50	07/10/88[1]	80

[1] Data kindly supplied by J.P. Leahy.

[2] Bandwidth of 25 MHz used.

[3] VLA mis-pointed by 1 minute of arc.

[4] Observed at two frequencies of 8.01 and 8.41 GHz.

Table 3.3: MERLIN observations of 3C 66B

Date	Time (hours)
18/12/1995	24
02/02/1996	10

Table 3.4: Properties of the images of FRI objects

Source	Fig. number	Region	Freq. (GHz)	Method	FWHM (arcsec)	FWHM (kpc)	σ_I (μJy)	σ_P (μJy)	Dynamic range
3C 66B	3.1	Field	1.5	C	12.50	7.6	310	–	3000
	3.2,3.3,3.7	Jet	8.2	C	0.25	0.15	25	10	7600
	3.4,3.6	Jet/counterjet	8.2	C	1.25	0.76	25	10	7600
	3.5	Counterjet	8.2	C	0.75	0.46	30	–	6000
3C 75	3.10	Whole	1.5	C	10.0	6.7	210	–	430
	3.11	Jets	8.4	C	0.75	0.50	38	11	1300
	3.12	Whole	8.4	C	2.00	1.34	35	11	1400
3C 130	3.13	Whole	1.5	C	10.0	27.2	210	–	780
	3.14	Jets and tails	8.4	CM	0.6	1.63	15	12	2000
	3.15	Spectral index	–	C	2.86	7.29	–	–	–
3C 296	3.16	Whole	1.5	C	12.0	8.0	160	–	680
	3.17	Inner jet	8.4	C	0.24	0.16	14	–	9000
	3.18	Jets	8.4	C	0.75	0.50	11	5.6	12000

Column 5 gives the deconvolution method. C denotes CLEAN and CM denotes a CLEAN/MEM hybrid as described in chapter 2. Columns 6 and 7 give the angular and corresponding linear size of the FWHM of the restoring beam used. In columns 8 and 9, σ_I and σ_P are the r.m.s. off-source noise on total and polarized intensity maps (where made) respectively. In several cases there are artefacts around cores at several times this level. The dynamic range (column 10) is defined as the ratio between the peak intensity and σ_I.

3.3 Sources in detail

For each source I observed, I show maps of the large-scale structure together with maps at high and intermediate resolutions of the jets. The properties and resolutions of these maps are tabulated in table 3.4. Negative contours are dashed on all contour maps. Position angles are defined east of north.

Polarization maps are also shown. The vector lengths represent the *degree* of polarization and the directions are perpendicular to the E-vector; they are therefore in the direction of the magnetic field if Faraday rotation is negligible. This is true (at an observing frequency of 8 GHz) for 3C 66B and 3C 296, though the polarization maps of 3C 66B have been corrected for the rotation of a few degrees implied by a constant RM of -90 rad m^{-2}, but the integrated rotation measures of 3C 75 and 3C 130 are not well known, so some care is necessary in the interpretation of polarization maps. (The RMs of these two sources will be discussed in the relevant sections.)

3.3.1 3C 66B

The literature

3C 66B is identified with an ED2 galaxy at a redshift of 0.0215 (Matthews, Morgan and Schmidt 1964). The jet in 3C 66B is one of only a few which are visible in both the optical and radio wavebands, and was originally discovered by Northover (1973): the optical jet was first detected by Butcher, van Breugel and Miley (1980). Maccagni and Tarenghi (1981) found extended X-ray emission around the source; they argued that it indicated densities sufficient to confine the lobes. Leahy, Jägers and Pooley (1986, hereafter LJP) presented detailed radio observations of the source as a whole and of the jet with the VLA at 1.4, 1.6 and 5 GHz, with the Cambridge 5-km telescope at 2.7 GHz and with the Westerbork telescope at 608 MHz, 1.4 and 5 GHz. Fraix-Burnet *et al*. (1989a, 1989b) identified five knots in the optical structure of the jet with five similarly-placed knots in the radio maps of LJP, and detected polarization in them, providing convincing evidence that the optical emission is synchrotron in origin. Macchetto, Albrecht and Barbieri (1991) presented an HST Faint Object Camera image at 3100 Å (with a resolution of 0.1 arcsec), which showed for the first time filamentary structure in the jet: Jackson *et al*. (1993: JSMM) compared this with a high-resolution (0.25 arcsec) VLA map at 15 GHz. On smaller scales, Giovannini *et al*. (1993) report unpublished VLBI observations showing a one-sided parsec-scale jet in 3C 66B in the same position angle as the bright kiloparsec-scale jet.

Overall source structure

Figure 3.1 shows a 12.5-arcsecond resolution map of the 3C 66 field at 1.4 GHz. The twin jets and lobes of 3C 66B are clearly visible. 3C 66A is the bright (2 Jy) confusing object to the northwest of the map, identified with a BL Lac at $z = 0.444$ (Hewitt and Burbidge 1987). Another bright (35 mJy) confusing object is to its northeast.

The radio nucleus

The radio nucleus of 3C 66B is variable on timescales of months. Table 3.5 summarizes the data available on the flux densities at different frequencies, generally estimated by integration of a small region around the nucleus (except in the case of the Ryle telescope observations, where the fluxes were estimated directly from appropriate baselines). Errors are due to the small uncertainty in primary flux calibration and the difficulty in ensuring that none of the surrounding diffuse structure is included in the integration.

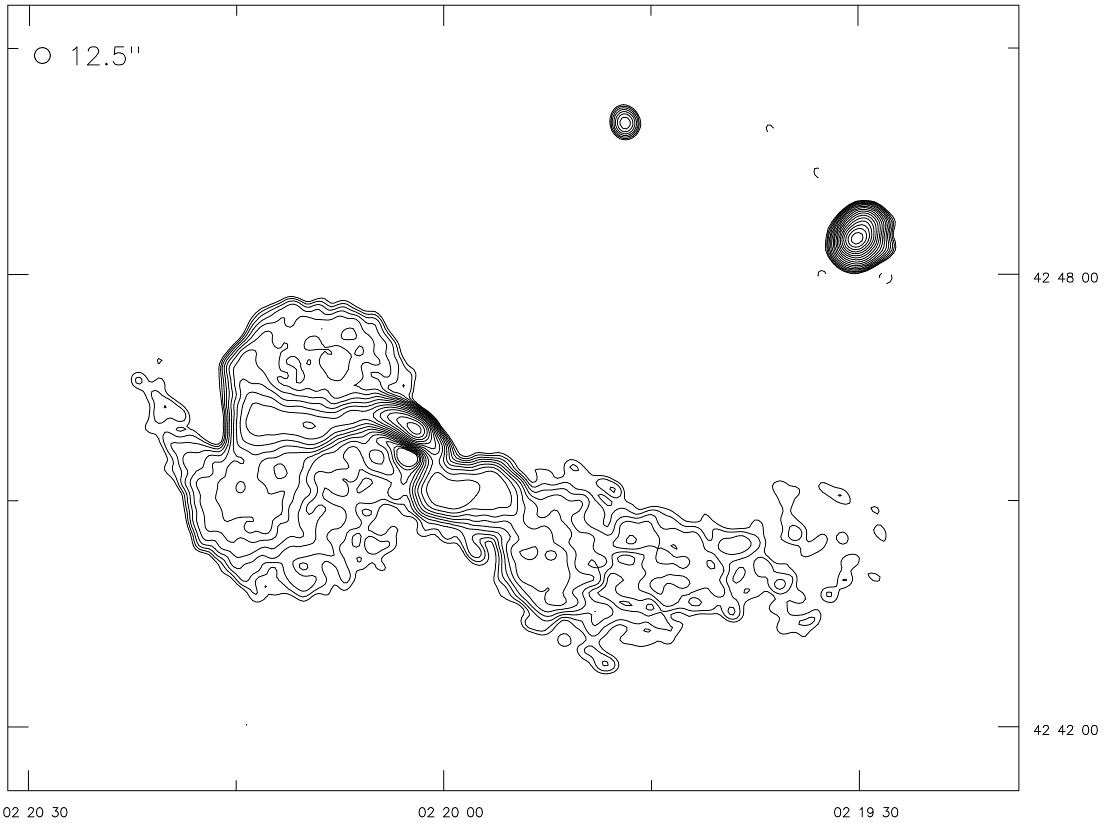

Figure 3.1: 1.4 GHz map of the field of 3C 66 at 12.50 arcsec resolution. Contours at $3 \times (1, \sqrt{2}, 2, 2\sqrt{2}, \ldots)$ mJy beam^{-1}. 3C 66B is to the southeast, 3C 66A to the northwest.

Table 3.5: Flux densities from the radio nucleus of 3C 66B

	$S_{1.4}$/mJy	$S_{1.6}$/mJy	S_5/mJy	$S_{8.4}$/mJy	S_{15}/mJy
1972 Jul[1]			240 ± 40		
1982 May[2]	188 ± 9	167 ± 10	182 ± 6		
1982 Sep[2]			256 ± 9		
1991 Jul 25[3]					207
1991 Aug 19[4]	178 ± 10	187 ± 10		223 ± 11	207 ± 10
1991 Nov 05[4]				191 ± 10	165 ± 8
1992 Jan 18[3]					172
1992 Nov[5]					175 ± 12
1994 Apr[5]					210 ± 15
1994 Nov 10[4]				238 ± 10	
1995 Mar 06[4]				213 ± 15	
1995 Apr[5]					202 ± 10
1995 Jul 27[4]	181 ± 10				
1995 Nov 28[4]	182 ± 10				
1995 Dec 18[6]	180 ± 10	185 ± 10			
1996 Feb 02[6]	182 ± 10	184 ± 10			

[1] Northover 1973. [2] LJP. [3] JSMM. [4] My VLA observations. [5] My Ryle telescope observations.
[6] My MERLIN observations.

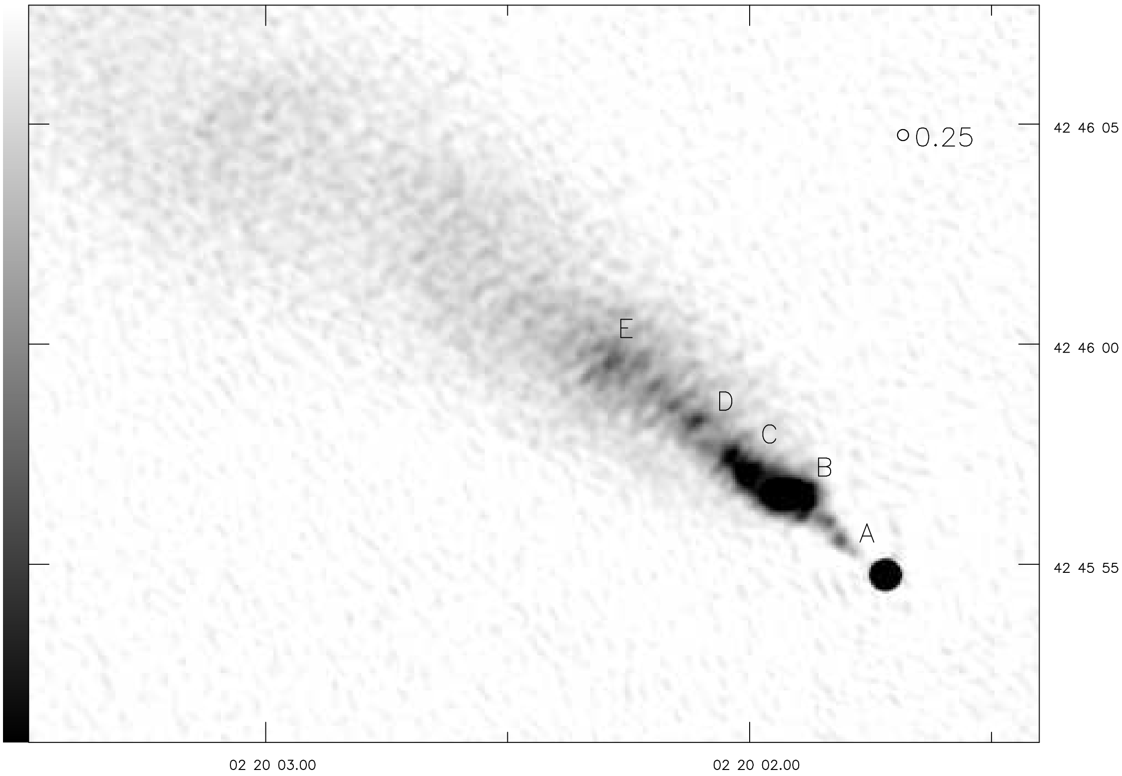

Figure 3.2: 8-GHz map of 3C 66B at 0.25-arcsec resolution; black is 1 mJy beam^{-1}.

Structure at high resolution

Figure 3.2 shows a linear greyscale of the 8-GHz map of the inner jet at 0.25-arcsec resolution. The 15-GHz dataset at similar resolution shows the same features but with less sensitivity; at the full resolution of the VLA at this frequency (0.15 arcsec) the noise is so high that only the radio nucleus can be detected above it. 15-GHz maps are therefore not presented.

The overall structure in my maps at this resolution agrees very well with that in the 15-GHz map of JSMM and the HST image of Macchetto *et al*. (1991). (The barring perpendicular to the jet visible on my 8-GHz image is an artefact which I believe to be due to the bright and variable nucleus.)

There are three small knots (A) at the base of the jet, the first at 0.9 arcsec from the nucleus (a projected distance of 550 pc) and the last at 1.8 arcsec (1.1 kpc). The jet becomes much brighter at knot B and reaches its brightest at about 2.9 arcsec (1.7 kpc) from the nucleus; at the same time its opening angle clearly increases. The shape of the region B is particularly interesting: the knot is at a distinct angle to

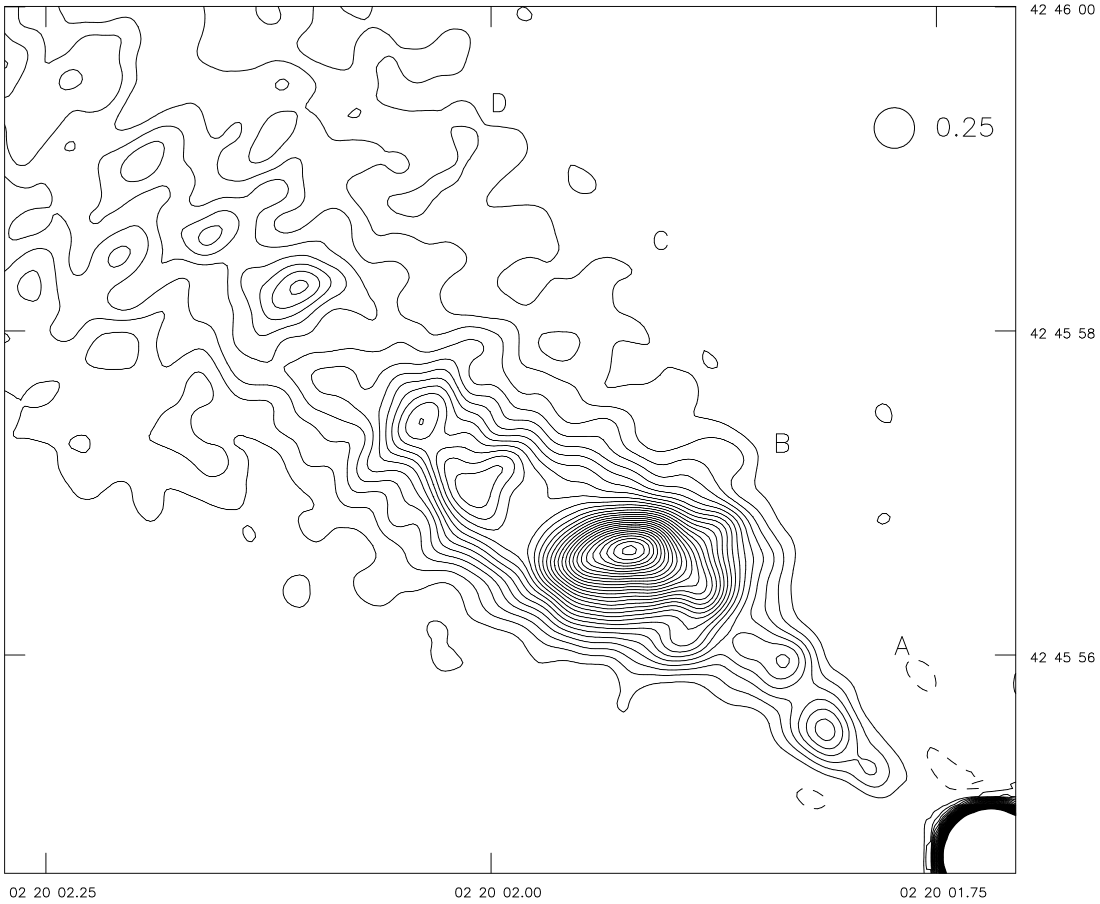

Figure 3.3: 8-GHz map of 3C 66B at 0.25-arcsec resolution. Contours at $-0.1, 0.1, 0.2, 0.3 \ldots 4$ mJy beam^{-1}. Negative contours are dashed.

both the entering and the leaving jets. The knots C, D and E are all visible on the HST image.

The images provide some evidence for the double filamentary structure claimed by Macchetto *et al*. in the optical and by JSMM at 15 GHz. However, as can be seen in the contour map (figure 3.3), even the clearest region where a double-stranded structure might be plausible (between knots C and D) involves brightness contrasts at only around the 3-4σ level. Much of the structure described in detail by JSMM is not consistent between their maps and mine. An image with still higher resolution and sensitivity is needed before a detailed analysis of the filamentary structure is warranted.

At this resolution and sensitivity the counterjet is almost invisible and no maps of it are shown.

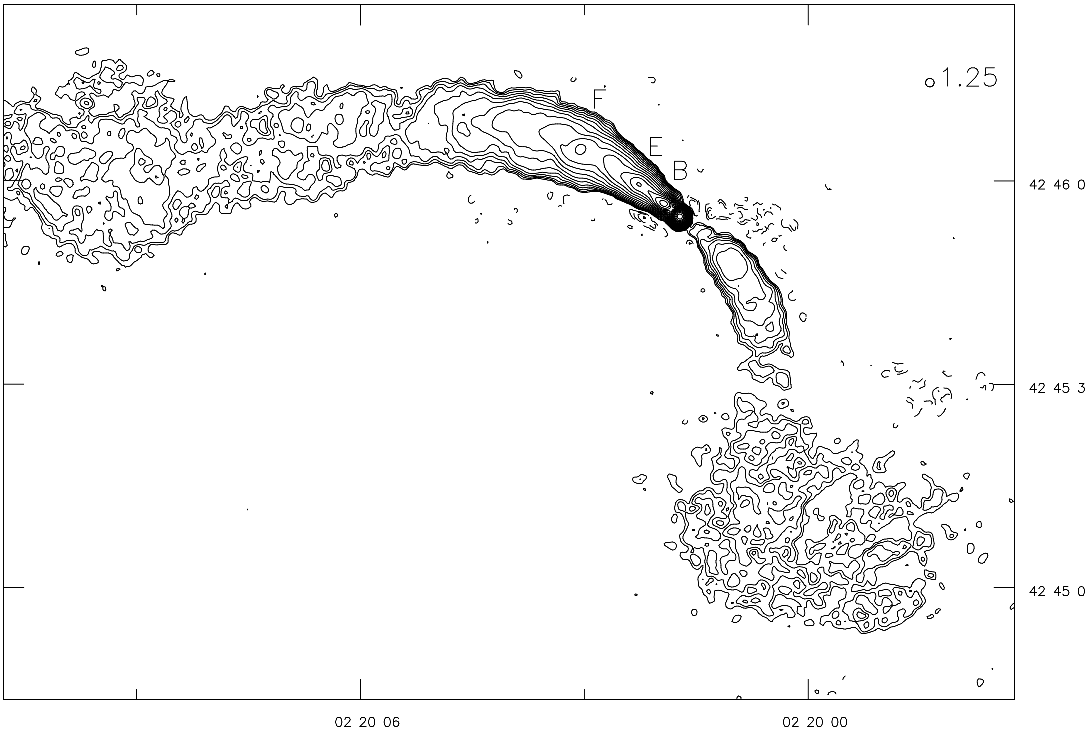

Figure 3.4: 8-GHz map of 3C 66B at 1.25-arcsec resolution. Contours at $0.1 \times (-1, 1, \sqrt{2}, 2, 2\sqrt{2}, \ldots)$ mJy beam^{-1}. Negative contours are dashed. Peak 180 mJy beam^{-1}.

Structure at intermediate resolution

Figure 3.4 shows an 8-GHz map of the jet and counterjet at 1.25-arcsec resolution (chosen to be comparable with the highest resolution available at L-band, as used in LJP): the brightest knots are labelled for comparison with the high-resolution images. The apparent lumpiness of the distant parts of the source is due partly to lack of sensitivity and partly to comparative undersampling of the *uv* plane at these structure scales. Low-surface-brightness extensions to the east and west are not shown.

This map shows for the first time structures in the fainter parts of the source. Particularly notable on the jet side are the quasi-periodic variations in the direction of the ridge line of the jet, starting on a small scale near knot E at about 10 arcsec (6 kpc) from the nucleus and increasing in amplitude for a further 25 arcsec before disappearing into the noise. These are visible at all frequencies.

The opening angles of the jet and counterjet appear more or less constant, although there is a point about 40 arcsec from the nucleus at which the jet appears to stay constant in width for a while. This is con-

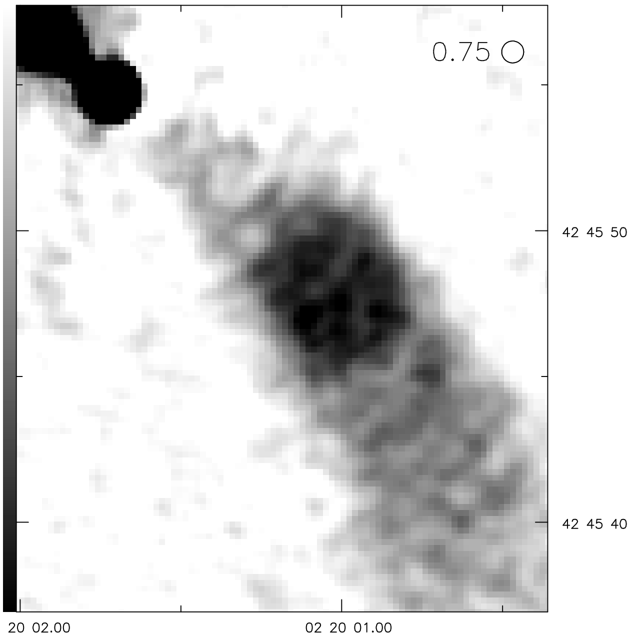

Figure 3.5: 8-GHz map of counterjet at 0.75-arcsec resolution; black is 0.4 mJy/beam.

sistent with the results of LJP.

Detailed structure in the counterjet is seen for the first time in the 8 GHz images (see figure 3.5). The counterjet appears much more diffuse than the jet, and is not so consistently centre-brightened.

Polarization structure

Figure 3.6 shows maps of degree of polarization and magnetic field angle at 8 GHz and 1.25 arcsec resolution. (Maps at other frequencies are similar but noisier and are not shown.) The nucleus itself appears to be polarized at the 0.5% level. The jet and counterjet are quite highly polarized (between 10 and 40% in the main part of the jet, and 20 – 50% in the counterjet) implying well-ordered magnetic fields on kpc scales. On the jet side the magnetic field is parallel to the jet for the first 1.2 pc (2 arcsec), best seen in the high resolution polarization map (figure 3.7): in the bright knots B and C there are regions where it is at an angle of about 30° to the jet direction (more or less aligned with the direction of elongation of the knot B) and by knot E (8 arcsec from the nucleus) the *B*-field in the centre of the jet is perpendicular. Figure 3.8 shows the variation of degree of polarization as a function of distance along the jet, taken along the ridge line; the change in polarization angle takes place in the region of depolarization between 6 and 10 arcsec (a projected distance of $\sim$ 2.5 kpc).

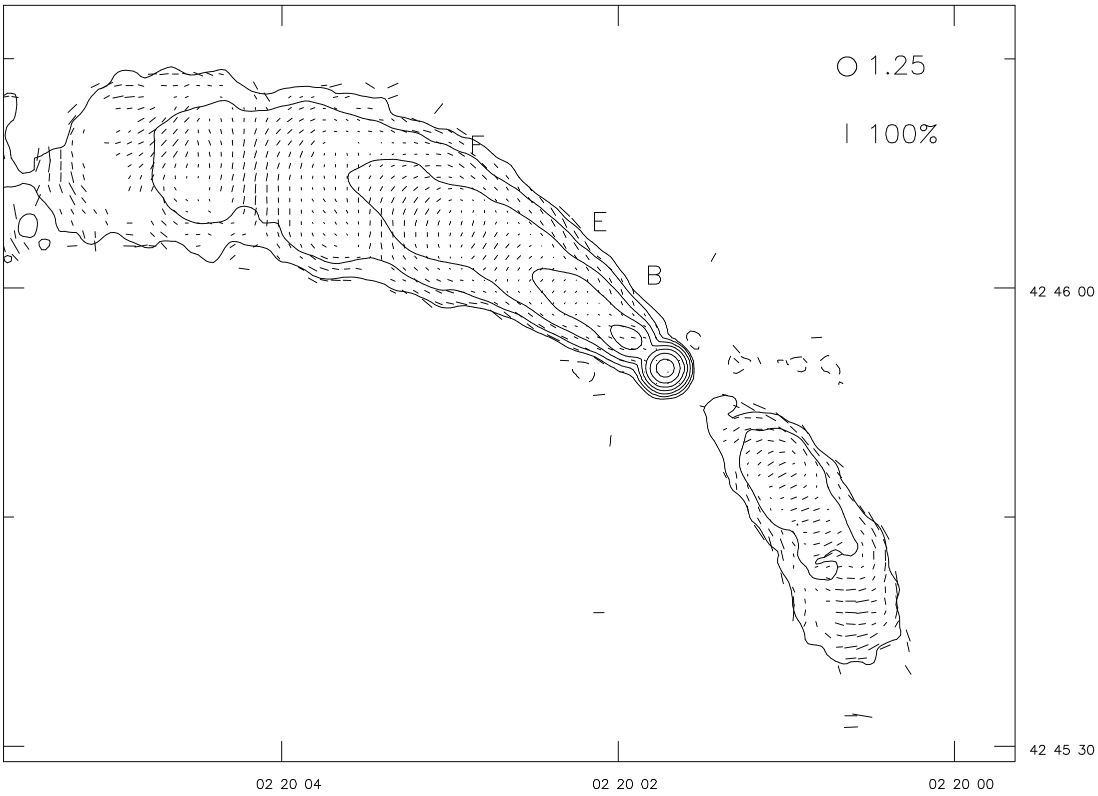

Figure 3.6: 8-GHz polarization map at 1.25-arcsec resolution. Contours at $0.2 \times (1, 2\sqrt{2}, 8, \ldots)$ mJy beam^{-1}.

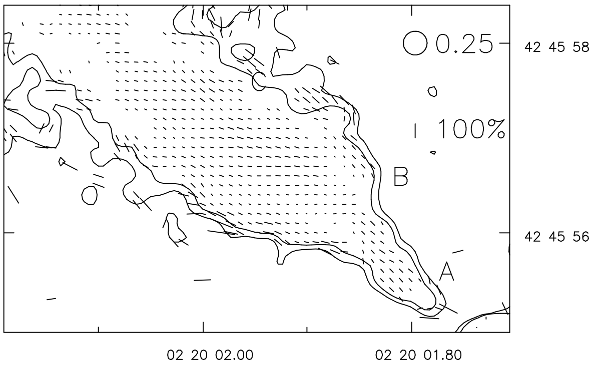

Figure 3.7: Detail of 8-GHz polarization map at 0.25-arcsec resolution. Contours at 0.1, 0.2 mJy beam^{-1}.

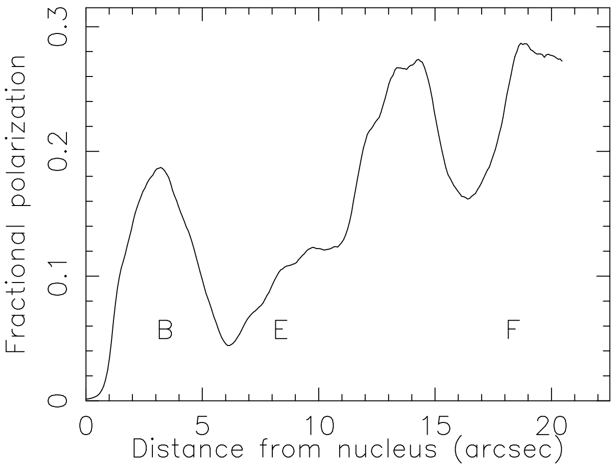

Figure 3.8: Variation of fractional polarization with distance along 3C 66B's jet.

At the edges of the jet the field remains parallel, with a higher degree of polarization (typically 30%, compared with around 10% in the jet centre). There is a clear region of depolarization between the parallel and perpendicular field alignments. A remarkable circular field structure can be seen centred at 18 arcsec from the nucleus, coincident with the large bright region F and presumably related to the change in jet direction that begins at about this point. Further out from the nucleus the field in the jet centre follows the wiggles in the jet closely, remaining more or less perpendicular to the jet axis in spite of its changes in direction. There are some indications that the parallel-field sheath is still present at 30 arcsec or more away from the nucleus.

The counterjet is unpolarized above the 3σ limit close to the nucleus. Further out, between 6 arcsec and about 15 arcsec, there is a clearly delineated central region with perpendicular B-field surrounded by a sheath with B-field parallel. The sheath in the counterjet appears to be about 1.3 arcsec (800 pc) thick, as opposed to that in the jet which is typically 0.8 arcsec (500 pc) across (just resolved in my 0.75-arcsec resolution maps). The lower limits placed on the sheath thickness by LJP were due to the lower sensitivity of their observations.

Further still from the nucleus, my polarization data are in good agreement with those of LJP, showing the highly polarized terminations of the jets.

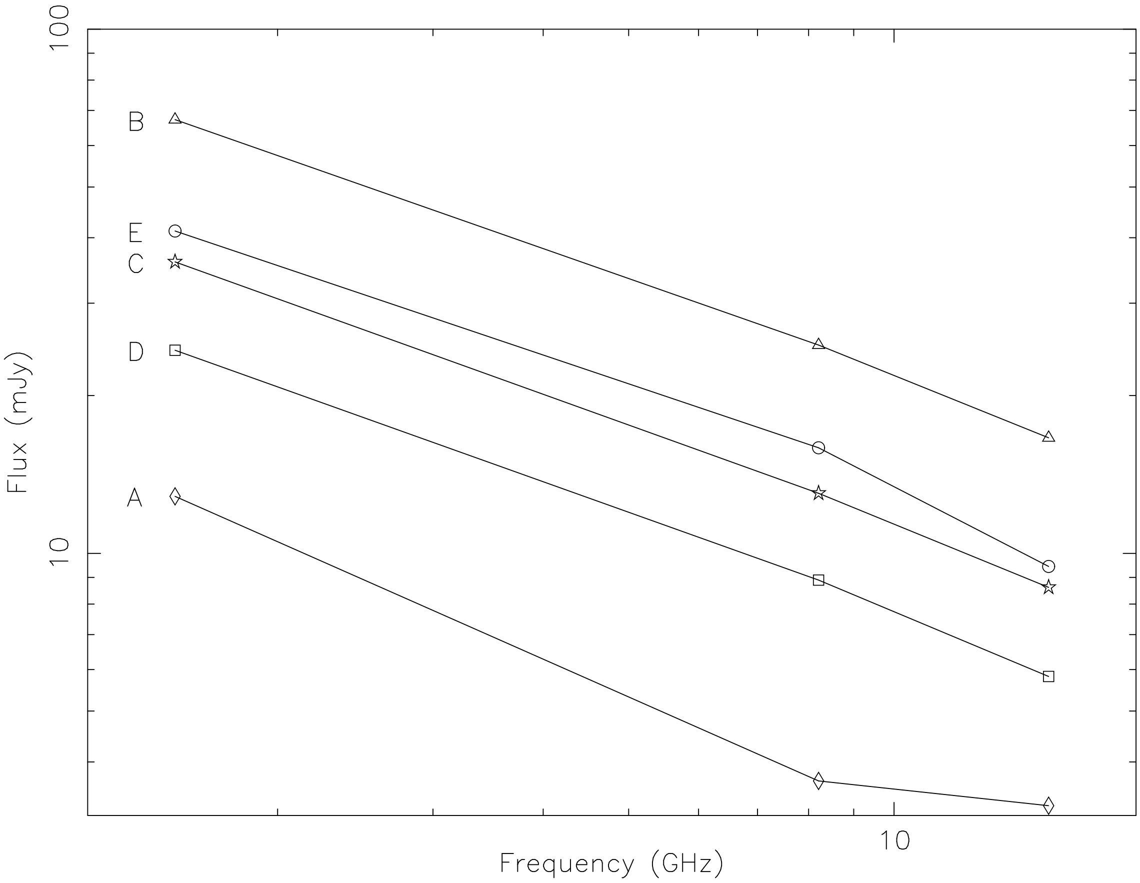

Figure 3.9: Spectra of the jet knots of 3C 66B.

Spectral indices, depolarization and rotation measure

The spectra of the five knots in the inner jet are shown in figure 3.9; the fluxes were measured by integrating over identical rectangles on VLA and MERLIN+VLA maps made at 0.25-arcsec resolution. Knots B–E show similar spectra, with the spectral index being typically 0.6. There is some indication of a steeper spectrum between 8.2 and 15 GHz, particularly in the knots further from the core, but this is possibly the result of undersampling of the 15 GHz dataset with respect to the other two. The knots in the inner jet, labelled A, have a steeper spectrum ($\alpha = 0.75$) between 1.5 and 8.4 GHz than the rest. (The 15-GHz data point here is contaminated by artefacts surrounding the core, and should be ignored.) These results are consistent with the high-resolution radio-optical spectral index maps of JSMM, which show a constant spectral index of 0.8 – 0.85 in the region within 5 kpc (8 arcsec) of the nucleus over the central 1 kpc of the jet.

On larger scales, matched-baseline spectral index mapping between 1.5 and 8.4 GHz suggests there is little change in the spectral index of the jet until approximately 40 arcsec (linearly) from the core, corresponding to the drop in surface brightness at the eastern edge of figure 3.6. The mean spectral index over this distance is 0.6 ± 0.05; after this it steepens rapidly to ~ 1. There is no evidence for spectral changes *across* the jet. The counterjet, where good measurements are available, has a similar spectral index (0.6 ± 0.1) until its disappearance. These results are in agreement with the lower-frequency measurements of LJP.

My data confirm, as far as is possible, the rotation measure map of LJP at 1.25-arcsec resolution. The Stokes' Q and U datasets of matched-baseline maps at 1.5 and 8.4 GHz are noisy, and so depolarization is not easily measured, but there appears to be no difference between jet and counterjet (DP ≈ 0.85 in both over the inner 25 arcsec). There is thus no evidence (so far) for any sort of Laing-Garrington effect in this source, though the inner jets are not the ideal place to look for it.

3.3.2 3C 75

The literature

3C 75 is the only clear example of a powerful source which is apparently created by outflows from two AGN in the same host galaxy (Parma, Cameron and de Ruiter 1991 show a possible second example which may, however, simply be projection of two unrelated objects). In the radio, it has not been well studied; the only published images which show it in enough detail to even begin to make the structure clear are those in Owen *et al*. (1985), who argue that the similar twists in the jets alone are sufficient to show that the two sources are spatially close. Optically, the host galaxy lies at the centre of the cluster

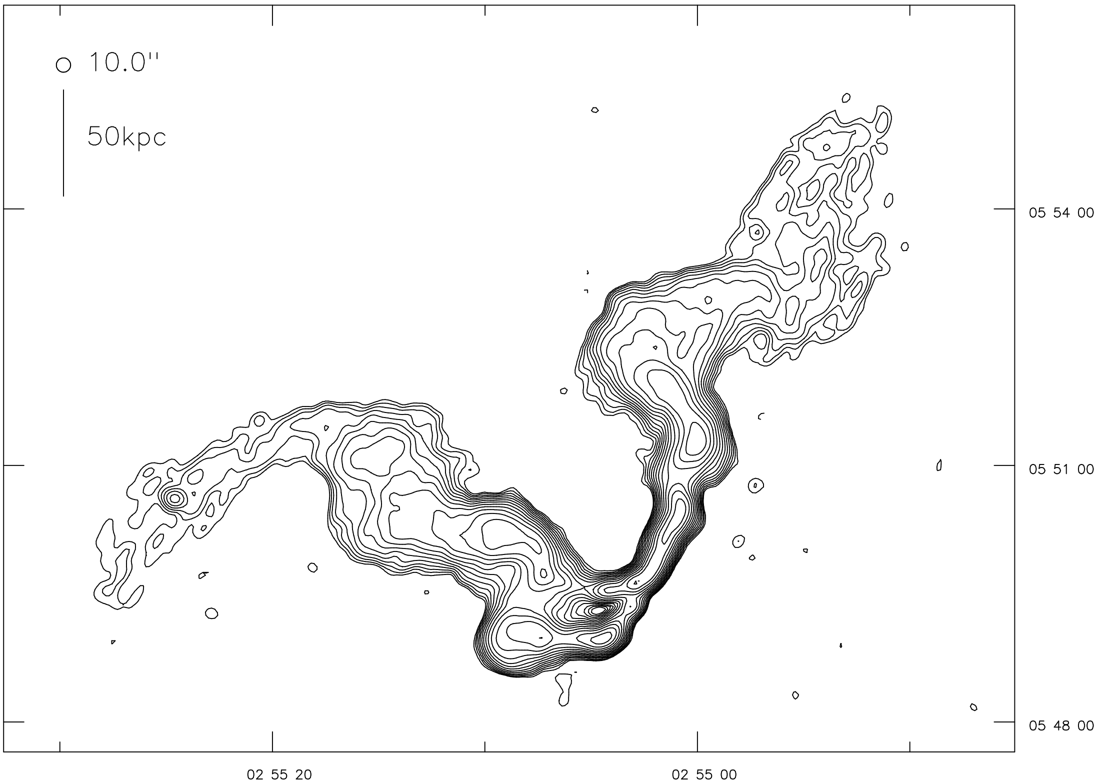

Figure 3.10: 1.4 GHz map of 3C 75 at 10.0 arcsec resolution. Contours at $1 \times (1, \sqrt{2}, 2, 2\sqrt{2}, \ldots)$ mJy beam^{-1}.

Abell 400, and there is an EINSTEIN detection of an X-ray halo surrounding it (Caganoff, Bicknell and Carter 1985 show the radio image superposed on the X-ray). The galaxy itself has a dumb-bell profile which can be interpreted as that of two ellipticals in superposition (Colina and Pérez-Fournon 1990) with the positions of the radio nuclei overlaying the two brightness peaks. Balcells *et al.* (1995) present evidence that the two AGN are considerably further apart than their projected separation distance would imply, though still associated.

Overall source structure

A low-resolution map of 3C 75 shows the whole source; the emission tails back into the noise. At this resolution it is only just possible to make out the multiple jets.

Table 3.6: Flux densities of the radio nuclei of 3C 75

Date	3C 75 N		3C 75 S	
	$S_{1.4}$/mJy	$S_{8.4}$/mJy	$S_{1.4}$/mJy	$S_{8.4}$/mJy
1994 Nov 10	–[a]	56	–[a]	17
1995 Mar 06	–[a]	51	–[a]	11
1995 Jul 23	26	60	18	22
1995 Nov 28	31	61	15	23

[a] Not possible to distinguish core from jet emission.

The radio nuclei

The radio nuclei of 3C 75 both varied over the timescale of my observations; I measured the variation by fitting Gaussians to the nuclear components. Details are shown in table 3.6.

The jets

Figure 3.11 shows the inner jets of both sources in 3C 75. Neither source has particularly one-sided jets. The sidedness of 3C 75N appears to change with distance along the jet — the eastern jet is brighter at first but the western one is brighter further out. Images at the full resolution of the dataset, ~ 0.3 arcsec, show that the eastern jet is indeed the brighter on the smallest scales. The jets of 3C 75S are very faint for the first 11 kpc; the point where the southern jet brightens is clear on this map, but the northern jet appears to cross the western jet of 3C 75N as or before it brightens. The magnetic field in the inner jets of 3C 75N is parallel to the source axis on both sides, turning to a perpendicular configuration 6 kpc from the core. The *B*-field in 3C 75S is not as clear, because of the faintness of the inner jets, but from the few points with sufficient signal it would seem that the field is parallel to the jet axis up to 8 kpc from the core (on the S side; less on the N side) and that it is definitely transverse to the source axis from 11 kpc or so.

The truncated appearance of the jets of 3C 75N is interesting — from this map it would appear that the western jet crosses the northern jet of 3C 75S and stops shortly after doing so, at around the same distance from the core as the end of the eastern jet. From larger-scale maps of the source it seems clear that 3C 75N is not a young object — the majority of the source's flux, at least on the western side, appears to have come from it — but perhaps this gap, though not seen on the maps of Owen *et al*. (1985), is evidence for intermittent flow in the beams.

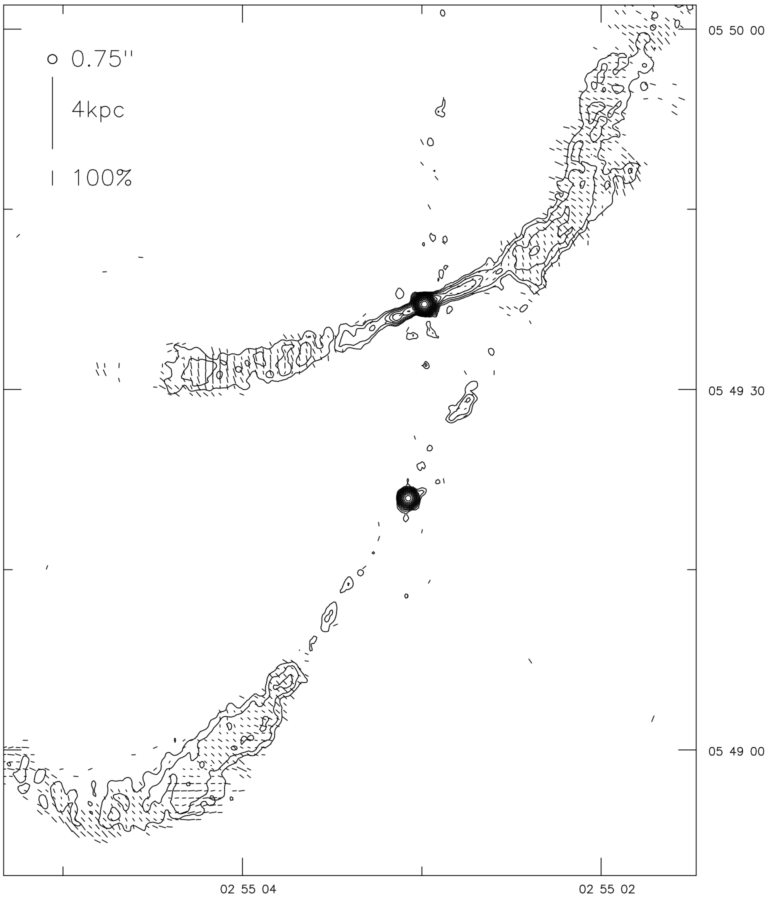

Figure 3.11: 3C 75 at 0.75 arcsec resolution. Contours at $0.2 \times (-\sqrt{2}, -1, 1, \sqrt{2}, 2, 2\sqrt{2}, \ldots)$ mJy beam^{-1}.

Intermediate scales

A map at 2.0-arcsec resolution (figure 3.12) allows the magnetic field direction in the outer parts of the source to be seen clearly. It is mostly transverse to the jet direction, as in the other twin-jet sources, and follows bends in the jet; in the regions where the jet expands, at the northwestern and eastern edges of this map, it follows the edges of the region. This polarization behaviour (compare 3C 130, below) reinforces the overall impression that the sources should be classed as twin-tailed jets rather than (as suggested by O'Donoghue, Eilek and Owen 1993) as wide-angled tails.

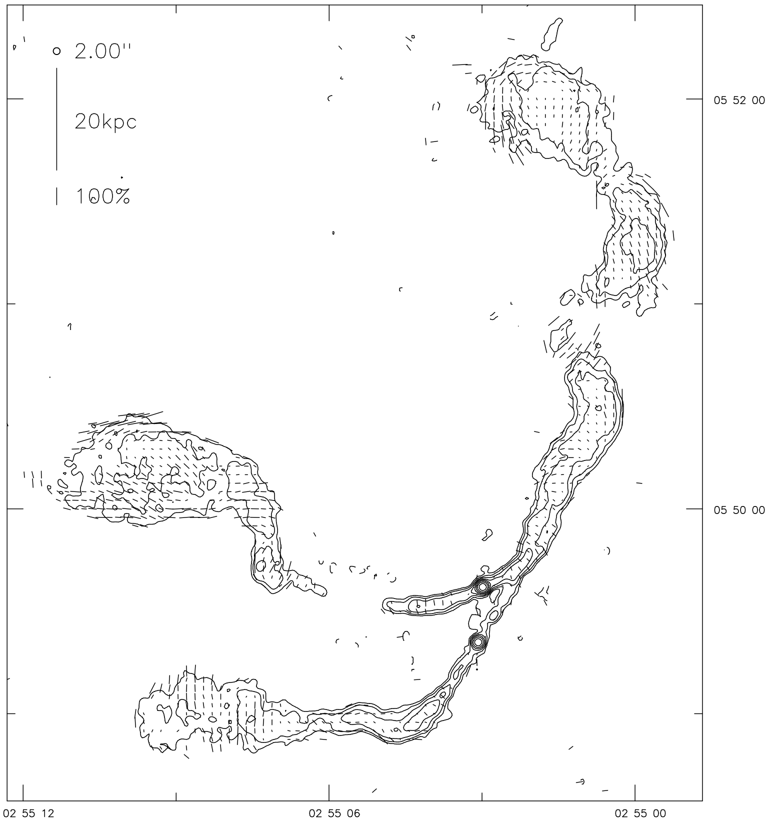

Figure 3.12: 3C 75 at 2.00 arcsec resolution. Contours at $0.2 \times (-2,-1,1,2,4,\ldots)$ mJy beam^{-1}.

Spectral index and depolarization

The spectral index between 1.5 and 8.4 GHz shows moderate steepening along the jet, with the inner jets having $\alpha \approx 0.5$ and the ends of the jets seen on figure 3.12 having $\alpha \approx 0.8$ to 0.9. The maps are noisy, however.

The source is depolarized, with a mean DP of around 0.4 between 1.5 and 8.4 GHz; the rotation measure is not constrained adequately by these two frequencies (i.e. there are variations of more than 36 rad m^{-2}). This is as expected for a source at the centre of a cluster. There is no obvious difference in DP in different parts of the source.

3.3.3 3C 130

The literature

3C 130 is a wide-angle tail source, although unusually its tails are essentially straight. Leahy (1985) shows the previous high-resolution radio map, while Jägers (1983) has a lower-resolution Westerbork image which shows the field of the source. The host galaxy is classed as a DE2 by Wyndham (1966) and appears to lie in a cluster, although strong galactic reddening makes optical identification of the cluster members difficult. The EINSTEIN detection of extended emission (Miley *et al*. 1983), the nearby aligned sources (Jägers 1983) and the many mJy radio sources in the field at 1.4 GHz make it plausible that the object is the dominant member of a cluster, as WATs normally are (chapter 1). Leahy (1985) also attempts to constrain the RM distribution of the source, but notes that it depolarizes rapidly (particularly in the S lobe) so that few good measurements are available.

Overall source structure

Figure 3.13 shows the large-scale structure of the source. There are several pronounced bends, in spite of the overall straightness of the source. The sudden change in direction at the end of the S tail is particularly noticeable; this feature is similar to several seen in the small sample of O'Donoghue, Owen and Eilek (1990). The source disappears into the noise on these images and may be even longer than the $\sim$ 1 Mpc seen here. Note the classical double source to the east, one of many radio objects which are nearby in projection.

The jets and hot spots

The high-resolution image in figure 3.14 shows two very well-collimated jets emerging from the core. The jets are reasonably symmetrical. The northern jet in 3C 130 is brighter, noticeably so at bends; over the inner section where both jets are straight (approximately 9 arcsec) the difference in brightness is roughly a factor 1.4. (This symmetry in the brightness of jets is reasonably common among WAT sources, compared to, say, FRIIs; e.g. O'Donoghue *et al*. 1993. The 'archetype' of the class, 3C 465 (Leahy 1984), appears to be unusual in having a very one-sided jet.) The bends in the jets, particularly the northern one, are very striking. The beams may be ballistic, implying some short-timescale wobble of the collimator ('garden-hose' behaviour), but if this is the case it is surprising that the jets are brighter at bends and that there is no symmetry between the jet and counterjet. If they are not it is equally remarkable that they remain collimated while undergoing oscillations of such large amplitude in so short a distance. The northern jet terminates in a hot spot, but there is a long filament which leaves the hot spot

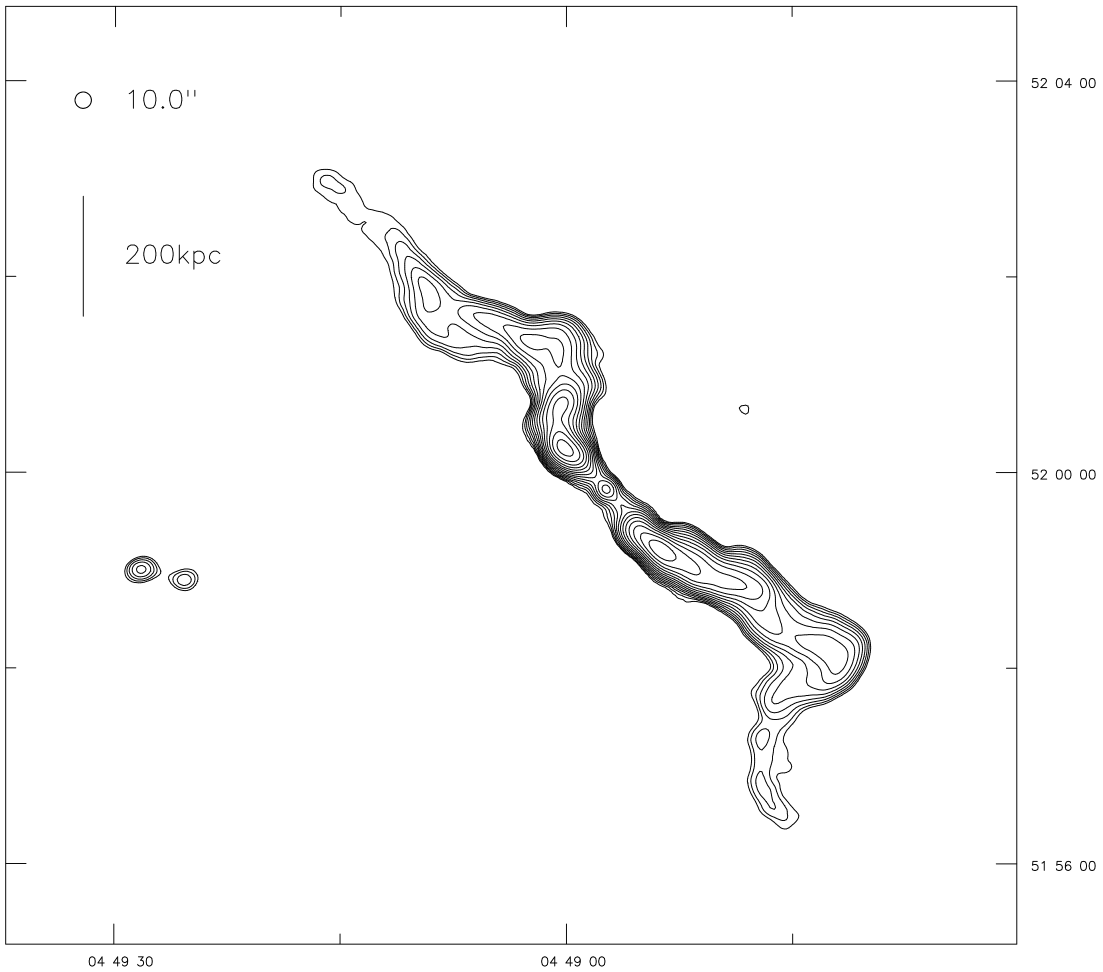

Figure 3.13: 1.4 GHz map of 3C 130 at 10.0 arcsec resolution. Contours at $1.5 \times (1, \sqrt{2}, 2, 2\sqrt{2}, \ldots)$ mJy beam^{-1}.

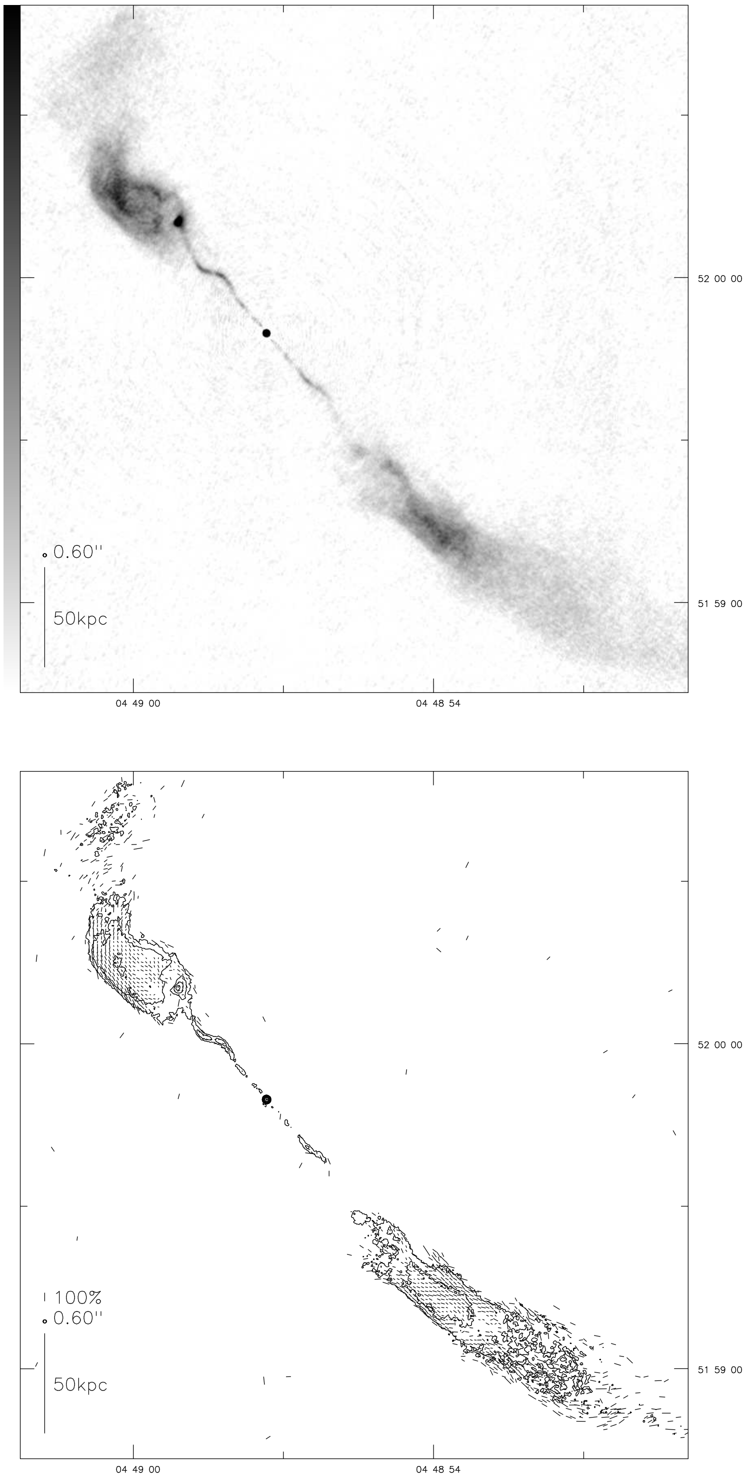

Figure 3.14: 3C 130 at 0.60 arcsec resolution. Above: linear greyscale; black is 0.5 mJy beam^{-1}. Below: contours at $0.1 \times (-2, -1, 1, 2, 4, \ldots)$ mJy beam^{-1}.

to the north, possibly suggesting some continued collimated outflow. At this resolution there is little compact structure at the end of the southern jet; the ‘hot spot’ seen in the maps of Leahy (1985, 1993) is resolved, with a size of around a second of arc. By contrast, the northern hot spot is only just resolved at the full resolution (0.24 arcsec; maps not shown) and its brightest component has a minor axis of ~ 0.3 arcsec. This use of the term ‘hot spot’ is stronger than that of O’Donoghue *et al*. (1993), who only used it to indicate a brighter, broader region; the hot spot seen here is comparable with those in FRIIs (see chapter 4). The northern jet is resolved at the bends at full resolution, and has a cross-sectional width of up to 0.8 arcsec. The jets have magnetic field parallel to their length where polarization is detected, assuming negligible Faraday rotation (see below); the field follows the bends in the northern jet. This confirms the prediction of Leahy (1993) that the jets in WATs would turn out to have fields similar to the jets in powerful FRIIs. The field in the hot spot is transverse to the jet direction and parallel to the hot spot’s direction of extension. Further out, the magnetic field is parallel to the tails, and the degree of polarization is high (this appears to be the behaviour in the best-studied WATs; e.g. Taylor *et al*. 1990, O’Donoghue *et al*. 1990, Patnaik *et al*. 1984).

Depolarization, rotation measure and spectral index

Using matched-baseline maps, I confirm the result of Leahy (1985) that the source is rapidly depolarized at low frequencies. The mean DP (averaged over the areas with good signal-to-noise in both maps) of the northern plume is 0.2, and that of the southern plume 0.1. It may be noteworthy that the southern lobe, with a weaker jet and less compact hot spot, is the more depolarized: this may be an example of a Laing-Garrington effect in WATs. To my knowledge there are no systematic observations of depolarization in this class of source.

The RM is not constrained by the rotation of polarization angle between 8.4 and 1.5 GHz. Rotations through all possible angles take place over the source, so there are variations in RM of more than 36 rad m^{-2}. This is consistent with the RM measurements of Leahy (1985). Good maps at a higher frequency are needed to constrain the RM adequately.

The spectral index of the source steepens rapidly with distance from the core. Figure 3.15 shows a map of spectral index; the matched baselines of the maps ensure the steepening is not an effect of under-sampling. Note the flat ($\alpha \approx 0.5$) spectral index of the jets and of the material they flow into. This is expected in the standard model in which the plumes flow slowly away from the source (compare the spectral index maps of Hydra A by Taylor *et al*. 1990).

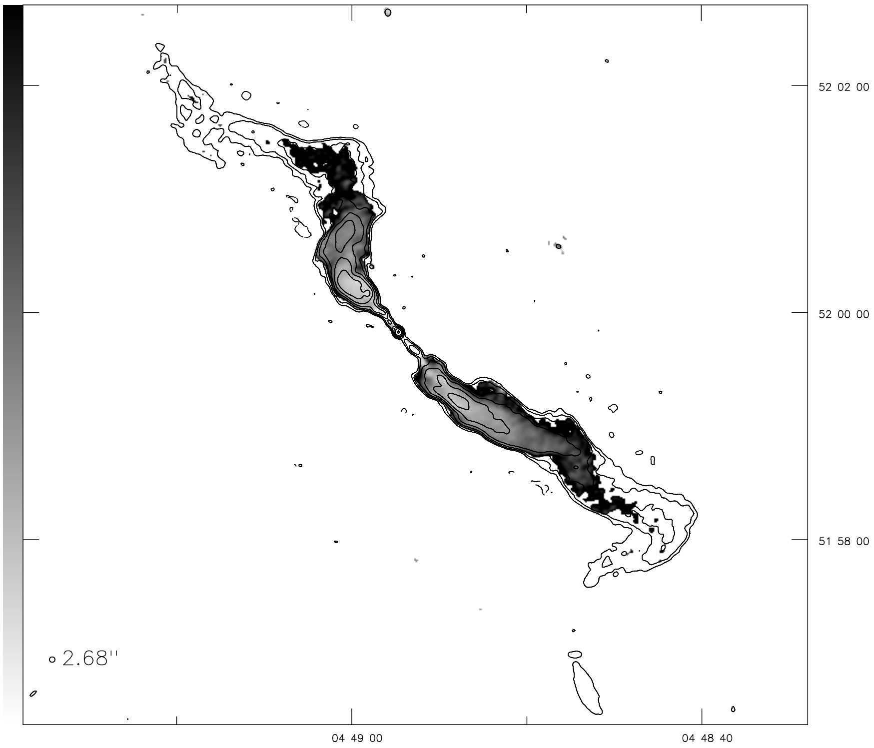

Figure 3.15: Spectral index between 8.4 and 1.4 GHz of 3C 130 at 2.86 arcsec resolution. Linear greyscale between 0.4 and 1.5; superposed are contours of total intensity at 1.4 GHz at $0.4 \times (-2,-1,1,2,4,\ldots)$ mJy beam^{-1}.

3.3.4 3C 296

3C 296 is imaged in Leahy and Perley (1991, hereafter LP); earlier maps are in Leahy (1985) and Birkinshaw, Laing and Peacock (1981). Keel (1988) fails to see any optical counterpart to the jets. The host galaxy (NGC 5532) is a large elliptical (Owen and Laing 1989) which is classified by Wyndham (1966) as an ED4. It is located in the Abell cluster A1890 and has a close small companion (Wyndham 1966; Colina and Pérez-Fournon 1990). Fabbiano *et al.* (1984) report a detection with EINSTEIN.

Overall source structure

A low-resolution image, figure 3.16 (made substantially with the data from LP) shows the very symmetrical twin jets of this object, which form well-defined symmetrical double lobes. (Compare the lobes of 3C 66B.)

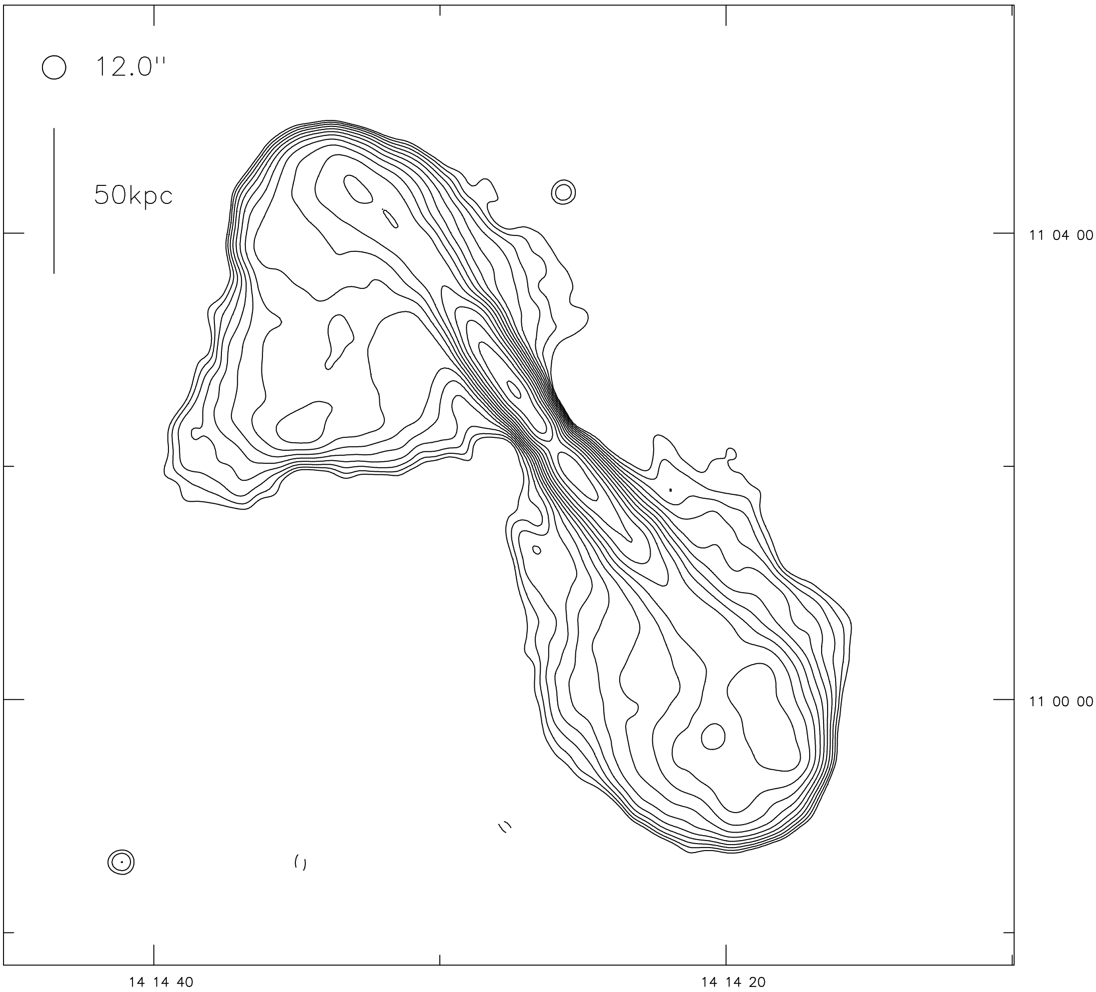

Figure 3.16: 1.4 GHz map of 3C 296 at 12.00 arcsec resolution. Contours at $1 \times (1, \sqrt{2}, 2, 2\sqrt{2}, \ldots)$ mJy beam^{-1}.

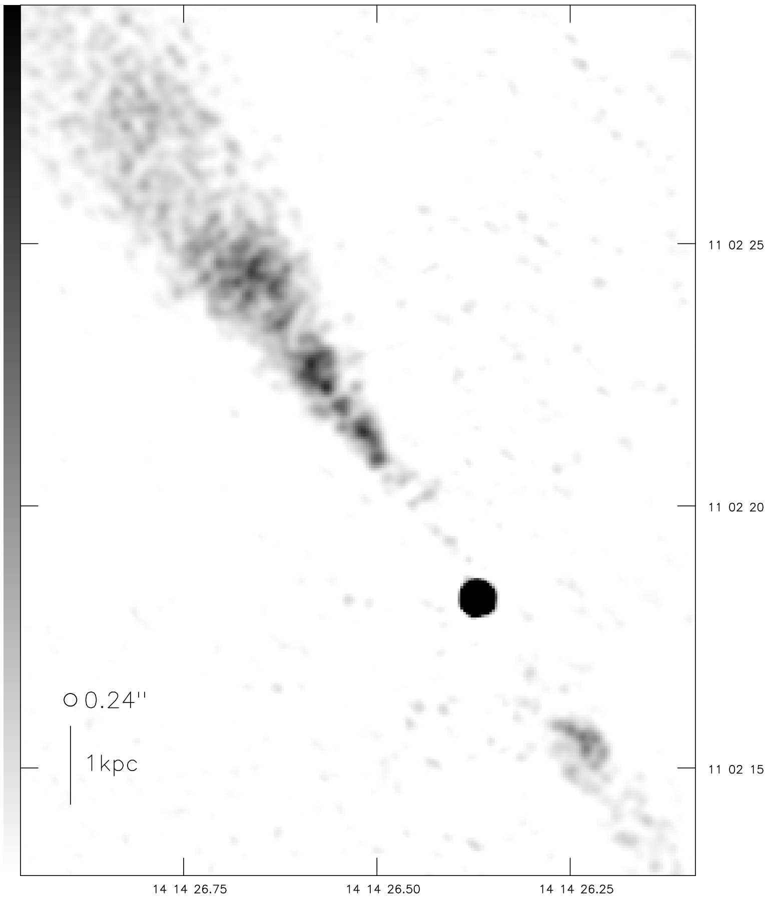

Figure 3.17: 3C 296 at 0.24 arcsec resolution. Linear greyscale; black is 0.4 mJy beam^{-1}.

Structure at high resolution

In figure 3.17 the inner parts of the jets of the source can be seen. The jet brightens at approximately 2 kpc from the nucleus, but does not show the bright flaring knot of 3C 66B; instead it appears to have a row of central compact knots in the first 2 kiloparsecs of bright emission, and is increasingly diffuse thereafter. There is little evidence for a bright FRII-like inner jet (compare 3C 66B). A knot in the inner part of the counterjet, again starting at around 2 kpc from the core, is seen to be elongated, with some faint compact structure, but there is no other compact structure in the counterjet.

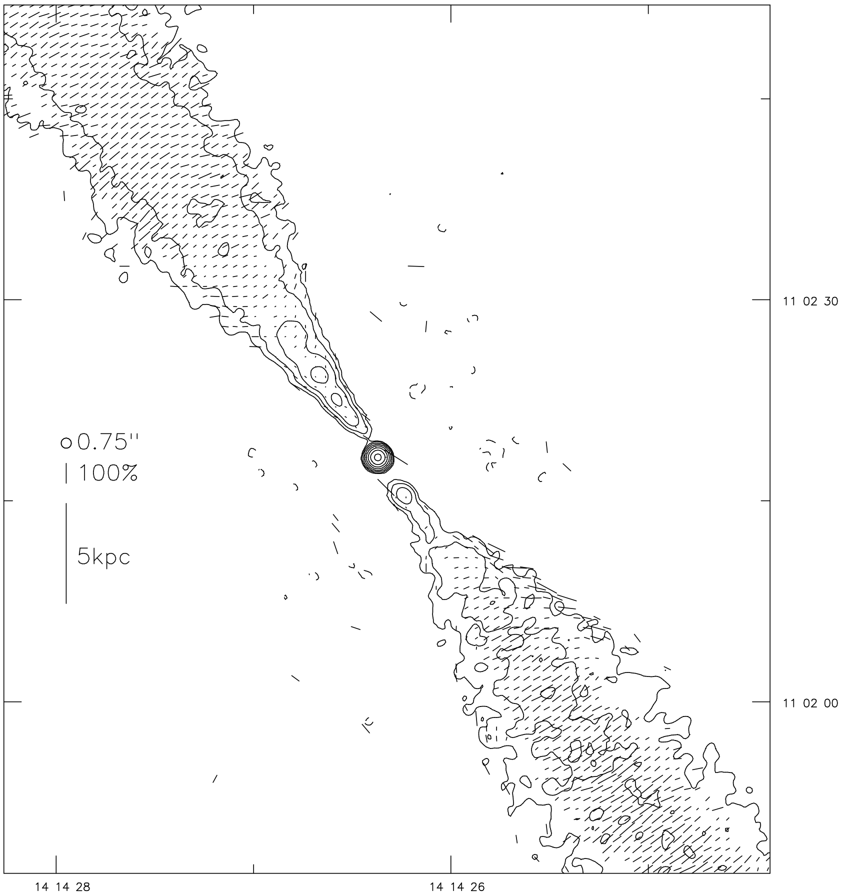

Figure 3.18: 3C 296 at 0.75 arcsec resolution. Contours at $0.2 \times (-2\sqrt{2}, -1, 1, 2\sqrt{2}, 8, 16\sqrt{2}, \ldots)$ mJy beam^{-1}.

Structure at intermediate resolution

Figure 3.18 shows the jets at 0.75-arcsec resolution. The knot in the counterjet has no counterpart in 3C 66B, but an almost identical knot is seen in the maps of 3C 31 by Laing (1996). The magnetic field is longitudinal for the first 6 kpc on the jet side and transverse thereafter; the change in field direction is accompanied by a marked increase in the degree of polarization (from $\sim$ 10% to $\sim$ 25%, rising to $\sim$ 40% by 10 kpc out on the jet side). On the counterjet side there is some indication of a longitudinal field in the inner few kiloparsecs, but it is definitely transverse to the jet direction by 4 kpc out. A parallel-field sheath, with a high degree of polarization, surrounds the counterjet (with a region of depolarization between the transverse- and longitudinal-field régimes) but there is no indication of one on the jet side. This can be confirmed from the polarization maps of LP.

Depolarization and spectral index

There is no evidence for significant depolarization in the jet or counterjet from maps made with matched baselines at 1.5 and 8.4 GHz. The spectral index in the inner part of the jet and counterjet is 0.6, and there is no evidence for spectral steepening along or across the jet in the areas where both maps are reliable (out to about 50 arcsec).

3.4 Discussion

In this section I discuss the similarities and differences between the three twin-jet sources discussed above.

3.4.1 Velocities in the jets

3C 66B and 3C 296, and to a lesser extent 3C 75N, exhibit substantial asymmetry in surface brightness between the jet and counterjet at distances up to a few kiloparsecs from the radio nucleus, while having lobes of more or less equal brightness on the largest scales. 3C 66B and 3C 75N and S also have strongly variable cores. The model most commonly proposed to explain this type of object is one in which the beams near the nucleus are symmetrical in efficiency (and thus rest-frame emissivity) but the emitting material is relativistic; the emission is then Doppler beamed toward or away from the observer, and as the beams decelerate the flux asymmetry decreases, so that the jets become less asymmetrical. This type of model is summarized in Laing (1996) and is supported by unified models (section 1.6.6) which require relativistic beaming to be significant in at least some parts of the source, and by the discovery of a Laing-Garrington effect in FRI sources (section 1.4.6). The alternative is a model in which the beams are symmetrical in power but intrinsically different in efficiency (e.g. Fraix-Burnet 1992), with no appeal to relativistic velocities necessary. In this section I show that the data on the jets of 3C 66B and 3C 296 are adequately explained by the relativistic beaming model, although it is hard to rule out a model in which the efficiency variations ‘conspire’ to produce the effects shown.[1]

The jet in 3C 66B is brighter than the counterjet as far as they can both be traced; the counterjet disappears into a ‘bubble’ of diffuse emission after about 25 arcsec. There are several complications in applying the relativistic beaming model to this object, however. Both jets are curved, and the angles made by the bulk flow with the line of sight therefore change with distance away from the nucleus. In

---

[1] Fraix-Burnet (private communication) has a possible detection of an optical counterjet in 3C 66B which is significantly brighter than would be predicted by the relativistic beaming model. If this result is confirmed, it will be a strong point in favour of a model in which the jets are intrinsically asymmetrical.

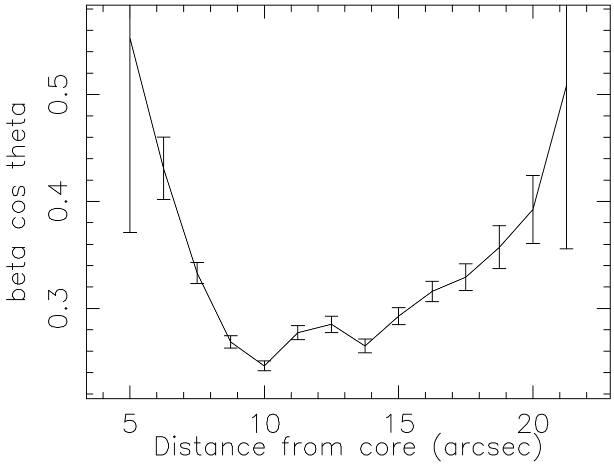

Figure 3.19: $\beta\cos\theta$ against distance from the nucleus for 3C 66B

general, the angles made with the line of sight in the jet and counterjet may be quite different, although they are likely to be similar close to the nucleus.

If we apply a naïve model in which all the flux asymmetry is due to relativistic beaming, all jet material moves at the same bulk velocity βc and the jet and counterjet make a single angle θ to the line of sight, the standard formula may be used[2]:

$$R = \left(\frac{1+\beta\cos\theta}{1-\beta\cos\theta}\right)^{2+\alpha}$$

(where R is the flux ratio between jet and counterjet). The integrated flux ratios of the jet and counterjet at different angular distances allow us to find $\beta\cos\theta$ as a function of distance from the nucleus. This is plotted for 3C 66B in figure 3.19. It can be seen that $\beta\cos\theta$ initially falls with distance from the nucleus, as would be expected for a decelerating jet with constant θ. Supposing the model to be more or less accurate for the inner few kiloparsecs of the jet (which is reasonable, since the jet appears straight in the high-resolution maps of figure 3.2) values of $\beta\cos\theta$ around 0.6 constrain the angle to the line of sight of the emerging jet to be $\theta \lesssim 53°$, while β here cannot be less than 0.6 for any θ. Further from the nucleus $\beta\cos\theta$ begins to rise again, corresponding to the disappearance of the counterjet here. This is not consistent with a simple model, but it is clear from my maps that the jets bend and that the assumption of constant θ, at least, must be wrong on these scales.

It is easier to fit the relativistic beaming model to the jets in 3C 296, since the jets are straight and appear to be exactly oppositely directed. In this case I can follow Laing (1996) and produce a 'sidedness map' of

---

[2] It must be borne in mind that with certain configurations of magnetic field the exponent $2+\alpha$ may be significantly wrong. It represents a best guess only.

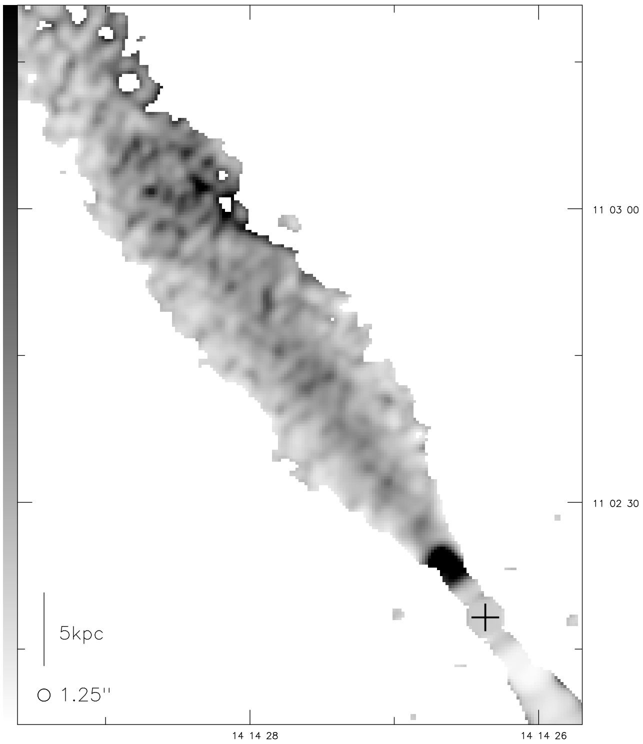

Figure 3.20: Sidedness map of 3C 296 at 1.25-arcsec resolution, showing jet-counterjet ratio as a function of position in the jet. Linear greyscale: white is $R = 0$ and black indicates $R > 5$. A cross indicates the position of the core.

the source, shown in figure 3.20. This is made by rotating the image, centered on the core, through 180° and dividing the original image by the rotated version; it thus shows jet-counterjet ratio as a function of position in the jet. The greatest jet-counterjet ratio on this map is 12, which translates to $\beta\cos\theta = 0.44$; thus $\theta \lesssim 63°$ in the beaming model, and the velocity of the jet $\beta \gtrsim 0.44$. It will be seen that the jet is very asymmetrical only at the base, with the side-to-side asymmetry parameter R falling, by 6 kpc from the core, to values around 2–2.5, corresponding to $\beta\cos\theta \approx 0.15$; this drop in R corresponds in position to the change from parallel to perpendicular field. There is then a long region where the sidedness remains constant, and here it can be seen that the central regions of the jet are more one-sided than the edges, as found in 3C 31 by Laing (1996). The mean value of the sidedness parameter in the edges is close to 1; it is therefore possible that we are seeing almost stationary material. Further out the jet becomes more one-sided, but this coincides with a bend in the ridge line of the jet and can be explained simply as brightening due to compression.

It is well known (Burch 1979c) that the brightness decline in the jets of FRIs is sub-adiabatic; that is, their surface brightness drops with distance along the jet much less rapidly than would be expected for a smooth uniformly expanding jet with no particle reacceleration. The most persuasive way to overcome this problem comes from the semi-empirical model by Bicknell and others (e.g. Bicknell 1986) in which the jets are turbulent and entrain external material as they decelerate; this both removes the assumption of constant velocity and allows particle reacceleration (discussed below in section 3.4.3). A fit of Bicknell's model to a sample of low-luminosity sources (Bicknell *et al*. 1990) has suggested jet velocities in the range 10^3 – 10^4 km s^{-1}. It has been thought to be difficult (e.g. Parma *et al*. 1993) to reconcile the two different velocity régimes required by the turbulent jet and relativistic beaming models: in the case of the two sources discussed above, deceleration by factors of between 10 and 100 over the inner few kiloparsecs would be required to allow both models to describe the source successfully. However, Bicknell (1994) has analyzed the dynamics of a relativistic entraining jet in some detail; he shows that the velocity at which a relativistic jet has decelerated to a trans-sonic Mach number (presumed to be the region at which large-scale turbulent entrainment begins) must lie between about 0.3–$0.7c$ (values consistent with the constraints on velocities found above) and that significant deceleration on the kiloparsec scale thereafter is dynamically feasible.

The sheath-like structure in the polarization maps suggests that there are two distinct régimes in the jet. This can be explained by a modification of the relativistic beaming model which supposes that the core of the jet is relativistic and is surrounded by a more rapidly decelerating shear layer, perhaps slowing by entrainment of surrounding material; this is the model put forward by Laing (1996). The parallel-field sheath observed in the jet and counterjet would correspond to the shear layer. The generally more edge-brightened and diffuse counterjet could be the emission from a slow outer sheath surrounding a core which is invisible or very faint due to beaming away from the observer; the jet side, as observed, would be expected to be centre-brightened at all times (unless its core velocity were very high indeed) and thus would give rise to the variations in sidedness across the jet seen above in 3C 296 and by Laing (1996) in 3C 31. The observed differences in the thicknesses of the longitudinal-field sheaths in the jet and counterjet would follow from the different beaming of the two cores. It will be noted, however, that the two apparent velocity regimes deduced from the sidedness of the 3C 296 jet *both* have transverse magnetic field, complicating the simple model.

3.4.2 Polarization

Laing (1993, 1996) uses a version of the core-sheath model described above to explain the change from longitudinal to transverse magnetic field direction seen in the inner jets of FRI sources. In Laing's model the jet cores have a magnetic field with no longitudinal component and the shear layers have a longitudinal magnetic field. Close to the nucleus the bulk velocities of the cores of the counterjet and jet are highly relativistic: the emission from the cores is therefore very strongly beamed and invisible to an observer (if the source is at a significant angle to the line of sight) so that the longitudinal field from the shear layer dominates. As the jet decelerates the transverse component in its centre becomes more important, so a changeover from parallel to perpendicular magnetic field direction is observed. In the case of 3C 66B, however, the model fails to explain the parallel polarization in the bright knots B and C: these are presumably features of the jet core and so in Laing's model should have a transverse field, while any region with longitudinal field structure should be edge-brightened if resolved. If we wish to retain a core-sheath model, we must assume that both the slow sheath and the fast core initially have longitudinal magnetic field, but that something happens early on to rotate the direction of the field in the core: on the jet side of 3C 66B this would occur near knot D (2.5 kpc from the nucleus), while in the counterjet it would have to take place somewhere before the first good detection of perpendicularly-polarized flux, also at 2.5 kpc from the nucleus. The inner region of 3C 296's jet is similarly resolved and centre-brightened (figure 3.17) in the regions where it has longitudinal magnetic field. Laing's model does not seem to work in detail in these sources.

In models other than Laing's, the changeover in polarization configuration can be understood in terms of a magnetic field initially dominated by a longitudinal component which becomes less important as the jet expands. The magnetic field may be ordered (uniform or helical) or partially ordered (Laing 1981a). Unfortunately, the presence of a longitudinal-field sheath makes it difficult to define the parameters of the region in which field turnover is occurring and therefore difficult to extract any information on the physics. In 3C 66B the change is not clearly related to any structure in total intensity, whereas for a model in which the jet is coming into equilibrium with its surroundings the change in orientation would be expected to be correlated with a drop in surface brightness (as in 3C 219, for example; Clarke *et al*. 1992). The field continues to be longitudinal after the knot B, and it would appear that (as in 3C 31; Fomalont *et al*. 1980) the expansion necessary to allow the transverse field to dominate must only be by a small factor. By contrast, the change between parallel and perpendicular field in 3C 296 occurs at a similar distance from the core to a pronounced drop in jet surface brightness; however, this does not appear to be true of 3C 75.

3.4.3 The jets of 3C 66B: detailed analysis

The discussion above has shown 3C 66B to be unlike ordinary FRI sources in a number of ways, particularly in its bright base with an optical counterpart. In this subsection I discuss details of the large- and small-scale structure in its radio and optical jets.

Bending and wiggles

The smooth bending on kiloparsec scales of the jets in the maps shown here is suggestive of a motion of the source to the northwest, similar to those which are thought to bend the tails of narrow-angle tail radio galaxies (which are often, like 3C 66B, outlying members of clusters). However, the large-scale lobe structure does not follow this curve, and includes some low-brightness regions which we would expect to be moving away from the nucleus at lower velocities (although they should also be denser) and so to be more affected by such a motion. A simple explanation of this sort is difficult to contrive.

Alternatively, the bending may just be the result of jet propagation into a non-symmetrical medium. The distorted isophotes of the host galaxy seen by Fraix-Burnet *et al*. (1989a) may be some evidence for this. 3C 66B is an interacting galaxy, with a companion to the SE of the radio source, but the mass of the companion is sufficiently low that orbital displacements are unlikely to have produced these large-scale variations in jet direction, and the orbital period is probably too long in any case (Balcells *et al*. 1995). It therefore does not seem possible to explain the large-scale structure of the source (i.e. the apparent sudden changes of direction of the outflow) without invoking a significantly clumpy environment. If the source axis is close to the line of sight then the bending is exaggerated by projection; LJP suggest that a model of this sort might explain a number of the peculiar features of the source on the large scale (see also section 3.4.1).

The small-scale (~ 1 kpc) wiggles in the jet ridge line, on the other hand, could be attributed to precession of the central collimator, to fluid flow instabilities or to gravitational effects from the companion galaxy. Precession seems physically unlikely: there is no obvious similar effect in the counterjet, and on the most conservative estimates of velocity the collimator would have to wobble through angles of several degrees on timescales of $\sim 10^5$ yr, which is several orders of magnitude less than the timescales for forced precession of a 10^8 solar-mass black hole (Rees 1978). Orbital interaction with the companion suffers from the same problem of implausibly short timescales, leaving some sort of fluid flow instability as the best answer. If these wiggles are evidence for similar motions in the parts of the jet nearest the nucleus, a model in which the inner jet is relativistically beamed and the angle between the bulk velocity and the line of sight is changing slightly might explain some of the small-scale variations of brightness and magnetic-field direction in this area.

Small scale structure

The jet mapped at high resolution (figure 3.2) is roughly 3.5 arcsec across (at knot E): at this resolution and sensitivity the images probably only show the core of the jet, and not much of the parallel-field sheath. The jet is strongly centre-brightened. There is some evidence for a double-stranded filamentary structure in both the radio and the optical wavebands. Macchetto *et al*. (1991) suggest that this structure might be explained in terms of the helical-field models of Königl and Choudhuri (1985): here the filaments (according to JSMM) would be the boundaries of a twisted helical magnetic field tube and the banding across it would represent twists in the helix. Apart from the tentative nature of the evidence for filaments in the radio, one important objection to this model is provided by the magnetic field structure in my maps. If the field were as described by Königl and Choudhuri, we would expect to see changes (from parallel to perpendicular and back) in the direction of the magnetic field in the jet, strongly associated with the positions of bright knots. In fact the field is parallel initially, slightly oblique in knot B and then parallel to the jet again, turning to a wholly perpendicular configuration before the end of the proposed filamentary structure (shortly after knot D).

Spectral index and reacceleration

An important problem is raised by the radio-optical spectral index results of JSMM. They find that the spectral index is approximately constant ($\alpha = 0.8$ between 15 GHz and the optical) over a region 1 kpc across in the inner 5 kpc of the jet. My radio spectral index results (section 3.3.1) show a flat radio spectral index ($\alpha \approx 0.6$) and in the optical the spectral index is steep (1.4: JSMM), so that the spectrum must be curved with a cutoff frequency $\lesssim 10^6$ GHz. Fraix-Burnet (private communication) suggests that the radio-near-IR spectrum is still approximately 0.6, which would constrain the break frequency to be $> 3 \times 10^5$ GHz. This would strongly constrain models such as those of Heavens and Meisenheimer (1987), which predict the relationship of break and cutoff frequencies. However, the important point is that the *spectrum* of the jet is constant between knots B and E.

As JSMM point out, the synchrotron lifetime of the optically radiating electrons is short. If the lifetime t is defined as the time taken for the synchrotron break frequency to become equal to the frequency of emission ν, then in a model with no particle reacceleration

$$t = \left(\frac{CB}{(B^2 + B_p^2)^2 \nu} \right)^{\frac{1}{2}} \tag{3.1}$$

(Leahy 1991) where B is the magnetic field strength, B_p is the equivalent magnetic field to the energy density in photons u_p ($B_p = \sqrt{2\mu_0 u_p}$; this term describes losses due to inverse-Compton scattering of background photons) and C is a constant which in useful units is 2.5×10^3 nT^3 Myr^2 GHz. The magnetic field strength B is not particularly well known. The only estimates come from minimum energy/equipartition arguments, but there is no reason to believe that equipartition holds in this case. The estimates vary considerably depending on the part of the jet on which the calculation is done; they depend on quantities such as the Hubble constant, the filling factor and the proton content of the jet about which little is known. Further, equation 3.1 holds for ageing in a constant B-field and photon energy density, and it is expected that both of these will change with distance from the nucleus; modelling the effect on particle energy distributions of this variation is difficult. The energy density in photons close to the nucleus will be dominated not by the cosmic background radiation but by starlight from the host galaxy (Owen, Hardee and Cornwell 1989: this should contribute an energy density of $\sim 10^{-12}$ J m^{-3} at 1 kpc, equivalent to $B_p = 1.6$ nT) and possibly by the continuum emission from the hidden AGN in 3C 66B. We must also note that the optically emitting particles are older than t, since the spectral index results above constrain the break frequency to be less than the frequency of optical emission.

With these caveats, some estimate can be made of the lifetimes of particles emitting in the optical. JSMM suggest an equipartition B-field of 10 nT; with $\nu = 10^6$ GHz (corresponding to the 3000-Å wavelength of the HST images) this gives a lifetime of 1.5×10^3 years. This field estimate is reasonable for the bright knots in the jet, through which (it is assumed) most of the electrons will have travelled; the equipartition field elsewhere in the inner jet is lower ($3-4$ nT, using a filling factor of unity, a cylindrical geometry for the jet, and assuming no energy in non-radiating particles) and so actual particle lifetimes may be higher. (It should be noted that either a lower filling factor, plausible given the suggestions of filamentary structure in the jet, or some contribution to the energy density from non-radiating particles would increase the equipartition B-field and so reduce the lifetimes. Highly relativistic bulk velocities make the observed surface brightness an overestimate of the emission in the bulk rest frame, and therefore reduce the inferred B-field, but the mildly relativistic velocities inferred from jet sidedness above should have little effect on the equipartition calculation.) The projected length of the optical jet is 5 kpc, so that the light travel time to the end of the optical jet is at least 1.5×10^4 yr. From the sidedness arguments above the bulk velocity of the electrons is unlikely to be greater than $0.5c$, and the deprojection factor is likely to be greater than 1.5; thus for some plausible jet parameters the most distant optically radiating particles have taken about 30 times their synchrotron lifetime to reach the end of the jet.

It can be seen from equation 3.1 that for a given B_p the maximum value of t is obtained when $B = B_p/\sqrt{3}$; thus without even knowing the magnetic field strength we can put limits on the lifetime from the energy density in photons. If $B = B_p/\sqrt{3} = 0.92$ nT, using the energy density given by Owen *et al*. (1989) for M87, then the maximum possible lifetime is 1.4×10^4 yr. This is still comparable to the light travel time to the end of the optical jet, and a factor of 3 or 4 shorter than a plausible electron travel time. For any other magnetic field strength the lifetime will be shorter. It would appear that we cannot retain a simple picture of acceleration in the nucleus while reproducing the observed constant spectrum unless the energy density in the photon background is less than $\sim 2 \times 10^{-13}$ J m^{-3}.

Possible alternative mechanisms include highly relativistic flow ($\gamma \sim 10$, $\beta \gtrsim 0.995$), transport of the electrons in a 'low-loss channel' where the magnetic field (or at least the component perpendicular to the direction of bulk velocity) is much weaker than the equipartition value, and local reacceleration. Very high bulk velocities in the inner 5 kpc seem unlikely both in terms of acceleration mechanisms and because of the problems of deceleration referred to above, but they are not explicitly ruled out by the observations. JSMM remark that if a low-loss (or high bulk velocity) central channel were present we would expect to see steepening of the radio-optical spectrum away from the jet axis on comparatively small scales (even supposing diffusion at speeds close to c), which is not observed: 1500 yr corresponds to 500 pc, similar to the radius of the optical jet. Felten (1968), in the context of the optical jet in M87, points out that such a low magnetic-field channel might well be unstable (plasma instabilities would lead to particle scattering and possibly amplification of the magnetic field) on timescales shorter than the light-travel time to the end of the jet. Further, a low-loss channel would suffer losses to inverse-Compton scattering, as described above.

Similar conclusions have been reached for the two other well-studied optical jets in radio sources, M87 (e.g. Biretta and Meisenheimer 1993) and 3C 273 (e.g. Röser and Meisenheimer 1991). The conclusions are slightly stronger in both, because the jets are brighter and narrower and the inferred equipartition B-fields stronger. In 3C 273 inverse-Compton losses in the radiation field of the quasar definitely rule out the low-loss channel models. In M87, the supposed synchrotron X-ray emission from the jet implies very short lifetimess.

If the hypothesis of local reacceleration is adopted in 3C 66B, the problem of where it is happening remains. One solution might be that the knots in the jet close to the nucleus are shocks at which first-order Fermi acceleration is taking place, as it is believed to do in the hotspots of classical double radio sources. However, the radio and radio-optical spectral indices of the knots are not distinguishable from those of the dimmer inter-knot material around them, which reduces the probability that they are privileged sites for particle acceleration. If acceleration took place only at the knots then there should be significant loss in the optical in the regions between them, again involving spatial scales of the order of 500 pc. However, the long mean free path lengths of the high-energy electrons (Meisenheimer *et al*. 1989) may 'smear out' the localization of the acceleration sites, and therefore make spectral variation less detectable. In this model it may be significant that there is little convincing evidence for optical emission from the knots A, and that the radio spectrum of this region appears steeper than that of the material in the optically emitting parts of the jet.

In simple versions of the 'turbulent jet' model described above (section 3.4.1), particle acceleration occurs by a second-order Fermi process driven by turbulence throughout the jet. However, the shear this would produce is sufficient to maintain a magnetic field parallel to the jets at all times (Leahy 1991) and this is not observed; a consistently parallel field is only seen in the outer edges of the jet. It seems that the reacceleration cannot be confined to a boundary layer in 3C 66B if we are to identify the entraining region with the sheath observed in polarization, since the optical jet is well within it (there is no evidence for optical emission from the sheath regions with the sensitivity so far achieved). It may therefore be necessary to postulate *two* reacceleration processes; large-scale turbulent reacceleration in the outer regions of the jet, sufficient to account for the sub-adiabatic brightness decline of the jet on large scales, and some unknown process, possibly associated with the bright jet knots, to drive the particle acceleration responsible for the optical jet. This latter process must also account for the constant and curved (rather than strictly power-law) spectrum along the jet, which is observed despite the large variations in surface brightness (and therefore inferred magnetic field).

In the Bicknell model the first bright knot B in 3C 66B would be identified with the site of the onset of turbulence, with the knots A being tracers of a much more efficient and free supersonic jet which undergoes a reconfinement shock at B when it comes into equilibrium with the pressure in the galactic atmosphere. Since the jet is still very one-sided after knot B, the relativistic beaming model requires that the post-shock velocity be relativistic, and at first sight it needs to be quite high to account for the brightness difference between knot B (which should be dominated by post-shock material) and its (unseen) counterpart in the counterjet. Bicknell (1994) claims that such brightness contrasts may be understood in terms of oblique relativistic shocks; the fact that the knot B appears to be aligned at an angle to the main jet axis may be some indication that this is correct. It should be possible to test whether the knot B is the standing shock commonly seen in hydrodynamical models of supersonic jets propagating into galactic atmospheres by searching for a proper motion; however, this would require very high-resolution multi-epoch observations. This has been done in M87 (Biretta, Zhou and Owen 1995) but would be much more difficult in 3C 66B because of its lower surface brightness and larger size scales. If knot B were moving at similar velocities to the brightest knot in M87 ($\sim 0.5c$, comparable to the velocity inferred from sidedness arguments for knot B) it would correspond to an angular motion of ~ 0.3 milliarcsec per year, nearly an order of magnitude smaller than the typical motions detected by Biretta *et al.*.

3.5 Comparison with other sources

Table 3.7 shows the properties of some well-known jets in nearby FRI sources for comparison with those observed here. Unfortunately, the best-mapped sources are also the least typical. The jet in M87 has been mapped exhaustively, and the similarity of its optical counterpart to 3C 66B's has been discussed above; but M87 is in many ways more similar to a classical double source than it is to a twin-jet FRI, and its jet is similar in opening angle (6°) and (as far as we can tell) in structure to those found in FRIIs or WATs. It has generally parallel magnetic fields (except at some bright knots) and is much shorter than the jets seen here. The model by Biretta (1993) suggests that the M87 jet is relativistic for much of its length and aligned at 40° to the line of sight: there is no observable counterjet, perhaps due to beaming effects. Biretta *et al.* (1995) claim to detect kpc-scale proper motion indicating $\gamma \sim 3$ in the inner jet. NGC 6251 is another one-sided jet with initial parallel-field structure: its knotty inner structure and areas of oblique magnetic field are superficially similar to those in the jet side of 3C 66B, but this inner region extends over 75 kpc (an order of magnitude longer than in 3C 66B). The jet-counterjet flux ratio is $\sim 130 : 1$ over the first 250 arcsec from the nucleus, implying an angle to the line of sight of less than 45° on a naïve relativistic beaming model. An HST image of NGC 6251 (Crane 1993) shows no optical jet, however.

Table 3.7: Parameters of some well-known jets in FRI sources

Source name	z	P_{178}	Length (kpc)	Sides	Polarization structure		Res’n (kpc)	Reference
					Parallel up to:	Perpendicular from:		
NGC 315	0.0167	0.51	480	2	12 kpc on jet side	12 kpc on jet side: parallel sheath in counterjet	0.6	1, 12
3C 31	0.0167	1.8	28	2	4 kpc on jet side, 2 kpc on counterjet side	2–4 kpc: parallel sheath	0.33	2
3C 66B	0.0215	4.3	90	2	3.75 kpc on jet side	3.75 kpc: parallel sheath	0.15	3, 4
3C 75N	0.0240	2.8	60	2	6 kpc on both sides	6 kpc	0.50	4
3C 75S	0.0240	2.8	60	2	$\sim$ 8 kpc on both sides	8–11 kpc	0.50	4
3C 83.1B	0.0255	6.6	36	2	24 kpc	24 kpc: parallel sheath	0.6	5
M84	0.0029	0.061	6.6	2	?	300 pc (or less)	0.46	6
M87	0.0041	6.6	3.6	1	Whole length, except at bright knots	N/A	0.012	7
IC 4296	0.0129	2.1	260	2	6 kpc on both sides	6 kpc (parallel at jet edges at bends)	1.2	8
3C 296	0.0237	2.8	100	2	6 kpc on jet side, $\sim$ 4 kpc on counterjet side	4–6 kpc; parallel sheath	0.16	9, 4
NGC 6251	0.024	2.3	320	1	60 kpc with regions of oblique field	60 kpc: parallel sheath	0.75	10
3C 449	0.0171	1.3	38	2	?	4.5 kpc (or less)	2.1	11

The units of P_{178} are 10^{24} W Hz^{-1} sr^{-1}. The powers of 3C 75A,B are the total power of 3C 75 divided by 2. Jet lengths are taken from Bridle and Perley (1984) modified to $H_0 = 50$ km s^{-1} Mpc^{-1}. References are (1) Venturi *et al.*1993 (2) Laing 1996 (3) Hardcastle *et al.* 1996 (4) This thesis (5) O’Dea and Owen 1986 (6) Laing and Bridle 1987 (7) Biretta 1993 (8) Killeen, Bicknell and Ekers 1986 (9) LP (10) Perley, Bridle and Willis 1984 (11) Perley, Willis and Scott 1979 (12) Willis *et al.* 1981

The jets in well-studied sources more similar to those discussed here have generally been mapped at spatial resolutions insufficient to reveal detailed sub-kpc structure of the jet close to the nucleus, so it is not clear whether the filamentary and knotty structure we observe is common to all sources. The best available images of NGC 315, 3C 31, IC 4296 (PKS 1333–33) and 3C 449 all show a perpendicular field structure beyond a few kpc from the nucleus, and in all but 3C 449 (which has the lowest resolution) the part of the jet closest to the nucleus shows a parallel field. The 'sheath' structure seen here is often lacking, but we have shown that high resolution and sensitivity are necessary for its detection (cf. the maps at 3-kpc resolution of 3C 66B in LJP, which show only a few traces of this structure). In NGC 315 the central parallel field is only detected on the jet side. This is very like what we find in 3C 66B at low resolution, and is consistent with a beamed jet at a moderate angle to the line of sight: NGC 315 has significant jet-counterjet asymmetry and a one-sided jet on small scales. High-resolution images of the jets in NGC 315 are strikingly similar to my maps of 3C 66B, showing a narrow bright jet and a shorter and more diffuse counterjet. Bicknell (1994) fits his model of a relativistic entraining jet to the parsec- and kiloparsec-scale features of NGC 315 with success. In contrast IC 4296, with two very symmetrical jets, has parallel magnetic fields in the inner 6 kpc of both. In the relativistic beaming model this would be interpreted as a source close to the plane of the sky. 3C 83.1B (NGC 1265) is a narrow-angle tail source which bends through a considerable angle before changing from a parallel to perpendicular field configuration. This is further evidence to suggest that the changeover is not directly connected with deceleration from a relativistic regime, if the shape of 3C 83.1B is due to ram pressure as is usually suggested. In the sources shown there is no obvious relation between source power and the position of the magnetic field changeover, but only a small range of powers is covered.

3.6 Conclusions

A compact hot spot is detected in the WAT 3C 130, and the jets are shown to have longitudinal magnetic field. The source is thus very like a classical double in some respects. The images support the model in which WATs are objects whose jets make the transition from super- to sub-sonic velocities in one step, rather than decelerating gradually; the absence of a hot spot in one lobe (as in Hydra A, the only WAT studied with comparable resolution) is puzzling, but might be attributed to relativistic beaming. The two-sided nature of the jets in 3C 130 (and other WATs), on the other hand, suggests small amounts of beaming (though not necessarily negligible; the estimate of O'Donoghue *et al*. 1993 that $\beta \approx 0.2$ is almost certainly low even for the emitting material, and of course only provides a limit on the velocities in the beam). If the emission comes from a slow-moving boundary layer to a faster-moving beam, these features can be explained. In this case the bright two-sided jets seen imply that the beams in the inner parts of 3C 130, and of WATs in general, must be less efficient than those of most FRIIs (but not all; compare 3C 438 in section 4.5.21 and see also chapter 6).

In the twin-jet sources, a model in which the jets are similar in power and consist of a relativistic central core surrounded by a slower outer sheath seems to fit the available data well, although significant deceleration on 10-kpc scales is necessary. Polarization maps show a clearly delineated parallel-field sheath on both sides of 3C 66B and the counterjet side of 3C 296, explained as a shear layer at which the jets are interacting with the surrounding medium. The field in the core of the jet changes orientation from a longitudinal to a transverse configuration in all three sources studied. There is evidence for this kind of behaviour in a number of other well-studied radio sources. The model of Laing (1993, 1996) appears to fail in 3C 66B and 3C 296 in that both have areas where the jet is centre-brightened and the magnetic field is longitudinal.

Local reacceleration in the core of the jet of 3C 66B is probably required to explain the radio and radio-optical spectral index. The jet in this object has much more compact structure than those of the other objects studied, and it seems likely that this is related to its optical brightness.

Chapter 4

FRIIs of intermediate luminosity

4.1 Introduction

In two recent papers (Black *et al*. 1992, hereafter B92; Leahy *et al*. 1996, hereafter L96) observations were presented of part of a sample of 29 radio galaxies taken from the 3CR catalogue (Spinrad *et al*. 1985) with $z < 0.15$ and $P_{178} > 1.5 \times 10^{25}$ W Hz^{-1} sr^{-1}. The primary aim of these observations was to provide high-resolution images of the hot spots in these objects. Their detailed images raised a number of new questions, since the structures revealed were complex and disparate. Earlier observations (e.g. Perley 1989; Laing 1989, hereafter L89) had suggested that hot spots tended to have no more than two components, but, as discussed in section 1.4.3, several objects in the $z < 0.15$ sample had more complicated structures which could not be classified as having at most one 'primary' (most compact) and one 'secondary' (more diffuse) component (using the classification of L89). L96 were able to identify some trends in the hot spot structures of the sample, and in many cases to define a primary component which could plausibly be identified as the current termination of the jet. It was not clear to what extent these observations were in conflict with the results of L89, which were based on observations of objects with $z > 0.3$; it is possible that the different hot spot structures in the $z < 0.15$ sample were a result of the proximity of these objects in radio power to the boundary ($P_{178} \approx 2 \times 10^{25}$ W Hz^{-1} sr^{-1}) between FRI and FRII structures.

These observations also revealed a number of new jets. Past observations of FRII radio galaxies had failed to detect jets in significant numbers; in a review of the observations Muxlow and Garrington (1991) suggested that no more than 10% of FRII radio galaxies had detected jets, although jets are much more plentiful in FRII quasars of similar power. In contrast, the observations described in B92 and L96 show jets to be present in 50 to 70% of their low-redshift sample (Black 1992, 1993; L96). Observations of statistically significant numbers of jets should provide information both on the power carried by the beam, which can be related to other indicators of the output of the AGN, and on the factors that affect its efficiency. Again, though, it was unclear whether this high jet detection rate is a consequence of the low luminosity of the $z < 0.15$ objects, or whether the observations of B92 and L96 were simply superior to and more systematic than those that had preceded them.

To address both these questions I have observed a new sample of objects which when combined with the sample of B92 extends it to higher radio power and redshift. In this chapter I discuss the selection of this new sample and the images I have obtained, with particular reference to the jet and hot spot physics of the individual sources, and summarize the jet and hot spot properties of this sample.

4.2 The selection of the sample

My sample was chosen to extend that of B92 to larger redshifts and higher luminosities. It consists of all 21 FRII radio galaxies in the sample of Laing, Riley and Longair (1983: hereafter LRL) with $0.15 < z < 0.3$: see table 4.1. The sources which met the redshift criteria but which were classed as FRIs by LRL were 3C 28 (Feretti *et al*. 1984), 3C 288 (Bridle *et al*. 1989) and 3C 346 (Spencer *et al*. 1991). A decision was taken at an early stage not to observe the four largest sources in the sample, 4C 12.03, 3C 33.1, 3C 61.1 and 3C 219, both for economy in observing time and because these sources were already relatively well-studied (respectively in Leahy and Perley 1991 [LP]; Rudnick 1984; LP; Clarke *et al*. 1992). The remaining sources were observed with the VLA, as described in section 2.2.1.

4.3 The observations with the VLA

Except where otherwise specified, the two standard 8-GHz observing frequencies (table 2.1) were used. I observed a typical large source in the sample for 10 minutes at D array, 45 minutes at C array, one hour at B array and 1.5 hours at A array. I did not observe the smaller sources (LAS less than 60 arcsec) in the D configuration, and the very smallest sources (LAS less than 20 arcsec) were only observed with B and A arrays. Sources smaller than 30 arcsec were only observed for half an hour in B array and an hour in A array. The largest sources were observed for two hours at A array. Because some of the data were provided by other workers, and for other reasons beyond my control, it was not always possible to stick to these timings. The complete observational information for the sample is given in table 4.2.

Table 4.1: The sample of radio sources

Source	IAU name	z	S_{178} (Jy)	α	P_{178}	scale (kpc/arcsec)	LAS (arcsec)	Size (kpc)	RM (rad m^{-2})
4C 12.03	0007+124	0.156	10.9	0.87	104	3.66	215.0	787	-4
3C 20	0040+517	0.174	46.8	0.66	543	3.99	53.6	214	159
3C 33.1	0106+729	0.181	14.2	0.62	178	4.12	227.0	935	-15
3C 61.1	0210+860	0.186	34.0	0.77	462	4.21	186.0	782	–
3C 79	0307+169	0.2559	33.2	0.92	930	5.33	89.0	474	-19
4C 14.11	0411+141	0.206	12.1	0.84	208	4.55	116.0	527	-19
3C 123	0433+295	0.2177	206.0	0.70	3873	4.74	37.8	179	-324
3C 132	0453+227	0.214	14.9	0.68	269	4.68	22.4	105	-38
3C 153	0605+480	0.2771	16.7	0.66	524	5.63	9.1	51	34
3C 171	0651+542	0.2384	21.3	0.87	505	5.06	32.5	165	43
3C 173.1	0702+749	0.292	16.8	0.88	624	5.83	60.5	353	-29
3C 219	0917+458	0.1744	44.9	0.81	536	4.00	190.0	760	-19
3C 234	0958+290	0.1848	34.2	0.86	466	4.18	112.0	469	42
3C 284	1308+277	0.2394	12.3	0.95	299	5.08	178.1	904	-4
3C 300	1420+198	0.272	19.5	0.78	604	5.56	100.9	561	-6
3C 319	1522+546	0.192	16.7	0.90	249	4.31	105.2	453	7
3C 349	1658+471	0.205	14.5	0.74	242	4.53	85.9	389	12
3C 381	1832+474	0.1605	18.1	0.81	181	3.75	73.2	274	25
3C 401	1939+605	0.201	22.8	0.71	362	4.46	23.6	105	–
3C 436	2141+279	0.2145	19.4	0.86	365	4.69	109.1	511	-53
3C 438	2153+377	0.290	48.7	0.88	1783	5.81	22.6	131	–

Column 4 lists the 178-MHz flux of the source. Column 5 gives the low-frequency (178–750 MHz) spectral index. Column 6 lists the luminosity at 178 MHz; its units are 10^{24} W Hz^{-1} sr^{-1}. Largest angular size, in column 8, was measured from the best available VLA maps. Integrated rotation measure, in column 10, is taken from Simard-Normandin, Kronberg and Button (1981), where available. All other data points are taken from LRL, with the 178-MHz flux corrected to the scale of Baars *et al.* (1977).

Because of the angular size restriction on the sources I observed, a bandwidth of 50 MHz (the largest bandwidth of the VLA) met the condition in equation 2.1 for all observations at B, C and D arrays. At A array I observed sources with sizes less than 45 arcsec with a 50 MHz bandwidth, sources with sizes less than 90 arcsec with 25 MHz bandwidth and the remainder with 12.5 MHz bandwidth to avoid bandwidth smearing.

4.4 New K-band magnitudes

New optical magnitudes at K-band have been obtained with UKIRT for five of the sources in the sample. These were measured with a 9-arcsec diameter aperture and are listed in table 4.3. Observational and data reduction details are as described in Best *et al*. (submitted). Images from these observations are shown in section 4.5. The seeing was typically between 1 and 1.2 arcsec.

4.5 Sources in detail

Except where otherwise stated, the information on galaxy identifications, redshifts and magnitudes is taken from Laing and Riley's update of the information presented in LRL (in preparation: LR). Maps at several resolutions are presented for most sources, in an attempt to show both the large-scale structure and details of the hot spots and jets (where present). The resolution of low-resolution maps is generally chosen to give 50 beamwidths across the source; the resolution of the highest-resolution maps is the best that could be obtained from the dataset for each source. The properties of the images shown are summarized in table 4.4. Negative contours are dashed on all contour maps. Position angles are defined east of north.

Polarization maps are also shown. Vectors are only plotted where both the total intensity and the polarized intensity exceed three times the r.m.s. noise. The vector lengths represent the *degree* of polarization and the directions are perpendicular to the E-vector; they are therefore in the direction of the magnetic field if Faraday rotation is negligible. At 8.4 GHz, Faraday rotation is likely to be significant (involving corrections of $> 5^\circ$) if the integrated rotation measure (RM) is greater than about 70 rad m^{-2}. This is true of 3C 20 and 3C 123 and may be true for the sources whose RMs are unknown to me. However, the integrated RM is in some sense a weighted average over the source. While a high integrated RM implies that rotation measure is high over at least some part of the source, a low integrated RM does *not* necessarily imply the converse. There is no way of correcting for the variation in RM across the source without multi-frequency observations, and therefore I have not attempted to do this.

For some sources maps of spectral index between 1.4 and 8.4 GHz are shown; these were made as de-

Table 4.2: Observational information for the FRII sample observed with the VLA

Source	A configuration		B configuration		C-configuration		D-configuration	
	Date of observation	t_{int} (mins)	Date of observation	t_{int} (mins)	Date of observation	t_{int} (mins)	Date of observation	t_{int} (mins)
4C 12.03	Not observed	–	Not observed	–	Not observed	–	Not observed	–
3C 20	25/11/88[4]	600	23/06/94	60	01/09/89[1]	80	Not observed	–
3C 33.1	Not observed	–	Not observed	–	Not observed	–	Not observed	–
3C 61.1	Not observed	–	Not observed	–	Not observed	–	Not observed	–
3C 79	06/08/95	90	23/06/94	60	01/09/89[1]	120	14/12/89[1]	15
4C 14.11	06/08/95	150	23/06/94	60	03/08/93	40	27/11/93	15
3C 123	06/08/95	60	23/06/94	60	03/08/93	40	Not observed	–
3C 132	06/08/95	60	23/06/94	30	Not observed	–	Not observed	–
3C 153	06/08/95	60	23/06/94	30	Not observed	–	Not observed	–
3C 171	06/08/95[3]	60	11/01/92[2]	35	10/04/92[2]	25	Not observed	–
3C 173.1	06/08/95	90	23/06/94	60	03/08/93	40	27/11/93	15
3C 219	Not observed	–	Not observed	–	Not observed	–	Not observed	–
3C 234	06/08/95	120	23/06/94	60	03/08/93	45	27/11/93	15
3C 284	Not observed	–	11/01/92[2]	30	10/04/92[2]	30	22/08/92[2]	20
3C 300	06/08/95[3]	120	11/01/92[2]	30	10/04/92[2]	25	26/08.93[2]	10
3C 319	Not observed	–	23/06/94	60	03/08/93	50	27/11/93	15
3C 349	06/08/95	90	23/06/94	60	03/08/93	50	27/11/93	15
3C 381	06/08/95	90	27/11/95	30	03/08/93	50	27/11/93	10
3C 401	06/08/95	60	23/06/94	30	03/08/93	40	Not observed	–
3C 436	23/07/95	120	23/06/94	60	03/08/93	50	27/11/93	10
3C 438	06/08/95	60	23/06/94	30	03/08/93	50	27/11/93	10

[1] Data kindly supplied by J.P. Leahy.

[2] Data kindly supplied by K.M. Blundell, observed at 8.065 GHz.

[3] Observed at frequencies of 8.065 and 8.115 GHz.

[4] Observations by W. Cotton and others from the VLA archives; observed at frequencies of 8.411 and 8.711 GHz.

Table 4.3: New K-band magnitudes

Source	Magnitude
4C 14.11	14.56 ± 0.02
3C 123	14.19 ± 0.05
3C 132	13.87 ± 0.03
3C 153	14.43 ± 0.03
3C 171	15.85 ± 0.05

scribed in chapter 2. The 1.4 GHz datasets used for this, and also for the depolarization analysis mentioned for some of these sources and described in detail elsewhere (Dennett-Thorpe *et al.*, in preparation), were kindly supplied by J.P. Leahy from the observations described in LP.

Some definition of terms is necessary in order to describe sources in a consistent way. Components which are thought to be tracers of the beam before its impact at the working surface are classified as jets or, if they fail to meet the criteria of Bridle and Perley (1984), as possible jets. I follow L96 in describing as a hot spot any feature which is not part of a jet and which has a largest dimension smaller than 10% of the main axis of the source, a peak brightness greater than ten times the r.m.s. noise, and a separation from nearby peaks by a minimum falling to two thirds or less of the brightness of the fainter peak. The most compact component is referred to as the primary hot spot, following L89, and the remaining components as the secondary hot spot or spots. I use this definition rather than the more restrictive one of B94 because my aim at this stage is to include as much as possible of the structure apparently associated with the beam termination in my discussion.

4.5.1 4C 12.03

The literature

The only recently published image of 4C12.03 is in LP; LRL have a 5-km map with poor signal-to-noise. There are indications in LP's image of a twin-jet structure and diffuse hot spots, and the lobes show prominent wings with X-symmetry. The source was reclassified by LR as an FRII on the basis of this image. The host galaxy is an elliptical with $B = 17.7$, possibly with some associated fainter objects. It is a low-excitation object (Laing, private communication).

4.5.2 3C 20

The literature

3C 20 is a well-studied object because of the prominent double hot spot in the E lobe. It was first imaged in detail by Laing (1981b) and high-resolution images of the hot spots appear in Laing (1982). There is strong evidence for outflow between the primary and secondary hot spots in the eastern lobe. Stephens (1987) observed 3C 20 at several frequencies and presents some spectral age information; Meisenheimer *et al.* (1989) investigated the spectrum of the western hot spot, which is an optical synchrotron source (Hiltner *et al.* 1994). The eastern lobe is the more depolarized (Hiltner *et al.*).

An unusually low fraction of the flux lies in the radio core, which was not detected in early radio maps.

Table 4.4: Properties of the images of FRII objects

Source	Fig. number	Region	Method	FWHM (arcsec)	FWHM (kpc)	σ_I (μJy)	σ_P (μJy)	Dynamic range
3C 20	4.1	Whole	C	1.10	4.39	63	19	4400
	4.2	Hot spots	CM	0.22	0.88	21	15	4900
3C 79	4.3	Whole	C	1.90	10.13	30	8	2700
	4.4	Hot spots	CM	0.24	1.28	13	14	800
4C 14.11	4.5	Whole	C	2.40	10.92	25	14	1200
	4.6	UKIRT overlay	C	2.40	10.92	25	–	1200
	4.7	Hot spots	CM	0.23	1.05	18	14	1600
	4.8	Spectral index	C	3.00	13.65	–	–	–
3C 123	4.9	Whole	C	0.85	4.03	260	47	8600
	4.10	UKIRT overlay	C	0.60	2.84	160	–	10300
	4.11	Whole	C	0.23	1.09	115	30	3900
	4.12	Hot spots	C	0.05	0.24	320	–	300
3C 132	4.13	Whole	C	0.50	2.34	38	12	1300
	4.14	Whole	C	0.80	3.74	75	–	800
	4.15	UKIRT overlay	C	0.50	2.34	38	–	1300
	4.16	Hot spots	CM	0.22	1.03	33	9	1200
3C 153	4.17	Whole	C	0.26	1.46	39	14	3000
	4.18	UKIRT overlay	C	0.26	1.46	39	–	3000
3C 171	4.19	Whole	C	0.70	3.54	55	18	2800
	4.20	UKIRT overlay	C	0.70	3.54	55	–	2800
	4.21	Hot spots	CM	0.35 × 0.25	1.52	73	19	1300
	4.22	HST overlay	CM	0.35 × 0.25	1.52	73	19	1300
3C 173.1	4.23	Whole	C	1.70	9.91	27	13	1500
	4.24	Hot spots	CM	0.30 × 0.20	1.45	28	26	330
	4.25	Spectral index	C	2.60	15.16	–	–	–
3C 234	4.26	Whole	C	2.30	9.61	58	16	2500
	4.27	Hot spots	CM	0.30	1.25	29	22	1200
	4.28	E hot spot	CM	0.50	2.09	27	–	1400
3C 284	4.29	Whole	C	3.60	18.29	22	16	1800
	4.30	Hot spots	CM	0.90	3.76	22	13	820
3C 300	4.31	Whole	C	2.10	11.68	33	–	4600
	4.32	Hot spot	C	0.23	1.29	38	60	340
	4.33	Core	C	0.23	1.29	38	60	340
3C 319	4.34	Whole	C	2.20	9.48	22	10	1000
	4.35	N hot spot	CM	0.90	3.88	22	13	800
3C 349	4.36	Whole	C	1.80	8.15	28	11	5000
	4.37	Hot spots	CM	0.25	1.13	28	22	900
	4.38	Spectral index	C	2.90	13.14	–	–	–

Table 4.4 continues overleaf.

Table 4.4: continued from previous page.

Source	Fig. number	Region	Method	FWHM (arcsec)	(kpc)	σ_I (μJy)	σ_P (μJy)	Dynamic range
3C 381	4.39	Whole	C	1.60	6.00	66	20	3200
	4.40	Hot spots	C	0.25	0.94	20	14	1900
	4.41	Spectral index	C	3.25	12.19	–	–	–
3C 401	4.42	Whole	C	0.50	2.23	18	8	1600
	4.43	Whole	CM	0.27	1.20	28	22	1100
3C 436	4.44	Whole	C	2.20	10.32	24	11	900
	4.45	Hot spots	CM	0.23	1.08	16	22	1000
3C 438	4.46	Whole	C	0.50	2.91	25	10	700
	4.47	Whole	C	0.23	1.34	26	13	600

Column 4 gives the deconvolution method. C denotes CLEAN and CM denotes a CLEAN/MEM hybrid as described in chapter 2. Columns 5 and 6 give the angular and corresponding linear size of the FWHM of the restoring beam used, or the major and minor axes where it was elliptical. In columns 7 and 8, σ_I and σ_P are the r.m.s. off-source noise on total and polarized intensity maps respectively. In several cases there are artefacts around bright hot spots at several times this level. The dynamic range (column 9) is defined as the ratio between the peak intensity and σ_I.

This led to initial uncertainty about the optical identification; Jenkins, Pooley and Riley (1977: JPR) show four candidate objects, and their object b, a 19th magnitude galaxy, is suggested by Riley, Longair and Gunn (1980) to be the most likely on the grounds of its appearance and proximity to the radio centroid. Radio observations by Hiltner *et al*. and my new maps confirm that object b is indeed the host galaxy. Hiltner *et al*. give a red magnitude of 19.15 ± 0.05. 3C 20 appears to be the dominant galaxy of a small group, although the field is crowded (Rawlings 1987). The centre of the host galaxy is elongated and de Koff *et al*. (1996: dK96) consider it a candidate for an optical jet.

The redshift of 3C 20 is now completely secure. A redshift of 0.35 was suggested by Smith and Spinrad (1980) but later withdrawn. Lawrence *et al*. (1986) give $z = 0.174$, and this is the value I have used throughout this work. A high-quality spectrum by Laing (private communication) confirms the Lawrence *et al*. redshift.

My maps

The A-configuration observations were made at observing frequencies of 8.4 and 8.7 GHz and a bandwidth of 12.5 MHz; the data from this was merged with the B and C-configuration datasets without correction for spectral index (negligible in any case). The long track at A array gives very good *uv* plane coverage, although the phase stability was poor over the later parts of the run due to snow. 3C 20 has a high integrated rotation measure, so polarization vectors may be misaligned with the true magnetic field direction by rotations of order 10°.

The low-resolution map in figure 4.1 shows the extended wings of the source, which is nearly as wide as it is long; the western lobe apparently bends north and the eastern lobe south. The edges of the lobes nearest the parent galaxy are highly polarized. At high resolution (figure 4.2) the jet in the W lobe (W1, W2) can be seen; the inner part (W1) is associated with a ridge of high polarization with the magnetic field perpendicular to the jet direction, but the magnetic field is parallel to the jet direction further out (W2). A possible counterjet feature in the E lobe (E1) is also highly polarized. The part of the jet nearest the host galaxy is resolved, but the area where the jet appears to undergo an S-bend is clearly seen. At both ends of the source a single compact 'primary' component can be identified. The primary in the E hot spot (E2) is elongated roughly towards the radio core and only weakly polarized; the bridge towards the more diffuse secondary (which actually contains two reasonably compact components, E3 and E4, which are not separate enough to count as multiple hot spots) is strongly polarized with the magnetic field direction being along its length. One of the components in this region, E5 is separate enough to count as a distinct object by the definition of L96. In the W hot spot, the situation is more complicated. The unresolved (or barely resolved) primary W3 has an inferred magnetic field direction pointing approximately towards the 'tail' to the north and west; the 'tail' then has its magnetic field directed along its length, before turning to a perpendicular configuration at the peak (W4) at its end. To the east of the end of the tail the field is parallel to the source axis. This might well be interpreted as a version in miniature of the situation at the E end, with a primary hot spot and outflow to a secondary, W4 (although W4 is not separate from W3 by the definition of L96); the tail would then represent the continued flow after the primary shock. A couple of facts confuse this simple picture. The first is the presence to the south of the primary of a further bright region (W5), sufficiently separate to count as a hot spot, not apparently connected to the primary but, like the secondary at the end of the tail, extending back into the western lobe. In the simple primary-secondary picture, this must be a defunct hot spot no longer being supplied with energy. Unfortunately the Hiltner *et al*. (1994) spectral index maps have no signal in this region. The second fact is the direction of the jet; where it is clearly seen it is pointing directly towards W4, so that to retain a simple picture with the beam terminating at the primary we need to propose another bend in the beam path over the 10 kpc or so between the jet's disappearance on the radio map and the primary hot spot W3. However, possible alternatives (such as that the 'jet' is really the continuation of collimated outflow from W4, or that the tail of W3 is a continuation of a jet which has turned round the head of the source) are even harder to believe.

4.5.3 3C 33.1

The best radio map of 3C 33.1 is in Rudnick (1984). JPR have an earlier map, as do van Breugel and Jägers (1982). The source has an unusual 'partial jet' in the S lobe, not completely unlike those in 3C 219

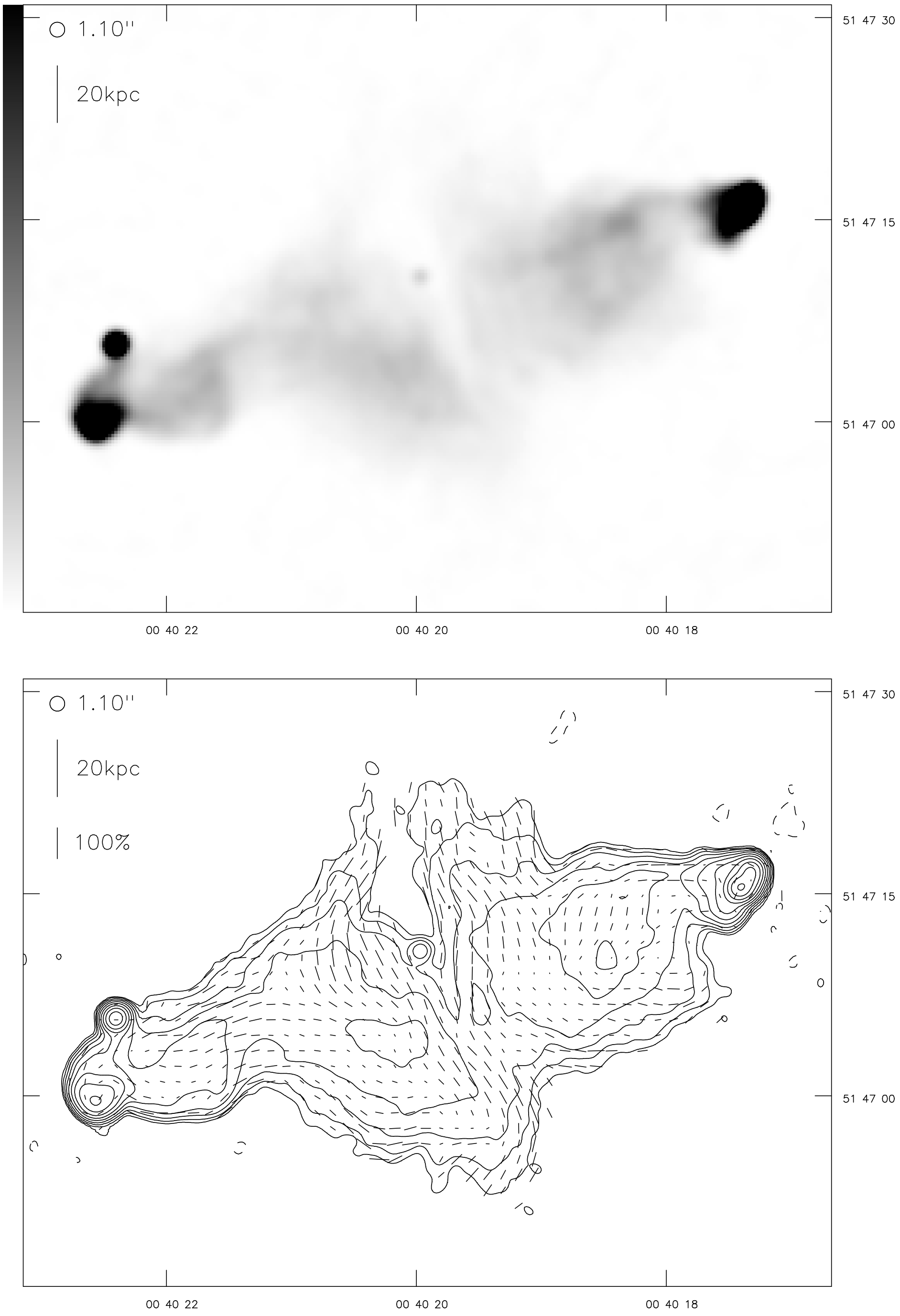

Figure 4.1: 3C 20 at 1.10 arcsec resolution. Above: linear greyscale; black is 20 mJy beam^{-1}. Below: contours at $0.25 \times (-2,-1,1,2,4,\ldots)$ mJy beam^{-1}.

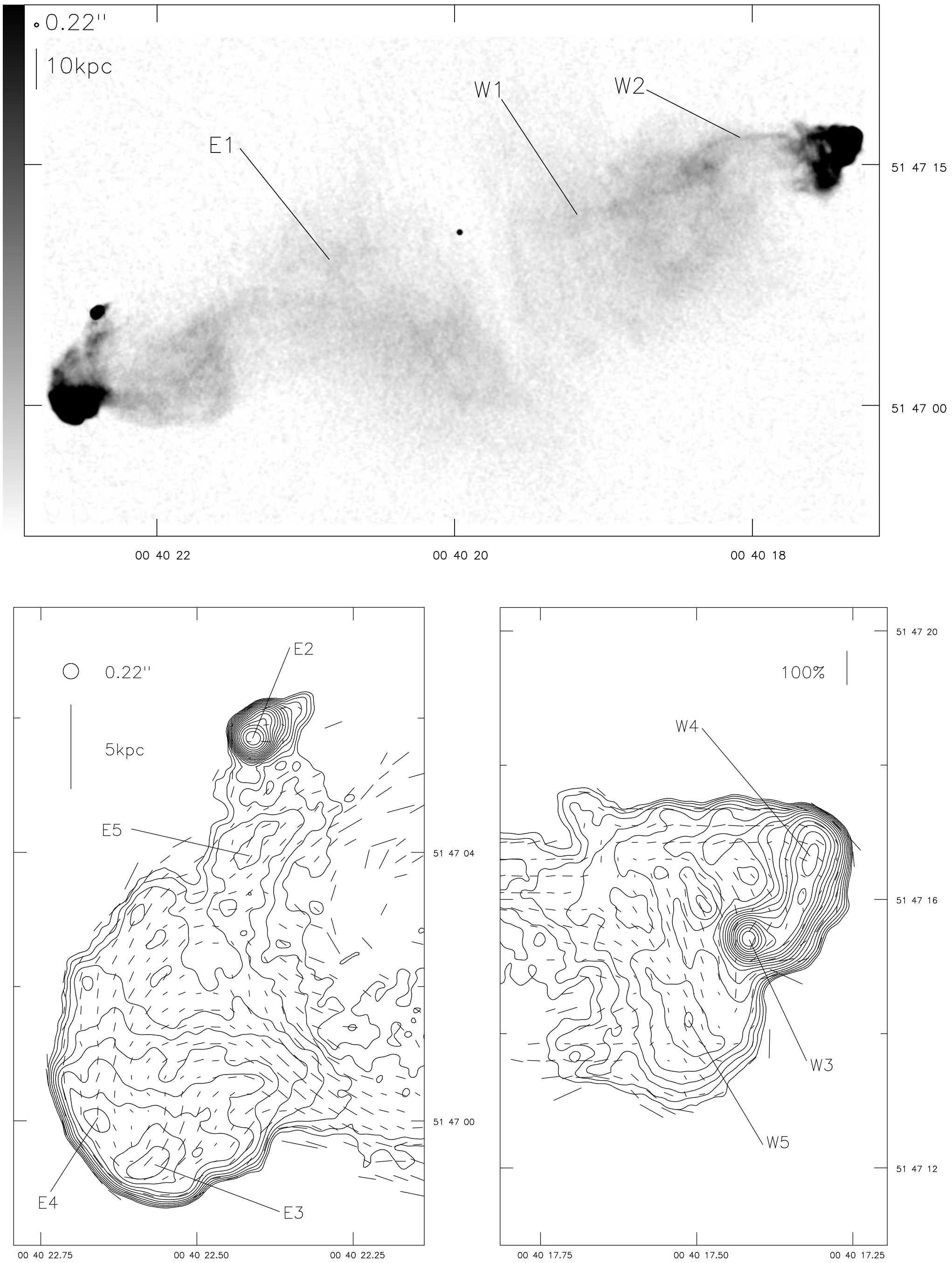

Figure 4.2: 3C 20 at 0.22 arcsec resolution. Above: linear greyscale; black is 1 mJy beam^{-1}. Below left: E hot spot; contours at $0.2 \times (-\sqrt{2}, -1, 1, \sqrt{2}, 2, 2\sqrt{2}, \ldots)$ mJy beam^{-1}. Below right: W hot spot, contours as left.

(see below) or 3C 445 (L96), starting 80 kpc out and continuing for roughly the same distance before disappearing again. Leahy (in preparation) has a high-resolution map showing complicated structure in and around the jet. The host galaxy is a broad-line object (Laing *et al*. 1994) and may lie in a small group (Rawlings 1987; dK96).

4.5.4 3C 61.1

LP present VLA observations at L-band with a resolution of 3.7 arcsec. Images with a comparable resolution but lower sensitivity are in Alexander (1985). Alexander's maps show a possible jet in the N lobe, but the lobes are of high surface brightness so a definite jet detection is difficult. The host galaxy is an NLRG with $R = 17.60$ and lies in a cluster (Rawlings 1987); it was detected in the X-ray by EINSTEIN (Feigelson and Berg 1983). There is no obvious interaction between the radio lobes and the disturbed optical morphology seen by the HST (dK96).

4.5.5 3C 79

The literature

3C 79 has been observed at a number of radio frequencies in spectral index studies, because of its high-surface-brightness lobes. The best VLA maps prior to this work are those in Spangler, Myers and Pogge (1984); 3C 79 has also been mapped by Antonucci (1985) with the VLA, by Burch (1979a) and Riley and Pooley (1975: RP) with the 5-km telescope, and by Stephens (1987) with MERLIN.

Burch (1979b), Myers and Spangler (1985) and Stephens (1987) all examine the spectral index of the source, and all find the expected steepening of the spectrum towards the nucleus. Stephens, using several frequencies, is able to produce 'age maps' showing that contours of constant age are concave towards the nucleus; this is consistent with a model in which the advance speed of the hot spots is greater than the speed of the backflow. He also derives velocities for the particles leaving the hot spots, based on fitting a continuous-injection model to their spectra and taking into account their size and surface brightness.

The redshift used for 3C 79 is given by Schmidt (1965). 3C 79's host galaxy has been classified as an N-galaxy with $R = 17.47$ (Sandage 1973a); N-galaxies normally have broad emission lines (Grandi and Osterbrock 1978) and so 3C 79 might have been assumed to be a broad-line radio galaxy. Laing (private communication) fails to detect any broad wings on the Hα line with a high-quality spectrum, so I have classified 3C 79 as a narrow-line object. The HST image shows no compact nucleus (dK96), and so the classification as an N-galaxy may have been erroneous.

Rawlings (1987) records a 2σ X-ray detection of 3C 79 by the EINSTEIN satellite. The galaxy may have one or two nearby companions (Taylor *et al*. 1996). A broad-band optical image by McCarthy *et al*. (1995) is unremarkable, but their image in the 5007-Å [OIII] line shows an extended region of gas to the NW which the western lobe appears to flow around. There is diffuse emission surrounding the nucleus, which McCarthy (1988) suggests is common in N-galaxies. At sub-arcsecond resolution the nuclear regions are complex and there is some alignment with the radio structure (dK96).

My maps

The core of 3C 79 appears to have varied by about 5 mJy, an increase of 70%, between the epochs of observation of the A- and B-array and the C- and D-array data. This was corrected for by subtraction from the A- and B-array datasets. A 1 mJy confusing source 75 arcsec to the NE of the pointing centre has been removed from the map.

The low-resolution map of 3C 79 (figure 4.3) shows the asymmetrical nature of the source. The western lobe is extended well to the south of the source axis, while the eastern lobe is more normal in shape. Both lobes have the unusual feature that the hot spot areas protrude in bottle-neck fashion from much broader lobes — compare 3C 234 and to a lesser extent 3C 132 and 3C 381 (see below). The lobes are not smooth — there is some evidence for structure in them even in the lower-quality maps of Spangler *et al*. (1984) and more is seen here. The bright region to the west of the hot spot in the east lobe, identified by Spangler *et al*. as a secondary hot spot, can also be seen clearly (E1). The source has no jets.

At high resolution, both hot spot regions are revealed to have complicated multiple structure. The eastern end of the source comprises four separate components. The most compact is the southeastern one (E5), which is slightly resolved and appears extended to the north and west; the magnetic field is directed roughly north-south. To the north of this is a less compact component, E4, extended southwards and northwestwards; to the northwest of this and joined to it by a bridge is a still more extended component, E3. A linear feature leaves this to the southwest and then appears to turn northwest, at E2, before disappearing; it points towards the extended region E1 which forms Spangler *et al*.'s 'secondary hot spot'. It is tempting to regard this sequence of more and more diffuse hot spots, connected by ridges of emission, as also being connected by real ongoing outflow; in this model the most compact hot spot would be the site of termination of the beam (invisible here) and the rest, with the possible exception of the very diffuse secondary E1, would be successive sites of outflow redirection and decollimation. The directions of the magnetic field vectors are points in favour of this model; in the compact components they are perpendicular to the presumed flow, as might be expected if deceleration were occurring here; elsewhere they are parallel to it.

The situation is not quite as complicated in the western hot spot complex. This consists of three com-

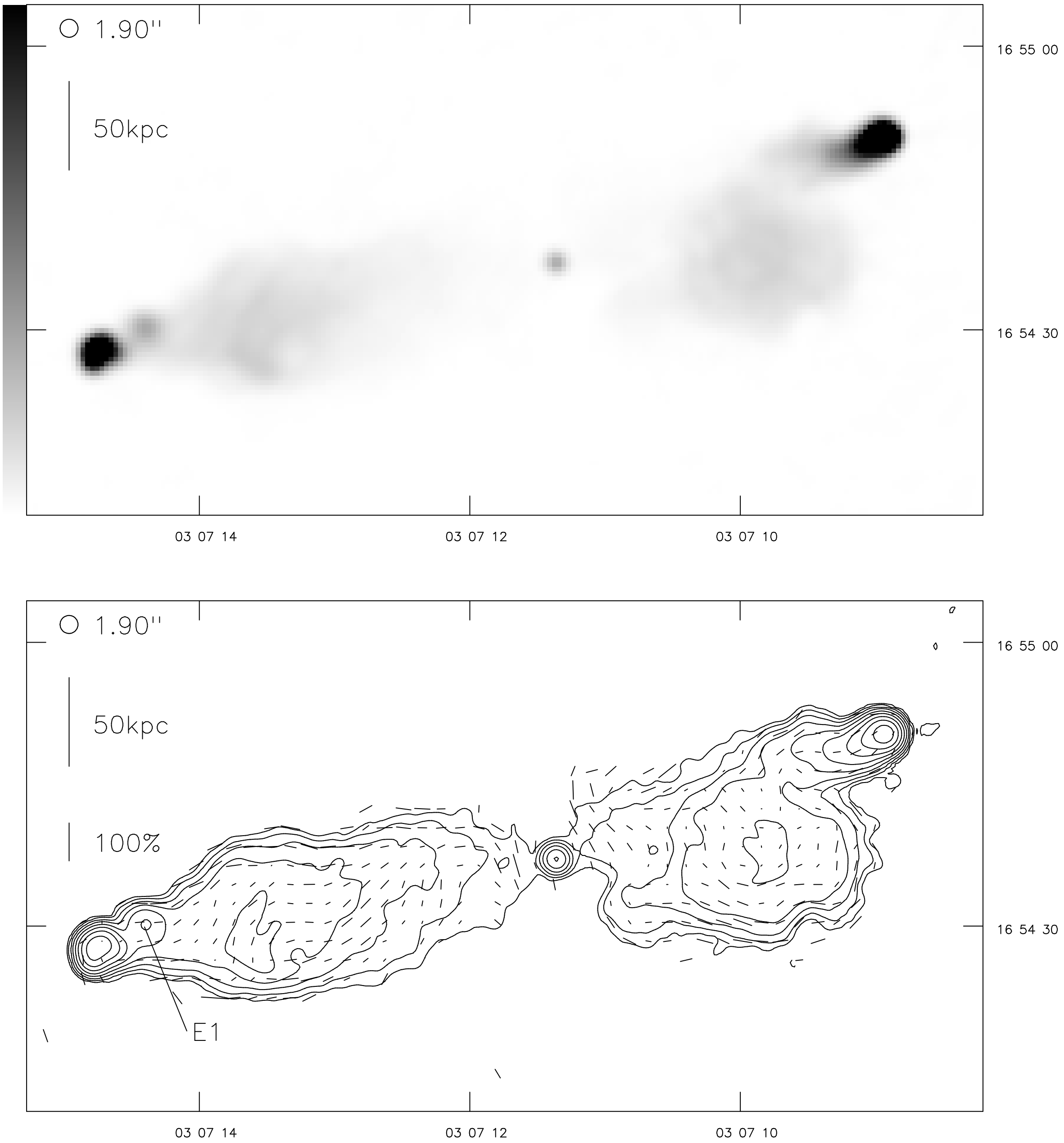

Figure 4.3: 3C 79 at 1.90 arcsec resolution. Above: linear greyscale; black is 20 mJy beam^{-1}. Below: contours at $0.20 \times (-2,-1,1,2,4,\ldots)$ mJy beam^{-1}.

pact components. In this case the relative degrees of compactness are not easy to determine by eye, but Gaussian fitting shows that the southern component (W1) is the most compact. It is extended north-

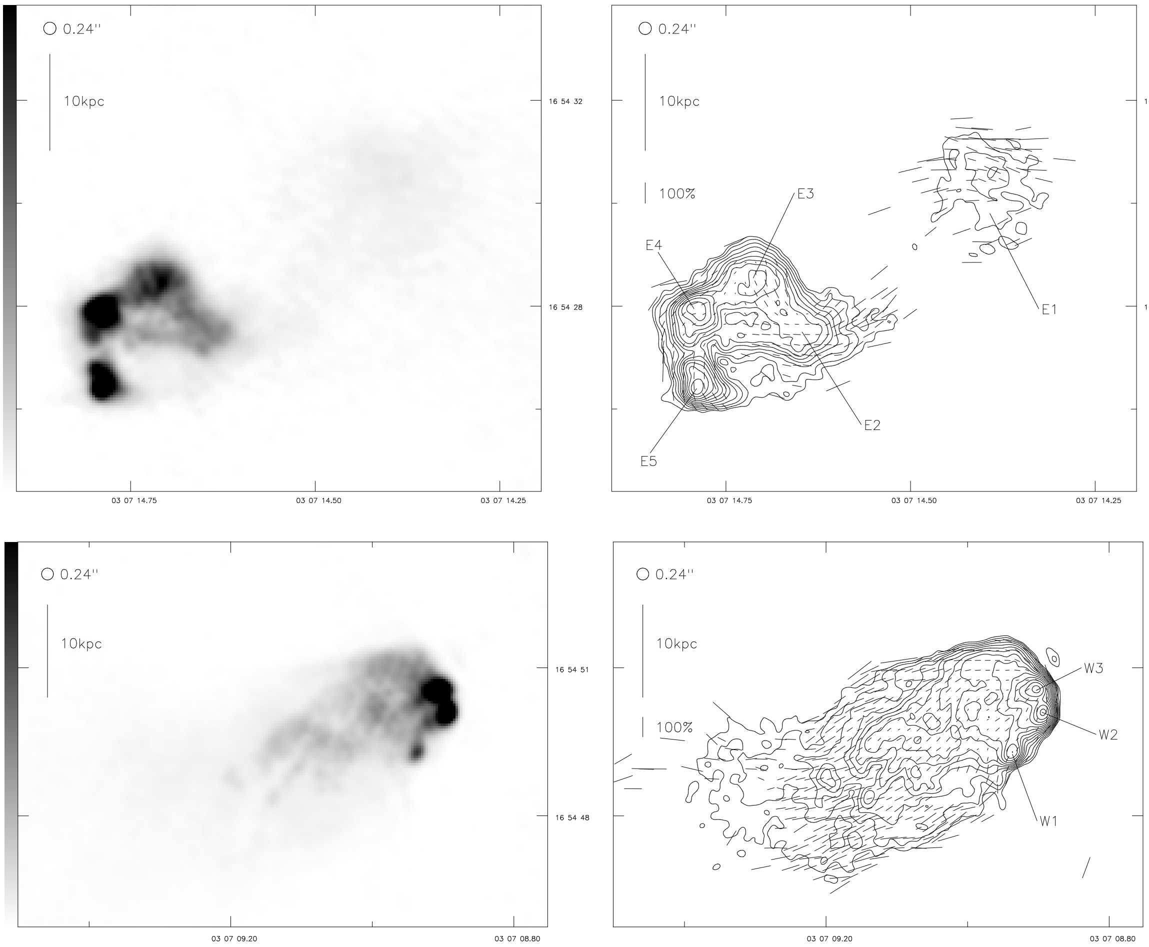

Figure 4.4: 3C 79 at 0.24 arcsec resolution. Above: E hot spot — left: linear greyscale; black is 2 mJy beam^{-1}; right: contours at $0.1 \times (-\sqrt{2}, -1, 1, \sqrt{2}, 2, 2\sqrt{2}, \ldots)$ mJy beam^{-1}. Below: W hot spot — left: linear greyscale; black is 4 mJy beam^{-1}; right, as above right.

wards by a bent ridge of emission, clear on the greyscale map, which leads into the second most compact component, W2; this in turn is extended northwards and connects to the northern and most diffuse component, W3. This is extended eastwards into a region of complicated structure, all of which is strongly polarized with the magnetic field directed along the source axis. By analogy with the eastern hot spot region, we might suggest that the most compact hot spot (the southernmost one) is the current site of beam termination, and that the connections between it and the others and the magnetic field structures imply continued outflow between them.

Table 4.5: The core flux of 4C 14.11

Date	Flux (mJy)
03/08/93	20.9 ± 0.3
27/11/93	31.1 ± 0.5
23/06/94	33.1 ± 0.2
06/08/95	28.9 ± 0.1

4.5.6 4C 14.11

The literature

4C 14.11 was imaged by LP, who noted the unusual multiple hot spot structure in the E lobe. Previous 5-km telescope images are given by Peacock and Wall (1982) and Rawlings (1987).

4C 14.11 is identified with a elliptical galaxy with $r = 19.1$ (Peacock *et al*. 1981). The redshift is due to Perryman *et al*. (1984), based on absorption features and a tentative [OIII]5007 line. Laing (private communication) has a high-quality spectrum which allows 4C 14.11 to be classified as a low-excitation object. Rawlings (1987) suggests that 4C14.11 may lie in a cluster.

My maps

The core of 4C 14.11 varied between our epochs of observation. The fluxes measured (by fitting a Gaussian plus baseline to the maps with AIPS task JMFIT) are shown in table 4.5. I corrected for this by adding to and subtracting from the *uv* data so as to make all the fluxes the same as that of the A-configuration.

The low-resolution map in figure 4.5 shows the multiple hot spots in both lobes. A curving filament leads out of the western hot spot complex into the lobe. The southernmost hot spot in the western hot spot complex is joined to the other two components visible at this resolution by a bridge of emission. There is a faint compact knot (E1) about 20 kpc to the southeast of the core. The lobes both extend to the northeast close to the host object, and the extended areas are highly polarized. The UKIRT image of the field (figure 4.6) shows an unremarkable host galaxy surrounded by many fainter objects, supporting the suggestion that the environment is a cluster.

At high resolution the knot E1 is seen to be a linear feature 2.8 arcsec in length and unresolved transversely, aligned with the axis between the hot spots and the core. I have classed this as a jet. The eastern

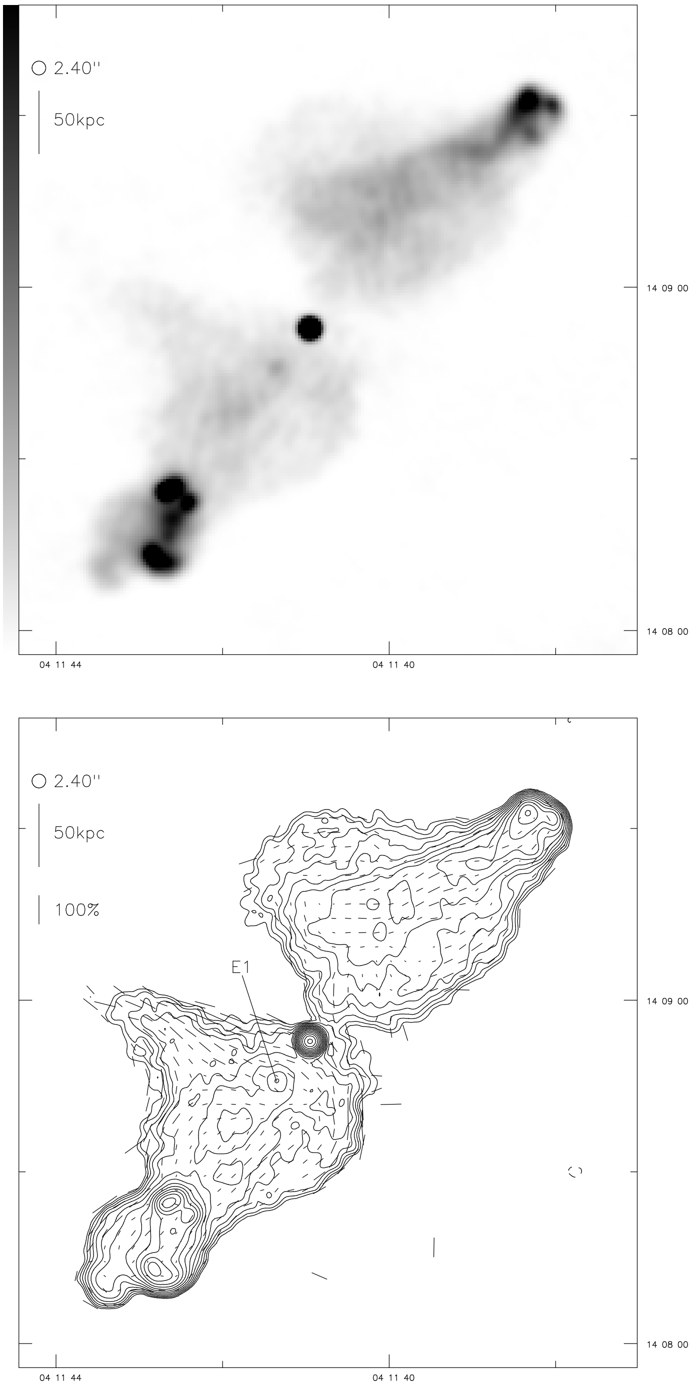

Figure 4.5: 4C 14.11 at 2.40 arcsec resolution. Above: linear greyscale; black is 5 mJy beam^{-1}. Below: contours at $0.15 \times (-\sqrt{2}, -1, 1, \sqrt{2}, 2, 2\sqrt{2}, \ldots)$ mJy beam^{-1}.

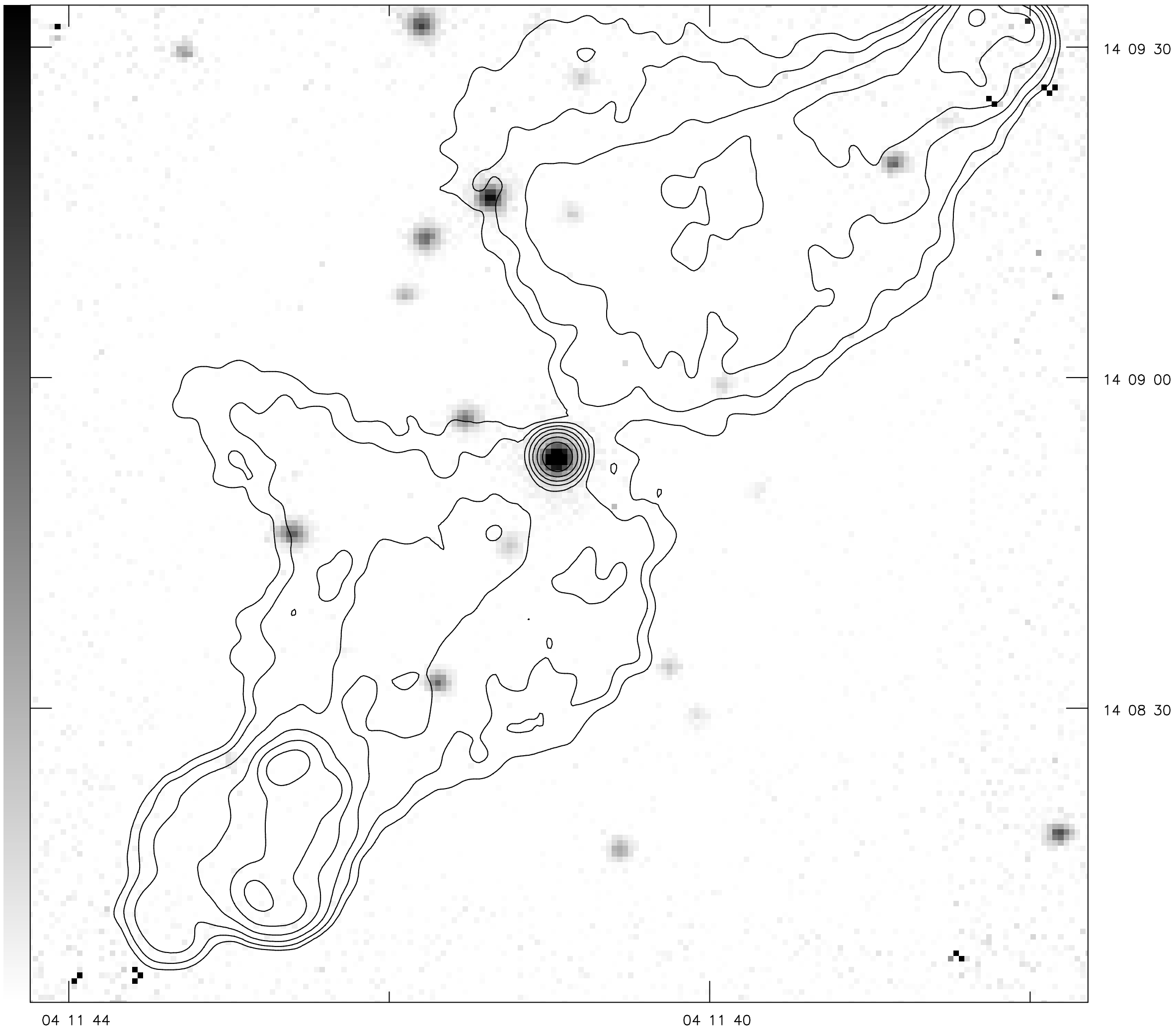

Figure 4.6: UKIRT image of the field of 4C 14.11. Greyscale in arbitrary units. Overlaid are contours of a 2.40-arcsec resolution radio map at $0.2 \times (-2, -1, 1, 2, 4, \ldots)$ mJy beam^{-1}.

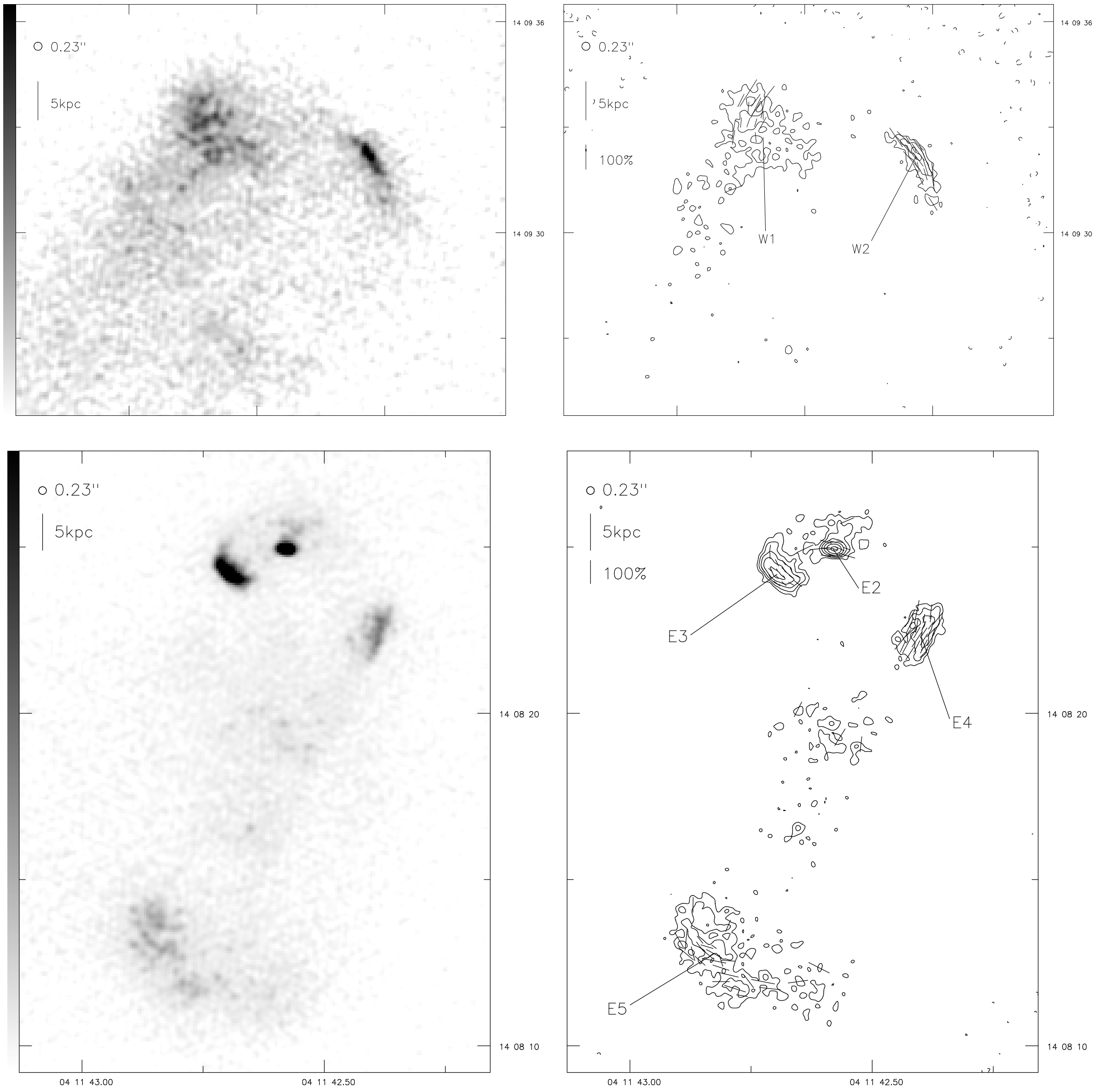

Figure 4.7: 4C 14.11 at 0.23 arcsec resolution. Above: E hot spot — left: linear greyscale; black is 500 µJy beam^{-1}; right: contours at $50 \times (-2, -1, 1, 2, 4, \ldots)$ µJy beam^{-1}. Below: W hot spot — left: linear greyscale; black is 200 µJy beam^{-1}; right, as above right.

hot spot consists of four components, of which one (the northernmost: E2) is clearly the most compact (it is slightly resolved in an east-west direction). At this resolution it can be distinguished from the component E3 to the southeast which is well resolved in position angle 45°. On the low-resolution map, these two appear as a single hot spot. To the southwest of this feature is another, E4, extended northwest-southeast, pointing towards the southernmost ‘hot spot’, E5, which was resolved even on the low-resolution map and which turns out to contain no compact structure at all. (It looks very like an extended, dimmer version of E3.) All these features have their magnetic fields in the direction of their longer axis.

It is not clear what the fluid flow is doing in this part of the source. E2 is the most compact hot spot, and so presumably the beam termination, but there is no evidence that it is ‘feeding’ E3. The diffuse components E4 and E5 resemble an old jet segment/hot spot pair which are no longer being powered by the beam. A simple dentist’s drill model, perhaps complicated by projection, may be the best explanation here.

In the western lobe the picture is simpler. There is only one truly compact hot spot, W2, and it is elongated transverse to the presumed beam direction, with magnetic field aligned along its length. The ridge line of the hot spot complex then connects it to a more diffuse region, W1 — approximately 10 kpc in size — whose magnetic field direction is transverse to a line drawn between its centre and that of the compact hot spot. This is consistent with a picture in which outflow is taking place from the compact to the less compact hot spot and thence out into the source via the curving filament described above.

A map of spectral index between 8.4 and 1.4 GHz, made at low resolution (figure 4.8) shows the hot spots to be the areas of flattest spectrum, as expected; the minima in spectral index ($\alpha \approx 0.7$) correspond to my identifications of the beam-termination hot spots. The entire southeastern end of the source has a reasonably flat spectrum ($\alpha \approx 0.8$) and this might be taken as an indication, along with the hot spots that appear to be no longer being supplied with energy, that the beam has been terminating further forward in the recent past. The spectral index elsewhere in the source steepens considerably transverse to the source axis; there is little evidence for a significant gradient *along* the axis.

The northern lobe appears significantly more depolarized between 8.4 and 1.4 GHz ($\mathrm{DP} = 0.68$) than the southern lobe ($\mathrm{DP} = 0.96$); as the jet lies in the southern lobe, this is in the sense predicted by the Laing-Garrington effect.

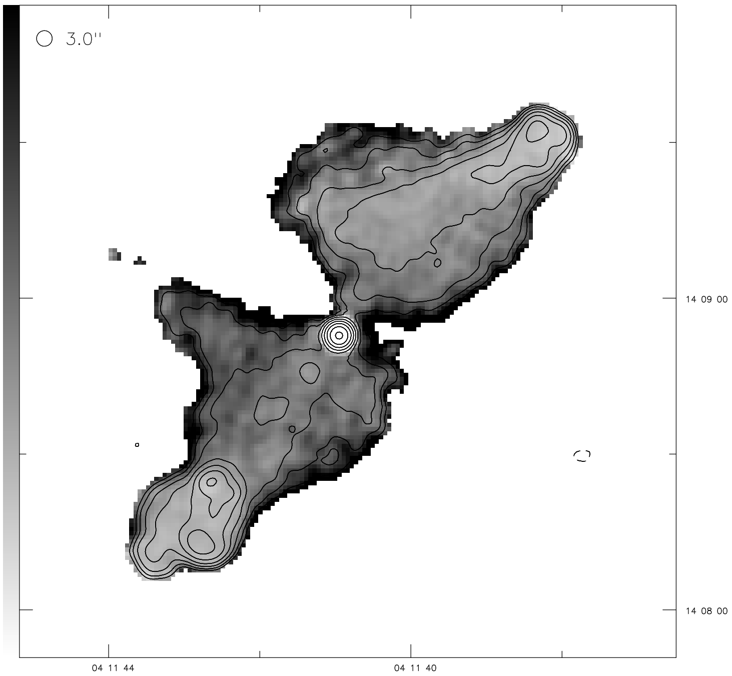

Figure 4.8: Spectral index between 8.4 and 1.4 GHz of 4C 14.11 at 3.00 arcsec resolution. Linear greyscale between 0.5 and 1.5; superposed are contours of total intensity at 8.4 GHz at $0.2 \times (-2, -1, 1, 2, 4, \ldots)$ mJy beam^{-1}.

4.5.7 3C 123

The literature

3C 123 has a strong claim to be the most bizarre object in LRL, with its peculiar S-shaped structure and spectacularly bright hot spots. Cox, Gull and Scheuer (1991) show Laing's otherwise unpublished VLA maps of it at 1.7, 4.9 and 14.9 GHz. Riley and Pooley (1978) observed the source with the 5-km telescope at 2.7 and 15 GHz, Kronberg and Strom (1975) observed it with the NRAO interferometer at 8.0 GHz, Stephens (1987) has imaged it with MERLIN at low frequencies, and Okayasu, Ishiguro and Tabara (1992) present a 98-GHz map made with the Nobeyama Millimetre Array. Neff *et al.* (1995) have a 1.4 GHz VLA snapshot. Meisenheimer *et al.* (1989) discuss the high-resolution radio spectral index of the eastern hot spot, which is detected in the sub-mm (230 GHz) but not the optical waveband. The spectral index and age maps of Stephens, although unable to resolve completely the plume in the Sf part of the source, indicate that the spectral index steepens (and the plasma ages) with distance away from the hot spots.

3C 123 is associated with an $R = 18.94$ magnitude galaxy with strong Galactic reddening. An optical CCD image given by Hutchings, Johnson and Pyke (1988) shows the galaxy to have a good deal of diffuse structure to the south and southwest of the nucleus, and Hutchings (1987) suggests that this may be the result of galaxy interaction. There are many faint small objects in the field, so the object may be part of a cluster (Longair and Gunn 1975; Rawlings 1987). EINSTEIN detected no X-ray source associated with the radio galaxy (Rawlings 1987). The optical spectrum is given by Spinrad (1978) and shows weak [OIII]; Laing (private communication) has a higher-quality spectrum confirming this result. On this basis, I have classified it as a low-excitation object; it is possible, however, that the reddening misleadingly biases the [OIII] flux and that it should be classified as a NLRG.

My maps

The rotation measure of 3C 123 is large and negative, probably due to the Galactic material that reddens the host in the optical — it lies in a region of the sky where many sources have large negative RM. Polarization vectors may thus misrepresent the true magnetic field direction by up to 25°. Attempts to assess the RM variation across the source using 5-GHz data available to me suggest that there may be variations in RM with respect to the mean of order 100 rad m^{-2} across the source, but variations of this order should not affect the polarization too badly.

A low-resolution map (figure 4.9) reproduces the structure seen in Cox *et al*. (1991). The polarization of the source follows the curves of the plumes well, with the magnetic field being consistently aligned along the plumes. (The fractional polarization map is made with points five times the r.m.s. noise in the polarization and total intensity maps, as the noise near the source is dominated by artefacts from the deconvolution of the bright hot spot.)

The UKIRT map of this field (figure 4.10) shows the many faint nearby objects and the diffuse nature of the host itself. There are no redshifts for the objects in the field, but it seems likely that some are associated with 3C 123. There is no convincing evidence of interaction between the radio structure and field objects, however.

At higher resolution filamentary structure can be seen in the plumes. Much of the lumpiness in figure 4.11 is an artefact of the CLEANing process, but many of the prominent linear features in the northern lobe can be identified on the 5-GHz map of Laing (private communication) and so are likely to be real. Better *uv* coverage is needed to constrain the complicated structure in this source.

The detailed structure of the hot spots (figure 4.11) is as unusual as that of the rest of the source. Both are double, but the eastern hot spot complex is extremely bright (over 4 Jy at 8.4 GHz). At the highest 8-GHz resolution it can be seen to consist of two components, the brighter (E4) being resolved while

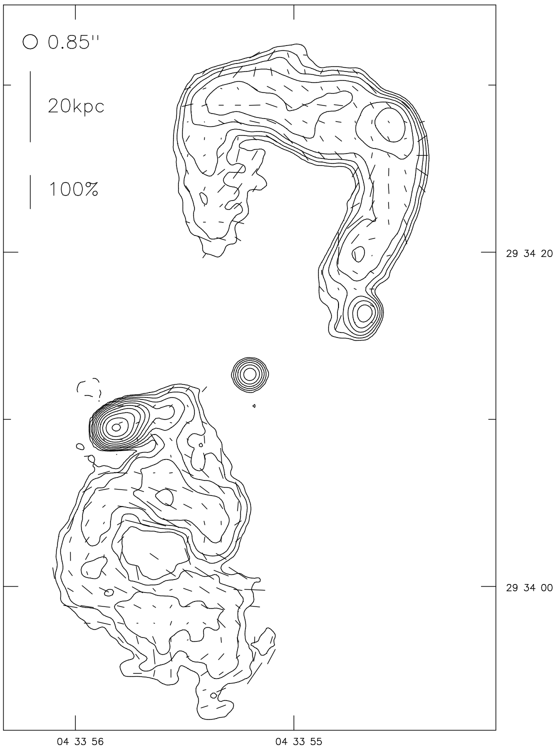

Figure 4.9: 3C 123 at 0.85 arcsec resolution. Contours at $2 \times (-2, -1, 1, 2, 4, \ldots)$ mJy beam^{-1}.

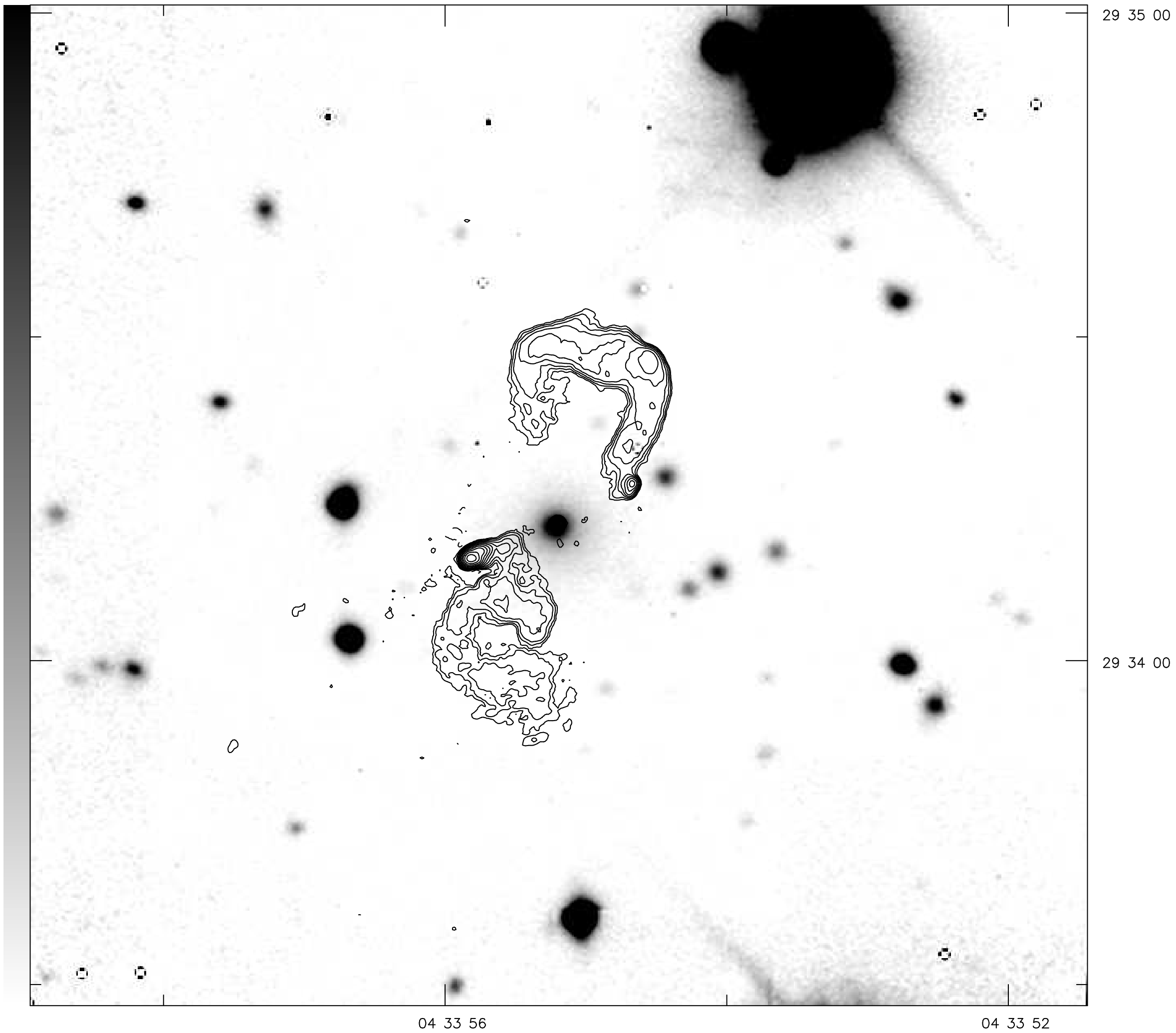

Figure 4.10: UKIRT image of the field of 3C 123. Greyscale in arbitrary units. Overlaid are contours of a 0.60-arcsec resolution radio map at $1 \times (-2, -1, 1, 2, 4, \ldots)$ mJy beam^{-1}. To the north is a bright star.

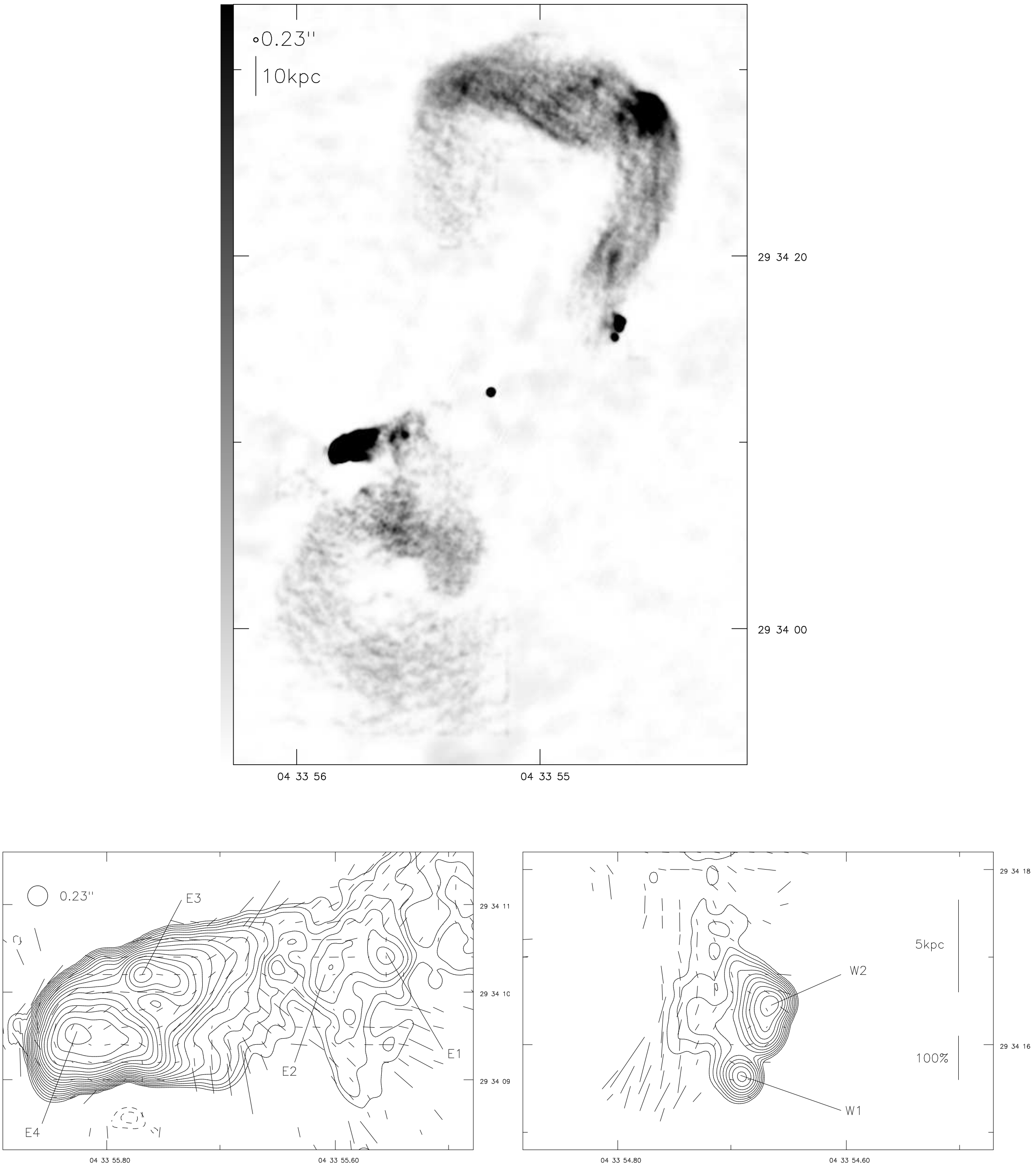

Figure 4.11: 3C 123 at 0.23 arcsec resolution. Above: linear greyscale; black is 10 mJy beam^{-1}. Below left: E hot spot; contours at $1 \times (-\sqrt{2}, -1, 1, \sqrt{2}, 2, 2\sqrt{2}, \ldots)$ mJy beam^{-1}. Below right: W hot spot, contours as left.

the dimmer (E3) contains an unresolved component. Both are extended east-west and their magnetic fields are largely speaking directed along this axis. Neither points towards the core. However, there are some knots (E1, E2) to the west of E3 which might trace the bending of a beam. Apart from these there is no indication of a jet at this resolution. The western hot spot complex is more normal; at 0.23-arcsec resolution the southern one, W1, is unresolved and the northern one, W2, is extended north-south. Both hot spots have a comparatively low degree of polarization.

I obtained 5-GHz MERLIN observations of 3C 123 (consisting of one 16-hour run on 27/06/95 with observing frequencies of 4.55, 4.86 and 5.18 GHz) to investigate the structures in the hot spots further. These (figure 4.12) provide three times the resolution of Laing's 15-GHz images in Cox *et al*. (1991), although a lack of short baselines means that structure on scales larger than 3.5 arcsec is not seen; the images are noisy as a consequence, since much of the flux of 3C 123 is on these scales. At this resolution E3 is resolved, showing a cylindrical shape with a length of around 3 kpc and a bright head (at the eastern end) whose size is around 0.7 kpc. E4 is fully resolved into an east-west line of three knots with bright filaments branching off them to north and south. The 'pits' of very low emission separating these filaments appear to be real, although they might be filled in to some extent by shorter-baseline data. The 'mushroom-cap' shape of the eastern end of E4 is suggestive of a bow shock. The whole complex is remarkably reminiscent of the western hot spots of Cygnus A (e.g. Perley and Carilli 1996), with the E3 hot spot corresponding to hot spot B in Cygnus A (it shows the same head-tail structure) and E4 corresponding to hot spot A. However, an understanding of the fluid flow in the source remains elusive. E3 must be identified, on the criteria I have used, as being the primary hot spot; but does its tail trace the incoming beam, or is it outflow into the lobe? Carilli, Dreher and Perley (1989) argue that the corresponding feature in Cygnus A west — the tail of hot spot B — traces flow into the secondary, but it is difficult to see how this might be happening in 3C 123. On the other hand, the brightness (and corresponding energy density) of E4 argue that it must have been connected to the beam until very recently, if it is not still being supplied with power. In favour of a model in which E4 is a disconnected former primary and E3 the new site of beam termination is their similarity in shape; it is not hard to imagine E4 as an inflated version of E3, possibly with some inflow and outflow still going on as in the models of Cox *et al*. (1991). W2 and W1, by contrast, appear to be a normal double hot spot pair very like those in other sources. W1 is clearly the primary, and there is evidence in the MERLIN image for flow between W1 and W2 and between W2 and the lobe (to the north and east). The fact that the two ends of the source are so different in their structure and inferred fluid flow means that a model explaining the hot spot brightness asymmetry in terms of relativistic beaming is difficult to sustain; it is more likely that the environments of the two hot spots are significantly different.

These observations shed a little light on the reasons for the peculiar large-scale structure of 3C 123. Firstly, the hot spot structures, although the eastern one is unusual, are understandable when compared to other objects and to the models described in section 1.6.4. 3C 123 is therefore an ordinary classical double source behaving in a peculiar way, rather than being something entirely unique. Two possible models remain to be distinguished. The first, initially proposed by Riley and Pooley (1978), is that the beam axis has precessed over the lifetime of the source, and that this together with projection is sufficient to explain its structure. The second is that the source axis has remained constant, but that outflow from the hot spots has formed plumes rather than lobes, in a manner similar to that proposed for 3C 171 below (section 4.5.10) and presumably caused by an unusual large-scale environment. The well-collimated and almost constant-width appearance of the plumes is a challenge for both models, but particularly for the precession model. The multiple nature of the hot spots has been adduced as evidence for beam precession (Cox *et al*. 1991) but multiple hot spots are now seen to be common; the fact that the primaries are in the correct positions for ongoing precession (in a north-through-west sense on the maps shown) is equally consistent with an outflow model. The fairly good alignment of the magnetic field with the plume axes (except at the very ends of the plumes) seems more consistent with a model with ongoing outflow. This field configuration is similar to that of the plumes of wide-angled tail sources (see chapter 3). The final argument against precession, and so by implication for a model involving outflow, is simply the amount of precession required; the beam axis would have to change direction by at least 70° over the lifetime of the source (a few $\times 10^6$ yr). With the possible — and debatable — exception of the winged sources (e.g. Leahy and Williams 1984) precession of this magnitude on these timescales has not been observed or inferred for any other classical double source; by contrast, many sources exhibit peculiar structures which can be attributed to an unusual environment. These arguments lead me to favour the outflow model. The question of what might be special about the environment of 3C 123 remains open, however.

4.5.8 3C 132

The literature

3C 132 has not been extensively studied; the best radio map prior to this study is in Neff *et al*. (1995). JPR identify the source with a 19th magnitude red galaxy; our map shows the radio core and confirms the identification. The galaxy is imaged by Hutchings *et al*. (1988) and is classed by Hutchings (1987) as an interacting irregular; there are several faint objects within a few arcseconds of the host galaxy. Some structure is observed in its centre (dK96). There is, however, no clear relationship between the radio and optical alignments.

A high-quality spectrum of the source in Laing *et al*. (1994) shows weak, narrow Hα and no sign of high-excitation lines such as [OIII]. 3C 132 is thus a prototype ‘dull FRII’ (section 1.5).

My maps

The dataset used to make these images needs a small amount of shorter-baseline data to sample the source completely. The result of the undersampling is a slight negative ‘bowl’ around the source.

3C 132 is an ordinary classical double of small size (figure 4.13). Both hot spot regions, but particularly the northern one, protrude in bottle-neck fashion from broader lobes, as seen in 3C 79 and 3C 234. The eastern lobe has an unusual brightening along its southern edge, starting at the hot spot and extending around the lobe, which might be interpreted as backflow. At slightly lower resolutions (figure 4.14) there is the suggestion of a linear feature (E1, E2) which appears to run from close to the core to the bright edge of the hot spot region. I have classified it as a possible jet. The UKIRT map of the field (figure 4.15) shows no obvious relationship between the field objects and the radio source. High-resolution maps (figure 4.16) resolve the hot spot areas — the western hot spot, W1, has a size of about 800 pc, and the eastern one, E1, is extended on scales of about 2 kpc. Both hot spots have inferred magnetic fields transverse to the source axis. A curving feature leaves the western hot spot to the southeast and then bends northeast about 7 kpc away from the hot spot before terminating in a diffuse region — this might also be interpreted as backflow.

4.5.9 3C 153

The literature

The only high-resolution radio maps are those of Lonsdale and Morison (1983) and Akujor *et al.* (1991), made with MERLIN, and that of Neff *et al.* (1995) with the VLA at 5 GHz; Pooley and Henbest (1974) have a 5-km telescope map.

Hutchings *et al.* (1988) have imaged the host galaxy, a $V = 18.5$ magnitude elliptical, but remark only that it is too small to note any structure. HST observations (dK96) show an elliptical nucleus. Rawlings (1987) suggests that the environment is a cluster.

3C 153 is a narrow-line object (Laing, private communication).

My maps

The southern lobe of 3C 153 is reasonably similar to those seen in larger sources. It has a clear double hot spot, one component of which (W3) is barely resolved (Gaussian fitting suggests a size of 0.5 kpc); the other, W2, is much more diffuse and has a tail leading back into the lobe. The magnetic field is

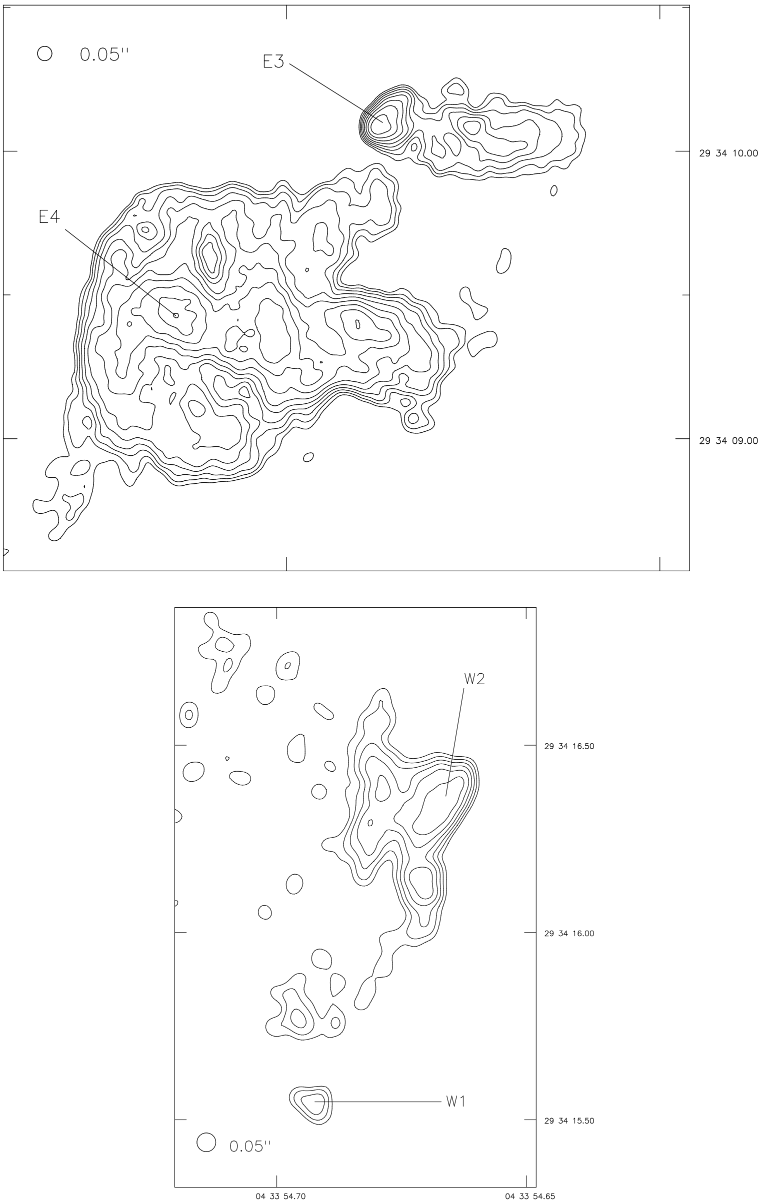

Figure 4.12: 3C 123 at 0.05 arcsec resolution. Above: E hot spot; contours at $2 \times (-\sqrt{2}, -1, 1, \sqrt{2}, 2, 2\sqrt{2}, \ldots)$ mJy beam^{-1}. Below: W hot spot, contours at $1 \times (-\sqrt{2}, -1, 1, \sqrt{2}, 2, 2\sqrt{2}, \ldots)$ mJy beam^{-1}.

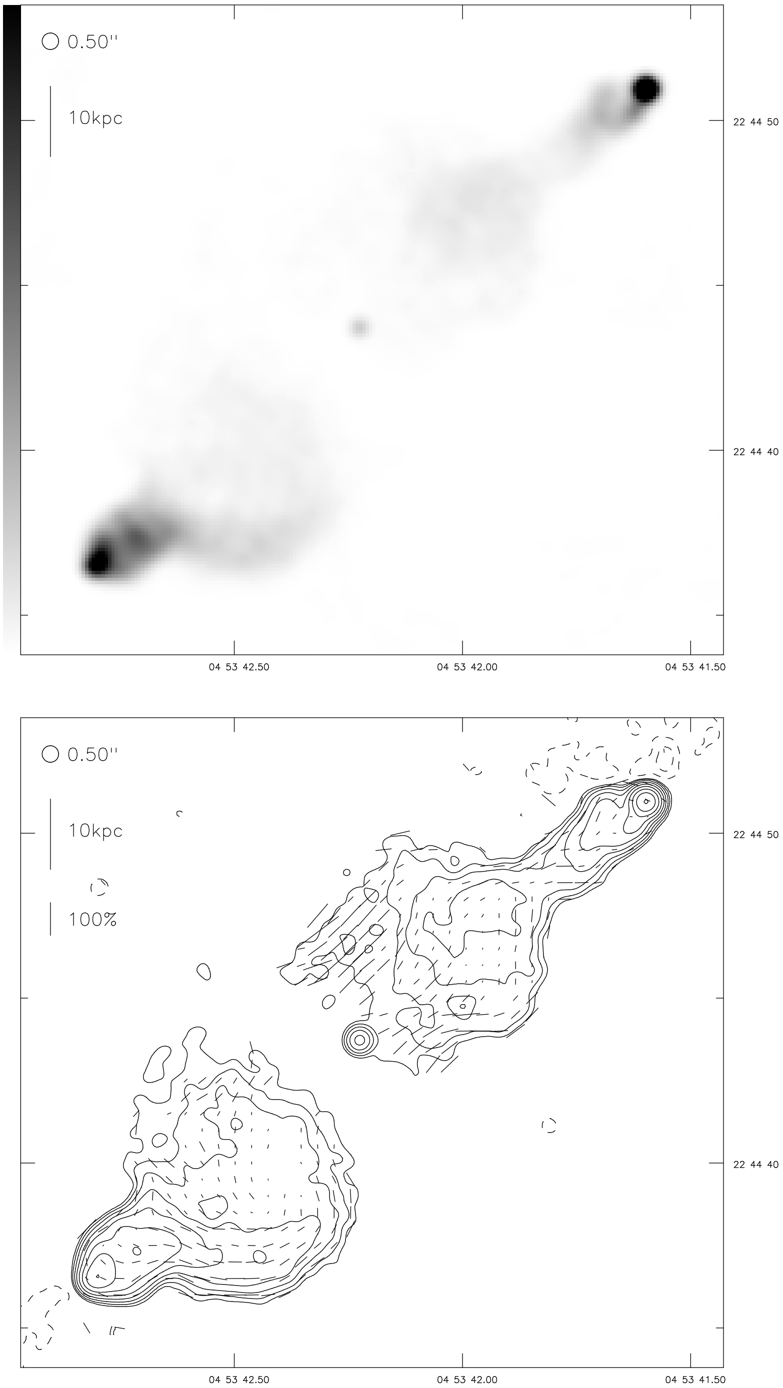

Figure 4.13: 3C 132 at 0.50 arcsec resolution. Above: linear greyscale; black is 20 mJy beam^{-1}. Below: contours at $0.2 \times (-2, -1, 1, 2, 4, \ldots)$ mJy beam^{-1}.

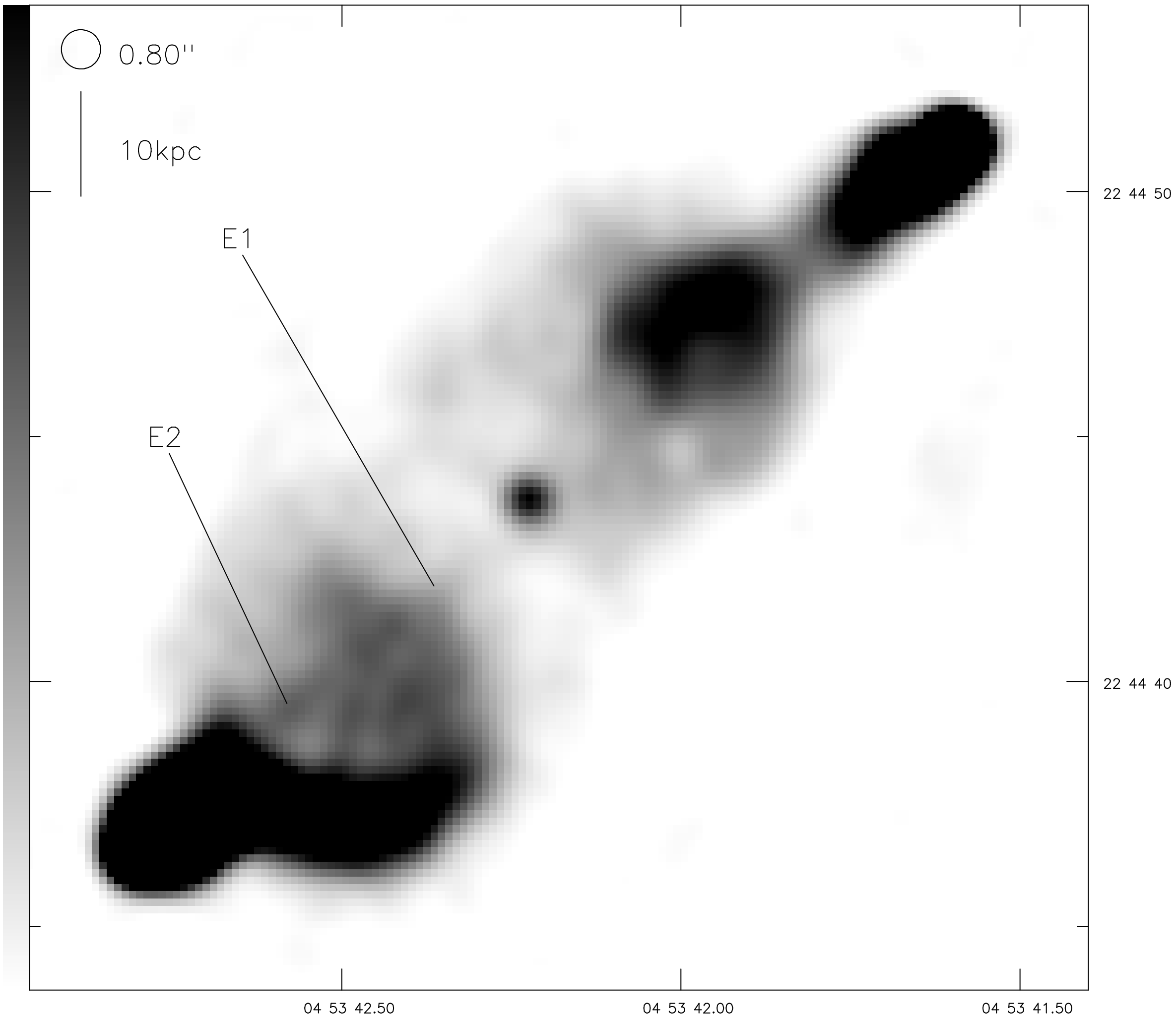

Figure 4.14: 3C 132 at 0.80 arcsec resolution. Linear greyscale; black is 5 mJy beam^{-1}.

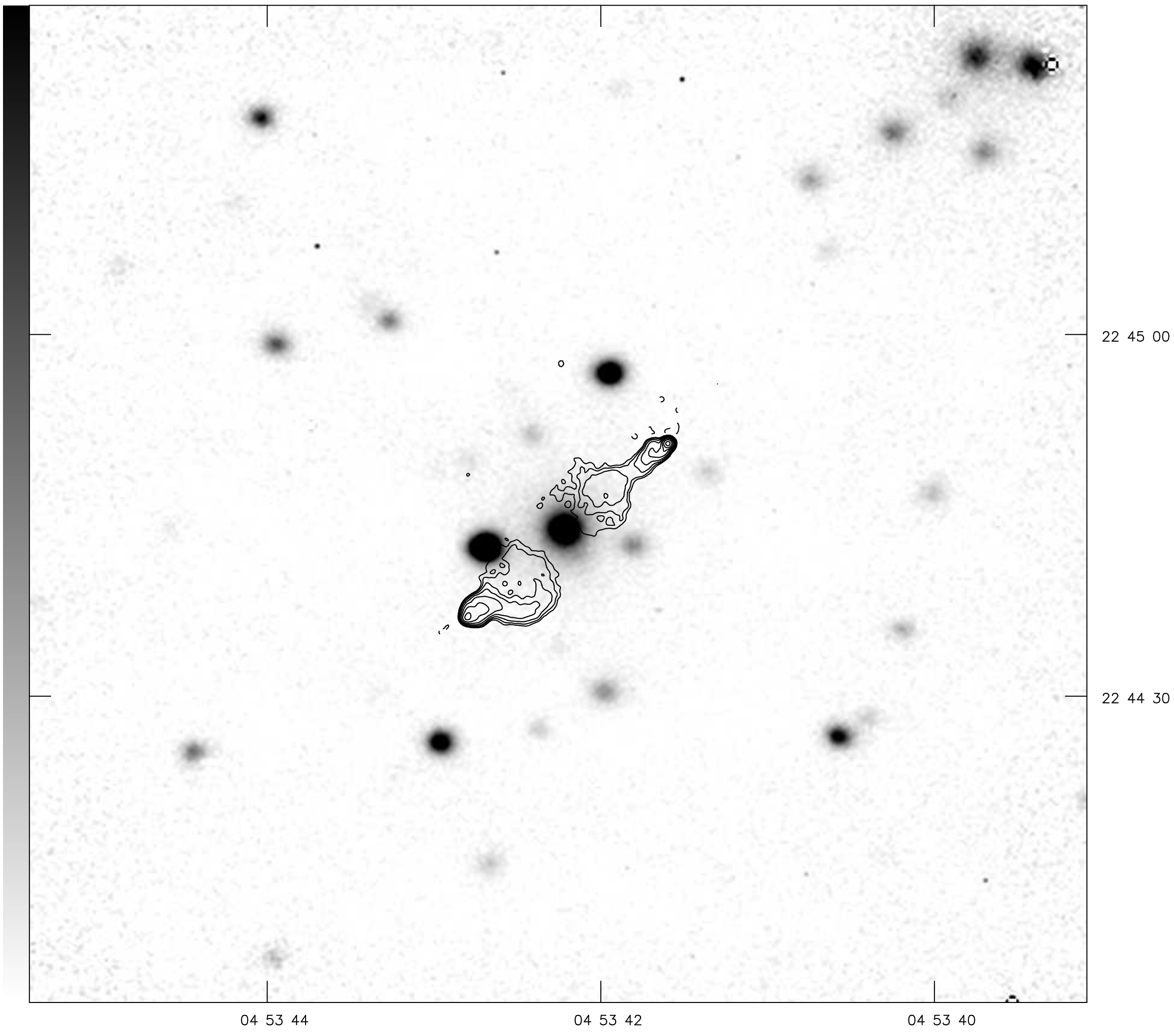

Figure 4.15: UKIRT image of the field of 3C 132. Greyscale in arbitrary units. Overlaid are contours of a 0.50-arcsec resolution radio map at $0.3 \times (-2, -1, 1, 2, 4, \ldots)$ mJy beam^{-1}. Immediately to the east of the galaxy is a foreground star.

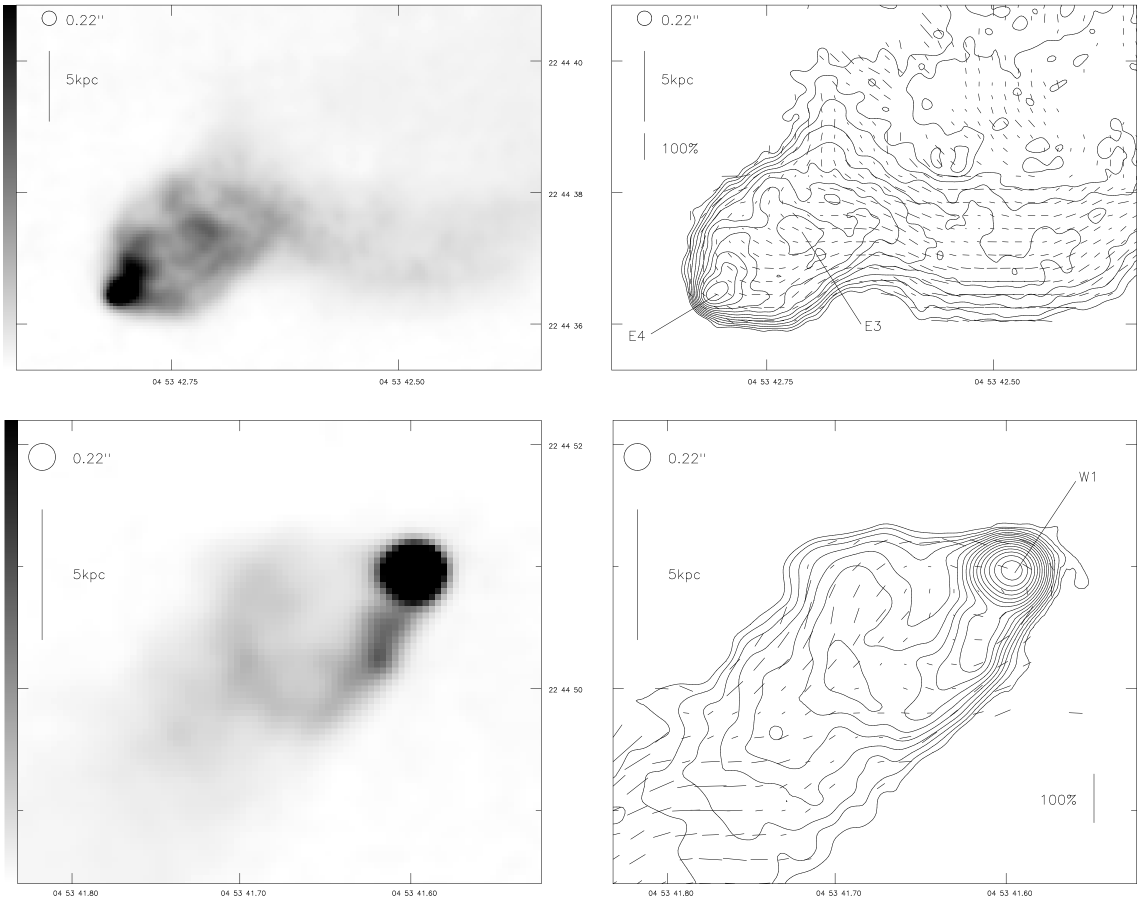

Figure 4.16: 3C 132 at 0.22 arcsec resolution. Above: E hot spot — left: linear greyscale; black is 5 mJy beam^{-1}; right: contours at $0.15 \times (-\sqrt{2}, -1, 1, \sqrt{2}, 2, 2\sqrt{2}, \ldots)$ mJy beam^{-1}. Below: W hot spot — as above.

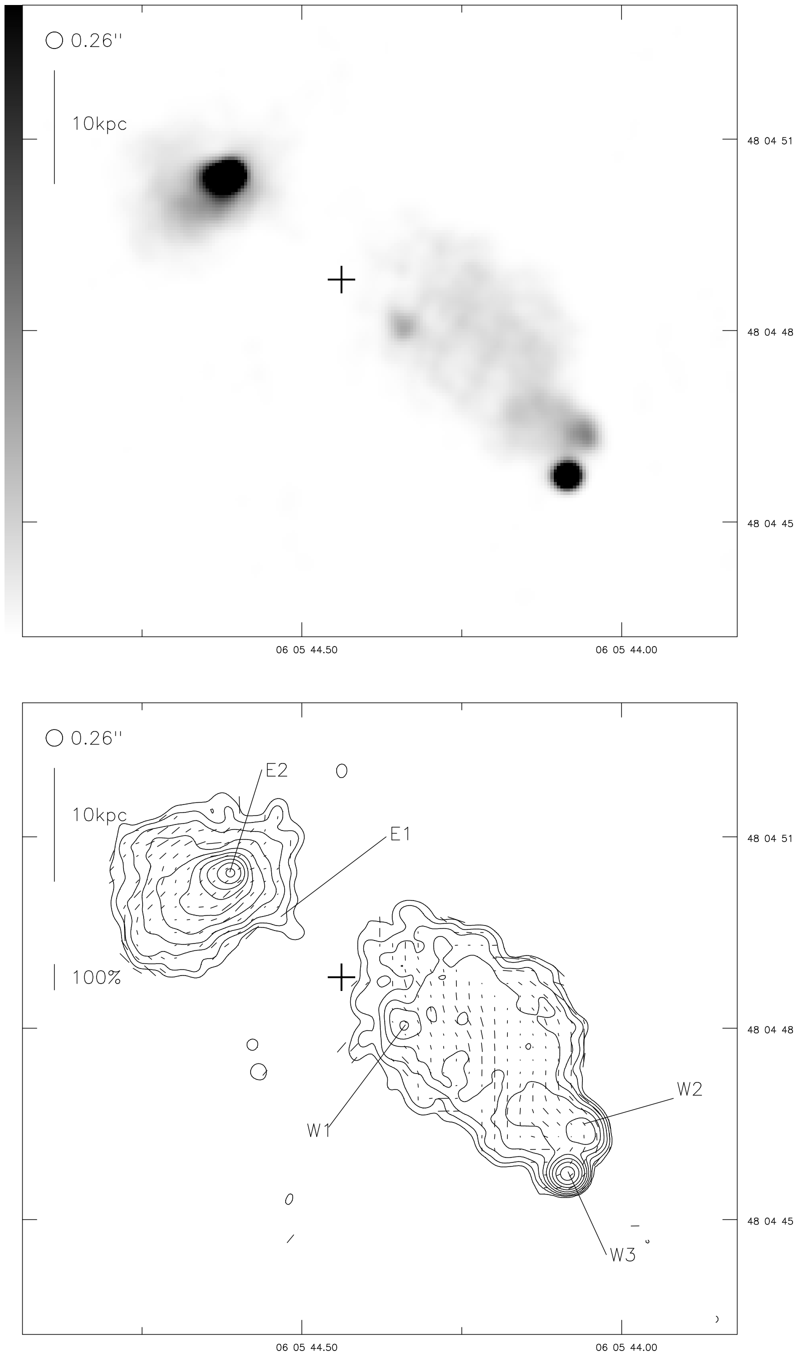

Figure 4.17: 3C 153 at 0.26 arcsec resolution. Above: linear greyscale; black is 20 mJy beam^{-1}. Below: contours at $0.2 \times (-2, -1, 1, 2, 4, \ldots)$ mJy beam^{-1}. The position of the optical identification is marked with a cross.

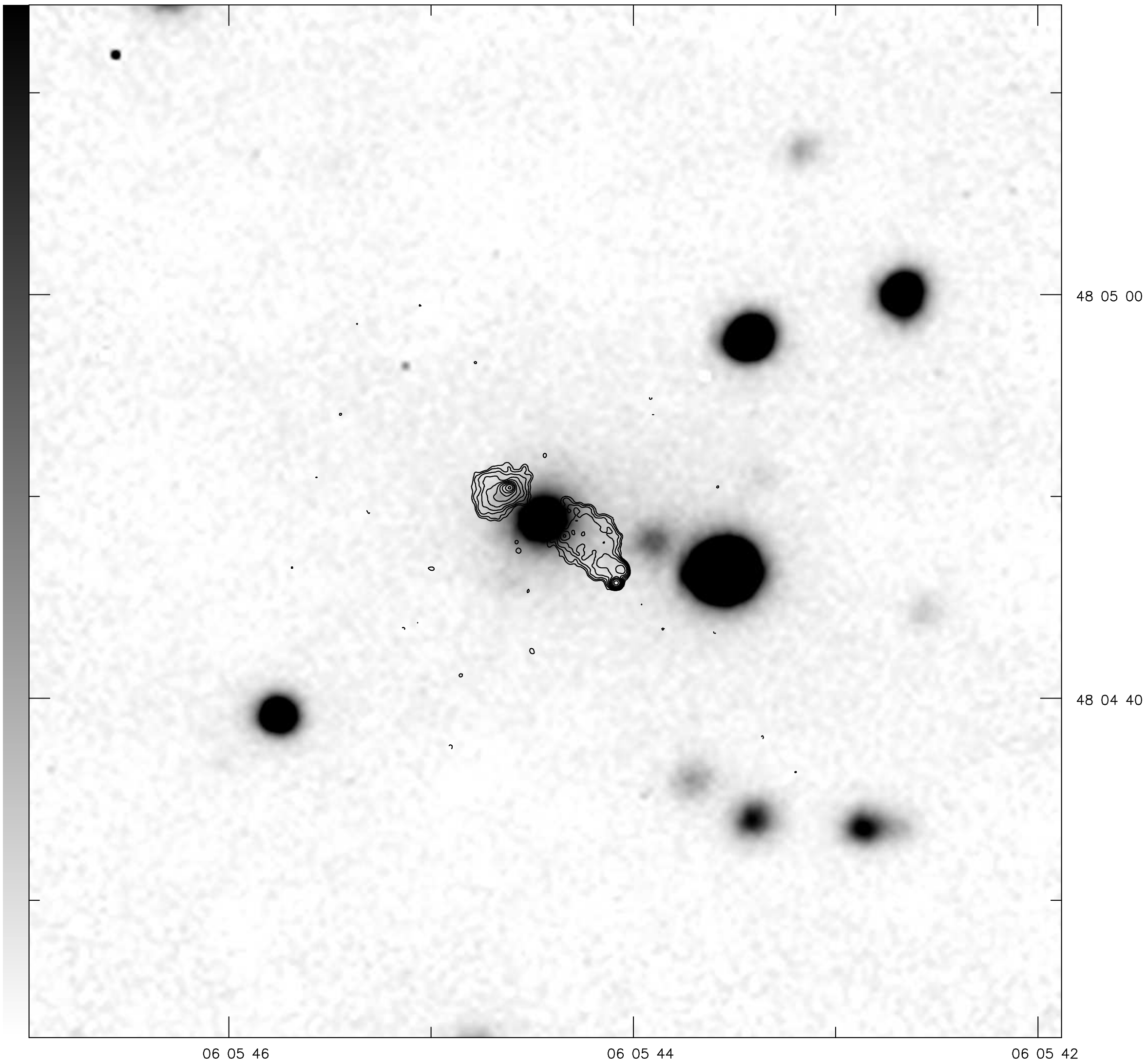

Figure 4.18: UKIRT image of the field of 3C 153. Greyscale in arbitrary units. Overlaid are contours of a 0.26-arcsec resolution radio map at $0.2 \times (-2, -1, 1, 2, 4, \ldots)$ mJy beam^{-1}. Immediately to the west of the galaxy is a foreground star.

transverse to the presumed beam direction in W3 and is in the same direction in the line linking W3 and W2, turning through 90° in W2; this follows the pattern seen in the larger sources. The knot W1 at the base of the southern lobe is not the core, as it is extended along the source axis and has a spectral index between 1.7 and 8.4 GHz of around 0.6 (the flux at 1.7 GHz being estimated from the map of Lonsdale and Morison); instead it is probably a tracer of the path of the beam. No core is detected; from estimates of the on-source noise and the confusing flux we can say that its flux must lie below about 0.5 mJy at 8.4 GHz.

The northern lobe is unusual in being broader than it is long and containing a hot spot, E2, which is located at the centre of the lobe rather than the leading edge. The hot spot is resolved and appears elongated approximately transverse to the source axis; this is confirmed by the higher-resolution map of Akujor *et al*.(1991). The magnetic field in the lobe is transverse to the axis almost everywhere. The linear extension of the lobe towards the southwest, E1 — lying on the straight line between E2 and W3 which also goes through W1 in the southern lobe and the optical identification position — is real (it appears on the map of Lonsdale and Morison and that of Neff *et al*. 1995) and may be another tracer of the beam. I have therefore classed 3C 153 as having two possible jets. The unusual structure of the northern lobe is almost certainly due to a complicated local environment; the source lies largely inside its parent galaxy. The UKIRT image (figure 4.18) shows little sign of the cluster environment suggested by Rawlings (1987), though there are a few resolved objects in the field, but does show a possible companion object around 25 kpc to the west of the host galaxy core.

4.5.10 3C 171

The literature

3C 171 has been studied in the radio at a number of wavelengths. Heckman, van Breugel and Miley (1984) show images at 15, 5 and 1.4 GHz; more recently, Blundell (1994) observed it at 1.4, 1.65, 4.9, 8.0, 8.4 and 15.0 GHz and studied its spectral and polarization properties extensively. The source appears to be a normal small FRII whose lobes have disrupted in an unusual way; in this respect it may be similar to 3C 123.

The host galaxy, an $R = 17.94$ magnitude object, is imaged by Hutchings *et al*. (1988) in the optical; it shows considerable elongation along the axis of the radio jets. This is even clearer in an HST snapshot (dK96) but may well be due to contamination of the optical passbands by line emission; my K-band image (figure 4.20) shows no such alignment. Heckman *et al*. (1984) have shown convincing evidence for an interaction between the radio-emitting plasma and the extended emission-line regions in the source. The emission-line regions are brightest just beyond the hot spots.

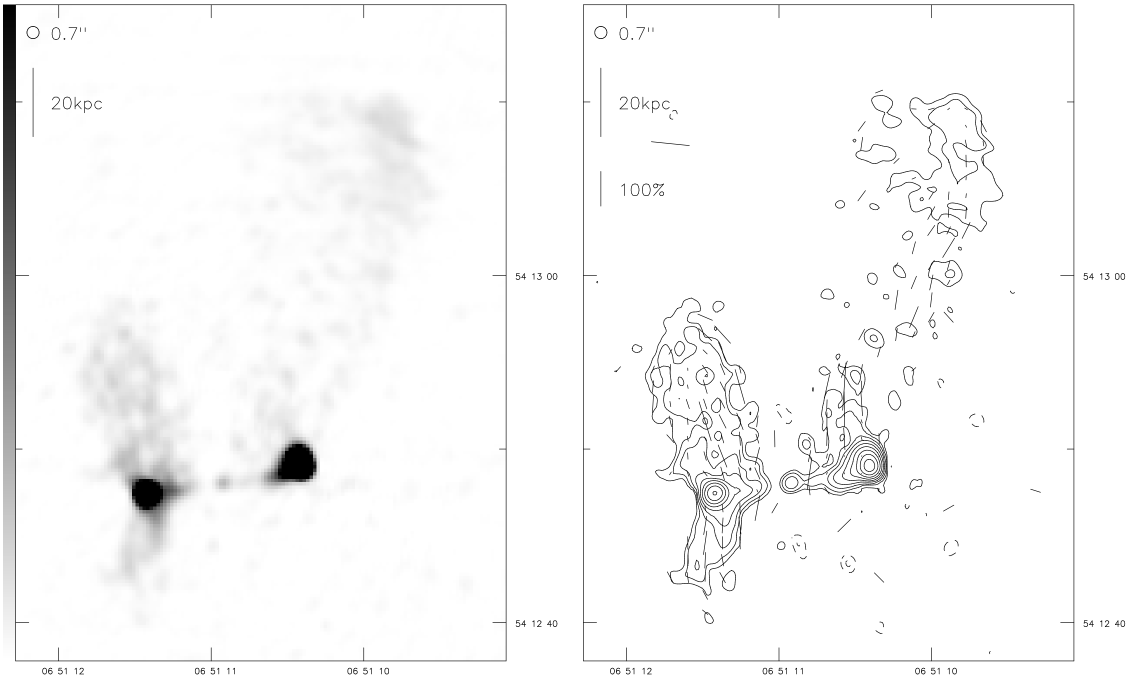

Figure 4.19: 3C 171 at 0.70 arcsec resolution. Left: linear greyscale; black is 10 mJy beam^{-1}. Right: contours at $0.4 \times (-2, -1, 1, 2, 4, \ldots)$ mJy beam^{-1}.

Laing *et al.* (1994) present a high-quality spectrum of the source which shows strong narrow [OIII] and Hα emission lines; 3C 171 is therefore a narrow-line radio galaxy in spite of its classification by Smith, Spinrad and Smith (1976) as an N-galaxy. This is independently confirmed by Eracleous and Halpern (1994). Wyndham (1966) lists the object as an ordinary red galaxy, but its colour in Sandage (1973a) is sufficient to put it in the section of parameter space normally occupied by N-galaxies. If 3C 171 really is an N-galaxy, it (like 3C 79, above) does not follow the strong trend noted by Grandi and Osterbrock (1978) for N-galaxies to be broad-line objects. It is likely, however, that the situation has been confused by the unusual continuum structure seen in the HST image of dK96. The nucleus in that image is resolved, suggesting that the object is not an N-galaxy after all.

My maps

Poor *uv* plane coverage at A-configuration means that I have had to use an elliptical restoring beam (0.35×0.25 arcsec in position angle 75°) at the highest resolution.

A low-resolution map (figure 4.19) shows the main unusual features of the source; bright hot spots,

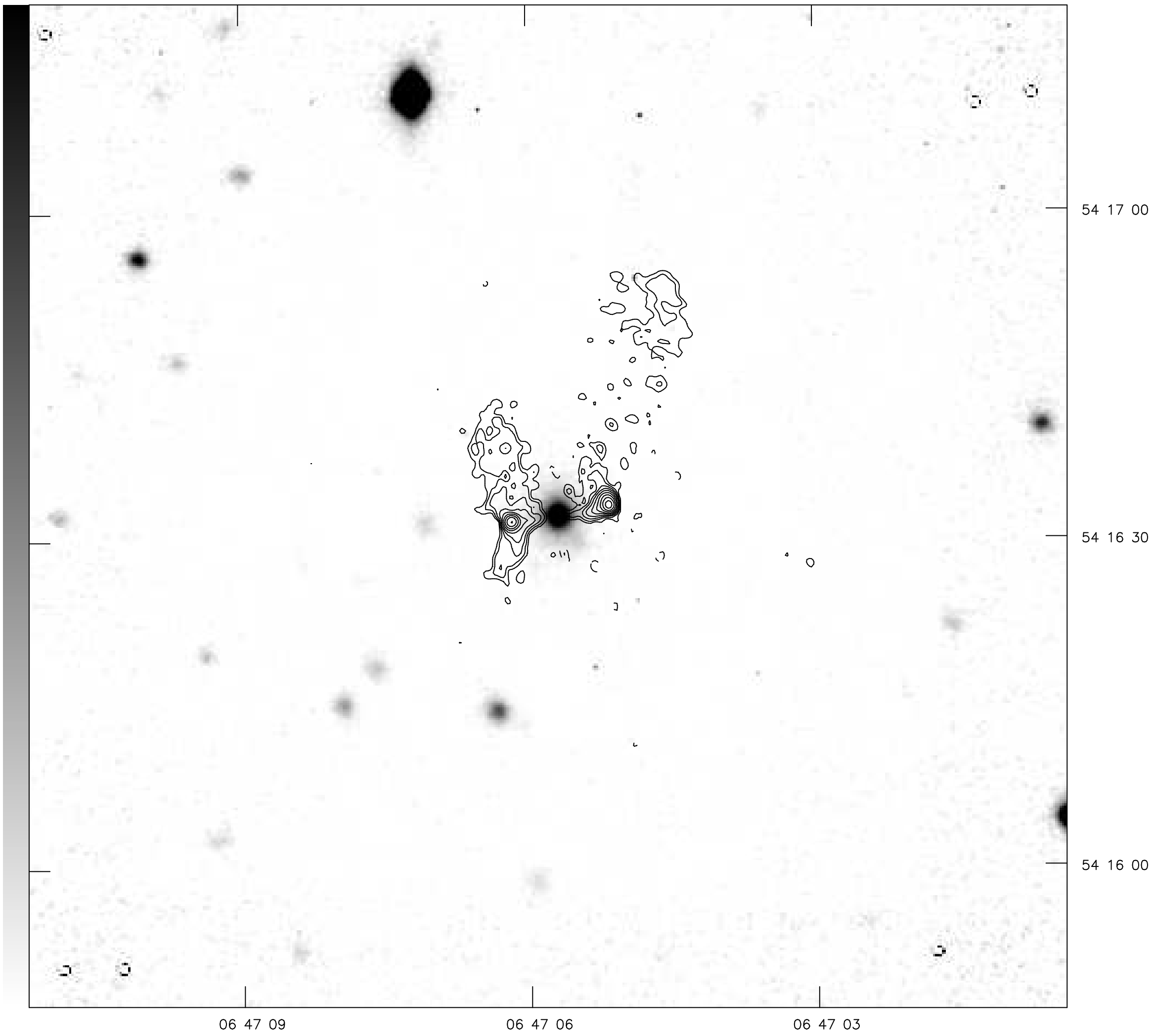

Figure 4.20: UKIRT image of the field of 3C 171. Greyscale in arbitrary units. Overlaid are contours of a 0.70-arcsec resolution radio map at $0.4 \times (-2, -1, 1, 2, 4, \ldots)$ mJy beam^{-1}.

twin jets and extended plumes transverse to the source axis. The sampling on the shortest baselines is poorer than is usual for this study and so the details of structures in the plumes should not necessarily be believed. The UKIRT image (figure 4.20) shows no alignment of the host galaxy with the radio, but does show a possible companion object to the east and a group of resolved objects of similar brightness further south and east. At high resolution (figure 4.21), the jets in both lobes (E1, W1) can clearly be seen. The hot spots are both slightly resolved and extensions from the hot spot areas into the lobes can be seen on both sides. The western hot spot, W2, is only weakly polarized, but the eastern hot spot, E2, is completely unpolarized — in fact, a whole strip of the eastern jet and lobe, passing through the hot spot, has almost no polarized emission. This is related to the line-emitting material associated with the jet, as can be seen in figure 4.22, which shows an overlay of the radio map on the HST snapshot of dK96. Not only does the optical material appear to be associated with the jets, but the polarization is clearly intimately related to the optical material — the 0.5 kpc-wide strip in the eastern lobe with no polarization is precisely cospatial with the optically emitting material, while the western hot spot is clear of optical emission and has some polarized flux.

Laing (1981b) suggests that the object is related to the class of wide-angled tail sources, and the resemblance is certainly striking up to a point; both have twin inner jets (see chapter 3) and bright hot spots. However, 3C 171's lobes are very different from the well-collimated plumes of a typical WAT, and the eastern lobe extends both north and south. There is no evidence that the host of 3C 171 is a dominant cluster galaxy, and no detection in the X-ray. It seems likely that the jets of 3C 171 disrupt not because they undergo reconfinement somewhere in the galactic environment but because they are interacting with the cold dense material traced by the optical line emission. If so, it is not surprising that the outflow from the hot spots is directed unusually.

4.5.11 3C 173.1

The literature

3C 173.1 was mapped by LP at 1.4 GHz with the VLA; previous maps use the 5-km telescope at 5 GHz and are of lower resolution (JPR; Rawlings 1987). A 5-GHz VLA snapshot by Giovannini *et al*. (1988) has the highest resolution (0.35 arcsec) but resolves out most of the source, showing only the hot spots with their multiple structure. LP suggest that the knot near the core in their image may be part of a jet.

The host galaxy of 3C 173.1 lies in, but is not the dominant member of, a poor cluster (Eales 1985b; dK96. It is a low-excitation object (Rawlings 1987; Laing, private communication). The nuclear continuum emission is aligned N-S approximately along the axis of the jet (dK96).

My maps

Poor *uv* plane coverage at A-configuration means that I have had to use an elliptical restoring beam (0.30×0.20 in position angle 75°) at the highest resolution.

3C 173.1 is one of the more ordinary sources in the sample. A low-resolution map (figure 4.23) shows the possible jet in the north lobe (N1); this can clearly be distinguished from lobe material at intermediate resolution (not shown). The jet is obscured by a region of high surface brightness (N2) on the western

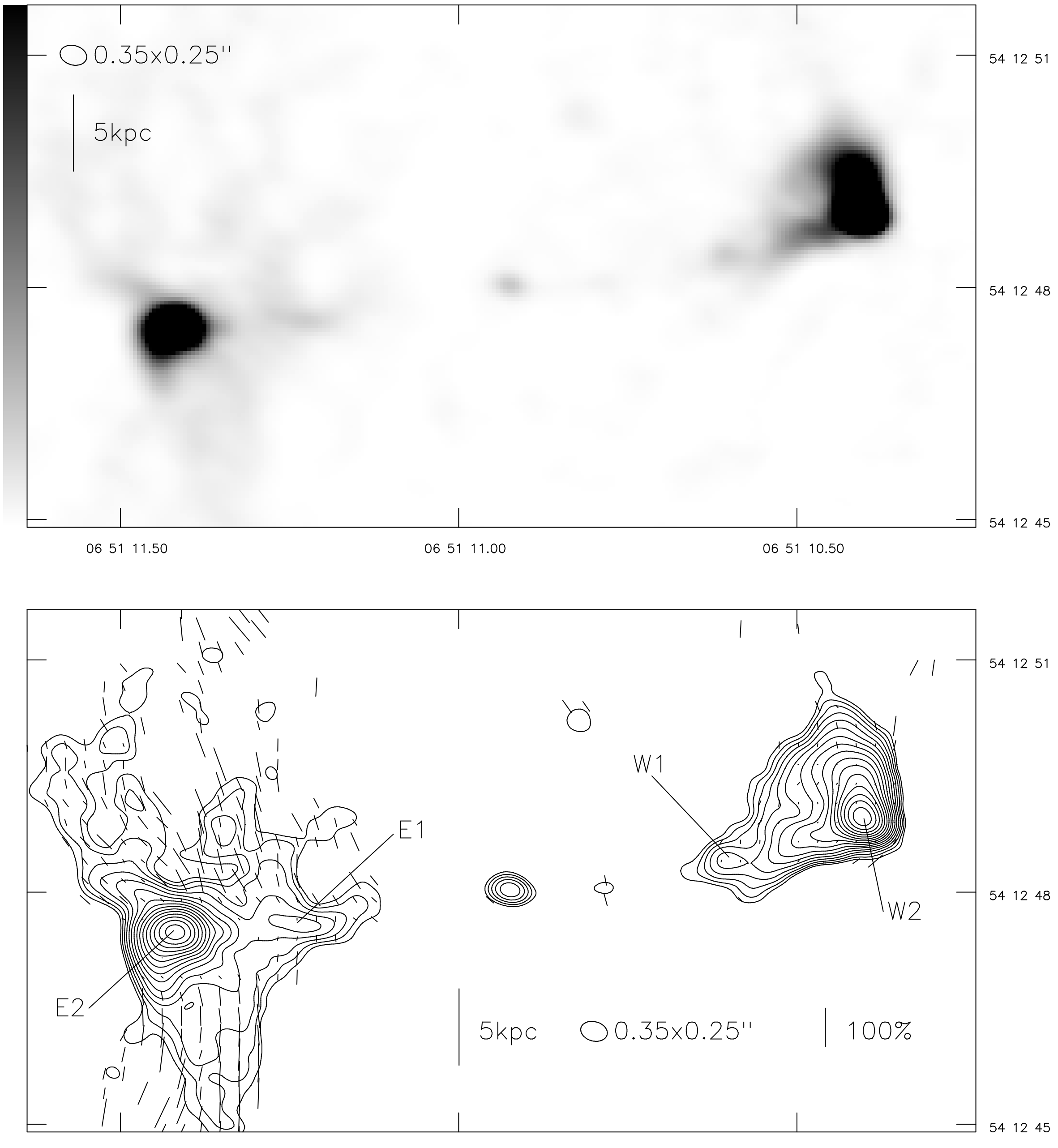

Figure 4.21: 3C 171 at 0.35×0.25 arcsec resolution. Above: linear greyscale; black is 10 mJy beam^{-1}. Below: contours at $0.4 \times (-\sqrt{2}, -1, 1, \sqrt{2}, 2, 2\sqrt{2}, \ldots)$ mJy beam^{-1}.

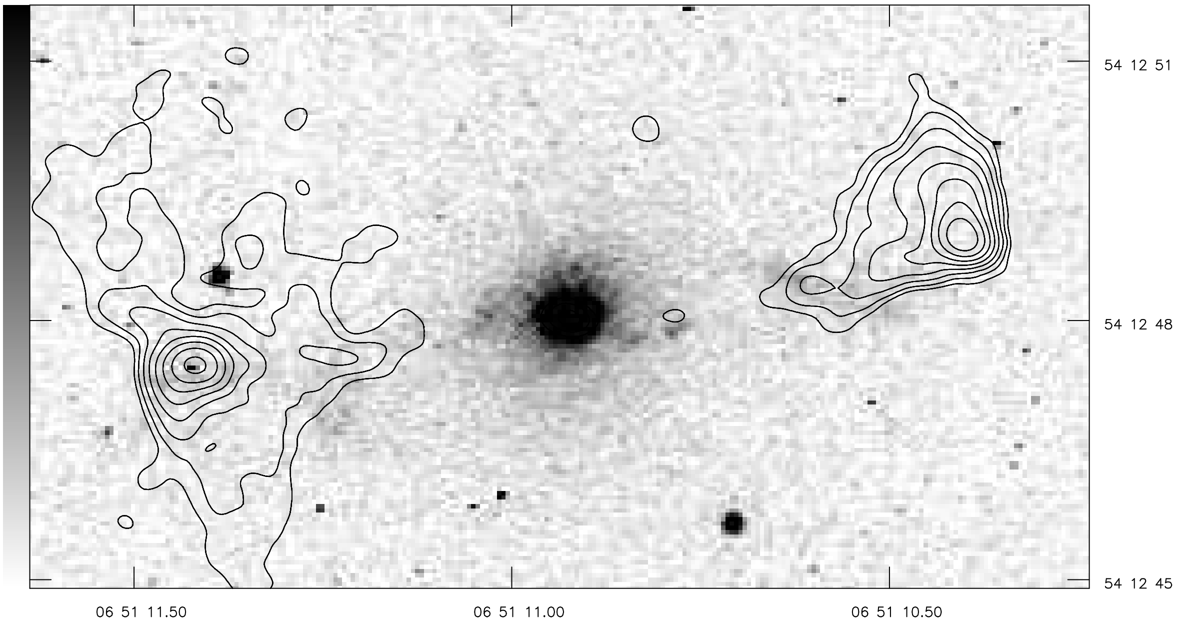

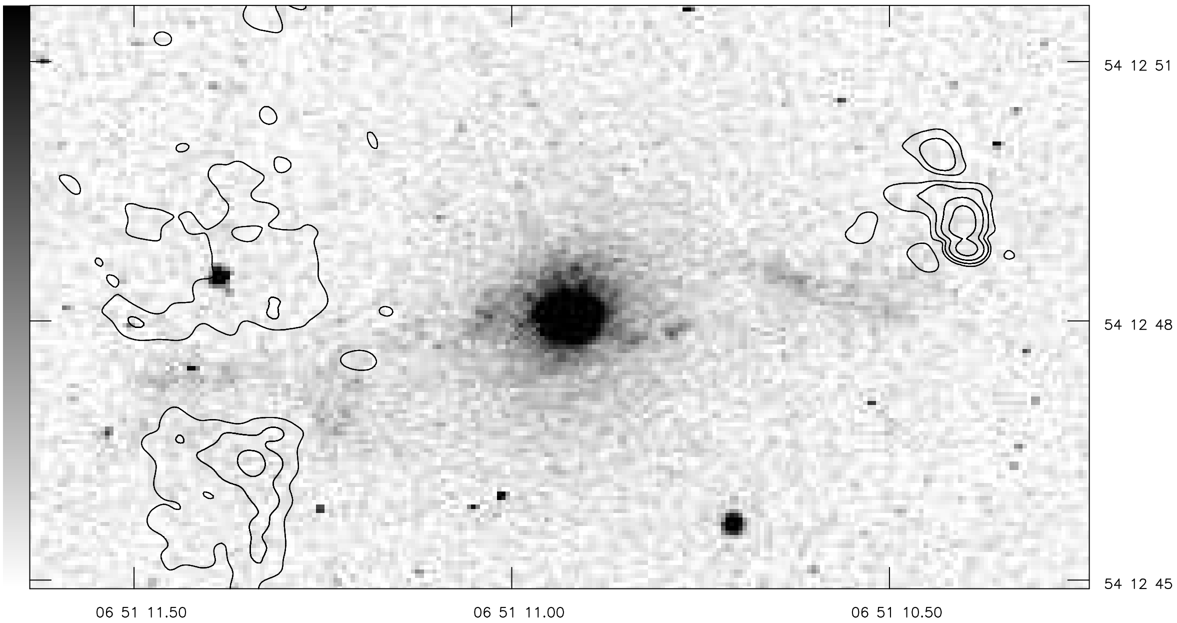

Figure 4.22: 3C 171 at 0.35×0.25 arcsec resolution overlaid on an HST snapshot. Greyscale in arbitrary units. Above: contours of total intensity at $0.4 \times (-2, -1, 1, 2, 4, \ldots)$ mJy beam^{-1}. Below: contours of polarized intensity at $0.2 \times (-2, -1, 1, 2, 4, \ldots)$ mJy beam^{-1}.

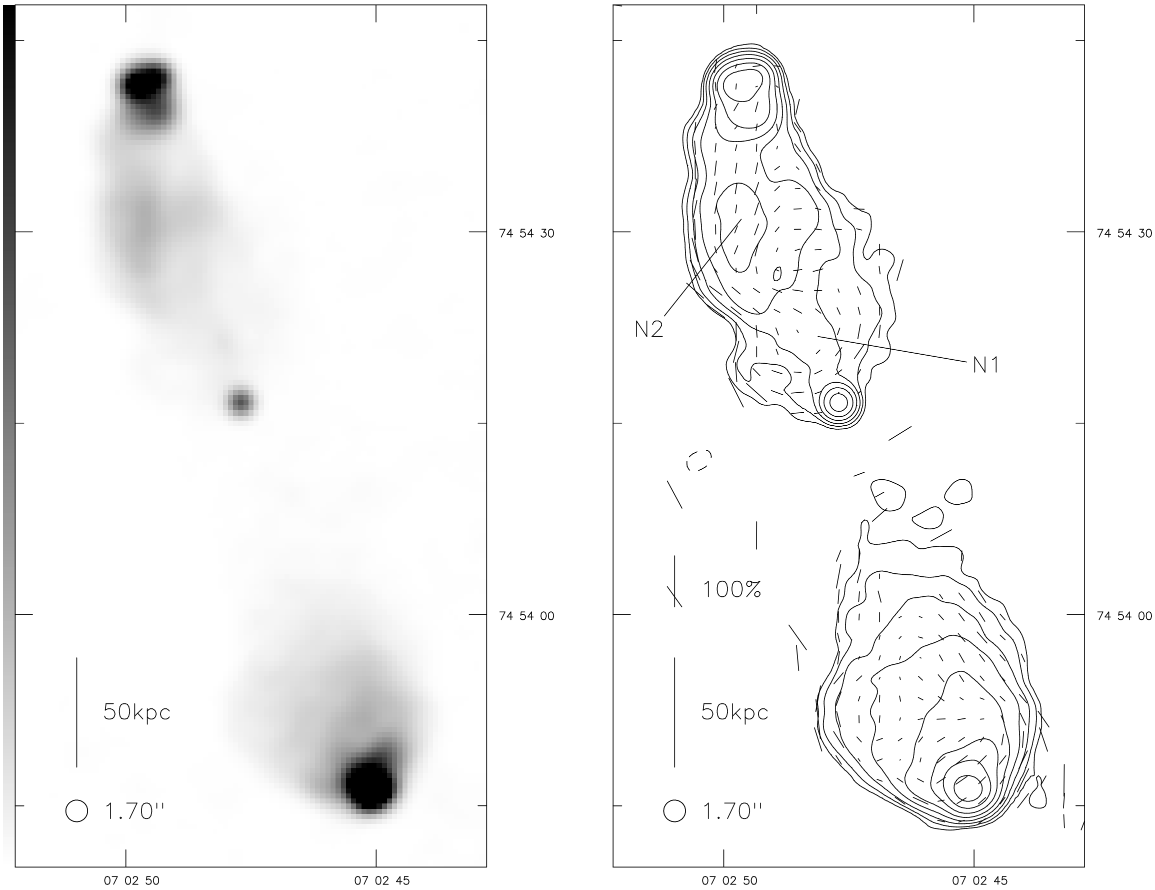

Figure 4.23: 3C 173.1 at 1.70 arcsec resolution. Left: linear greyscale; black is 15 mJy beam^{-1}. Right: contours at $0.2 \times (-2,-1,1,2,4,\ldots)$ mJy beam^{-1}.

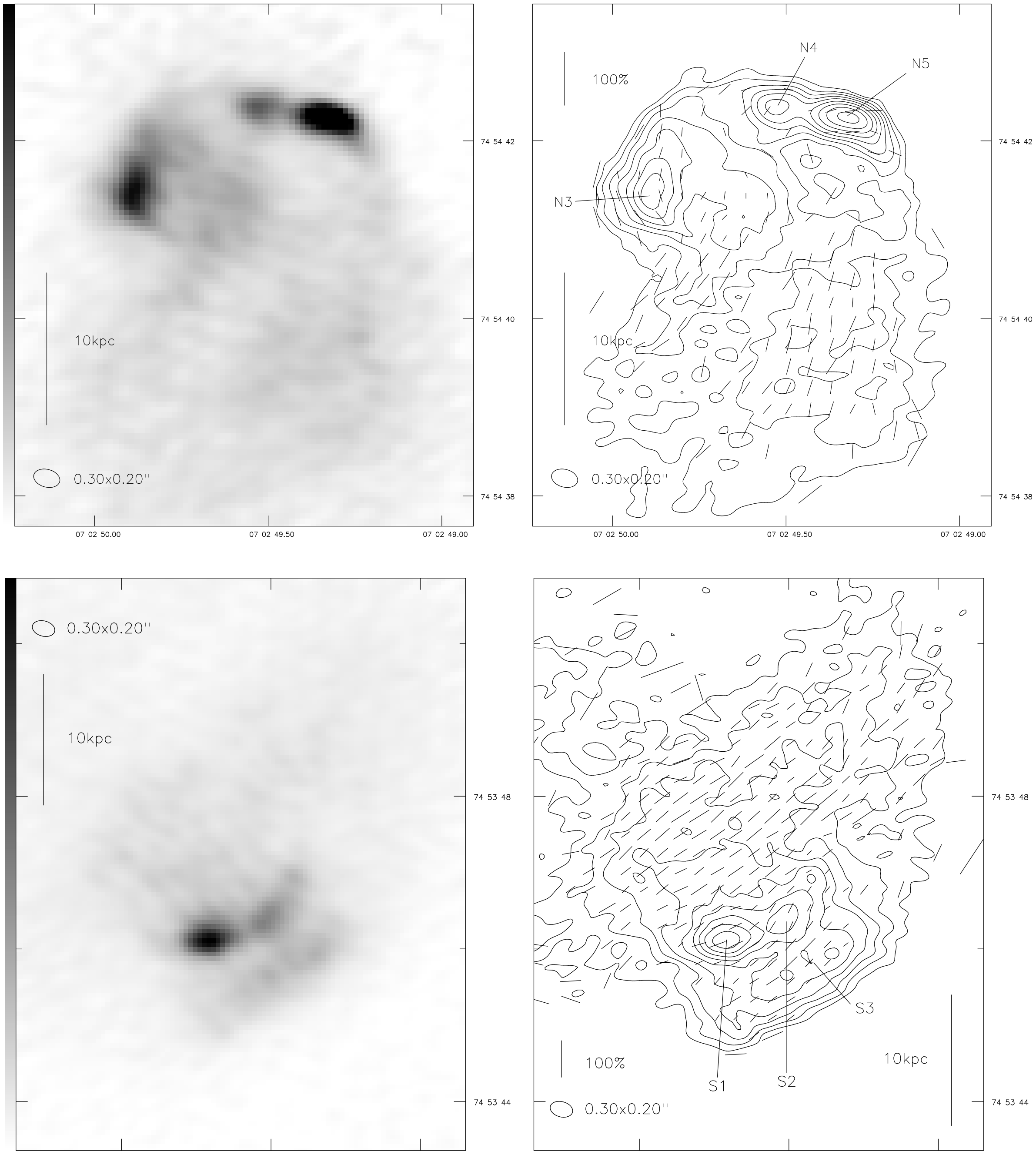

Figure 4.24: 3C 173.1 at 0.3×0.2 arcsec resolution. Above: N hot spot — left: linear greyscale; black is 2 mJy beam^{-1}; right: contours at $0.2 \times (-\sqrt{2}, -1, 1, \sqrt{2}, 2, 2\sqrt{2}, \ldots)$ mJy beam^{-1}. Below: S hot spot — left: linear greyscale; black is 4 mJy beam^{-1}; right, as above right.

side of the north lobe; this is linked to the hot spot region by a bridge of emission.

At high resolution (figure 4.24) the northern hot spot is seen to consist of three components. The westerly component, N5, is the most compact — it is just resolved at this resolution — and has magnetic field roughly transverse to its direction of extension. A faint and marginally less compact second component N4, just separate from N5, is to the east, and the most diffuse component, N3, is on the eastern edge of the source, with magnetic field alignment approximately north-south. The bridge described above leads from this hot spot into the lobe. The images are consistent with N3 being fed from N5/N4. It is interesting, however, that the jet when last seen is pointing towards N3 rather than N5.

The southern hot spot again has multiple sub-structure, though none of the components is distinct by the definition of L96. The brightest point is a resolved but reasonably compact hot spot S1, elongated transverse to the source axis, and to its west is a curving ridge of emission S2. To the southwest of these and joined to them there is a diffuse bar of emission (S3) whose relation to the other components is unclear. The hot spots, and indeed this whole region of emission, have their magnetic field direction transverse to the source axis.

A map of spectral index between 1.4 and 8.4 GHz (figure 4.25) does not have enough resolution to distinguish the spectra of the various hot spot components. It does show, however, that the region of high surface brightness (N2) in the northern lobe has a flatter spectrum ($\alpha \approx 0.9$) than the material immediately to its west ($\alpha \approx 1.2$). This may be further evidence for collimated backflow in this source. The steepest-spectrum material is that at the edges of the lobes where they are closest to the nucleus, as expected from simple models of spectral ageing.

The source is moderately depolarized between 1.4 and 8.4 GHz, with the jetted lobe being *more* depolarized ($\mathrm{DP} = 0.40$) than the opposing one ($\mathrm{DP} = 0.62$); this is contrary to the sense of the Laing-Garrington effect.

4.5.12 3C 219

3C 219 is a well-studied large object with an unusual 'partial jet' which disappears abruptly long before the hot spot. VLA images are to be found in Clarke *et al*. (1992). The host galaxy is a 17.5 magnitude cD object, the brightest member of a compact Zwicky cluster, and was detected by EINSTEIN (Fabbiano *et al*.1984). Until recently the source was thought to be a narrow-line object, but Laing *et al*. (1994) detect broad Hα and so I have classified it as a BLRG. It has a compact bright optical nucleus (dK96).

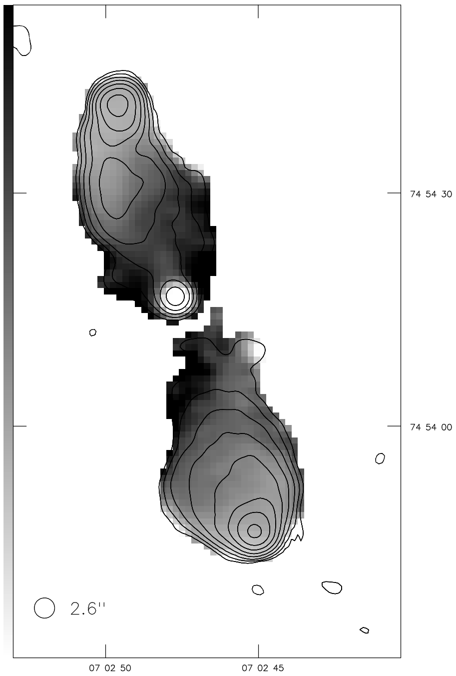

Figure 4.25: Spectral index between 1.4 and 8.4 GHz of 3C 173.1 at 2.60 arcsec resolution. Linear greyscale between 0.5 and 1.5; superposed are contours of total intensity at 8.4 GHz at $0.4 \times (-2,-1,1,2,4,\ldots)$ mJy beam^{-1}.

4.5.13 3C 234

The literature

3C 234 has been mapped at a number of frequencies in the radio; the first map to show the main features of the source was that of RP at 5 GHz with the 5-km telescope. Burch (1979b) and subsequently Alexander (1985, 1987) have investigated the spectral index variation across the source at low resolution. Alexander found that the spectral steepening away from the hot spots was largely consistent with simple spectral ageing models, but suggested that turbulent acceleration was necessary in the western lobe to account for an apparent decrease in electron age close to the nucleus. Zukowski (1990) investigated the polarization of the source but found no significant variation of depolarization across it. His 1.4-GHz image (1.7 arcsec resolution; VLA A, B and C configuration data) is remarkable for showing the jet-like feature at the end of the eastern lobe in polarized but not in total intensity. The highest resolution map of the whole source before this study was that of Burns *et al.* (1984) with the VLA at 5 GHz (1.2 arcsec resolution), in their search for jets; they failed to find one in 3C 234, but noted the multiple hot spot structure in the eastern lobe. Dreher (1981) mapped the primary hot spots only at high resolution with the partially completed VLA (15 GHz, maximum resolution 0.38×0.21 arcsec); his maps show similar structure to those presented here, as do the 5 GHz snapshots of Neff *et al*. (1995).

3C 234's host is an N-galaxy with $R = 16.52$ which appears to be located on the edge of a small group of fainter galaxies of similar size (Eales 1985a,b). It was detected in the X-ray by the EINSTEIN satellite (Feigelson and Berg 1983). The host galaxy was imaged by Hutchings *et al*. (1988) who note four small, red close companion objects. An HST continuum image of the nuclear regions (de Koff *et al*. 1996) shows extension to the east and west – in particular, a curved region of emission extending two arcseconds to the west. This may be due to emission-line contamination.

Antonucci's (1982) discovery that 3C 234 has broad lines which are strongly polarized perpendicular to the radio axis (together with a strongly polarized featureless continuum in the optical) has made it the canonical example of a 'hidden quasar' in unified schemes (e.g. Antonucci 1993). Because of this belief, it has been classified throughout this work as a NLRG in spite of the fact that its broad lines show up strongly in total-intensity spectra.

My maps

3C 234 is the most striking example of the 'bottle-neck' lobe structure found in this sample (compare 3C 79). Its lobes are broad at their base but are connected to the hot spots by well-collimated necks of emission (150 kpc long and only 35 kpc across in the eastern lobe). The magnetic field in the necks is parallel to the source axis; in the bases of the lobes it is largely transverse. The eastern lobe shows a secondary hot spot, E2, very like that seen in the eastern lobe of 3C 79; there is also some evidence for a jet, in the form of a faint linear feature (E1) passing through the broad faint lobe before disappearing into the neck. The neck in the western lobe is unusual in appearing to be bent through 20° or so from the axis of the rest of the source.

At the full resolution available, the eastern hot spot shows complicated structure. The most compact component, E5, is clearly resolved, and is extended in position angle 107°. The extension to the north seen on this map is an artefact. Perpendicular to the direction of extension (slightly west of south) a bright knotty ridge E4 leaves the hot spot and extends back into the lobe, curving as it does so. This ridge is real, and is readily distinguishable in intermediate-resolution maps both in polarized intensity (as mentioned above) and in total intensity (figure 4.28); it seems most likely that it is a tracer of the beam (particularly as the ridge E1 points at that edge of the lobe) and I have classed it as a jet. If it is a jet, the beam has to bend through some 35° in the 8 kpc or so immediately before the hot spot. E5 has magnetic field transverse to its direction of extension; E4 has a longitudinal field. A 'tail' of emission, E3, which is not separate from E5, leaves E5 parallel to its direction of extension and then seems to bend

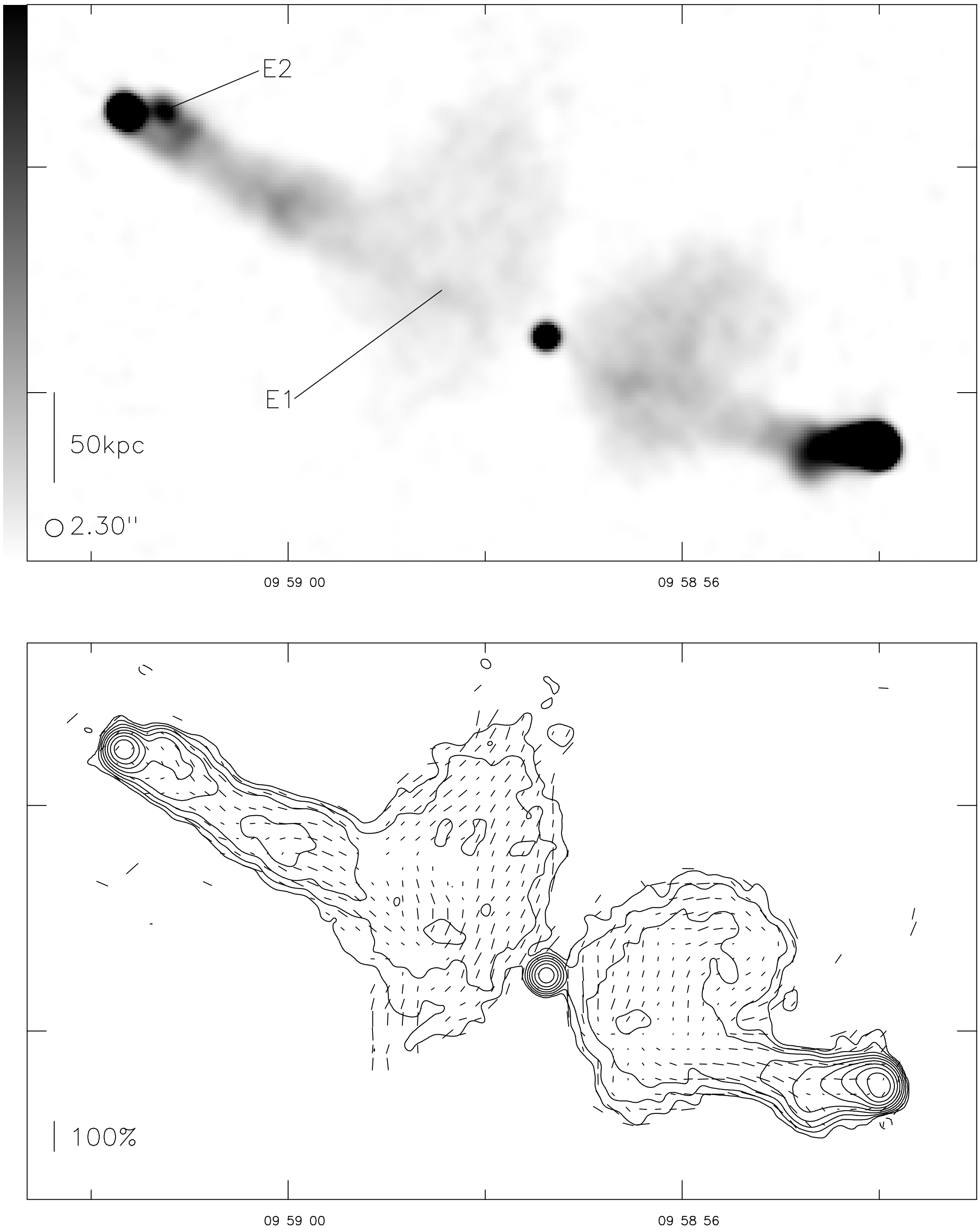

Figure 4.26: 3C 234 at 2.30 arcsec resolution. Above: linear greyscale; black is 8 mJy beam^{-1}. Below: contours at $0.3 \times (-2, -1, 1, 2, 4, \ldots)$ mJy beam^{-1}.

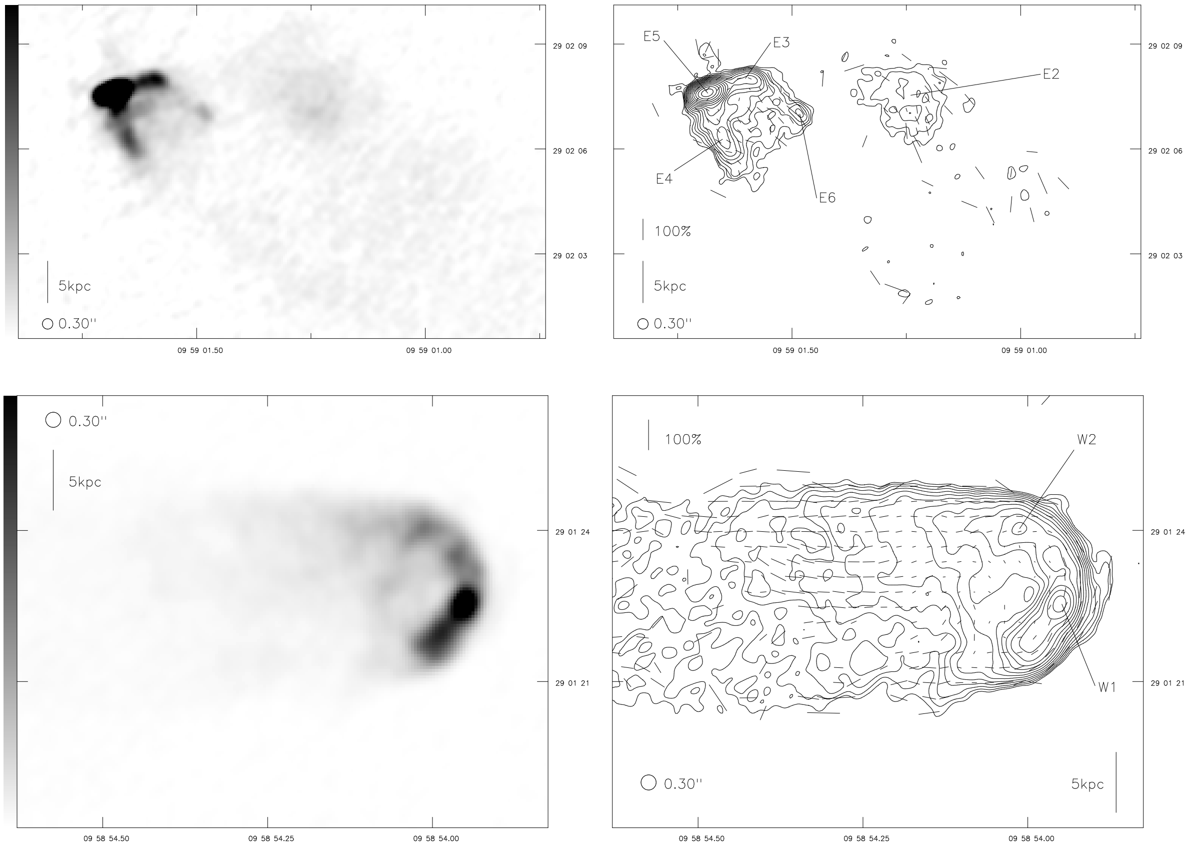

Figure 4.27: 3C 234 at 0.30 arcsec resolution. Above: E hot spot — left: linear greyscale; black is 2 mJy beam^{-1}; right: contours at $0.15 \times (-\sqrt{2}, -1, 1, \sqrt{2}, 2, 2\sqrt{2}, \ldots)$ mJy beam^{-1}. Below: W hot spot — left: linear greyscale; black is 10 mJy beam^{-1}; right, as above right.

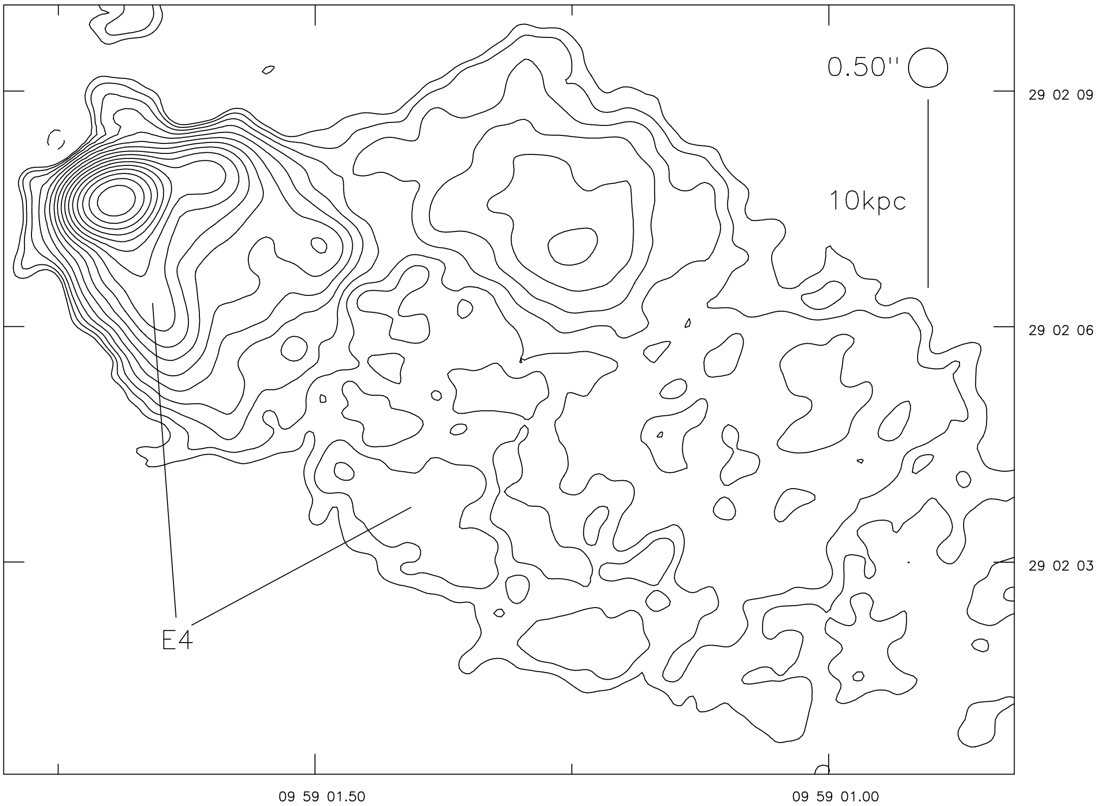

Figure 4.28: E hot spot of 3C 234 at 0.50 arcsec resolution. Contours at 0.15 × $(-\sqrt{2}, -1, 1, \sqrt{2}, 2, 2\sqrt{2}, \ldots)$ mJy beam^{-1}.

south towards a faint component E6. It is not obvious whether E2 is still connected to the fluid flow; where polarization is detected in this component the magnetic field is roughly parallel to the source axis.

The situation is simpler in the western hot spot. There is a single compact component, W1, extended roughly north-south and with magnetic field parallel to the direction of its extension. Ridges leave the hot spot on either side and bend back into the lobe, suggesting symmetrical outflow; one component of the northern ridge (W2) is a separate hot spot according to the definition of L96. There is no sign of an incoming jet.

4.5.14 3C 284

The literature

3C 284 is one of the larger and more ordinary sources in the sample, and has not been extensively studied. RP have a low-sensitivity map with the 5-km telescope which points up the side-to-side asymmetry of the source. Leahy and Williams (1984) have a 5-arcsec resolution map at 1.4 GHz; Gregorini *et al*. (1988) show one at the same frequency at 4.9×4-arcsec resolution. The host galaxy is an $R = 17.41$ magnitude object (Eales 1985a); Eales (1985b) shows a CCD image of the field, which Rawlings (1987) suggests may contain some associated galaxies and McCarthy *et al*. (1995) class as a moderately rich cluster. The nucleus of the host galaxy is roughly aligned with the radio axis (dK96).

My maps

A low-resolution map (figure 4.29) shows few remarkable features.

High resolution maps (figure 4.30) reveal a double hot spot in the eastern lobe; this follows the pattern seen in other sources, in that the magnetic field direction of the most compact hot spot, E2, is transverse to the source axis while the field direction of the more diffuse one, E1, is more or less along the source axis. The hot spots appear to be joined by a bridge of emission. The western hot spot, W1, is extended in position angle $-30°$;its magnetic field is roughly transverse to its direction of extension.

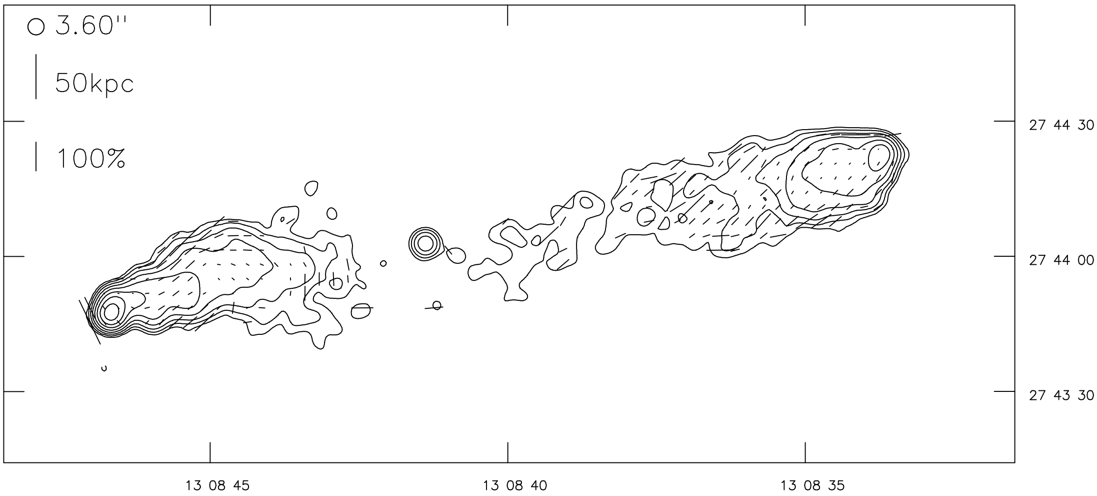

Figure 4.29: 3C 284 at 3.60 arcsec resolution. Contours at $0.2 \times (-2, -1, 1, 2, 4, \ldots)$ mJy beam^{-1}.

4.5.15 3C 300

The literature

3C 300 was one of the sample of RP and was also mapped by Leahy and Williams (1984). Burch (1979b) investigated its spectrum and polarization. Its spectrum was studied in more detail by Alexander and Leahy (1987). Blundell (1994) has a map of the spectral index between 1.4 and 8 GHz, and overlays the radio contours on optical continuum and [OIII] images from McCarthy (1988); the latter shows extended emission. She notes the jet in the N lobe. The source lies in a poor cluster (McCarthy 1988). In the image of dK96 the nucleus appears extended to the NW.

My maps

The polarization information in the B and D configurations at 8.0 GHz was not well calibrated owing to problems with the observing run, and so low-resolution polarization maps are not shown. A polarization map made at a different frequency can be found in Blundell (1994).

A low-resolution map in total intensity (figure 4.31) shows the asymmetrical nature of the source and the jet (W1-4) in the western lobe. This can be traced all the way from the core to the end of the lobe, as the high-resolution image around the core (figure 4.33) shows. There is insufficient signal-to-noise at the full resolution to see reliable details of the dim northwestern end of the source, and an image is

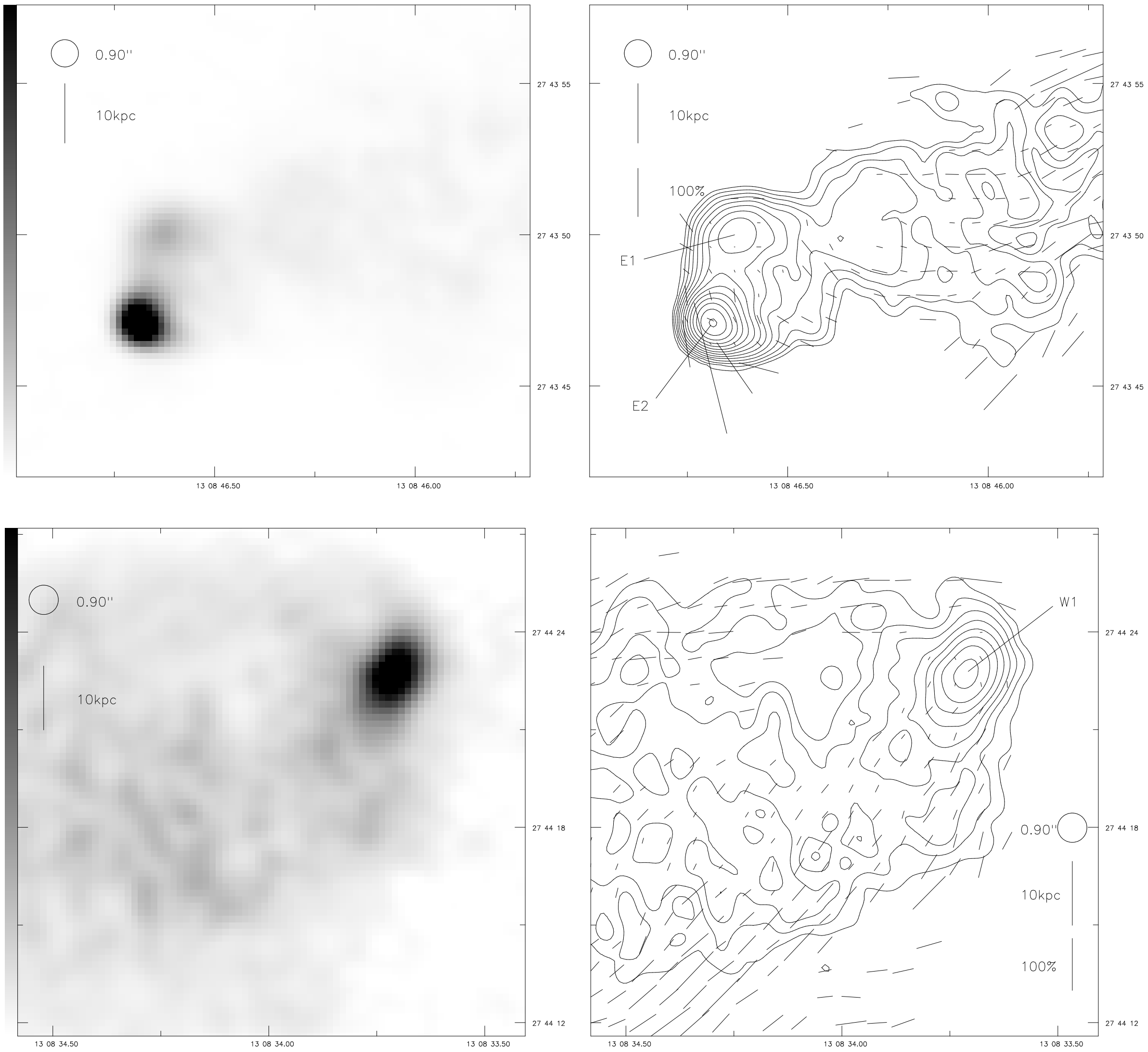

Figure 4.30: 3C 284 at 0.90 arcsec resolution. Above: E hot spot — left: linear greyscale; black is 10 mJy beam^{-1}; right: contours at $0.2 \times (-\sqrt{2}, -1, 1, \sqrt{2}, 2, 2\sqrt{2}, \ldots)$ mJy beam^{-1}. Below: W hot spot — left: linear greyscale; black is 2 mJy beam^{-1}; right, as above right.

therefore not shown; but Gaussian fitting to maps at intermediate resolution suggest that there is some sub-kiloparsec structure at the source's tip. The bright eastern hot spot (figure 4.32) shows clear double structure at the highest resolutions, with one component (E3, at the western edge of the hot spot region) being extended towards the other, much brighter component (E2), which in turn is extended back towards the core. The two components are similar in size and lie in an area of high surface brightness. They are joined by a ridge of emission — they are only marginally separate components by the defini-

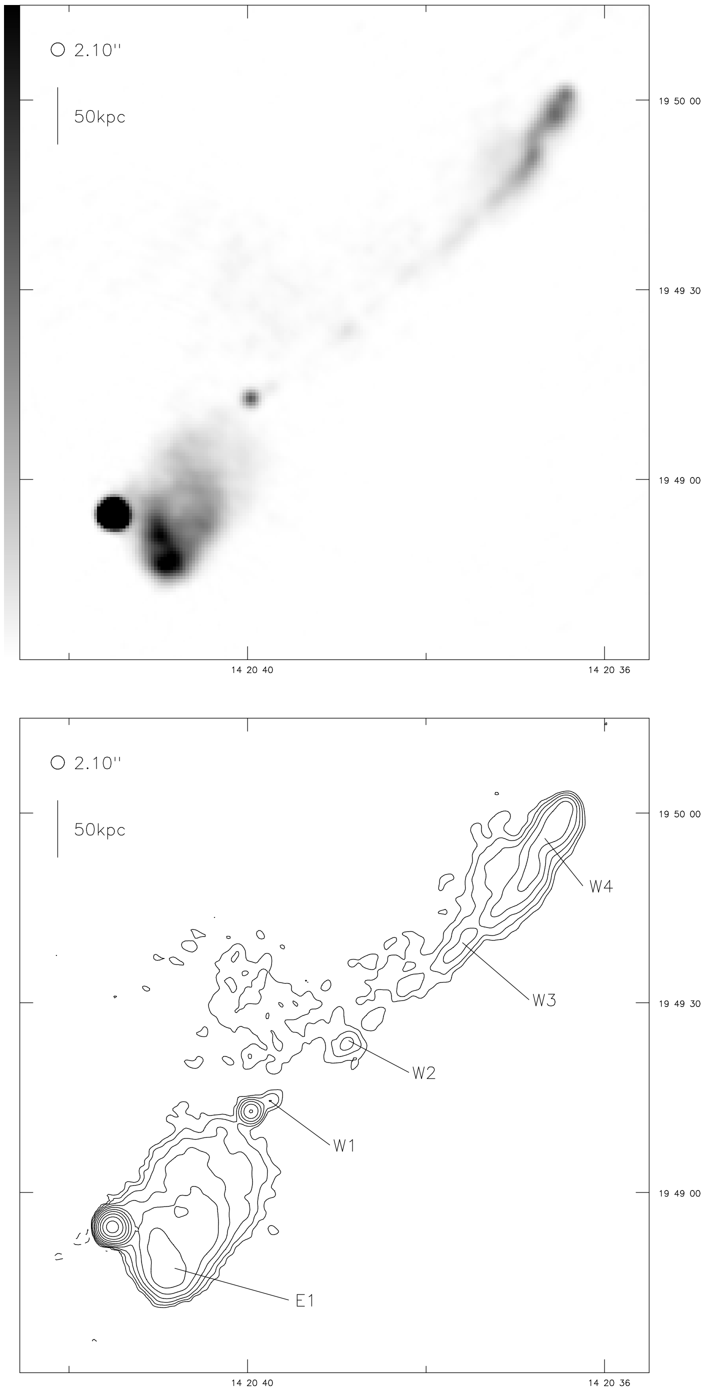

Figure 4.31: 3C 300 at 2.10 arcsec resolution. Above: linear greyscale; black is 10 mJy beam^{-1}. Below: contours at $0.2 \times (-2, -1, 1, 2, 4, \ldots)$ mJy beam^{-1}.

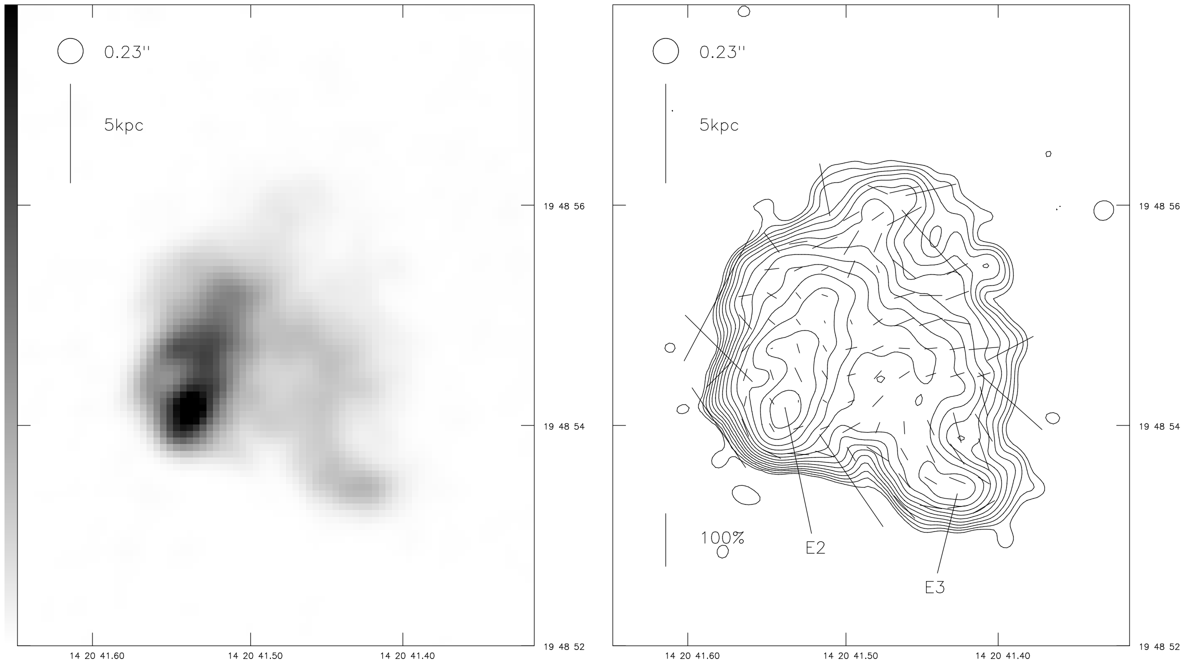

Figure 4.32: East hot spot of 3C 300 at 0.23 arcsec resolution. Left: linear greyscale; black is 10 mJy beam^{-1}; right: contours at $0.1 \times (-\sqrt{2}, -1, 1, \sqrt{2}, 2, 2\sqrt{2}, \ldots)$ mJy beam^{-1}.

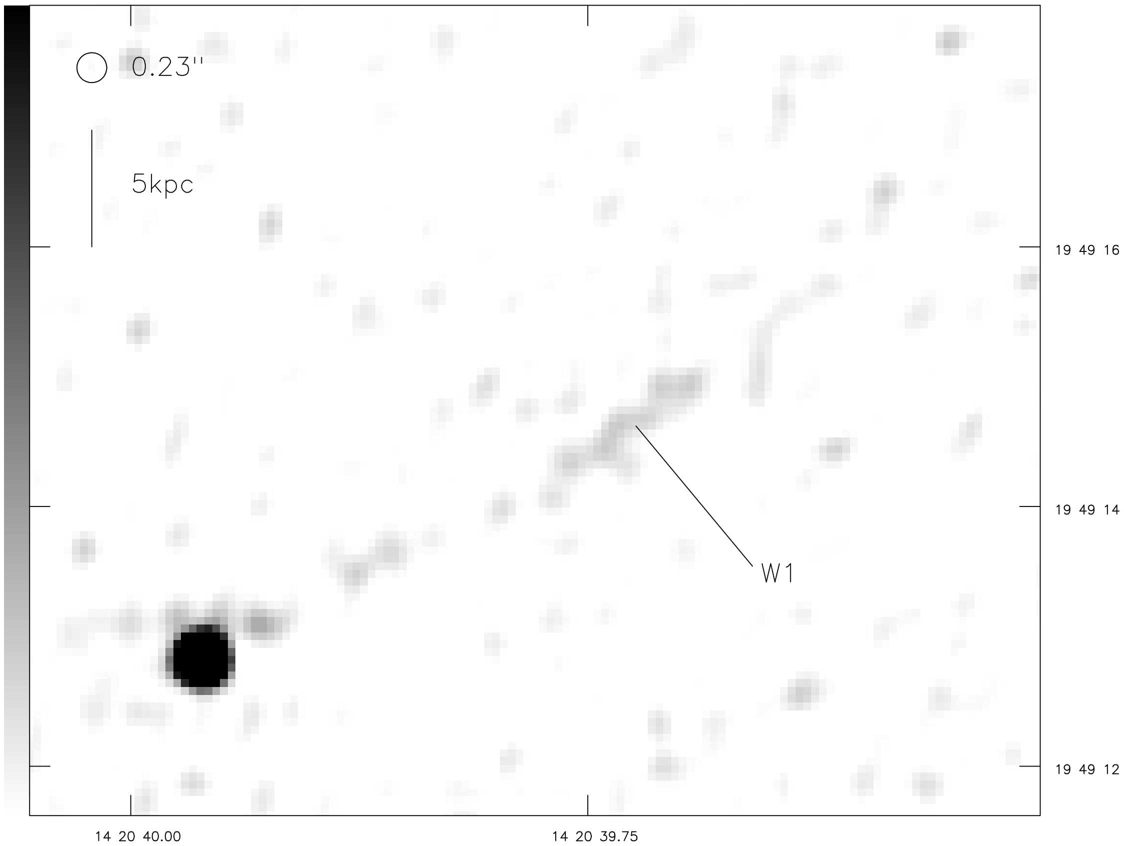

Figure 4.33: Core and jet of 3C 300 at 0.23 arcsec resolution. Linear greyscale; black is 0.5 mJy beam^{-1}.

tion of L96 — and both have magnetic field direction transverse to the source axis; it is not clear which is the current beam termination point, or what the relation is between this hot spot and the lobe to the southwest, which contains a region (E1) that counts as a diffuse secondary hot spot in its own right. The angle between the beam as traced by W1 in figure 4.33 and that terminating in E3/E2 is some 10 to 15° short of 180°; the jet in the western lobe also appears bent. Some of the inferred bending in the beams may be related to the unusual environment implied by the east-west extended [OIII] emission seen by McCarthy *et al*. (1995).

4.5.16 3C 319

The literature

3C 319 is in the sample of JPR and of Leahy and Williams (1984). Maps at 1.4 and 5 GHz made with the partially completed VLA are in Bridle and Fomalont (1979), who were the first to suggest that the source was probably a classical double. They discuss the significance of the 20th magnitude optical object coincident with the radio hot spot. Crane, Tyson and Saslaw (1983) suggest that this is directly associated with the hot spot, because of its similar elongation (it does appear to be very similar in shape to the brightest radio contours on my higher-resolution radio map). However, Keel and Martini (1995) show that the optical spectrum of this object is identical to that of an elliptical galaxy at the redshift of 3C 319, and conclude that the superposition is a chance one.

Macklin (1983) presents a spectral index map which shows steepening from the ends of both lobes towards the centre and the presumed identification (a galaxy with $R = 18.07$; Eales 1985a) and so makes it clear that the source is an FRII in spite of the absence of a hot spot in the S lobe. Alexander and Leahy (1987) find a reasonable fit with their simple model of spectral ageing. No radio core has been detected.

The field of 3C 319 contains a number of faint red objects (JPR; Eales 1985b; Rawlings 1987) at least two of which have redshifts which show them to be associated with the source, and another two of which have colours consistent with being at the same redshift (Keel and Martini 1995). On larger scales galaxy counting suggests the source is in a cluster of Abell class 0 (Harvanek, private communication). Rawlings (1987) reports a 4σ marginal detection from the EINSTEIN satellite. The nuclear regions of the host galaxy appear normal (dK96). The galaxy is a low-excitation object on the basis of the equivalent width of [OIII].

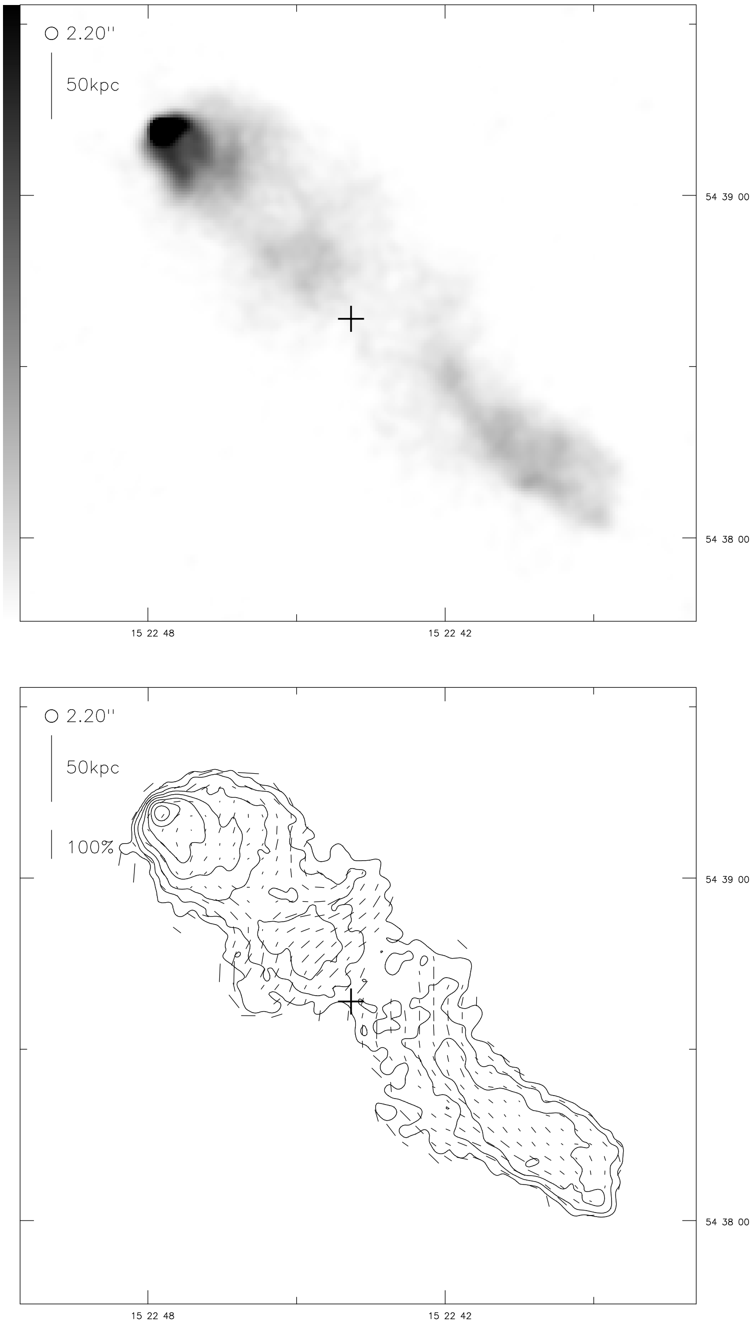

Figure 4.34: 3C 319 at 2.20 arcsec resolution. Above: linear greyscale; black is 5 mJy beam^{-1}. Below: contours at $0.2 \times (-2, -1, 1, 2, 4, \ldots)$ mJy beam^{-1}. A cross marks the position of the optical identification.

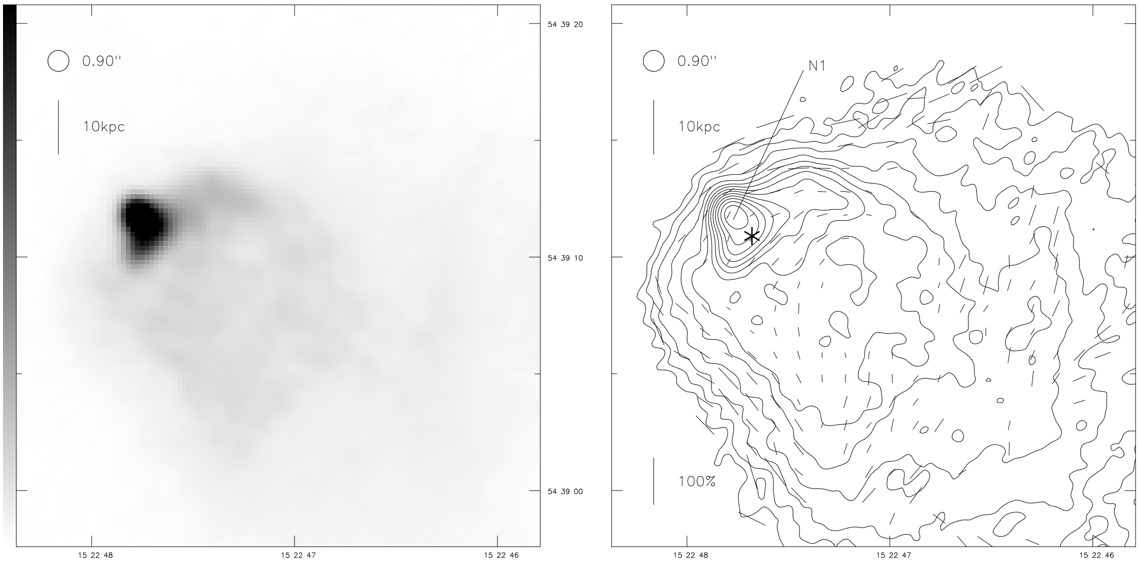

Figure 4.35: 3C 319 at 0.90 arcsec resolution. Left: linear greyscale; black is 5 mJy beam^{-1}. Right: contours at $1 \times (-\sqrt{2}, -1, 1, \sqrt{2}, 2, 2\sqrt{2}, \ldots)$ mJy beam^{-1}. The position of the 20th magnitude object coincident with the hot spot is marked with an asterisk.

My maps

The low-resolution map of 3C 319 shows the features that make the source unusual; it has no core or southern hot spot. Unsurprisingly, no jet is detected. From the position of the optical identification it seems that the core, if it exists, should lie in the low-surface-brightness region at the centre of the source; the polarization behaviour of the lobes supports this. From an estimate of the on-source noise in this region I can say that the core is very unlikely to be brighter than 0.3 mJy. A high-resolution image shows that the hot spot, N1, is extended roughly along the source axis and has its magnetic field transverse to it. Fainter extensions leave the hot spot to the northwest and southeast.

4.5.17 3C 349

The literature

3C 349 is in the sample of JPR. Rawlings (1987) has a more detailed 5 GHz map made with the 5-km telescope, but the best map prior to the present study is that of LP at 1.4 GHz.

3C 349's host galaxy ($R = 17.84$) appears to have a close small companion (Eales 1985a,b) but is not in a cluster (Harvanek, private communication).

My maps

A low-resolution map (figure 4.36) shows a reasonably ordinary source. There is a bright well-defined region of emission N1 in the middle of the northern lobe, connected to the hot spot by a ridge, and the end of the northern lobe has the bottle-neck shape seen in 3C 234 and 3C 79. At the end of the southern lobe a pronounced constriction in the lobe boundary (at S1) divides the hot spot region from the rest of the source; this type of feature occurs in a number of objects (e.g. 3C 135; L96). The magnetic field in the lobes is directed along the source axis except at N1.

The high-resolution maps (figure 4.37) point up the large differences between the brightnesses of the hot spot areas. The northern hot spot is largely resolved, with no bright structure visible on sub-kpc scales. The brightest component, N2, has its long axis transverse to the source axis and a tail — the precursor of the ridge described above — leads back into the lobe. The southern hot spot (S2), by contrast, clearly still has unresolved structure. It is extended and has its magnetic field direction transverse to the source axis. A diffuse bright region extends from the hot spot back into the lobe; a faint region to the east of S2 (S3) counts as a faint secondary hot spot. The only sign of a jet is a knot 4.5 arcsec SE of the core, also remarked upon by LP; in the high-resolution images it is seen to be extended along the source axis, but

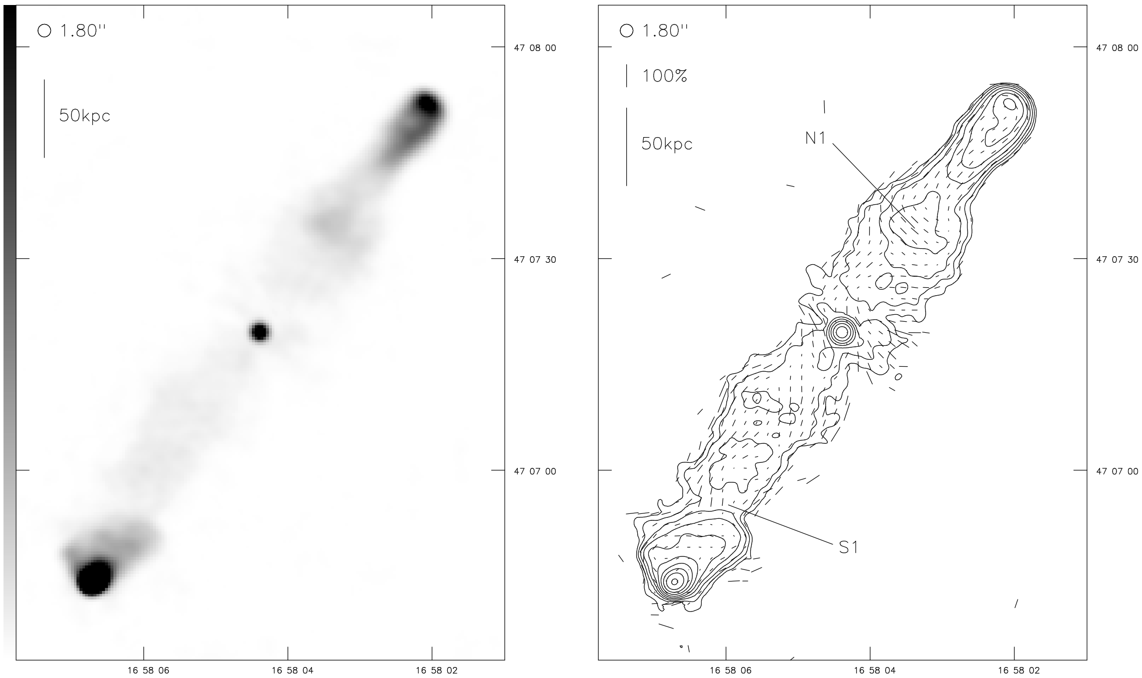

Figure 4.36: 3C 349 at 1.80 arcsec resolution. Above: linear greyscale; black is 15 mJy beam^{-1}. Below: contours at $0.25 \times (-2,-1,1,2,4,\ldots)$ mJy beam^{-1}.

it is not long enough to be a jet according to the criteria of Bridle and Perley (1984). It has been classed as a possible jet.

A map of spectral index (figure 4.38) between 1.4 and 8.4 GHz shows the expected spectral steepening along the source axis. In addition, correlations between spectral index and flux density changes are visible in both lobes — the spectrum steepens suddenly to the southeast of the bright region in the northern lobe, N1, and to the northwest of the constriction at S1.

There is little depolarization between these two frequencies (DP ≈ 0.85) and no significant difference in depolarization between the lobes. There is, however, a significant variation in depolarization along both lobes; suitably integrated, the DP varies from 1 (i.e., no depolarization) at the hot spots to a low of 0.6 around the core. This is consistent with a model in which the depolarization is caused by the halo of the host galaxy — which must then have a diameter comparable to the size of the source. This phenomenon is seen in other sources (e.g. Johnson, Leahy and Garrington 1995; Strom and Jägers 1988).

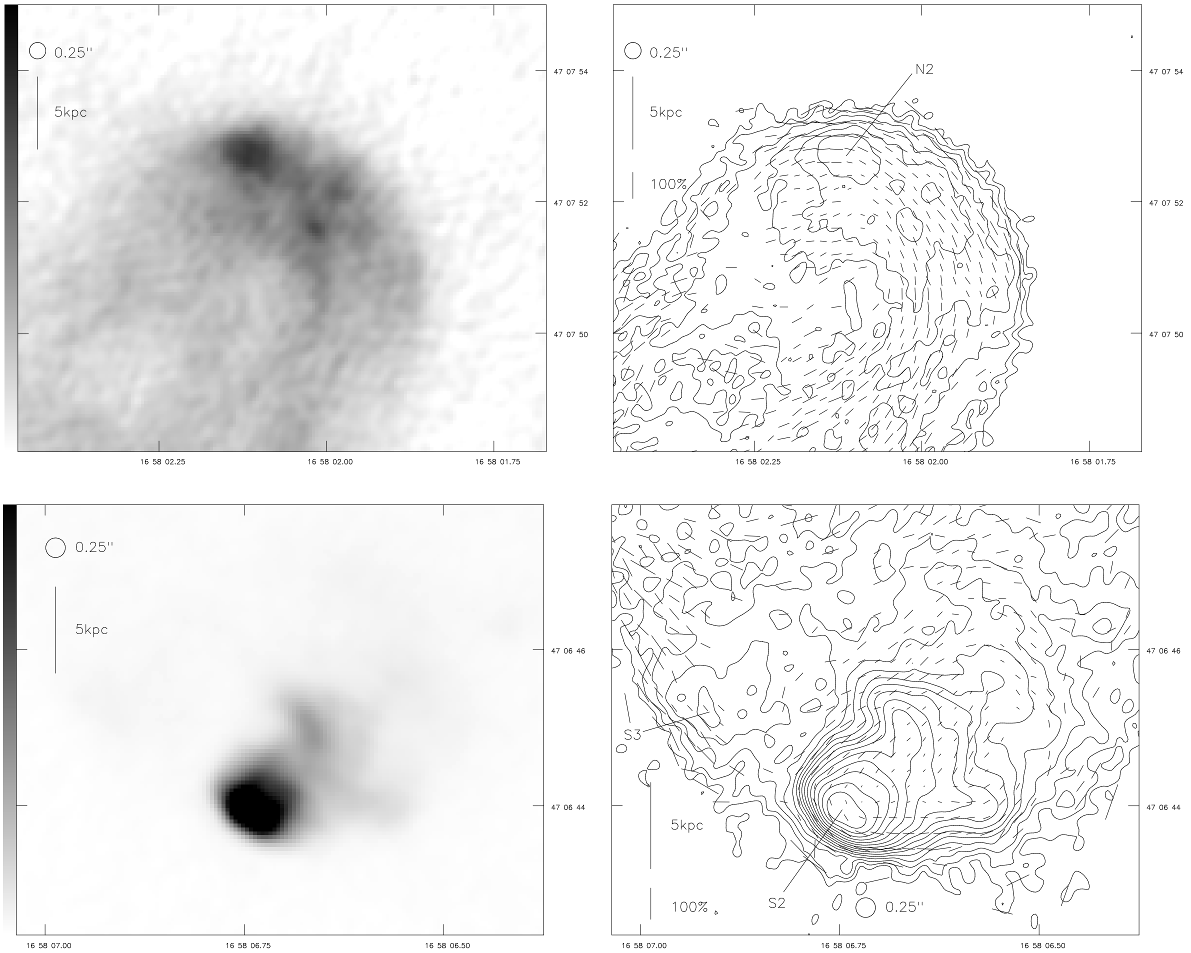

Figure 4.37: 3C 349 at 0.25 arcsec resolution. Above: N hot spot — left: linear greyscale; black is 10 mJy beam^{-1}; right: contours at $0.1\times(-\sqrt{2},-1,1,\sqrt{2},2,2\sqrt{2},\ldots)$ mJy beam^{-1}. Below: S hot spot — left: linear greyscale; black is 1 mJy beam^{-1}; right, as above right.

4.5.18 3C 381

The literature

Radio maps of 3C 381 are in RP and Antonucci (1985); LP have the best maps to date, with 1.25-arcsec resolution at 1.4 GHz. Both LP and Antonucci's maps show the curious extended structure in the S hot spot. LP's maps show the source to have X-symmetry, with incipient 'wings' of the sort found in a number of low-power sources (compare 3C 20; see section 1.4.4).

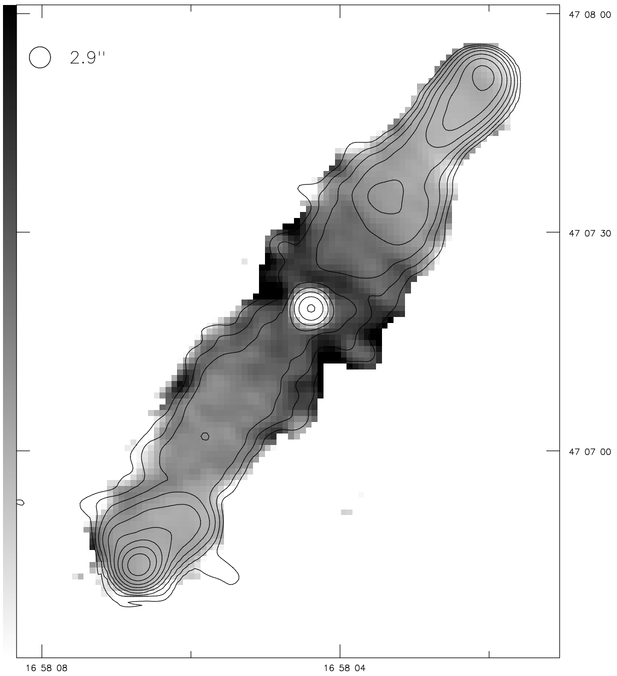

Figure 4.38: Spectral index between 8.4 and 1.5 GHz of 3C 349 at 2.90 arcsec resolution. Linear greyscale between 0.5 and 1.5; superposed are contours of total intensity at 8.4 GHz at $0.4 \times (-2,-1,1,2,4,\ldots)$ mJy beam^{-1}.

Wyndham (1966) classifies the host galaxy as G(ND:) — the only galaxy so classified, in contrast to his usual description of N-galaxies as N. He remarks that the galaxy appears “almost stellar” on the red plate. This classification and identification appear to be the basis for Grandi and Osterbrock’s (1978) classification of the source as an N-galaxy; they report weak broad Hα in addition to a strong narrow component of the same line. It would appear, therefore, that neither the classification as an N-galaxy nor that as a BLRG is particularly secure. The nuclear HST image of dK96 is similar to that of an ordinary elliptical.

3C 381’s host galaxy lies in a small group, with a nearby companion, and has $R = 16.86$ (Sandage 1973b). It was not detected in the X-ray by EINSTEIN (Fabbiano *et al*. 1984). A broad-band image by McCarthy *et al*. (1995) shows the companion; their [OIII] image shows a separate linear feature which corresponds to the base of the ‘bar’ in the radio (see figure 4.39), providing direct evidence for interaction between the radio lobe material and emission-line gas. The HST image of dK96 shows tails to the north and south of the optical nucleus.

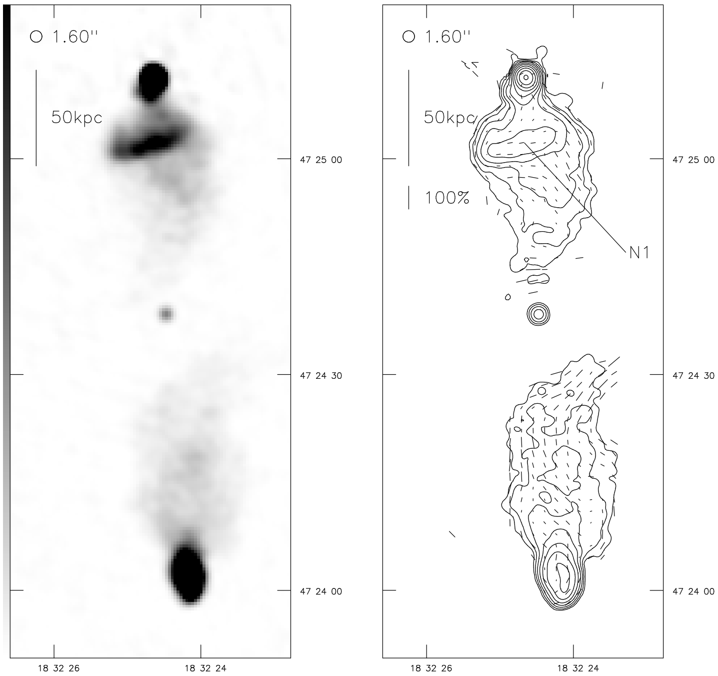

Figure 4.39: 3C 381 at 1.60 arcsec resolution. Above: linear greyscale; black is 10 mJy beam^{-1}. Below: contours at $0.4 \times (-2,-1,1,2,4,\ldots)$ mJy beam^{-1}.

My maps

A bright (40 mJy) steep-spectrum confusing point source lies 200 arcsec west of the pointing centre and was subtracted from these maps.

The low-resolution maps (figure 4.39) show a reasonably normal source whose most striking feature is the bright bar, N1, in the northern lobe. This is connected at its western end by a bridge to the hot spot, and appears to curve to the north again at its eastern end. As the bar is bounded to the south by a region of cool gas (see above) it is very difficult to interpret this feature in terms of anything other than strong backflow. The magnetic field in the bar is parallel to its direction of extension.

The high-resolution map shows the very different natures of the two hot spots. The northern hot spot clearly has double substructure, with the more compact but weaker component, N2, to the southwest; this is unresolved at 0.25-arcsec resolution. The northeastern component, N3, is slightly resolved and extended southwards. The magnetic field in N2 is in position angle 45°; that in N3 varies along its length. Both components sit on a bright background region about 5 kpc across, and do not count as separate hot spots by the definition of L96. The extensions to the northeast and northwest are artefacts

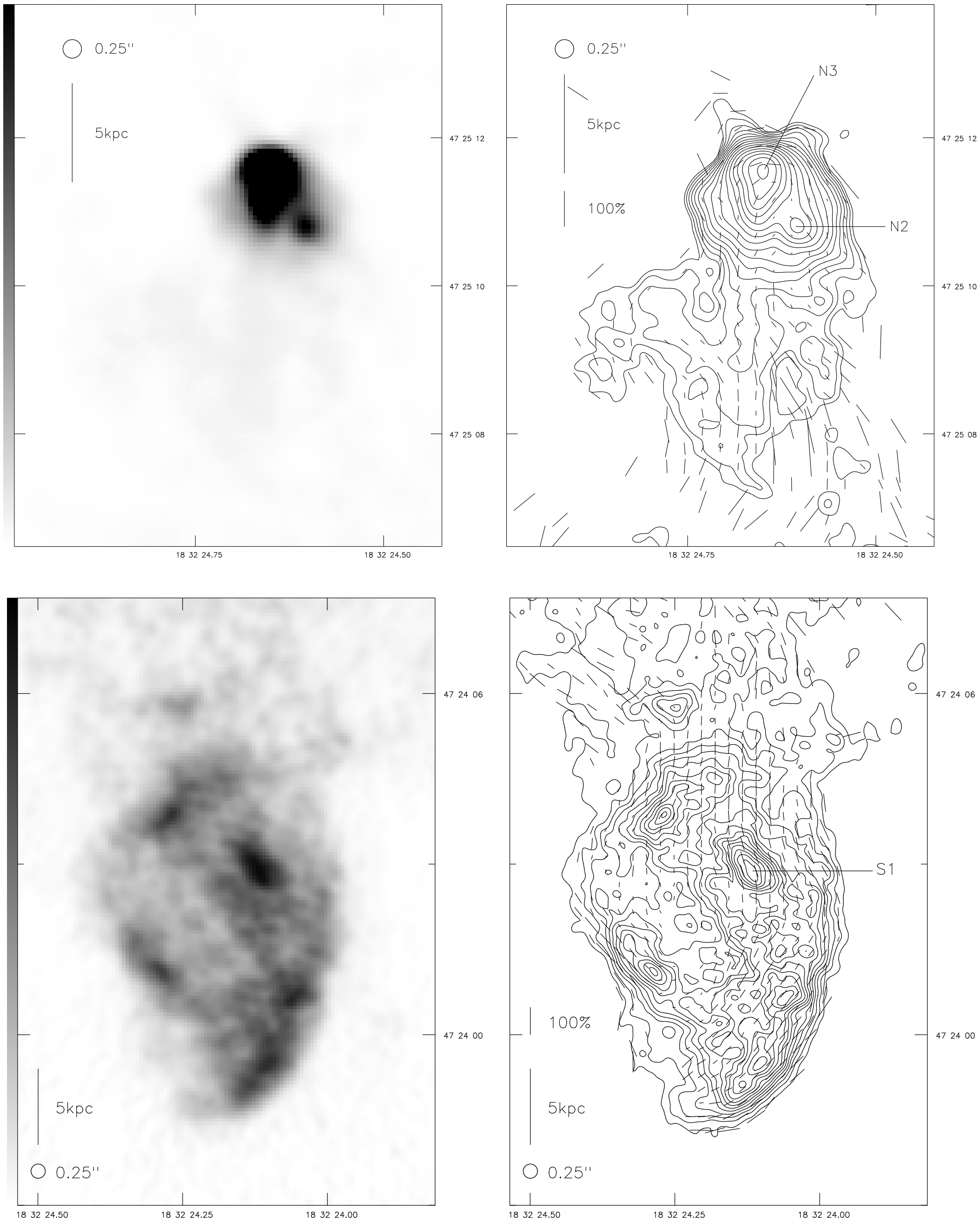

Figure 4.40: 3C 381 at 0.25 arcsec resolution. Above: N hot spot — left: linear greyscale; black is 10 mJy beam^{-1}; right: contours at $0.2\times(-\sqrt{2},-1,1,\sqrt{2},2,2\sqrt{2},\ldots)$ mJy beam^{-1}. Below: S hot spot — left: linear greyscale; black is 1.5 mJy beam^{-1}; right, *linear* contours at $0.1\times(1,2,3,4\ldots)$ mJy beam^{-1}.

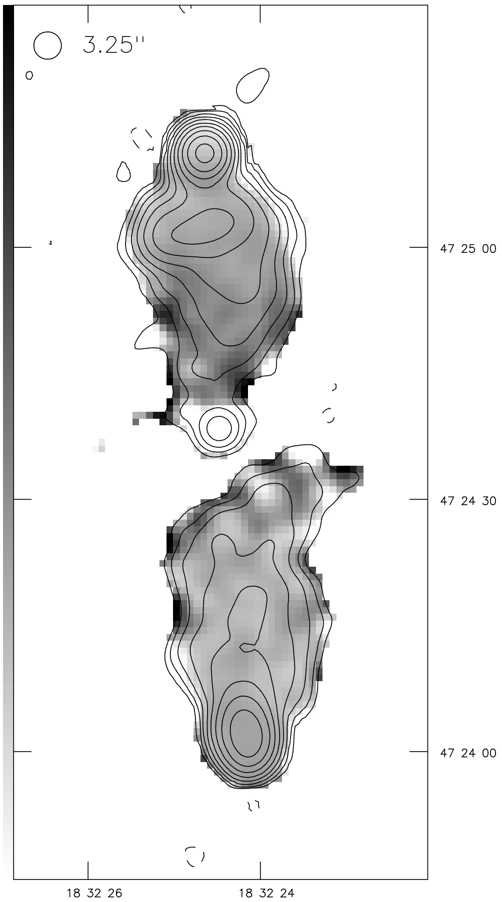

Figure 4.41: Spectral index between 8.4 and 1.5 GHz of 3C 381 at 3.25 arcsec resolution. Linear greyscale between 0.6 and 1.2; superposed are contours of total intensity at 8.4 GHz at $0.4 \times (-2,-1,1,2,4,\ldots)$ mJy beam^{-1}.

caused by the brightness of the hot spot region; the ridge which can be seen running southwards from the hot spot and then bending northeast is real, however, and may represent a change of direction for the backflow responsible for producing the bar. By contrast, the southern hot spot region appears to have no single compact component; a number of knots of similar size are distributed throughout the hot spot region. The brightest is S1 but there are at least five separate components by the definition of L96. We might hypothesise that strong turbulence within the lobe has caused the beam to disrupt and distribute energetic particles over a wide region at this point in the source's lifetime, a phenomenon seen in numerical simulations (e.g. Hardee and Norman 1990); in this case a bright compact hot spot might well form again on timescales of a few thousand years.

A map of spectral index (figure 4.41) between 1.4 and 8.4 GHz shows little variation along the source, though the curving bases of the lobes appear to have considerably steeper spectra than the rest of it. There is some evidence that the spectrum of the bar in the northern lobe is flatter than that of the material immediately to the north of it; this is evidence either of compression or of reacceleration in the bar.

There is little depolarization (DP ≈ 0.9) between the two frequencies. The northern lobe is marginally more depolarized than the southern one. The parts of the source closer to the nucleus are noticeably more depolarized on both sides, as in 3C 349.

4.5.19 3C 401

The literature

3C 401 was in the sample of JPR, who provide the identification with an 18th magnitude object. The best map prior to this study was the 5-GHz VLA map of Burns *et al*. (1984) with 0.6×0.3 arcsec resolution. The jet in the S lobe is sufficiently bright to be detectable even in JPR's map, but is first clearly seen in the 15 GHz 5-km map of Laing (1981b).

3C 401 is embedded in a faint diffuse region of X-ray emission (Feigelson and Berg 1983). The host galaxy appears double or interacting on the plate of Longair and Gunn (1975), and appears to lie in an optical cluster of Abell class 1 (Harvanek, private communication). The degree of polarization at low resolution and 2.7 GHz is unusually low (Laing 1981b). These facts seem to indicate an unusual (presumably unusually dense) environment for 3C 401.

My maps

The integrated rotation measure of 3C 401 is unknown, and so magnetic field directions should be inferred from the polarization vector directions with caution.

A low-resolution map of 3C 401 (figure 4.42) shows the jet in the southern lobe that makes this source so unusual. The southern lobe also has an extension to the east, much like the proto-wings of 3C 381, which is highly polarized. Neither lobe has a compact hot spot. At the full resolution available (figure 4.43) the jet (S1) can be seen to be knotty, bent at several places and has inferred magnetic field parallel to its length (behaviour unlike the jets in FRIs; see chapter 3) in contrast to the mainly transverse magnetic field configuration of the bases of the lobes. The jet can be traced into the 'warm spot' — approximately 10 kpc across — at the tip of the southern lobe (S2), with inferred magnetic field transverse to its direction of extension and to the direction of the incoming jet. There is no sign of a counterjet in

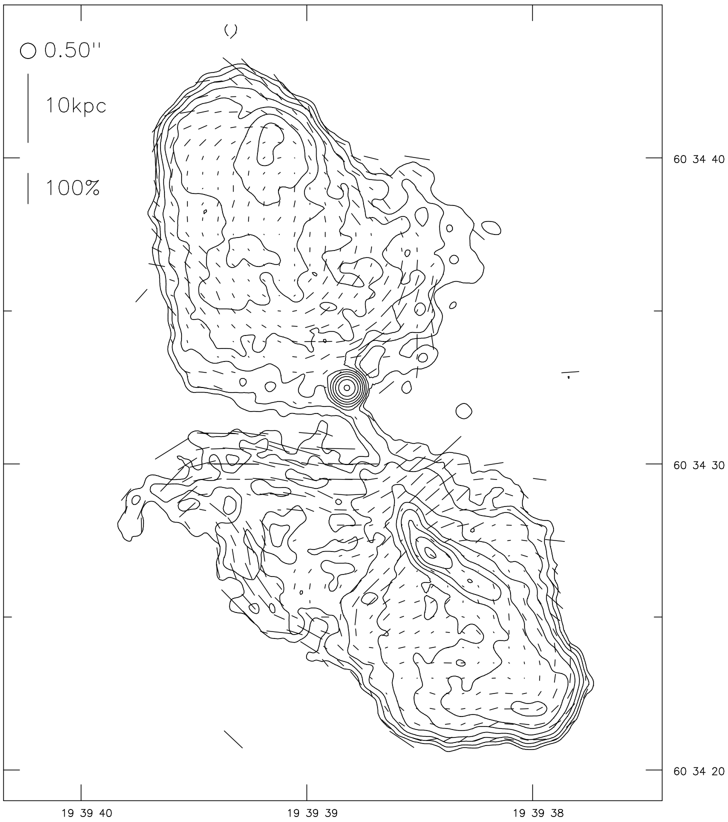

Figure 4.42: 3C 401 at 0.50 arcsec resolution. Contours at $0.1 \times (-2, -1, 1, 2, 4, \ldots)$ mJy beam^{-1}.

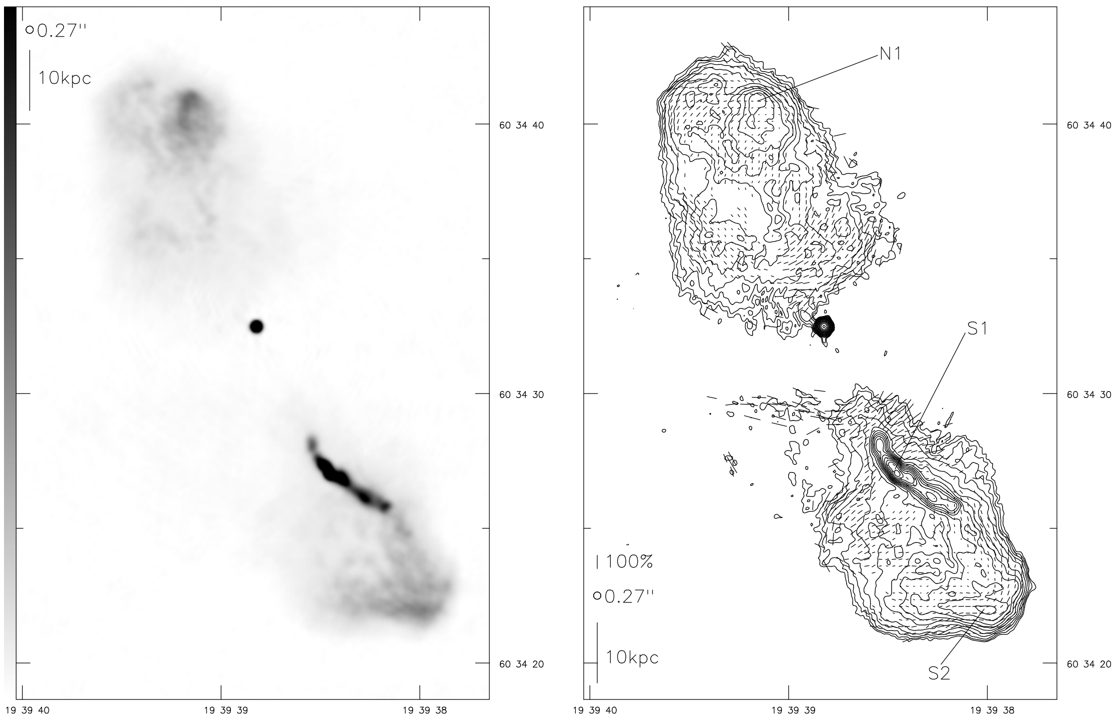

Figure 4.43: 3C 401 at 0.27 arcsec resolution. Left: linear greyscale; black is 5 mJy beam^{-1}. Right: contours at $0.1 \times (-\sqrt{2}, -1, 1, \sqrt{2}, 2, 2\sqrt{2}, \ldots)$ mJy beam^{-1}.

the northern lobe, but there is again a ‘warm spot’ N1 with a tail that extends back towards the core. The resolved areas in both lobes with low or absent polarization are striking.

4.5.20 3C 436

The literature

3C 436 was mapped by RP with the 5-km telescope; the sensitivity was too low to show the low-surface-brightness lobes. A higher-sensitivity map with the same instrument is in Rawlings (1987). No VLA map appears to be available in the literature as yet, although DeGraaf and Christiansen (private communication) have high-sensitivity maps at several frequencies.

The host galaxy has $R = 17.32$. There are some fainter objects in the field, and galaxy counting suggests that the object lies in a cluster of Abell class 0 (Harvanek, private communication). The nucleus shows dust features and appears to be aligned N-S (dK96).

My maps

A 3 mJy confusing source 110 arcsec to the NW of the pointing centre has been removed. It appears to be extended in roughly the same direction as 3C436, and to be a twin-jet FRI; its jets have transverse inferred magnetic field.

The low-resolution map (figure 4.44) shows the main features of the source. The two lobes are symmetrical on the large scale but there is a jet (S1, S2) and prominent double hot spot in the southern lobe while the northern lobe has weak hot spots and no jet. The jet appears to have transverse magnetic field, but its contrast with the surrounding material is low, so this may not indicate the true field in the jet. There is no gap between the northern and southern lobes.

At the full available resolution (figure 4.45) the hot spots in the northern lobe (N1, N2 etc.) are barely visible above the noise; they evidently contain no bright structure on size scales below a few kpc. By contrast, the southern lobe has a very compact hot spot, S3 (Gaussian fitting suggests a sub-kpc minor axis). This lies at the end of the jet, has magnetic field transverse to it, and is extended north and westwards. There is also a bright but diffuse secondary hot spot, S4, at the tip of the source. It is noteworthy that a jet that appears to be resolved, with a width of a few kpc, should produce such a compact hot spot. S4 has a magnetic field aligned along its direction of extension.

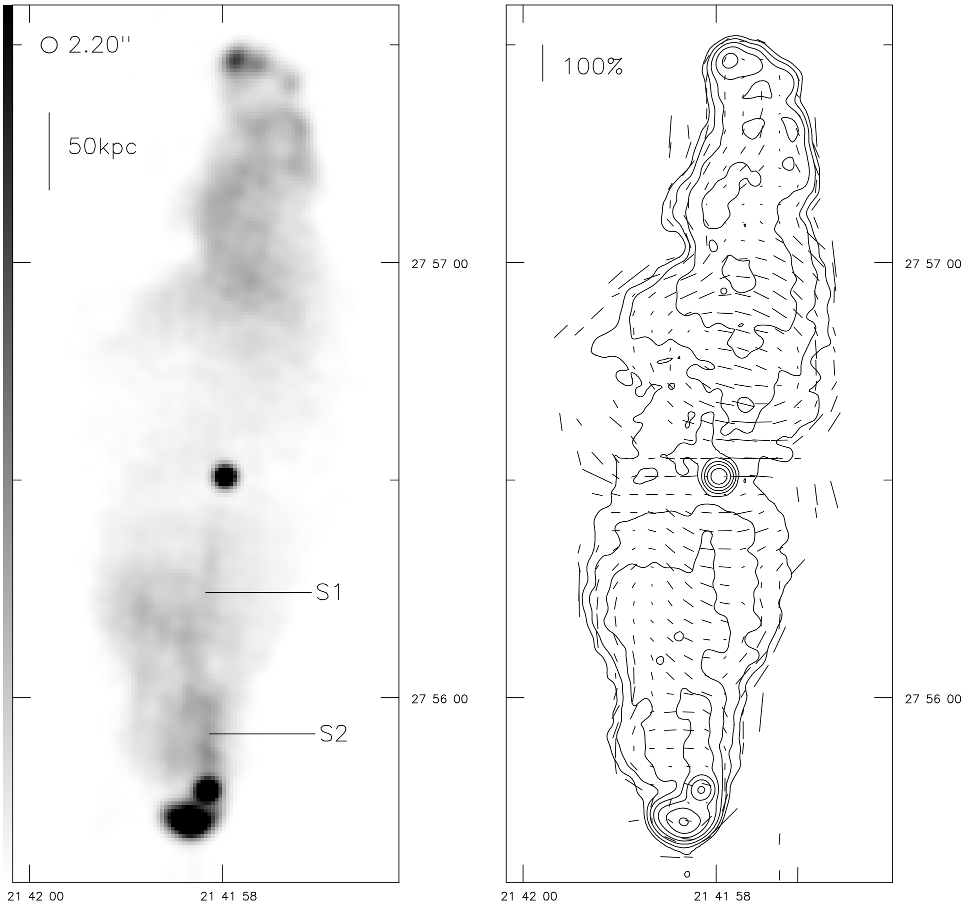

Figure 4.44: 3C 436 at 2.20 arcsec resolution. Above: linear greyscale; black is 8 mJy beam^{-1}. Below: contours at $0.3\times(-2,-1,1,2,4,\ldots)$ mJy beam^{-1}.

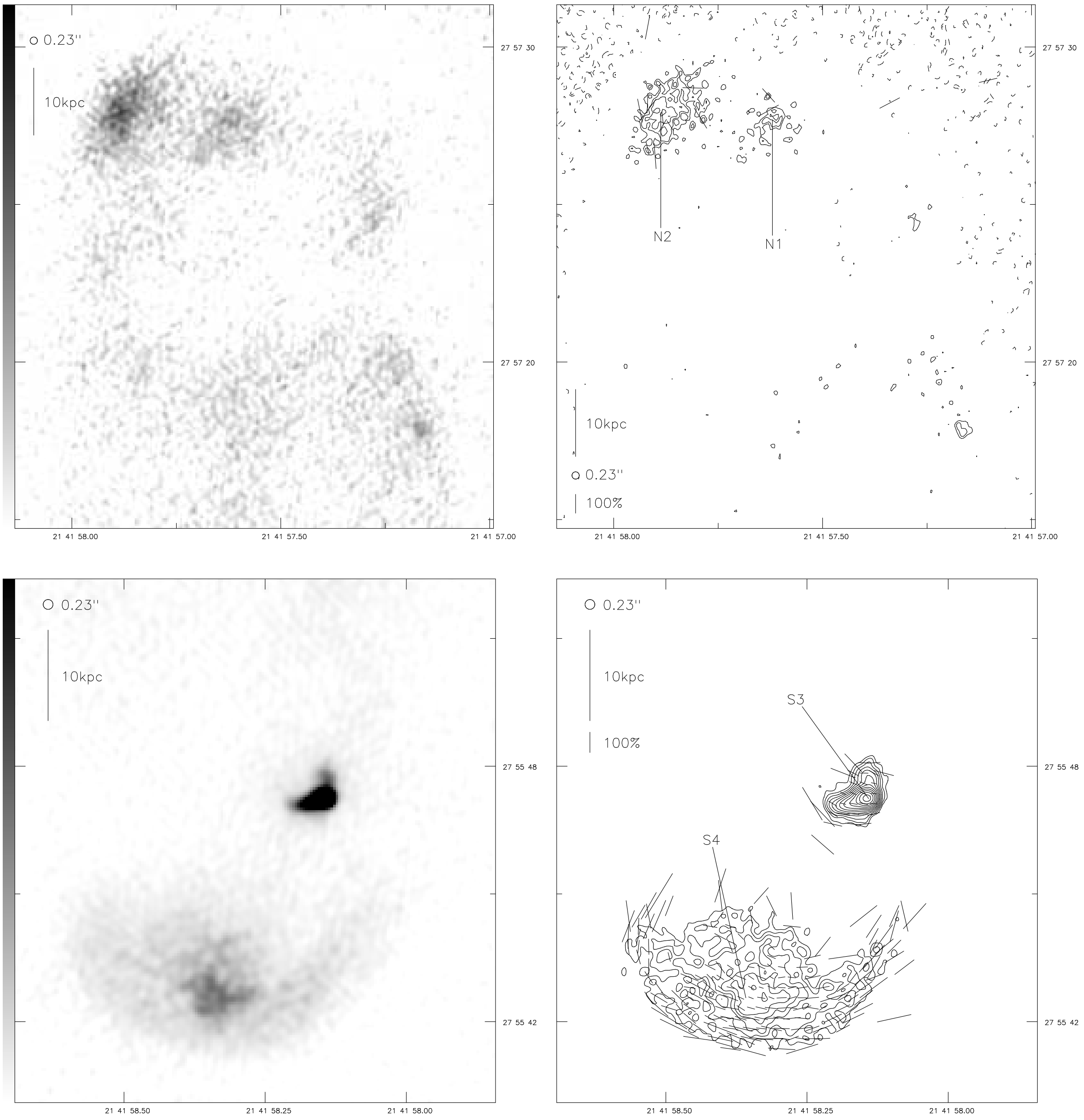

Figure 4.45: 3C 436 at 0.23 arcsec resolution. Above: N hot spot — left: linear greyscale; black is 200 μJy beam^{-1}; right: contours at $50 \times (-\sqrt{2}, -1, 1, \sqrt{2}, 2, 2\sqrt{2}, \ldots)$ μJy beam^{-1}. Below: S hot spot — left: linear greyscale; black is 1 mJy beam^{-1}; right, as above right but contours start at 100 μJy beam^{-1}.

4.5.21 3C 438

The literature

JPR have a map of 3C 438, as does Laing (1981b); his 15 GHz observations give the first indication of the twin jets that make this source so remarkable. LP's 1.5 GHz VLA image does not really have enough resolution to show the jets clearly; they cite an unpublished snapshot by Laing which does. The source is completely unpolarized in the images of LP; Laing (1981b) comments that the polarization is unusually low at 2.7 and 5 GHz (at low resolution). LP's map shows the wing-like extensions to the lobes, with something approaching X-symmetry.

3C 438 was detected in the X-ray by EINSTEIN (Feigelson and Berg 1983) and is the brightest galaxy in a rich cluster (Longair and Gunn 1975). This seems to be a case, like 3C 401, of an unusually dense environment producing an unusual radio source.

My maps

A nearby bright (9 mJy) confusing point source was removed from the map.

The integrated rotation measure of 3C438 is not known (observations by Inoue *et al*. 1995 fail to constrain it well), so magnetic field direction must be inferred with caution from the vectors plotted.

The low-resolution map (figure 4.46) shows some of the extended structure seen in the map of LP. LP saw an extension of the N lobe to the SW which is not seen here; since the short baselines are well sampled, this implies that the far edges of the lobes have a very steep spectrum. The source is not strongly polarized even at this frequency (averaging about 10%). The prominent jets are visible. The northern jet has inferred magnetic field along its length turning to a transverse configuration later on, while the southern jet appears to have a magnetic field roughly transverse to its length (initially nearly north-south) as soon as polarization is detected. However, it is unsafe to infer magnetic field direction from the vectors shown here, as the depolarization at low frequencies may well indicate large differences in rotation measure across the source.

The high-resolution map (figure 4.47) shows the jets in detail. Both are unresolved or at best slightly resolved, and the opening angle is at most a few degrees. The north jet (N1) is straight and, although it disappears before the end of the source, the structure there is consistent with the jet's terminating without bending further; the elongated knot at the far end of the lobe (N2) could be described as the beam termination hot spot, although it is not separate from the bright structure to its north and east. The jet in the southern lobe (S1), on the other hand, is bent in several places — in fact, the jets do not make an

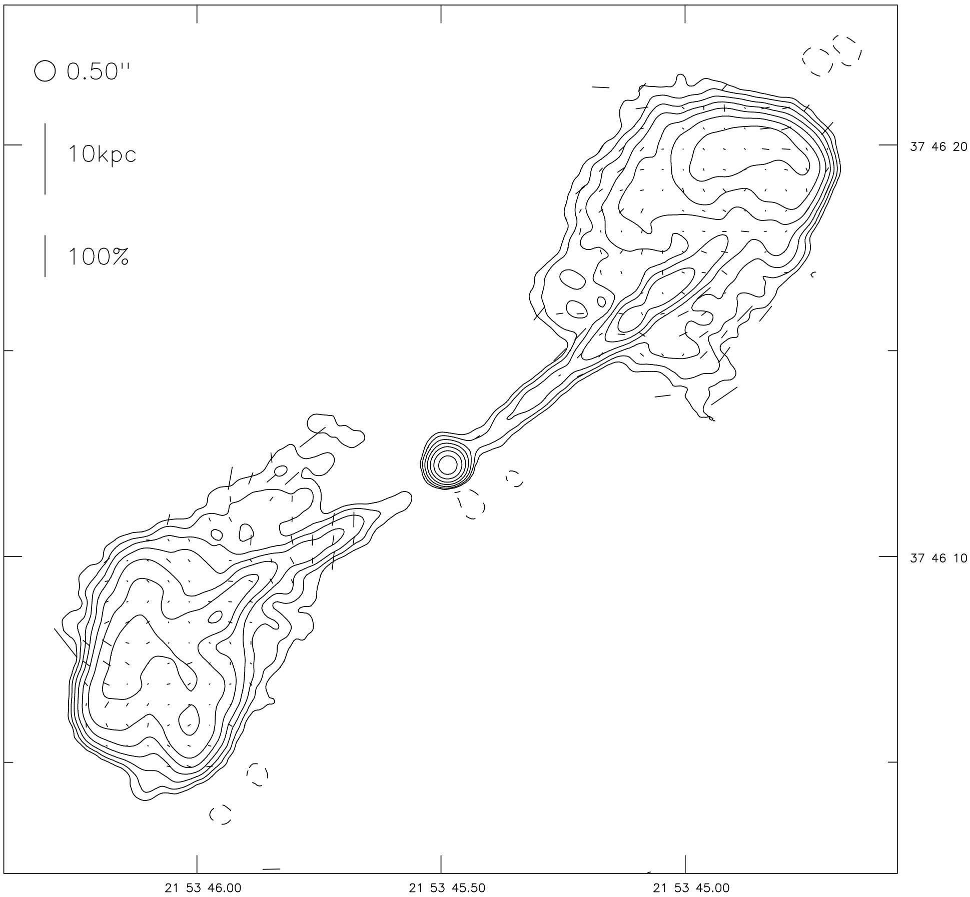

Figure 4.46: 3C 438 at 0.50 arcsec resolution. Contours at $0.15 \times (-2, -1, 1, 2, 4, \ldots)$ mJy beam^{-1}.

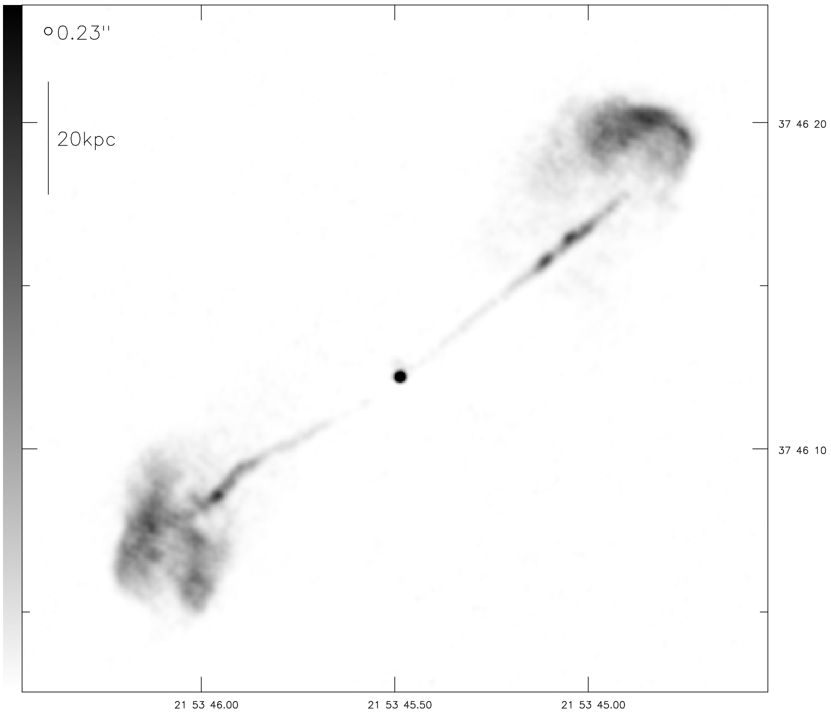

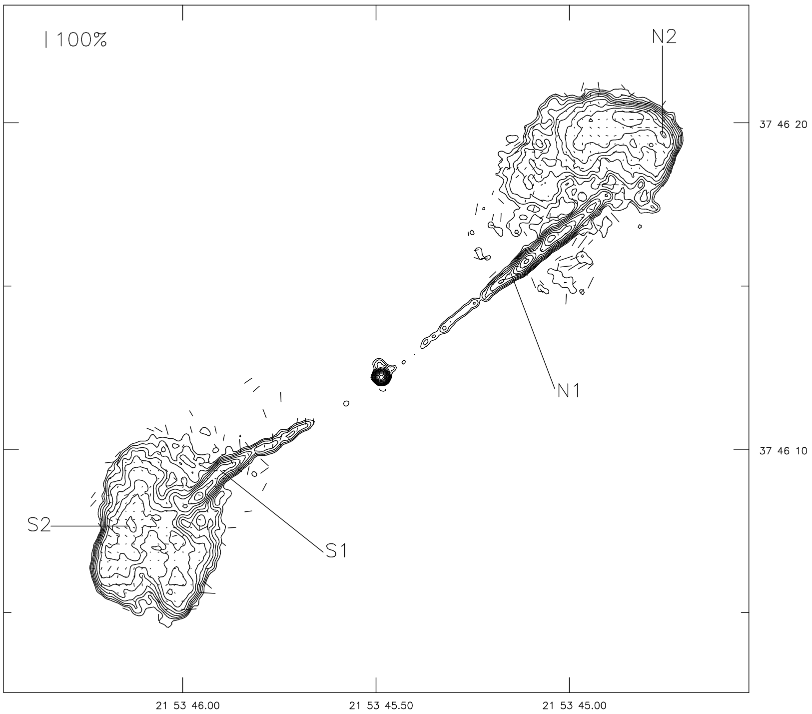

Figure 4.47: 3C 438 at 0.23 arcsec resolution. Above: linear greyscale; black is 5 mJy beam^{-1}. Below: contours at $0.2 \times (-\sqrt{2}, -1, 1, \sqrt{2}, 2, 2\sqrt{2}, \ldots)$ mJy beam^{-1}.

angle of 180° at the core, so the beam must bend even before the jet becomes visible if they are initially oppositely directed. It can be traced to a bright knot in the middle of the lobe but its eventual termination point is not clear; it may be the bright region S2. The structures in the lobe — there are at least two separate hot spot regions — together with the bends in the jet, are suggestive of a ‘flapping’ jet which may quite recently have been terminating in the southern end of the lobe. Both jets fade significantly as they enter the bright parts of the lobes, and the tails of the lobes are curved at lower resolutions and frequencies. These facts make a model plausible in which buoyancy due to the hot cluster gas has pushed the lobes away from the central regions of the source, leaving the jets to interact directly with the IGM over most of their length (cf. Williams 1991). 3C 438 may thus have something in common with the class of wide-angled tails.

4.6 Summary

Seventeen sources have been mapped in detail, with a resolution approaching 1 kpc in most cases. Quantitative analysis of the properties of the objects in this sample will be carried out in chapter 5; however, a few qualitative points about the images presented are made here.

4.6.1 Overall source properties

Four of the sources presented here (3C 123, 3C 171, 3C 401 and 3C 438) are not typical classical doubles. The first two have distorted lobes, but (as argued above) are probably nevertheless classical doubles in their essential physics; the last two have bright jets and diffuse hot spots. The jet of 3C 401 is one-sided; it may be related to the class of objects with dominant one-sided jets which have been given the name ‘jetted doubles’ by Law-Green *et al*. (1995). There are several similar objects with bright one-sided jets in the sample of B92 (e.g. 3C 15, 3C 277.3). 3C 438 appears unique in having bright dissipative twin jets which remain ‘FRII-like’ in their structure and opening angle, but may be related to the jetted-double class; if these are one-sided because of relativistic beaming 3C 438 may be an example close to the plane of the sky, while if they are one-sided because of unusual dissipation on one side only it seems plausible that there should exist two-sided versions. (The properties of this class of objects will be discussed in more detail in chapter 6.) The remaining sources in the sample, with the possible exception of 3C 319, are more or less conventional classical doubles.

The different shapes of the heads of the lobes have been pointed out in the text. As in the study of B92, there are many sources whose two lobes are very different from one another. Some of these differences may be attributed to short-timescale variations of the beam termination behaviour (examples might include 3C 381 or 3C 349). In other cases (e.g. 3C 300) the differences must have been maintained over a long time period, and if the beams themselves are symmetrical a strong environmental asymmetry is required. Particularly noticeable in this sample are the sources in which the hot spots are connected to the rest of the lobe by a long narrow ‘bottle-neck’, a feature also noticed by LP in their overlapping sample. Lobes of this kind, of which 3C 234 E is the prototype, are consistent with the working surface having encountered a sudden drop in the density of the external medium. The shape of the head of the lobe in simple models without variations in jet direction is governed by the relative velocities of hot spot advance (governed by ram-pressure balance) plus backflow, and post-hot spot expansion, in which the material that has passed through the jet termination shock expands sideways into the shocked IGM as well as linearly into the cocoon. If the external density drops, ram pressure balance ensures that the hot spot advance speed increases. The speed of sideways expansion should also increase, but because the density of post-hot spot material should fall as the hot spot advance speed increases, the dependence of this speed on the external density is weaker; the net effect is thus a narrowing of the head of the lobe. Sources such as 3C 234, where the bottle-neck is on scales comparable to the size of the whole source, are the exception rather than the rule, which suggests that in general variations in the jet direction can smooth out the front of the lobe. (3C 381 S may be an example of a lobe where this process is just about to occur.)

The sources shown here provide two further examples of objects (out of four studied) whose depolarization clearly decreases with distance away from the host galaxy, providing further evidence for the suggestion that this depolarization is due to the galaxy’s own halo. The depolarization in the other two objects shows no significant trend with distance, however.

4.6.2 Hot spots

With the definition of hot spots I have adopted, almost all sources in this sample have distinguishable hot spots in both lobes. L96 tabulate the positions and multiplicities of the hot spots in the low-redshift sample, and for comparison I have done the same, attempting to use comparable classifications. Table 4.6 summarizes these properties. Hot spots are classed as single (1), double (2) or multiple (M); in addition, components ten times fainter than the peak brightness of the hot spot complex are counted after a plus sign, so that ‘2+1’ means ‘double with an additional faint component’. Their location, as in L96, may be ‘tip’ (at the very end of the lobe), ‘side’ (on the lobe boundary, but not at the end) or ‘middle’ (anywhere else in the lobe). The location is of the whole hot spot complex, but I have noted cases where the location of the primary is significantly different. Comments are generally self-explanatory; ‘diffuse’ implies that there is little compact structure at the resolution of the map used, while ‘extended’ implies that a bright hot spot is significantly extended and so has a good chance of being resolved into multiple components at higher resolution. ‘Rim’ implies that multiple hot spots form a bright rim around the leading edge of the source or other structure in the hot spot complex; these features are common in the

$z < 0.15$ sample (L96).

Double and multiple hot spots are common in this sample, as they were in that discussed by L96. Of the 42 lobes in table 4.6, at least 18 (43%) have more than one bright hot spot, which should be compared with $\sim$ 50% in the sample of L96. In the majority of such sources one hot spot (the primary) is unambiguously more compact than any of the others, as in L89; these usually have a magnetic field direction transverse to the seen or inferred incoming beam direction. In the majority of these the primary hot spot is recessed with respect to the other components (though there are several counterexamples; 3C 79 E, 3C 234 E). The data presented here provide little direct evidence to identify the primary hot spot with the jet termination point; however, in two cases a jet is clearly seen to enter the primary hot spot (3C 234, 3C 436) and there are no cases in which a jet enters a secondary hot spot. These results are consistent with earlier work (L89). Most of the hot spots lie at the tip of the source; this trend is more pronounced than it was in L96, and there are fewer sources which show a distinct internal hot spot region (the clearest exception being 4C 14.11).

The physical significance of the numbers of hot spots is not clear. Higher-resolution observations of these objects would almost certainly reveal more hot spots (according to my classification) in a number of cases (compare the MERLIN and VLA images of 3C 123). The fundamental limit on the size scale of emission from the beam termination region is the cross-sectional size of the beam itself, and there is no reason to suppose that the spatial resolution achieved in this or other studies approaches that size. (The jet and hot spot in the southern lobe of 3C 436 provide some evidence that the jet width is not necessarily a good indicator of the beam width.) It is therefore hard to compare these results with those from other samples in an unbiased way. When I note that the hot spots in this sample seem less complicated than those of B92 and more complicated than those of L89, it must be borne in mind that this is certainly at least partly an effect of decreasing spatial resolution. Nevertheless, with this caveat, the overall impression is of a set of hot spots which, while being equally diverse, are slightly easier to classify and to understand in terms of pre-existing models than are those of B92 and L96.

The more diffuse (secondary) hot spots often have a magnetic field transverse to a line between themselves and the more compact hot spots. Although it is dangerous to argue too strongly from this, because this is often also the (circumferential) direction of the field lines in the rest of the end of the lobe, I have suggested in several particular cases that this, together with the bridges of emission linking the hot spots in several cases, implies that they are being fed directly from the compact hot spot (in a manner similar to that seen in the 'splatter-spot' models of Williams and Gull 1985 or the wall-jet mechanism of Norman and Balsara 1993; see also Laing 1982, Lonsdale and Barthel 1986) rather than being disconnected from the energy supply (as in the 'dentist's drill' model of Scheuer 1982) or being fed by the remains of a discontinued beam (as in the models of Cox *et al*. 1991). In these last two models the magnetic field in secondary hot spots might be expected to remain transverse to the beam direction until the hot spot had expanded to be considerably larger than the new primary; there are several compact secondaries in

Table 4.6: Hot spots and jets

Lobe	Type	Location	Comment	Jet?
4C 12.03 N	1	tip	diffuse	Y?
4C 12.03 S	1	tip		Y?
3C 20 E	2+1	tip	primary at side	Y?
3C 20 W	1+1	tip	tail	Y
3C 33.1E	1?	tip	low resolution	
3C 33.1W	1?	tip	low resolution	Y
3C 61.1 N	1	tip	extended	Y?
3C 61.1 S	1+1	tip	extended; recessed secondary	
3C 79 E	M+1	tip	rim?; recessed secondary	
3C 79 W	M	tip	rim	
4C 14.11 E	2+2	middle	secondary on edge	Y
4C 14.11 W	2	tip		
3C 123 E	2+M	tip	primary recessed; cylindrical; substructure	
3C 123 W	2	tip		
3C 132 E	2	tip	dim recessed secondary	Y?
3C 132 W	1	tip	tail	
3C 153 E	2	tip		Y?
3C 153 W	1	middle		Y?
3C 171 E	1	tip	jet enters hot spot	Y
3C 171 W	1	tip	jet enters hot spot	Y
3C 173.1 N	M	tip	rim	Y
3C 173.1 S	1	tip?	primary recessed, multiple sub-components	
3C 219 N	2	middle	curved rim around primary	Y?
3C 219 S	1	middle		Y
3C 234 E	1+2	tip	jet enters primary	Y
3C 234 W	2	tip	tails; rim?	
3C 284 E	2	tip		
3C 284 W	1	tip	extended	
3C 300 N	1?	tip	jet/hot spot confused	Y
3C 300 S	2+1	side	equal size	
3C 319 N	1	tip		
3C 319 S	0			
3C 349 N	1	tip	diffuse; tail?	
3C 349 S	1+1	tip	extended	
3C 381 N	1	tip	double substructure; primary recessed	
3C 381 S	M	tip		
3C 401 N	1	middle	diffuse	
3C 401 S	1	tip	jet enters; diffuse	Y
3C 436 N	M	tip	rim; diffuse	
3C 436 S	2	tip	jet enters recessed primary	Y
3C 438 E	1?	tip	jet nears; diffuse	Y
3C 438 W	2?	side	jet nears; diffuse	Y

which this is certainly not the case. Equally, there are objects (e.g. 3C 123) which seem better fitted by the model of Cox et al. As the most recent numerical simulations can reproduce both types of secondary hot spot, the conclusion that there is no single model for multiple hot spots is probably uncontroversial. I believe, however, that the observations presented here provide further evidence for the possibility of comparatively well-collimated outflow from hot spots.

4.6.3 Jets

New jets are detected in 3C 20, 4C 14.11, 3C 234 and 3C 436; jets are confirmed and well imaged for the first time in a number of other sources (see table 4.6). Jets which meet the criteria of Bridle and Perley (1984) unambiguously are found in 11 out of 21 objects, or 52%. Possible jets are found in a further five objects (3C 132, 3C 153 and 3C 349 are discussed in the text; the possible jets in 4C 12.03 are discussed in LP and that in 3C 61.1 in Alexander (1985); I have also identified a knot in 3C 219 N as a possible counterjet). The total number of jets detected may therefore be as high as 16, or 76 per cent. Only two objects have definite two-sided jets (3C 171, 3C 438) and both of these are unusual in other ways; there are possible two-sided jets in 3C 219, 3C 153, 4C 12.03 and (very tentatively) 3C 20, so that the number with two-sided jets may be 6, or 29%. With the exceptions of the jets in the unusual sources 3C 171, 3C 401 and 3C 438, and of those in the well-known objects 3C 219 and 3C 33.1, jets are generally faint, representing a very small fraction of the total flux of the source even at this high frequency, and can seldom be traced all the way from core to hot spot. These results are similar to those of Black (1992, 1993) and L96; the similar rate of jet detection allows me to conclude that the high rate of jet detection in that sample was not simply an effect of its proximity in luminosity to the FRI/FRII boundary.

The properties of the jets in the combination of the sample described here and that of B92, and their consequences for quasar-radio galaxy unification, will be discussed in chapters 5 and 6.

Chapter 5

Analysis of FRIIs with z < 0.3

In this chapter I discuss methods for extracting quantitative data from radio maps, and tabulate them for a large sample of objects.

5.1 The sample

The sample to be used in this chapter and the following one comes from combining my $0.15 < z < 0.3$ sample, drawn from LRL (table 4.1) with that of B92. The source information for the combined sample is shown in table 5.1.

B92 selected 3CR sources with $P_{178} > 1.5 \times 10^{25}$ W Hz^{-1} sr^{-1} and $z < 0.15$. They excluded sources known not to have hot spots and three giant sources. In addition, they did not image the sources included by LRL from outside the 3CR catalogue; DA 240 and 4C 73.08 would have met their selection criteria but could be excluded as giants in any case. Conversely, almost all the sources selected by B92 but not LRL are only excluded from LRL's sample on the grounds of position on the sky (the exceptions are 3C 197.1, 3C 223.1 and 3C 277.3 which have $S_{178} < 10.9$ Jy on the Baars *et al*. (1977) scale). All the sources in my LRL-based sample meet the power criterion used by B92, and sources from 3CR are only excluded on the basis of position on the sky or $S_{178} < 10.9$ Jy. Thus, although the combined sample is not strictly complete, it is not seriously biased, and a complete sub-sample consisting of the non-giant LRL sources (34 in total) can be constructed if completeness is an issue. Possibly more serious than the power and flux constraints from the point of view of bias is the exclusion from my LRL-based sample of sources classed as FRIs. These classifications were often done on the basis of low-resolution maps, and it seems likely that some exclusions have been, in retrospect, quite arbitrary (in particular, 3C 288 (Bridle *et al*. 1989) and 3C 346 (Spencer *et al*. 1991) are excluded, though they are as FRII-like as, say, 3C 438 or 3C 15). Generally this bias manifests itself as an exclusion of sources which have structure intermediate between classical FRIs and FRIIs, and so does not affect conclusions based on the sample of sources with classical FRII structure (the most obvious indicator of this being well-defined hot spots).

178-MHz fluxes were taken from LR where possible, and otherwise determined following the prescription in LRL, but correcting to the scale of Baars *et al*. (1977). This procedure generally produced the same results as those of Spinrad *et al*. (1985), but in two cases the flux quoted by Spinrad *et al*. is significantly in error, leading to an implausible spectral index for the source. For 3C 403 they use the 4C flux (Gower, Scott and Wills 1967) although the source will have been resolved by the 4C interferometer; I (and L96) have used the original 3CR flux (Bennett 1962), corrected to the scale of Baars *et al*. (1977). For 3C 223.1 the correction from Véron (1977) (reducing the flux from 10.4 to 6.5 Jy on the scale of Baars *et al*.) for confusion in the 3CR survey appears to have been excessive in view of the 6C 151-MHz flux of 10.39 Jy (Hales, Baldwin and Warner 1988), the B3 flux at 408 MHz (Ficarra, Grueff and Tomasetti 1985) and the fluxes at frequencies other than 178 MHz given by Kellermann, Pauliny-Toth and Williams (1969: KPW) as corrected to the Baars *et al*. scale by Laing and Peacock (1980). I have therefore adopted an interpolated flux of 8.1 Jy. The flux given for 3C 405 (Cygnus A) is the value given by the formula of Baars *et al*.

Spectral indices are taken from LR where possible. Where a source was not in LRL B92 used the spectral indices of Spinrad *et al*. (1985) which are based on the uncorrected 178- and 750-MHz fluxes of KPW. Correction to the Baars *et al*. scale by the factors given by Laing and Peacock (1980) suggest that spectral indices calculated in this way should be too low by 0.03 in all cases. I have therefore recalculated the spectral indices of the sources not in LRL from the re-scaled KPW data, with the exception of the three described above; these are 3C 15, 3C 105, 3C 111, 3C 135, 3C 136.1, 3C 197.1, 3C 227, 3C 277.3, 3C 327, 3C 353, 3C 424, 3C 430 and 3C 445. This recalculation ensures consistency in the data.

In table 5.2 some general information about the sources in the sample is given, together with references to the literature describing them.

5.2 Analysis of radio maps

High-resolution radio maps were available to me for most (43/50) of the sources in the combined sample.[1] I used them to measure various quantities which might provide information on the energy transport

---

[1] The omission of the remaining 7 objects does not bias the sample, since they have very little in common with one another.

Table 5.1: The combined sample of FRII radio sources

Source	IAU name	z	S_{178} (Jy)	α	P_{178}	LAS (arcsec)	Size (kpc)
4C 12.03	0007+124	0.156	10.9	0.87	104	215	787
3C 15	0034–014	0.0730	17.2	0.67	33	48.0	92
3C 20	0040+517	0.174	46.8	0.66	543	53.6	214
3C 33	0106+130	0.0595	59.3	0.76	75	254	404
3C 33.1	0106+729	0.181	14.2	0.62	178	227	935
3C 61.1	0210+860	0.186	34.0	0.77	462	186	782
3C 79	0307+169	0.2559	33.2	0.92	930	89.0	474
3C 98	0356+109	0.0306	51.4	0.78	17	310	264
3C 105	0404+035	0.089	19.4	0.61	56	335	764
4C 14.11	0411+141	0.206	12.1	0.84	208	116	527
3C 111	0415+379	0.0485	70.4	0.76	59	215	283
3C 123	0433+295	0.2177	206.0	0.70	3873	37.8	179
3C 132	0453+227	0.214	14.9	0.68	269	22.4	105
3C 135	0511+008	0.1273	18.9	0.95	118	132	409
3C 136.1	0512+248	0.064	15.3	0.72	22	460	781
3C 153	0605+480	0.2771	16.7	0.66	524	9.1	51
3C 171	0651+542	0.2384	21.3	0.87	505	32.5	165
3C 173.1	0702+749	0.292	16.8	0.88	624	60.5	353
3C 184.1	0734+805	0.1182	14.2	0.68	73	182	530
3C 192	0802+243	0.0598	23.0	0.79	29	200	319
3C 197.1	0818+472	0.1301	8.8	0.72	56	24.0	76
3C 219	0917+458	0.1744	44.9	0.81	536	190	760
3C 223	0936+361	0.1368	16.0	0.74	113	306	1007
3C 223.1	0938+399	0.1075	8.1	0.73	35	140	376
3C 227	0945+076	0.0861	33.1	0.70	89	230	510
3C 234	0958+290	0.1848	34.2	0.86	466	112	469
3C 277.3	1251+278	0.0857	9.8	0.58	26	49.0	108
3C 284	1308+277	0.2394	12.3	0.95	299	178	904
3C 285	1319+428	0.0794	12.3	0.95	29	180	371
3C 300	1420+198	0.272	19.5	0.78	604	100	561
3C 303	1441+522	0.141	12.2	0.76	92	47.0	159
3C 319	1522+546	0.192	16.7	0.90	249	105	453
3C 321	1529+242	0.096	14.7	0.60	49	307	748
3C 327	1559+021	0.1039	38.5	0.64	152	302	788
3C 349	1658+471	0.205	14.5	0.74	242	85.9	389
3C 353	1717+009	0.0304	257.2	0.74	83	284	240
3C 381	1832+474	0.1605	18.1	0.81	181	73.2	274
3C 382	1833+326	0.0578	21.7	0.59	26	185	286
3C 388	1842+455	0.0908	26.8	0.70	81	50.0	116
3C 390.3	1845+797	0.0561	51.8	0.75	58	229	345
3C 401	1939+605	0.201	22.8	0.71	362	23.6	105
3C 403	1949+023	0.059	28.3	0.74	35	230	362
3C 405	1957+405	0.0565	9660.0	0.74	11001	130	197
3C 424	2045+068	0.127	15.9	0.88	98	35.0	108
3C 430	2117+605	0.0541	36.7	0.75	38	90.0	131
3C 433	2121+248	0.1016	61.3	0.75	233	68.0	174
3C 436	2141+279	0.2145	19.4	0.86	365	109	511
3C 438	2153+377	0.290	48.7	0.88	1783	22.6	131
3C 445	2221–021	0.0562	27.0	0.76	30	570	859
3C 452	2243+394	0.0811	59.3	0.78	142	280	588

Notes as for table 4.1, but RM not shown.

Table 5.2: General information on the combined sample

Source	Jets?	Reference to radio map used	Frequency of radio map (GHz)	Clustering environment	Reference for clustering	Line Type	Nuclear [OIII] line flux	Reference for [OIII]
4C 12.03	○○	–	–	G?	1	E		
3C 15	●●	2	8.4	G?	21	E	3.3	9
3C 20	●○	1	8.4	G?	1	N		
3C 33		–	–	I	18	N	175.0	10
3C 33.1	●	–	–	G?	1	B	10.5	11
3C 61.1	○	–	–	G	18	N		
3C 79		1	8.4	S	1	N	55.0	10, 14
3C 98	●	2	8.4	I	17	N	130.0	10
3C 105	○	2	8.4	I	17	N	5.6	9
4C 14.11	●	1	8.4	G	18	E	1.8	10
3C 111	●	2	8.4	—		B		
3C 123		1	8.4	C	1, 18	E	2.9	10
3C 132	○	1	8.4	C?	1, 18	E		
3C 135	●	2	8.4	I	19	N		
3C 136.1		2	8.4	—		?		
3C 153	○○	1	8.4	S?	1	N		
3C 171	●●	1	8.1	S?	1	N	34.7	12
3C 173.1	●	1	8.4	G	1	E	1.2	10
3C 184.1	○	2	8.4	I/S	19, 18	N	97.0	10
3C 192	○	2	8.4	G	17, 18, 21	N	86.0	10
3C 197.1		3	8.4	G	3	E		
3C 219	●○	16	4.9	C	16	B	19.0	10
3C 223	○○	2	8.4	I	18	N	60.0	10
3C 223.1	○	3	8.4	I	18, 19	N		
3C 227		3	8.4	I	17	B	57.6	9, 13, 23
3C 234	●	1	8.4	G	1	N	308.0	10
3C 277.3	●	–	–	I	17	E		
3C 284		1	8.1	G?	1	N	17.0	10, 11
3C 285	●○	7	4.9	C?	7, 17	N	6.7	10
3C 300	●	1	8.1	G	1, 18	N	19.3	10, 11
3C 303	●	15	1.5	G?	18, 19	B	15.0	10
3C 319		1	8.4	G	1	E	<1.0	10
3C 321	●	–	–	I	17, 19, 21	N	120.0	10
3C 327	○○	2	8.4	—		N	53.2	9, 23
3C 349	○	1	8.4	S	1	N	4.7	10
3C 353	●●	8	8.4	C	8, 21	E	1.6	9, 23
3C 381		1	8.4	G	1	B	7.0	10, 14
3C 382	●	3	8.4	G	3, 18	B	130.0	10
3C 388	●○	5	4.9	C	10	E	2.1	10
3C 390.3	●○	4	8.4	G	17, 18, 19	B	430.0	10, 12
3C 401	●	1	8.4	C	1	E	2.5	10
3C 403	●	3	8.4	I	3	N	61.7	9, 23
3C 405	●●	6	4.5	C	22	N	210.0	12
3C 424	●	3	8.4	G?	19	E		
3C 430		–	–	—		E		
3C 433	●	3	8.4	G	3	N	3.6	14
3C 436	●	1	8.4	G	1	N	6.8	10
3C 438	●●	1	8.4	C	1	E	3.1	10
3C 445	●○	2	8.4	I?	17, 19	B	252.1	9
3C 452	●●	3	8.4	S?	18	N	16.9	10

Table 5.2 continues overleaf.

Table 5.2: continued from previous page.

References are as follows:
(1) this thesis, chapter 4, and references therein.
(2) Leahy *et al*. (1996) [L96].
(3) Black *et al*. (1992) [B92]; Black (1992).
(4) Jane Dennett-Thorpe, private communication.
(5) Roettiger *et al*. (1994).
(6) Perley, Dreher and Cowan (1984)
(7) van Breugel and Dey (1993).
(8) Swain, Bridle and Baum (1996).
(9) Tadhunter *et al*. (1993).
(10) Rawlings *et al*. (1989) and references therein.
(11) Jackson and Browne (1990).
(12) Baum and Heckman (1988).
(13) Prieto *et al*. (1994).
(14) McCarthy *et al*. (1995).
(15) Leahy and Perley (1991) [LP].
(16) Clarke *et al*. (1992).
(17) Prestage and Peacock (1988).
(18) Rawlings (1987).
(19) Allington-Smith *et al*. (1993).
(20) Burns and Gregory (1982).
(21) Longair and Seldner (1979).
(22) Carilli and Harris (1996) and references therein.
(23) Simpson *et al*. (1996).
(24) Fasano, Falomo and Scarpa (1996).

Information on jet detection is taken from L96 and chapter 4. A filled circle in column 2 indicates a definite jet and an open circle a possible jet. Cluster environments are classified as I (isolated), S (a few associated objects), G (a number of associated objects, but the source is not classified as a dominant galaxy) and C (the source is the dominant galaxy of a cluster). Line types are E (low-excitation), N (narrow-line radio galaxy) or B (broad-line radio galaxy). Emission line types are taken from LR or from the spectrophotometry of Laing (Laing *et al*. 1994: Laing, private communication) for sources in LRL. The non-LRL sources have been classified from the following literature: 3C 15, 3C 105, 3C 403, Tadhunter *et al*.(1993); 3C 111, Sargent (1977); 3C 135, 3C 445, Eracleous and Halpern (1994); 3C 227, 3C 327, 3C 353, Simpson *et al*. (1996); 3C 197.1, 3C 424 (tentatively), 3C 430, Smith, Spinrad and Smith (1976); 3C 223.1, Cohen and Osterbrock (1981); 3C 277.3, Yee and Oke (1978); 3C 405, Osterbrock and Miller (1975). 3C 136.1 has strong emission lines (Smith *et al*. 1976) but is not classified as broad or narrow-line. Cluster environment determination and [OIII] flux information are described in section 5.3. Line fluxes are measured in 10^{-18} W m^{-2}.

in the sources, as described below.

With the exceptions noted in individual tables, the fluxes given are taken from VLA maps, and are therefore subject to errors of a few per cent because of the limiting accuracy of the absolute calibration of the VLA. This error has not been included in the errors quoted.

For ease of tabulation, I have divided the jets, lobes and hot spots of each source into ‘north’ and ‘south’.

5.2.1 Total and lobe fluxes

A reliable measurement of the total flux of an object could be obtained from direct integration on low-resolution maps only if the object had been observed with sufficient short-baseline coverage to sample all the large-scale structure. This was true of all the objects observed in chapter 4, with the possible exception of 3C 132, but a number of the objects from the sample of B92 were undersampled due to insufficient observation or large angular size. In these cases (discussed in table 5.3) integrated fluxes from the literature or (as a last resort) from interpolation from other frequencies were used. Reliable fluxes of individual lobes are clearly only available for the well-sampled sources, and so these are only tabulated (table 5.4) where a good measurement was possible; even in these cases it was sometimes not easy to separate the two lobes, and so the errors on the quantities may be large. Largest angular sizes of the sources are measured directly from the maps, and the distance from the core to the most distant region of lobe emission was also always tabulated in order to define a measure of hot spot recession comparable with that of B94 — in the few ‘winged’ sources where the greatest distance or the largest angular size was in a direction transverse to the source axis, this is noted and an alternative distance given.

5.2.2 Cores

In general the radio nuclei of the objects in the sample were unresolved with the highest resolution of the VLA. The cores were therefore well fitted by an elliptical Gaussian plus baseline (using the AIPS task JMFIT) and the integrated flux was similar to the peak value. Hardly any of the cores were polarized at any significant level.

The measurements of the core fluxes given in table 5.3 are therefore the integrated fluxes fitted by JMFIT.[2] Errors in the core flux determination are the formal 1σ errors from the fitting routine, and as such are likely to be underestimates.

---

[2] Note that in chapter 4 the *peak* fluxes were used when measuring core fluxes: fluxes in this chapter are therefore slightly different from those quoted there.

Table 5.3: Basic measured quantities

Source	Frequency (GHz)	Total flux (Jy)	Error	Core flux (mJy)	Error
3C 15	8.35	1.00		27.99	0.05
3C 20	8.44	2.29		3.32	0.06
3C 79	8.44	0.694		6.04	0.01
3C 98	8.35	3.08	0.07	6.1	0.1
3C 105	8.35	1.68		18.9	0.5
4C 14.11	8.44	0.500		29.69	0.03
3C 111	8.35	4.8	0.2	1276	1
3C 123	8.44	9.44		108.9	0.3
3C 132	8.44	0.674		4.1	0.2
3C 135	8.35	0.520		1.0	0.2
3C 136.1	8.35	1.00	0.05	1.53	0.03
3C 153	8.44	0.712		< 0.5	
3C 171	8.06	0.690		2.0	0.1
3C 173.1	8.44	0.461		9.64	0.02
3C 184.1	8.35	0.785		6.0	0.5
3C 192	8.35	1.38	0.08	4.0	0.2
3C 197.1	8.35	0.320		6.0	0.1
3C 219	4.87	2.27	0.06	51.6	0.1
3C 223	8.35	0.89	0.05	8.5	0.2
3C 223.1	8.35	0.53	0.01	6.4	0.4
3C 227	8.35	2.05	0.04	13.2	0.6
3C 234	8.44	0.919		34.46	0.04
3C 284	8.06	0.340		2.79	0.02
3C 285	4.86	0.740		6.8	0.4
3C 300	8.06	0.645		6.2	0.1
3C 303	1.48	2.45		106.6	0.3
3C 319	8.44	0.362		< 0.3	
3C 327	8.35	2.01	0.05	25	1
3C 349	8.44	0.723		24.21	0.02
3C 353	8.44	14.1		151.0	0.2
3C 381	8.44	0.906		4.7	0.1
3C 382	8.35	1.30		251.2	0.1
3C 388	4.87	1.80		57.9	0.1
3C 390.3	8.35	2.8	0.1	733	5
3C 401	8.44	0.844		28.54	0.03
3C 403	8.35	1.50		7.1	0.2
3C 405	4.53	415		776	3
3C 424	8.35	0.357		7.0	0.3
3C 433	8.35	2.08		1.2	0.3
3C 436	8.44	0.592		17.90	0.02
3C 438	8.44	0.780		16.2	0.1
3C 445	8.40	1.34	0.08	83.9	0.4
3C 452	8.35	2.14		125.8	0.3

Table 5.3 continues overleaf.

Table 5.3: continued from previous page

The total fluxes for 3C 98, 3C 136.1, 3C 192, 3C 227, 3C 327 and 3C 445 are taken from the single-dish measurements of Stull (1971), as these sources were all seriously undersampled by the VLA observations. These fluxes are to be treated with caution. Stull's flux scale is not consistent with that of Baars *et al*. (1977), but the systematic error is much less than 1%. The random error due to the calibration process is tabulated above and is as given by Stull. In addition, the fluxes have not been corrected from 8.0 GHz to the VLA frequency, which makes them systematically high by up to 5%. The 5-GHz flux of 3C 219 is from Laing and Peacock (1980). The fluxes for 3C 223 and 3C 390.3 were interpolated from other frequencies, and the errors assigned to them are estimates of the error in the interpolation. Elsewhere errors are only assigned where the integration was problematic because of off-source noise, but the VLA calibration errors apply in addition to these and to any source with no error assigned. Noise or mild undersampling means that the fluxes of 3C 105, 3C 111, 3C 171, 3C 197.1, 3C 284 and 3C 382 may be too low. The flux of 3C 303 is taken from LP. The core fluxes of 4C 14.11, 3C 79, 3C 111 and 3C 390.3 are variable (see chapter 4, L96 and Leahy and Perley 1995). I took the southern component of 3C424's core to be the true core (*pace* B92).

5.2.3 Jets and counterjets

It is possible, as discussed in B94, to measure the flux of these in a number of different ways. Clearly a simple measurement of the flux of the jet region (as in B92) is not useful, even if the jet region is well defined, because of the necessity of correcting for background flux (particularly important in these objects where the jets have low contrast with the lobes). However, the jet region is not always well defined, particularly where the jet is entering a hot spot.

Because I would later be comparing my measurements with those of B94, I chose to extract jet flux from my maps in the same ways as they did. I measured total jet flux by taking three independent integrations around the area that clearly contained jet emission with the AIPS verb TVSTAT, correcting for the background flux by integrating a similarly-shaped area on either side and subtracting the average of these measurements, normalised to the area of the jet integration, from the value obtained by integrating over the jet. Errors are assigned by considering the standard deviation of the integrated and the normalising values, and combining the resulting errors in quadrature. It will be seen that where there is a substantial difference between the background fluxes on the two sides of the jet, this will dominate the error assigned.

I also measured straight jet flux; this quantity is important when considering relativistic beaming (see chapter 6). The straight jet region was defined, following B94, to be a rectangle over which the line of the jet deviates from the centerline of the rectangle by less than a jet radius and which avoids any significant confusion with lobe flux. (Thus, when the jet enters a hot spot or region of high surface brightness, the straight jet is considered to end.) Identically-sized rectangles on either side of the straight jet region were integrated to provide an estimate of the background flux. The same rectangular region on the other

Table 5.4: Fluxes and sizes of lobes

		North lobe			South lobe		
Source	Frequency (GHz)	Flux (Jy)	Error	Length (arcsec)	Flux (Jy)	Error	Length (arcsec)
3C 15	8.35	0.54	0.01	24.6	0.41	0.01	23.6
3C 20	8.44	1.23	0.02	27.2	1.06	0.02	28.7
3C 79	8.44	0.386		38.3	0.302		50.8
3C 98	8.35	1.67		138	1.44		178
3C 105	8.35	0.356		162	1.31		171
4C 14.11	8.44	0.231	0.005	58.6	0.239	0.005	57.5
3C 111	8.35	–		123	–		93.9
3C 123	8.44	3.31		19.2	6.02		17.6
3C 132	8.44	0.273	0.005	11.7	0.397	0.005	11.0
3C 135	8.35	0.186	0.005	78.8	0.337	0.005	51.7
3C 136.1	8.35	–		191	–		267
3C 153	8.44	0.355	0.002	4.3	0.356	0.002	4.8
3C 171	8.06	0.386		24.4	0.302		12.1
3C 173.1	8.44	0.201		27.2	0.250		33.4
3C 184.1	8.35	0.397	0.001	107	0.382	0.001	82.0
3C 192	8.35	–		109	–		93.0
3C 197.1	8.35	0.147	0.005	16.0	0.170	0.005	11.6
3C 219	4.87	–		97.8	–		92.1
3C 223	8.35	0.440		156	0.320		152
3C 223.1	8.35	0.180		81.0	0.215		60.0
3C 227	8.35	1.03		113	0.660		121
3C 234	8.44	0.334	0.005	64.6	0.551	0.005	48.0
3C 284	8.06	0.152	0.003	106	0.185	0.003	72.6
3C 285	4.86	0.408		87.0	0.325		103
3C 300	8.06	0.154	0.005	70.2	0.485	0.005	31.8
3C 303	1.48	1.90	0.02	27.8	0.40	0.01	20.8
3C 319	8.44	0.25	0.01	48.9	0.12	0.01	57.9
3C 327	8.35	–		199	–		108
3C 349	8.44	0.269	0.008	41.7	0.430	0.008	44.2
3C 353	8.44	8.5	0.1	142	5.5	0.1	142
3C 381	8.44	0.570		33.2	0.331		40.0
3C 382	8.35	0.790		87.9	0.580		91.0
3C 388	4.87	0.869		27.9	0.873		22.5
3C 390.3	8.35	–		132	–		92.0
3C 401	8.44	0.348	0.005	10.7	0.467	0.005	12.9
3C 403	8.35	–		95.0	–		116
3C 405	4.53	205		70.6	209		60.6
3C 424	8.35	0.120	0.005	13.0	0.230	0.005	21.0
3C 433	8.35	0.237	0.005	41.0	1.84	0.01	32.5
3C 436	8.44	0.27	0.01	59.2	0.30	0.01	49.6
3C 438	8.44	0.368	0.005	11.9	0.397	0.005	10.8
3C 445	8.40	–		299	–		280
3C 452	8.35	0.940		141	1.07		135

Table 5.4 continues overleaf.

Table 5.4: continued from previous page.

Fluxes are listed only where maps were available to me that appeared to reproduce the large-scale structure well. Errors have been assigned where there was some difficulty in separating the north and south lobes, and so where some flux might be assigned to either; the errors are rough estimates of the variation over multiple attempts at integration. These are in addition to the errors due to VLA flux calibration, which apply to all the measurements. Lengths are measured from the core to the most distant visible region of emission. In several cases these lengths are substantially away from the source axis: these, with their on-axis lengths, are 3C 105N (156 arcsec), 3C 171N (5.0) and S (4.8), 3C 197.1N (7), 3C 300S (30), 3C 403N (55.5) and S (52.8) and 3C 433N (24.6).

side of the core was integrated to provide an estimate of the flux from the counterjet, if present, or an estimated limit on its flux if not (if the central value was higher than the values on either side, their average was subtracted; if not, the modulus of the difference between the lower value and the central value was used as an upper limit). As for the total jet fluxes, three measurements were made on each source and averages taken; errors were assigned in the same way as for the total jet fluxes. The rectangle was generally taken from the core to the furthest extent of the straight jet, even where the straight jet was only visible in part of the lobe, to maximise the chances of a counterjet detection. (It may be noted in passing that most of the objects with well-defined counterjets had an angle of not quite 180° between jet and counterjet; counterjet measurements of this sort can thus underestimate the counterjet flux. On the other hand, the counterjet rectangle can intersect confusing flux in the counterjet lobe, and therefore seriously overestimate the counterjet flux. These results should be treated with some caution, therefore.)

All the errors on the jet flux determinations are conservative, because of the difficulty in deciding which parts of the object should be treated as a jet or counterjet. In a few cases interpretation is crucial, including

- 3C 192: I have only counted the jet seen near the S hot spot complex in the high resolution maps of L96. The inclusion of the faint linear feature seen in the S lobe at low resolution — which is not clearly aligned either with the core or with the hot spots — would increase the jet flux substantially and provide a real straight jet.
- 3C 234: I have only counted the jet leading into the northern hot spot. If the ridge E1 were included (as it is in the straight jet flux determination) the integrated jet flux would be substantially higher.
- 3C 300: It is not clear how much of this object's north lobe should be classed as a jet. I omitted the last few arcseconds where there is no surrounding lobe emission. The flux might be increased by up to 15 mJy if this region were included.
- 3C 327: I have differed from L96 in counting the faint linear features in both lobes as possible jets. If only the jet candidate around the core is integrated, the flux is around 0.4 mJy.

Table 5.5: Fluxes and lengths of jets

		North jet			South jet		
Source	Freq. (GHz)	Flux (mJy)	Error	Length	Flux (mJy)	Error	Length
3C 15	8.35	210	10	9.50	3.6	0.9	6.20
3C 20	8.44	23	6	18.3	*3.7	0.9	6.80
3C 79	8.44	< 3.8			< 1.3		
3C 98	8.35	90	20	121	< 0.79		
3C 105	8.35	< 8.3			*40	10	17.2
4C 14.11	8.44	< 2.5			1.9	0.3	2.80
3C 111	8.35	100	10	114	< 2.8		
3C 123	8.44	< 2.1			< 30		
3C 132	8.44	< 7.2			*3	2	5.97
3C 135	8.35	< 3			3.1	0.4	21.4
3C 136.1	8.35	< 2.6			< 2.7		
3C 153	8.44	*1.9	0.6	1.20	*13	2	1.40
3C 171	8.06	15	1	3.80	6.3	0.9	3.50
3C 173.1	8.44	2.4	0.8	10.2	< 2.4		
3C 184.1	8.35	*14	3	32.2	< 1.3		
3C 192	8.35	< 3.2			*8	1	13.9
3C 197.1	8.35	< 1.9			< 0.85		
3C 219	4.87	*2.09	0.09	1.40	56.1	0.5	16.5
3C 223	8.35	*8	2	29.4	*5	9	42.0
3C 223.1	8.35	*2.5	0.7	19.2	< 7.7		
3C 227	8.35	< 15			< 27		
3C 234	8.44	3	2	6.20	< 2.3		
3C 284	8.06	< 2.8			< 6.6		
3C 285	4.86	36	7	74.6	< 2.1		
3C 300	8.06	38	4	62.6	< 1.7		
3C 303	1.48	66	4	14.2	< 7.4		
3C 319	8.44	< 0.12			< 1.8		
3C 327	8.35	*11	3	107	*11	3	60.4
3C 349	8.44	< 2.1			*0.24	0.04	1.10
3C 353	8.44	90	10	71.0	30	8	37.0
3C 381	8.44	< 2.9			< 1.3		
3C 382	8.35	31	2	77.9	< 0.14		
3C 388	4.87	*10	2	4.58	49	8	12.7
3C 390.3	8.35	34	5	81.3	*2	1	21.0
3C 401	8.44	< 4			114	9	5.85
3C 403	8.35	7.8	0.6	24.0	–		–
3C 405	4.53	2300	300	50.3	380	40	24.1
3C 424	8.35	< 11			15	1	3.04
3C 433	8.35	47	9	24.1	< 1.4		
3C 436	8.44	< 0.51			19	3	38.8
3C 438	8.44	43	9	8.90	40	3	7.40
3C 445	8.40	*1.3	0.3	5.60	10.3	0.7	60.0
3C 452	8.35	16	3	95.4	31	7	108

Fluxes of jets classed as ‘possible’ in table 5.2 are marked with an asterisk.

Table 5.6: Fluxes and lengths of straight jets

		North straight jet		South straight jet		
Source	Freq. (GHz)	Flux (mJy)	Error	Flux (mJy)	Error	Length
3C 15	8.35	96	3	< 1.4		4.17
3C 20	8.44	7	5	* < 9		12.4
3C 79	8.44	–		–		
3C 98	8.35	50	20	< 13		101
3C 105	8.35	–		–		
4C 14.11	8.44	< 0.45		1.14	0.04	15.0
3C 111	8.35	90	20	< 58		101
3C 123	8.44	–		–		
3C 132	8.44	< 13		*2	3	5.00
3C 135	8.35	< 1.6		10	4	30.2
3C 136.1	8.35	–		–		
3C 153	8.44	*8	1	*13	5	1.70
3C 171	8.06	6.0	0.7	6.3	0.8	3.07
3C 173.1	8.44	2.1	0.9	< 0.29		11.2
3C 184.1	8.35	–		–		
3C 192	8.35	–		–		
3C 197.1	8.35	–		–		
3C 219	4.87	*56.5	0.3	2.1	0.1	17.1
3C 223	8.35	*11	4	* < 5.8		34.1
3C 223.1	8.35	*3	1	< 21		21.9
3C 227	8.35	–		–		
3C 234	8.44	10	8	< 19		59.1
3C 284	8.06	–		–		
3C 285	4.86	19	2	< 14		51.6
3C 300	8.06	2.4	0.2	< 0.23		4.70
3C 303	1.48	63	5	< 13		12.3
3C 319	8.44	–		–		
3C 327	8.35	*16	6	* < 140		119
3C 349	8.44	< 0.053		*0.31	0.04	1.27
3C 353	8.44	70	10	< 34		66.5
3C 381	8.44	–		–		
3C 382	8.35	14	1	< 1.1		48.3
3C 388	4.87	*30	5	34	6	8.40
3C 390.3	8.35	20	10	* < 650		88.6
3C 401	8.44	< 5.7		33.8	0.4	5.67
3C 403	8.35	6	1	< 3.8		19.6
3C 405	4.53	1200	600	500	800	40.8
3C 424	8.35	< 8.4		16.7	0.9	2.99
3C 433	8.35	9.8	0.1	< 8.3		4.43
3C 436	8.44	< 0.27		3.8	0.8	20.2
3C 438	8.44	40	4	< 9.8		8.67
3C 445	8.40	* < 1.9		14	3	78.1
3C 452	8.35	9	2	13	2	46.4

Fluxes of jets classed as ‘possible’ in table 5.2 are marked with an asterisk.

- 3C 390.3: I only count material closer to the core than knot B of Leahy and Perley (1995), on the grounds that knot B is the primary hot spot.
- 3C 403: I only count the regions F7, F8 of B92 as true jet, on the grounds that F6 is the primary hot spot. Counting F6 and the jet-like components F4 and F5 would increase the flux to 80 mJy.
- 3C 424: I have not counted the northern 'jet' of this object as a true jet. It is quite possible that some of the internal structure in this northern component should be treated as jet material, however. I have treated S3 as the only jet component in the southern lobe. The reasons for this treatment are discussed in L96.

Where even the most tentative jet or counterjet candidate is detected, I have chosen to record its flux. (Fluxes of 'possible' jets are marked as such in table 5.5.) Where there was no detection of any sort, I have tried to determine an upper limit on the flux of a present but undetected jet. There is no way in which a truly conservative upper limit can be set on flux from an unseen jet, given the number of possible forms that jets can take, but some reasonable approximations can be made to a plausible limit which most unseen jets will not exceed. For compatibility with the limits put on straight jets (and thus with the measurements of B94) I defined total jet limits in a similar way. On maps of intermediate resolution I integrated over the rectangle two beamwidths wide between the core and the primary hot spot (chosen as the most plausible path for a jet) or the closest approach which did not intersect bright confusing lobe emission, and over the two rectangles on either side of it. If the flux in the central rectangle was larger than that in the other two, I subtracted the mean flux of the edge rectangles from that of the central one and used the result as an upper limit. Otherwise, I used the modulus of the difference between the central flux and the lower of the two edge fluxes as the upper limit. This way of assessing the upper limits has the advantages that the number obtained increases with the inhomogeneity of the lobe (the correct behaviour, since jets are hidden by confusing lobe structure as much as by on-source noise), and that when measured on a lobe that *does* have a jet the upper limit is a reasonable measure of the jet's true flux. The limits obtained can be used when a limit is needed on either total jet flux or straight jet flux. The obvious disadvantage of this method is that it is patently resolution- and sensitivity-dependent, and that a subjective decision must be taken to make the measurements from a particular map; where only low-resolution maps were available to me, the limits are higher.

5.2.4 Hot spots

As described in section 1.4.3, I attempt to identify a 'primary' hot spot in each lobe. Measurements are made only of these components, which are identified where there might be ambiguity.

B94 measure the fluxes and dimensions of the hot spots in their quasar sample by fitting with a Gaussian

Table 5.7: Fluxes and sizes of hot spots

		North hot spot					South hot spot				
Source	Freq. (GHz)	Flux (mJy)	Error	θ_{maj}	θ_{min}	Dist.	Flux (mJy)	Error	θ_{maj}	θ_{min}	Dist.
3C 15	8.35	–		–	–	–	*5	1	1.5	1.0	18.2
3C 20	8.44	160	10	0.21	0.16	24.1	89	2	0.22	0.18	23.3
3C 79	8.44	4	1	0.21	0.08	36.8	15	2	0.53	0.34	50.4
3C 98	8.35	*40	10	4.1	3.4	132	27	5	3.9	2.0	155
3C 105	8.35	3.2	0.6	1.7	0.80	155	110	5	0.28	0.20	171
4C 14.11	8.44	1.7	0.5	1.2	0.10	58.1	3.3	0.1	0.29	0.09	36.4
3C 111	8.35	300	10	1.3	0.70	123	76	1	1.9	1.1	74.1
3C 123	8.44	21	2	0.15	0.08	7.3	162	5	0.11	0.08	7.9
3C 132	8.44	53	1	0.19	0.15	11.3	22	4	0.40	0.25	10.9
3C 135	8.35	1.7	0.2	0.55	0.25	72.3	*77	5	4.6	1.7	45.0
3C 136.1	8.35	*56	8	20	10	173	*23	5	12	12	255
3C 153	8.44	133	2	0.19	0.08	2.4	87	1	0.11	0.07	4.8
3C 171	8.06	120	10	0.27	0.07	4.9	95	2	0.29	0.19	4.6
3C 173.1	8.44	8.3	0.3	0.47	0.18	26.4	10	2	0.50	0.25	31.9
3C 184.1	8.35	*7	2	2.6	1.0	103	19	1	0.95	0.50	78.2
3C 192	8.35	*80	20	4.0	3.0	103	2.0	0.2	1.2	0.90	88.5
3C 197.1	8.35	3.4	0.1	0.33	0.30	6.8	8.5	0.5	0.75	0.35	9.6
3C 219	4.87	2.9	0.2	0.99	0.36	72.6	76	1	3.2	1.6	73.1
3C 223	8.35	10	1	3.5	1.3	140	*6	2	6.0	2.0	147
3C 223.1	8.35	*14	4	2.0	0.80	40.3	13	1	0.90	0.40	38.5
3C 227	8.35	17	1	0.90	0.60	108	*7	1	1.0	0.50	109
3C 234	8.44	55.8	0.1	0.51	0.20	63.9	50	10	0.73	0.35	47.4
3C 284	8.06	*6	2	1.5	0.75	104	27	2	0.76	0.57	72.4
3C 285	4.86	*4	1	3.0	2.0	78.8	*4	1	9.0	7.0	92.5
3C 300	8.06	*1.0	0.5	0.30	0.30	69.7	29	1	0.44	0.26	29.3
3C 303	1.48	650	10	$<$ 1.7	1.1	16.9	5.0	0.5	0.90	0.50	16.9
3C 319	8.44	19	3	1.4	0.90	47.7	–		–	–	–
3C 327	8.35	3.5	0.2	0.40	0.30	182	20	1	1.0	0.35	99.1
3C 349	8.44	*4	1	0.50	0.30	40.3	90	5	0.65	0.47	42.9
3C 353	8.44	*70	10	4.5	2.5	94.4	63	2	3.2	1.8	123
3C 381	8.44	9	1	0.20	0.17	32.5	*7	2	0.80	0.40	35.5
3C 382	8.35	45	5	2.2	2.0	86.5	*8	2	2.3	2.1	82.4
3C 388	4.87	40	10	2.8	1.6	15.9	55	2	1.2	0.90	16.4
3C 390.3	8.35	67	2	2.5	1.2	104	450	20	4.1	2.0	88.4
3C 401	8.44	*5	2	0.50	0.50	8.8	*4	2	0.60	0.20	12.3
3C 403	8.35	30	1	0.40	0.21	28.5	*20	10	4.0	0.90	47.8
3C 405	4.53	3060	20	0.61	0.35	63.2	2320	50	1.0	0.47	53.1
3C 424	8.35	2.7	0.2	0.20	0.15	8.7	24	2	0.50	0.20	4.2
3C 433	8.35	–		–	–	–	*6	2	0.65	0.55	0.0
3C 436	8.44	*2	1	2.2	1.0	57.4	11	1	0.34	0.21	43.5
3C 438	8.44	*4	2	0.30	0.10	11.4	*2	1	0.30	0.10	8.9
3C 445	8.40	43	2	2.2	1.0	291	60	10	3.7	1.4	275
3C 452	8.35	*20	10	3.5	1.2	130	31	1	1.0	0.84	126

Table 5.7 continues overleaf .

Table 5.7: continued from previous page.

All distances in arcseconds. ‘Dist.’ is the distance between the hot spot and the core. Fluxes marked with an asterisk, and their associated major and minor axes ($\theta_{\rm maj}$ and $\theta_{\rm min}$), were measured by integration rather than by Gaussian fitting. In several cases it was not clear which object was the primary; in these cases fits were made to each candidate component and the results for the most compact components were used here. The relevant objects are 3C 173.1N (N4 was used rather than N3), 3C 227N (F1a of B92 was used) 3C 285N (southern candidate object was preferred), 3C 300S (E2 was used rather than E3) and 3C 403N (F6 of B92 was taken to be the primary rather than F1).

and baseline. They remark that such models do not always represent the hot spots well, and the situation is still more difficult in the present sample with its considerably higher spatial resolution and with a more relaxed definition of the term ‘hot spot’. The procedure I have adopted is as follows, therefore: I have tried to fit models consisting of a Gaussian and baseline to all but the most obviously resolved hot spots, running the fitting routine a number of different times on slightly different regions or with slightly different initial guesses. Where these different fits gave essentially the same results, I have tabulated (in table 5.7) the average values of the integrated fluxes and major and minor axis lengths, with an estimate of the error on the fluxes (which may be taken as an indication of the likely error of the axes) derived from the range of the results of different measurements. Where the fits were obviously poor, and diverged significantly (say, by a factor of 1.5 in flux either way) on small alterations of the initial parameters of the fitting routine, I measured the sizes of the components by taking slices through them and estimating the FWHM, or in extremely resolved cases by simple measurement from maps; I measured the fluxes by integration from the maps, with a rough correction for background flux from integration over a nearby part of the lobe. The errors in the derived hot spot fluxes in these cases are an estimate of the error from direct integration, taking into account the difficulty of deciding exactly which was the hot spot region.

The distances of the hot spots from the cores are also tabulated.

5.3 Environmental indicators

For each source, where the information was available in the literature, I have tabulated the flux of the nuclear [OIII]λ5007,4959 lines (hereafter [OIII]) and an indication of the cluster environment. I have chosen to use the [OIII] doublet because measurements of its strength, or that of the [OIII]λ5007 line, are widely available in the literature; the suitability of the line as a measurement of AGN activity will be discussed in chapter 6. Where only the luminosity or intensity of the [OIII]λ5007 line was available, I scaled the measurement by 4/3 (following Rawlings *et al*. 1989). In a few cases, marked as such in the table, two or more independent measurements of the [OIII] flux existed in the literature; I normally used the mean value as a best guess (the one exception being 3C 381 where the measurement of McCarthy *et al*. (1995) is clearly contaminated by the bright extended emission line region). The measurements were seldom significantly different from one another.

A quantitative measure of the cluster environment must be derived from systematic counting of the local galaxy population from optical plates or sensitive X-ray observations, or both. This is not generally available. Even a simple qualitative classification will be useful in what follows, however, and so in table 5.2 I have classified the environment of each object for which information was available to me as described in the notes to that table. Where local galaxy population counts or cross-correlation amplitudes were available, principally for the lower-redshift objects in the sample (Longair and Seldner 1979; Eales 1985b; Prestage and Peacock 1988; Allington-Smith *et al*. 1993; Harvanek, private communication) I used a large excess in the statistics as an indication of cluster membership and a large deficit as an indication of isolation; intermediate values of B_{gg}, the cross-correlation amplitude, appeared to be consistent with membership of a small group of galaxies. In a few cases these statistics are misleading because the radio source is projected on to an unrelated cluster. At higher redshifts I used the results of Rawlings (1987), who classified galaxies in a similar way from optical plates, and classifications of individual objects from the literature described in chapter 4. In chapter 6 these classifications will be used to point out some simple trends in radio galaxy properties.

Chapter 6

Discussion

In this chapter I discuss trends in the sample of 50 sources described in chapter 5 (particularly those for which good images were available to me), and their implications for the physics of radio sources as a whole.

I first discuss unified models (section 1.6.6) in the context of this low-redshift sample, and outline the expected relationships between observed quantities in the standard model for radio sources. I go on to point out some general trends in the properties of the lobes, hot spots, jets and cores in the combined sample, and their relations to one another, re-analysing some of the trends discussed in Black (1992). I then discuss the application to this sample of other indicators of jet power. Using Monte Carlo methods, I address the question of whether the standard models can be said to work in this sample of objects, and deduce some physical parameters of the sources. Finally I outline the implications of my results.

The high-frequency fluxes I use in plots in this chapter have all been 'corrected' to an observing frequency of 8.4 GHz for ease of comparison, unless otherwise specified. Cores are assumed to have flat spectra ($\alpha = 0$) and jets to have $\alpha = 0.8$. Total fluxes are scaled using the *low-frequency* spectral index, because this was easily available for the whole sample. Errors in these corrections should not badly affect the results of the analysis performed here.

Colours in the plots on pages 202 – 217 distinguish low-excitation sources (green), narrow-line radio galaxies (dark blue), broad-line radio galaxies (light blue) and quasars (red). The one unclassified object, 3C 136.1, is plotted in black and is not included with any class of object where the objects are separated by emission-line class.

Throughout, the subscript c denotes a quantity relating to the radio core and j one relating to the jet or beam.

6.1 Unified models at $z < 0.3$

In section 1.6.6 I discussed the problems of unified models at low redshifts. If unified models are correct, the absence of quasars from the sample discussed here implies the presence in it of other objects aligned at a small angle to the line of sight which should be detectable by anisotropic optical and radio emission. Barthel (1989) believed the broad-line radio galaxies to be intermediate between quasars and radio galaxies, which may be true in some cases (e.g. 3C 234); but in this sample at least it seems more likely that some or all of the objects classed as BLRG are true quasars whose optical continuum is insufficiently bright for them to be classed as such optically.[1]

However, the situation is rendered more complicated by the low-excitation galaxies. If, as discussed in section 1.6.6, these appear optically identical no matter what their angle to the line of sight, then they will certainly confuse any attempt to analyse orientation effects from radio data (Barthel 1994) unless they are treated separately. If this is done carefully they should be able to provide a valuable population for comparison with BLRG and NLRG, provided no other effects are present. However, I shall show that other effects do appear to be present in the sample discussed here.

In what follows I will therefore discuss the overall properties of the sample with the emission-line classifications of the sources in mind. I will compare the properties of this sample with those of others, particularly the high-resolution images of quasars in B94; the place of these objects in unified models should be borne in mind.

In the present sample there are 15 low-excitation objects, 9 BLRG and 25 NLRG. If the low-excitation objects are discarded, the proportion of BLRG to NLRG is consistent with the critical angle of 40–50° of Barthel (1989).

6.2 Beam power and the standard model

It has been suggested that the most fundamental measure of the power of a radio source is the energy supplied to its beam (or beams), usually called the beam power. If unified schemes are correct and line

---

[1] It is important to realise that classifications in terms of broad or narrow lines are dependent on high-quality spectra which are not in general available for this sample. Laing *et al.* (1994) have shown that the classifications can change significantly with improved observations. The classifications used here must be viewed as best guesses only.

luminosity is a good measure of the beam power, as suggested by Rawlings and Saunders (1991) (see also sections 1.5.3 and 6.7.1) then an ideal source at an angle θ to the line of sight and with beam power Q (constant over the source lifetime) should have the following properties:

1. Forbidden line power $\propto Q$
2. Observed core power $\mathcal{P}_c \propto Q$ but also depending on θ and the bulk velocity in the central regions of the source, β_c.
3. Observed jet power *per unit length* $\mathcal{P}_j \propto Q$ but also depending on θ and the bulk velocity on kpc scales, β_j. (I assume that the beam is efficient enough that only a small amount of its power is radiated on the way to the hotspots. Lengths measured on the sky must be corrected for a projection factor.)
4. Jet-counterjet ratio (sidedness) depending on θ and β_j.
5. Total intensity at low frequencies (or, equivalently, total extended flux) depending on Q but also on environment and source age.

This assumes that beam efficiency is similar in all sources on both kpc- and sub-kpc scales. (The model is unaffected if beam efficiency is different on sub-kpc (core) scales than on kpc scales, though this is largely a matter of conjecture as good VLBI information is sparse; it *is* affected if the efficiency of the beam or the bulk velocity of the emitting material varies significantly over the length of the source, but observations do not seem to reveal any trend in jet surface brightness with length.)

The predictions of this model will be tested in what follows.

6.3 Large-scale structure

Figure 6.11 shows the power-linear size diagram for the whole sample. The sources populate a range of two decades in luminosity, if the brightest objects (Cygnus A, 3C 123 and 3C 438) are not counted, and approximately 1.5 decades in linear size (the upper limit in this plot is due to the exclusion of the giants; the lower limit is due to the absence of compact sources from LRL at low redshifts).

It will be seen that there is a tendency for the low-excitation sources to be smaller, made clearer on a histogram of linear sizes (figure 6.12); the distribution of linear sizes of these objects is strongly peaked around the 100-kpc range. I will return to this initially surprising fact, first noted by Black (1992) for his sub-sample of these objects, in a later section. The distribution of linear sizes of BLRG does not appear significantly different from those of NLRG, although the mean is somewhat smaller. The absence of the giant sources is probably important here (though some of these are low-excitation objects: Laing *et al*. 1994). In the larger and higher-power sample of Laing *et al*. (1994) the broad-line objects are significantly smaller.

6.4 Hot spots

There is a strong positive correlation, with slope approximately unity, between source linear size and hot spot size in the 43 sources in the sample with measured hot spots (figure 6.13). (Hot spot size is defined here as the average of the sizes of the two hot spots at either end; the size of an individual hot spot is defined as the geometric mean of the largest and smallest angular sizes). It is dangerous to compare the sizes of hot spots in different objects, because they have been measured from maps of differing resolution; objects of large angular size are more likely to have been mapped at lower resolution in this sample. However, since this correlation is present even when considering only those measurements made from maps of ~ 0.23 arcsec resolution, it is not entirely fictitious. It may provide some support for suggestions in L89 and B94 that the hot spot sizes scale with source linear size. Black (1992) found no such correlation in the sub-sample of these objects that he analysed. If the correlation is real, it may imply that the beam is not pressure-confined over all of its length, or it may be evidence for 'tired jet' models in which the jet decelerates with distance from the core (B94).

Comparing the sizes of hot spots within a single source is less dangerous. Of the 32 sources with detected jets or possible jets and measurements of hot spot size, 24 had hot spots that differed in area by more than 25%. Of these 15 (62%) had the brighter or only jet pointing towards the more compact hot spot. This lack of a significant trend contrasts with the results of B94 who found that the jets in their sample of quasars universally pointed towards the more compact hot spots where the hot spots were significantly different in size. They also found a dependence of hot spot size ratio on core power which is absent in this sample. B94 also found a trend for the hot spot on the jetted side to be more recessed (where recession is measured by the ratio of the core-hot spot distance to the lobe length) but the jetted hot spot was *less* recessed in 21 (65%) of the 32 sources in the present sample, a marginally significant trend.

22 sources in the present sample had one hot spot brighter than the other within the errors assigned. The brighter or only jet pointed towards the dimmer hot spot in 7 cases and towards the brighter in 15 (68%) — a marginally significant trend. This may be contrasted with the results of L89, who found that 26/30 sources with jets had the jet pointing towards the brighter hot spot in a sample of powerful radio galaxies and quasars. It would appear that all the trends relating to hot spots are weaker, if present at all, in this sample than in high-redshift samples containing quasars. This is understandable if the trends in the B94 sample are due to relativistic effects (as suggested by theory; e.g. Komissarov and Falle 1996), since at

least some of the objects studied here cannot be strongly beamed towards us.

Best *et al*. (1995) have analysed the hot spot separation ratios of a large sample of FRII radio sources (with some overlap with the present sample, but including many high-power sources), showing that there are significant differences between the distributions of radio galaxies and quasars. The quasars are more asymmetrical. They attribute this to mildly relativistic hot spot advance speeds. They concluded that in the low-redshift régime there was no difference between the distributions of broad- and narrow-line radio galaxies, but were unable to test whether the low-excitation objects formed a distinct population. In figure 6.14 I show a histogram of the fractional separation difference x ($x = (\theta_1 - \theta_2)/(\theta_1 + \theta_2)$, where θ_1 and θ_2 are the lengths of the longer and shorter lobe respectively) for the 41 objects in this sample with measured hot spot positions. It will be seen that the distributions are not markedly different for the NLRG and the low-excitation objects, and a Mann-Whitney U-test finds no significant probability that the two are drawn from different distributions. The broad-line objects appear *more* symmetrically distributed than the narrow-line objects (a result significant at the 97% level on a Mann-Whitney U-test), but this is strongly dependent on the positions of a few objects. These results are both rather surprising; in the simple models outlined above we would expect BLRG and low-excitation objects to be more asymmetrical than the NLRG, because of their smaller mean angle to the line of sight. This may be evidence that in this comparatively low-redshift and low-power régime environmental effects on source symmetry are dominant over light travel time (see also section 1.6.5).

6.5 Jets

There appears to be no dependence of jet detectability on luminosity over the luminosity range studied here, as shown in figure 6.15, a plot of jet prominence against luminosity for the 43 sources with measured jets or possible jets or upper limits. (The prominence of a component is the ratio of its background-subtracted flux to the total *extended* flux of the source, i.e. with core and jets subtracted.) In all but the most extreme cases jets have less than 6% of the extended flux of the source, and the typical value is nearer to 1%. In the sample as a whole 29/50 (58%) of objects have definite jet detections and 40/50 (80%) have possible or definite jets.

Jets are one-sided. In the sample as a whole 16 objects (32%) have possible counterjet detections, but only 6 (12%) have definite detections, and these include the unusual objects 3C 15, 3C 171 and 3C 438, together with the two bright, deeply imaged objects 3C 405 and 3C 353. The counterjet candidate detection fraction is thus below that of B94 in their sample of quasars (54% have counterjet candidates), which is a surprising result in the context of unified models.

In the only independent search for jets recently conducted, Fernini *et al*. (1993) imaged a sub-sample of five objects with powers matched to those of the B94 quasars, and found only one definite jet (but three possible jets). Because of the higher redshift of these objects and the lower angular resolution of the observations, the spatial resolution in this study was lower by a factor 2, although the sensitivity should have been comparable to that of my observations. Too much should not be read into the differing jet detection fractions; one further jet detection, in their sample of five objects, would bring their fractions broadly into line with those in the present study.

Perhaps surprisingly, the jet detection fraction is not very different in the different classes of object studied here. Of the 15 low-excitation objects, 9 (56%) have definite jets and 11 (73%) have possible or definite jets. For the 9 BLRG, the figures are 7 (78%) with definite jets and the same number with definite or possible. The 25 NLRG have 13 definite jets (52%) and 22 definite or possible (88%). It is perhaps unexpected, if the BLRG are thought to be quasar counterparts, that there should be two (3C 227 and 3C 381) with no indication of a jet — compare the universal jet detection in the B94 quasars. Several of the BLRG that do have jets are very similar in appearance to the quasars, on the other hand. Laing *et al*. (1994) found a much more marked difference between the jet detection fractions of broad-line objects and NLRG in their higher-power sample. In the present sample the jets of the BLRG, when detected, are at the higher end of the prominence range, but not sufficiently high to explain the results of Laing *et al*. simply as an effect of poorer observation; this raises the possibility that the dispersion in prominence is higher at higher powers.

Black (1992) noted a tendency for jets to be detected in shorter objects. In the present sample 19 of the 29 sources (66%) with definite detected jets, but only 24 of the 40 sources with definite or possible jets (60%), have linear sizes less than 400 kpc; these results are weaker than those of Black (1992), probably because of the detection or possible detection of a number of faint jets in larger sources. It can be seen from figure 6.16 that there is a weak trend for jet prominence to be related to length, entirely because of the existence of a number of short, low-excitation objects with bright jets.

There is no tendency for the brighter or only jet to lie in the longer lobe (17/32). (In naïve relativistic beaming/light travel time models, the lobe pointing towards the observer would have the brighter jet and appear longer.) In the cases where jet and lobe measurements were available, the brighter or only jet lay in the brighter lobe (after hot spot and jet flux had been subtracted) in 16/25 objects (64%). This result, though not statistically significant, may be a weak indication of some relationship between jet and secondary hot spot structure.

6.6 Cores

The prominences of radio cores are a commonly used orientation indicator in studies of beaming in radio galaxies and quasars (e.g. Orr and Browne 1982). Figure 6.17(a) shows a plot of core prominence against radio luminosity for the 43 objects in the present sample with measured fluxes (note that this includes two upper limits, 3C 153 and 3C 319). Figure 6.17(b) shows the quasars of B94 on the same plot. Various authors (e.g. Kapahi and Murphy 1993; Laing *et al*. 1994; Morganti *et al*. 1995) have attempted to show consistency between the distribution of core prominences and unified schemes. The present sample appears to be consistent with the predictions of the simple unified models discussed above, in that the BLRG tend to have brighter cores than the NLRG (the arithmetic mean core prominence is greater by more than a factor 10) and that the BLRG are comparable in core prominence to the B94 quasars. Note that the core prominences for both broad-line and narrow-line objects have a scatter of 2–2.5 orders of magnitude. The low-excitation objects have a less broad distribution in core prominence (a result noticeably different from that of Laing *et al*. 1994) and have a mean intermediate between the broad- and narrow-line objects (as in Laing *et al*. 1994). In the simplest versions of unified models we might expect their core prominences to be distributed like those of the broad- and narrow-line objects combined, which is clearly not the case in this sample.

If we believe that the core is a beamed parsec-scale jet (as suggested by VLBI observations) and that the one-sidedness of jets is a relativistic effect, there should in principle be a relationship between the prominence of jet and core (see section 6.2). The formula for Doppler boosting of a feature with velocity $v = \beta c$ and Lorentz factor $\gamma = (1-\beta^2)^{-\frac{1}{2}}$ is

$$S_{obs} = S_{rest}[\gamma(1-\beta\cos\theta)]^{-(m+\alpha)} \tag{6.1}$$

(Ryle and Longair 1967) where θ is the angle made with the line of sight, α is the spectral index, and m is a constant reflecting the geometry of the beamed component — $m = 2$ will be used for jets. In general, the velocity in the core may not be equal to that in the kiloparsec-scale jet, and so the slope of a jet-core prominence relation will not be unity. B94 investigate the relation between core and jet prominence for their sample of quasars, and conclude that there is deceleration between the parsec- and kiloparsec- scales.

Figure 6.18(a) shows a plot of total jet prominence against core prominence for the present sample. There is not much difference between the jet prominences of the BLRG and NLRG; although the BLRG perhaps have slightly more prominent jets than the NLRG average, the difference is not significant. (I note in passing that the two BLRG with the weakest cores are those without detected jets.) Figure 6.18(b) shows the same figure with the B94 quasars added. The quasars have much more prominent jets than either the BLRG or the NLRG, though they include objects such as 3C 9 which are almost entirely jet. The most prominent jets in the radio-galaxy sample are those of the low-excitation objects 3C 15, 3C 401, 3C 424 and 3C 438, closely followed by 3C 388.

B94 chose to investigate the relationship between the core and *straight* jet prominence. They point out, correctly, that a well-defined relationship between the core and jet beaming factors only occurs when the two are at the same angle to the line of sight. As soon as the jet is seen to bend, the emission is beamed differently and the simple relationship is lost. This could be used to explain the absence of a strong relationship in the plots of figure 6.18.

In figure 6.19 I plot the relationships between (brighter) straight jet and core prominence for the present sample and for the quasars of B94. Unlike them, I have made no attempt to assign some of the flux from the core to the straight jet, as I have little information on the VLBI properties of the radio galaxies. This weakens the correlation observed by B94 for their sample, though it is still significant at the 90% level on a Spearman-Rank test. There is a weak but not significant correlation between the core and straight jet prominences of the NLRG and BLRG when considered separately (ignoring upper limits). The objects with the brightest straight jets remain the low-excitation objects discussed above. When the quasars are added, their positions are consistent with their being a population similar to the BLRG, but their straight jets are in the main not significantly brighter than the *detected* straight jets in radio galaxies. If the quasars are thought to be more beamed than the radio galaxies, we might expect their straight jets to be significantly brighter. Instead, it seems that although the bent parts of jets in quasars are more prominent, the straight jets are on the whole not.

The use of straight jets is not as straightforward for the radio galaxy sample as it was for the quasars. B94 found that the objects in their sample tended to have well-defined initial straight jets. In the radio galaxy sample the jets are rarely traced all the way from the core to the hot spot (the exceptions to this are mainly BLRG) and the straight jet segment may be a region in the middle of the lobe. In addition, straight jets may simply disappear, without bending, in the radio galaxies. 4C 14.11's jet exemplifies both these features, which imply a local change in beam efficiency not catered for in the simple model. This particular plot is in any case not a perfect diagnostic tool. Ideally we would be plotting quantities which directly measured the beaming in the radio source, with the only scatter being due to variations in beam efficiency. The prominence-prominence plot has scatter introduced by the normalisation with respect to extended flux and by the integration over the whole straight jet (points 3 and 5 of section 6.2).

6.7 Beam power and emission lines

6.7.1 Introduction

Rawlings and Saunders (1991) and others have presented evidence that the narrow-line power of FRIIs is related to their beam power and suggest that both are measuring the fundamental power of the AGN (see section 1.5.3). The connection is assumed to be photoionization of the narrow-line regions by the AGN. There is some evidence for this, but also some evidence for shock ionization in extended emission-line regions; it is reasonable to consider only the nuclear emission-line regions so as to exclude the debatable extended regions. Typically 90% of the flux comes from the inner 2.5 kpc (Zirbel and Baum 1995). Where no information about the spatial distribution of the gas is available, the total emitted flux is therefore a reasonable estimator of the flux from the nuclear regions.

6.7.2 Orientation-dependence of [OIII]

As discussed in section 1.5.3, it has been suggested that [OIII]λ5009,4959 lines (hereafter [OIII]) are not orientation-independent (Jackson and Browne 1990); Hes, Barthel and Fosbury (1993) suggest that they come preferentially from a region within the torus and so are at least partially obscured. They prefer the lower-ionization [OII]λ3727 line and show that its luminosity distribution as a function of 178-MHz total luminosity in a sample of quasars is indistinguishable from that of a matched-redshift sample of radio galaxies, whereas the Jackson and Browne objects show a clear offset. In figure 6.20 I show these effects for an incomplete sample of objects with $z < 0.6$ for which I have emission-line data, including the present sample, the objects from Jackson and Browne (1990) and the B94 quasars.[2] The quasars and BLRG do show a tendency to have brighter [OIII] emission at a given radio luminosity, but the [OII] powers are indistinguishable. (Note that the samples shown in this plot are overlapping but not identical, particularly at high radio luminosities.) The low-excitation objects, unsurprisingly, have the lowest [OIII] powers at a given radio luminosity; the large amount of obscuration inferred by Jackson and Browne (1990) was certainly in part the result of comparing quasars with low-excitation objects rather than with NLRG.[3] It would therefore be better to try to use [OII] emission as an indicator of beam power. Unfortunately there are many more [OIII] fluxes available in the literature than [OII] for low-redshift samples; I have chosen to use the [OIII] flux as my indicator of beam power and to attempt to work around the fact that it is not orientation-independent.

---

[2] The sources for the [OII] fluxes are Hes (1995), Saunders *et al.* (1989), McCarthy *et al.* (1995), Tadhunter *et al.* (1993), and Simpson *et al.* (1989).

[3] Similar conclusions were reached by Laing *et al.* (1994).

6.7.3 Relationships between [OIII] and straight jet

An obvious question is whether there is a relationship between the power emitted in the (straight) jet and the power in [OIII] (as an indicator of beam power). Figure 6.21 shows a plot of these two quantities for the 34 objects in the sample which have [OIII] fluxes and measured jet properties. It can be seen that the relationship is, if anything, less good than the well-known relationship between [OIII] power and total radio luminosity, plotted for the same sources in figure 6.22. The trend in both plots is weakly positive but the scatter is very large. Unsurprisingly, the low-excitation objects stand out in both plots. In figure 6.21 the most conspicuous low-excitation objects are the brightly-jetted group (3C 15, 3C 388, 3C 401, 3C 438) discussed above. The narrow-line object with jet and total radio power 'too high' for its [OIII] luminosity is Cygnus A; the low-excitation object with the weakest [OIII] power is 3C 353. There appears to be no clear difference between the BLRG and NLRG on these plots. Clearly if [OIII] power is a beam power indicator there is considerable scatter in the relationship between beam power and observed jet power. This scatter could arise (see section 6.2) because of beaming, because of differences in beam efficiency between sources, or because of the varying lengths of straight jets. Interestingly, the [OIII]-straight jet correlation for the 7 quasars from the sample of B94 with measured [OIII] fluxes is much stronger on a Spearman-Rank test than the corresponding [OIII]-total power correlation. The sample is too small to allow strong conclusions to be drawn from this.

6.8 Sidedness

The jet-counterjet ratio should be an indicator of the velocities involved and the projection angles in models based on relativistic beaming. If the jet and counterjet are intrinsically symmetrical, then their relative fluxes are found from equation 6.1. In general the ratio J is given by

$$J = R\left(\frac{1+\beta_j\cos\theta}{1-\beta_j\cos\theta}\right)^{2+\alpha_j} \tag{6.2}$$

where R is the degree of *intrinsic* asymmetry (the ratio between the rest brightnesses of jet and counterjet) and might represent the effects of different environments on the efficiencies of the two beams. It follows from this formula that, if relativistic beaming effects are dominant in the jets, objects at smaller angles to the line of sight should have larger jet-counterjet asymmetries.

Figure 6.23 shows the distribution of straight jet sidednesses for the radio galaxies with detected jets and for the B94 quasars. Dashed areas of the histogram represent *lower* limits on the jet-counterjet ratio (since they are calculated using upper limits on the counterjet flux). Clearly selecting on detected jets biases the sample; in the context of unified models, sources without detected jets will be preferentially unbeamed and so the more two-sided sources are excluded from the plot.

The plot as it stands can at best be said to be consistent with unified schemes (which would not be the case if, for example, the radio galaxies were obviously more one-sided than the quasars). However, the paucity of counterjet detections in the radio galaxy population is surprising if unified schemes are true (though the counterjet detection fraction is underestimated by this plot which excludes non-aligned counterjets in, for example, 3C 15 and 3C 438).

B94 fail to find a significant correlation between core prominence and jet-counterjet ratio, which may indicate (particularly when combined with their results about *where* a counterjet is found) that counterjet detection and prominence is partly determined by environmental factors. If this is so, and for all the other reasons discussed in their section 6.2, jet sidedness analysis must be undertaken with caution.

6.9 Modelling

The results above have appeared broadly consistent with versions of unified models for the low-redshift objects in which there is considerable beaming in the cores, some beaming in the jets and a range of beam efficiencies. Using Monte Carlo simulation, we can try to constrain the parameters that are needed. The general approach I adopt is to generate a set of model data under some assumptions and estimate its probability of coming from the same dataset as the observed data, using a statistical test such as Kolmogorov-Smirnov (see e.g. Press *et al*. 1992 for information on implementation): the initial parameters can then be varied and a table of the probabilities associated with them can be built up. This technique has two disadvantages; one, it does not allow direct testing of *relationships* between model and data quantities, since the Kolmogorov-Smirnov test is based on a one-dimensional distribution; two, it does not easily allow for the presence of limits in the data[4]. Nevertheless, the approach is worth attempting.

6.9.1 Sidedness

Wardle and Aaron (1996) have applied a similar Monte Carlo approach to the determination of the jet speeds in the B94 quasars with some success, finding velocities of $\beta_j = 0.65$ to 0.7 and little intrinsic

---

[4] To conduct this analysis rigorously in the presence of limits techniques from the field of survival analysis should be applied. Prescriptions exist for deciding the probability of two datasets having been drawn from the same distribution when the datasets are subject to random censoring; the best in this case would probably be a modified Kolmogorov-Smirnov test (e.g. Fleming *et al*. 1980) because of its sensitivity to differences at any point in the distributions being compared. Their problem is a lack of robustness when only one dataset is censored, as in the present case. I have chosen the easier path of attempting to point out the probable errors introduced by considering upper limits as measurements.

asymmetry best fit the data. I initially followed Wardle and Aaron in modelling sidedness to try to constrain β_j, the velocity in the jets, and the degree of intrinsic asymmetry. Like them, I treated all the sidedness limits (section 6.8) as *measurements*. (This is more dangerous in the present sample than it was in that of Wardle and Aaron, because there are few true measurements in the distribution. I will discuss the effect this has on the results below.) The variables in my simulation were the range of angles ($\theta_{min} < \theta < \theta_{max}$), the jet velocity β_j and the maximum intrinsic asymmetry parameter, R_{max}. I assumed that the probability that a source was at an angle θ to the line of sight was proportional to $\sin\theta$, so that each simulated angle θ_i was given by

$$\theta_i = \cos^{-1}[\cos\theta_{max} \ldots \cos\theta_{min}] \tag{6.3}$$

where $[x \ldots y]$ denotes a random number chosen between x and y with a uniform probability distribution. The simulated intrinsic asymmetries were given by

$$R_i = [1 \ldots R_{max}]$$

where R_{max} was a variable in the simulation.

I generated a large number of datasets (typically several hundred) from each set of parameters, each containing sidedness measurements derived from equation 6.2 ($\alpha_j = 0.8$) for the same number of simulated objects as the real dataset contained. For each one I measured the probability that the simulated and measured datasets were drawn from the same population with a Kolmogorov-Smirnov test. I recorded the mean probability as a function of the variables β_j and R_{max} on a fine grid. The principal results are summarized below.

- NLRG only. With $\theta_{min} = 45°$, $\theta_{max} = 90°$ (the ‘unification’ angle range) the best fits (probability of being drawn from matching datasets $p > 0.55$) from simulation to the 17 sources with sidedness measurements had $0.5 < \beta_j < 0.6$, $R_{max} \approx 1$ (figure 6.1).[5] This implies little intrinsic side-to-side asymmetry and moderate relativistic beaming. With $\theta_{min} = 0°$, $\theta_{max} = 90°$, the fits are poorer but give $0.4 < \beta_j < 0.5$, $R_{max} \approx 1$. There is no good fit with $\theta_{min} = 0°$, $\theta_{max} = 45°$: $\beta_j = 0$, $4 < R_{max} < 5$ or $6 < R_{max} < 7$ are the best solutions with $p \approx 0.20$.
- BLRG and NLRG. The measured dataset contained 23 objects. With $\theta_{min} = 0°$, $\theta_{max} = 90°$ the best fits have $0.45 < \beta_j < 0.55$, $R_{max} \approx 1$ (figure 6.2). Note that this angle range may be too wide; in unified models, there should be some core-dominated objects at $\theta \approx 0°$ which would not appear

---

[5] Note that only the un-contoured regions of parameter space in this figure, with $p < 0.05$, can be formally rejected at a high level of confidence.

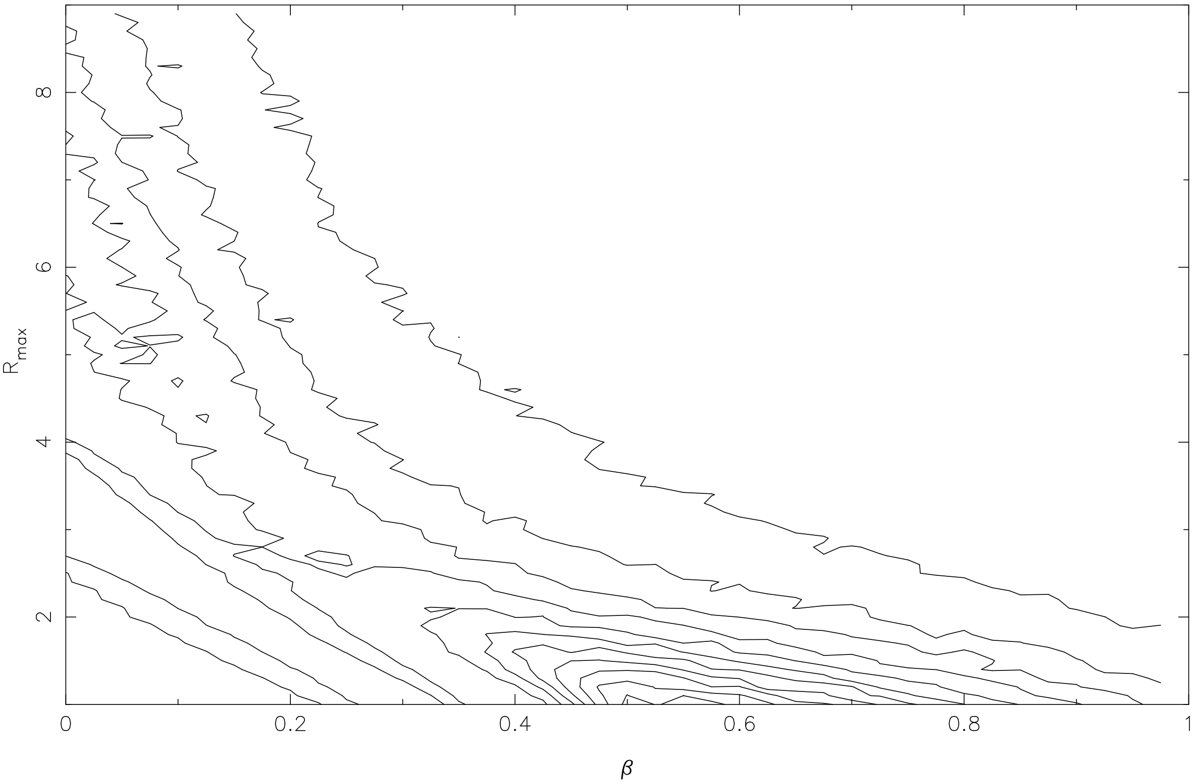

Figure 6.1: Probability contours for sidedness simulations: NLRG with $\theta_{min} = 45°$, $\theta_{max} = 90°$. Contours at $p = 0.05, 0.1, 0.15\ldots$

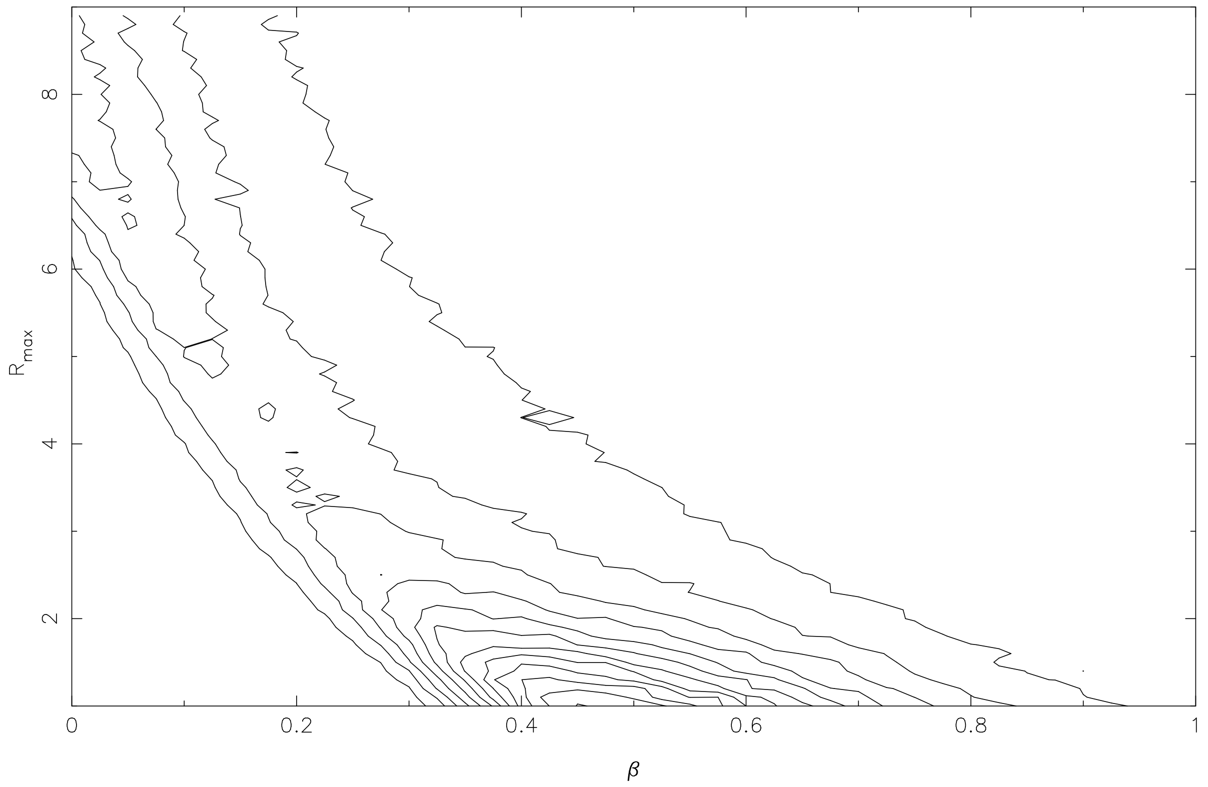

Figure 6.2: Probability contours for sidedness simulations: BLRG and NLRG with $\theta_{min} = 0°$, $\theta_{max} = 90°$. Contours at $p = 0.05, 0.1, 0.15\ldots$

in this sample. However, the probabilities associated with small angles are low. Attempting to correct for this by using an angle range $\theta_{min} = 10°$, $\theta_{max} = 90°$ makes no difference to the results above. For $\theta_{min} = 45°$, $\theta_{max} = 90°$ a poorer fit was found with $0.6 < \beta_j < 0.7$, $R_{max} \approx 1$. There was no good fit with $\theta_{min} = 0°$, $\theta_{max} = 45°$, as before.

- Low-excitation objects. In these 9 objects there was little distinction in probability, whatever the angle range chosen, between fits with $R_{max} \approx 1$ and low β_j ($\beta_j \approx 0.4$ for $\theta_{min} = 0°$, $\theta_{max} = 90°$, the appropriate range according to Laing *et al*. 1994) and fits with $\beta_j \approx 0$, $R_{max} \approx 8$. This suggests there is either substantial side-to-side asymmetry, or jets with $\beta_j \lesssim 0.4$, or both, in these objects. The sample is small, however.

- Quasars. As a 'sanity check' on my fitting routines I verified that there was no good fit to the B94 quasar sidednesses with $\theta_{min} = 45°$, $\theta_{max} = 90°$. I did not attempt to replicate the results of Wardle and Aaron because of the necessity to take selection effects into account in modelling their sample of quasars.

This modelling suggests that the observations of at least the BLRG and NLRG are consistent with unified models and with moderate values of jet velocity β_j. The low-excitation objects are not well fitted with any model; this may reflect the fact that they are an inhomogeneous sample. It must be noted, however, that a more sophisticated model for intrinsic asymmetry, rather than the top-hat probability distribution adopted, might fit the data better.

The use of limits as measurements is not as obviously wrong as might be supposed at first, because it seems likely that the upper limits assigned to counterjet flux are in fact reasonably close to the true values. The factors limiting jet and counterjet detection appear now to be confusion with other structures in the lobe, rather than sensitivity, so that the method I adopted of measuring counterjet limits is likely to produce a number which is not too far different from the true value. If this is not the case, and the asymmetries are much larger than these lower limits, the true velocity β_j could be substantially larger than the best fits of around 0.6. However, the sample used here is also biased by the exclusion of the objects with no detected straight jets. Since these objects are likely on the average to be less beamed than those with detected jets, the true velocity might be substantially *less* than that fitted here.

6.9.2 Core prominence

I next investigated the distribution of core prominences, in an attempt to constrain the possible angles to the line of sight and the velocities in the nuclear regions. Without beaming, we would expect the core flux to be proportional to the total flux, although the relationship should involve some scatter (see section 6.2 above). Following Urry, Padovani and Stickel (1991) I therefore treated the prominence P_c

as the product of the *intrinsic* ratio between the core and unbeamed fluxes or powers, k, and the factor due to relativistic beaming (equation 6.1):

$$P_c = k[\gamma_c(1-\beta_c\cos\theta)]^{-(m+\alpha_c)}$$

with $m = 2$, as before, and $\alpha_c = 0$ to reflect the flat-spectrum nature of the cores. The parameters to vary in this relationship are clearly β_c and k. I made provision in the simulations for k to be drawn from a range, to mimic the intrinsic scatter, so that the value for each simulated observation was given by

$$k_i = [k_{min} \ldots fk_{min}]$$

where f was a parameter of the simulation as a whole; however, the results appeared to be unaffected by changes in f for $f \lesssim 5$. The results shown have $f = 1.1$, i.e. very little variation in intrinsic prominence. The variables in the simulation were thus β_c and k_{min}. As before, I generated several hundred simulated datasets to compare with the real distribution, with the angle to the line of sight θ_i for each simulated object being drawn from the distribution of equation 6.3. I treated the upper limits on core prominences as measurements; there were only two of these, so the results should not be affected significantly. The results are summarized below.

- BLRG and NLRG. For $\theta_{min} = 0°$, $\theta_{max} = 90°$ the core prominence distribution for the 30 sources with measured cores (figure 6.24) was only well fitted with relativistic velocities; this is because of the wide range of core prominences in the sample. Figure 6.3 shows that a wide range of parameters is formally possible (the formal errors on best-fit quantities are therefore large). The best fits were around $\beta_c = 0.985$, $k_{min} = 0.075$ (probability $p = 0.69$), corresponding to $\gamma_c = 5.8$. This best fit is plotted with the data in figure 6.24. Regions of parameter space with similar, though smaller, probabilities range from $\beta_c = 0.958$, $k_{min} = 0.025$ to $\beta_c = 0.996$, $k_{min} = 0.26$. The only constraints we have on γ_c for this sample are those from VLBI measurements of superluminal motion in the cores of the two BLRG 3C 111 ($\gamma_c \gtrsim 6.9$, Preuss *et al*. 1990) and 3C 390.3 ($\gamma_c \gtrsim 3.6$, Alef *et al*. 1996). The Lorentz factor derived from the best fits is therefore compatible with these observations, although since the speeds of VLBI components may not reflect the true bulk velocity in the core regions this result is not a strong one.

  For $\theta_{min} = 45°$, $\theta_{max} = 90°$ there is no fit to the data with probability better than $p = 0.26$ ($\beta_c = 0.988$, $k_{min} = 0.165$). $\theta_{min} = 0°$, $\theta_{max} = 45°$ (the case in which all the objects are preferentially oriented with respect to the line of sight) has reasonably good ($p \approx 0.6$) fits around $\gamma_c = 25$, $k_{min} = 0.1$.

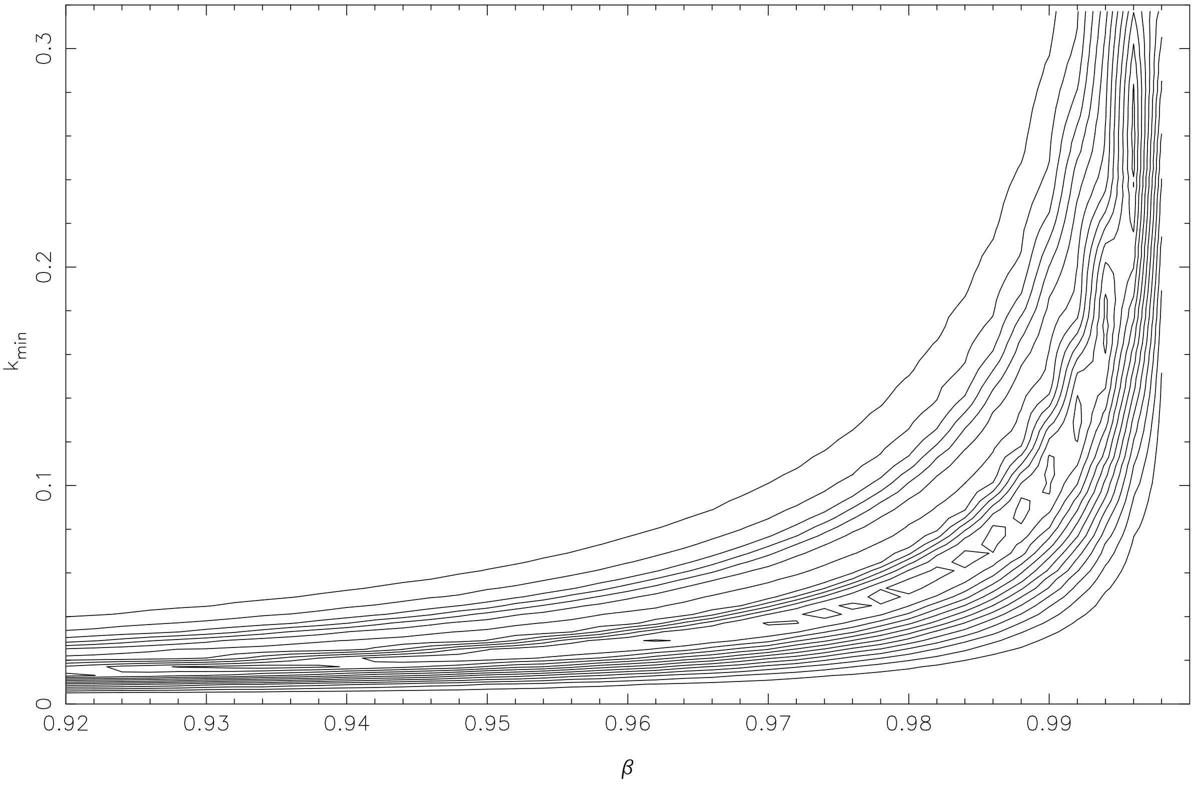

Figure 6.3: Probability contours for core prominence simulations: BLRG and NLRG with $\theta_{min} = 0°$, $\theta_{max} = 90°$. Contours at $p = 0.05, 0.1, 0.15\ldots$

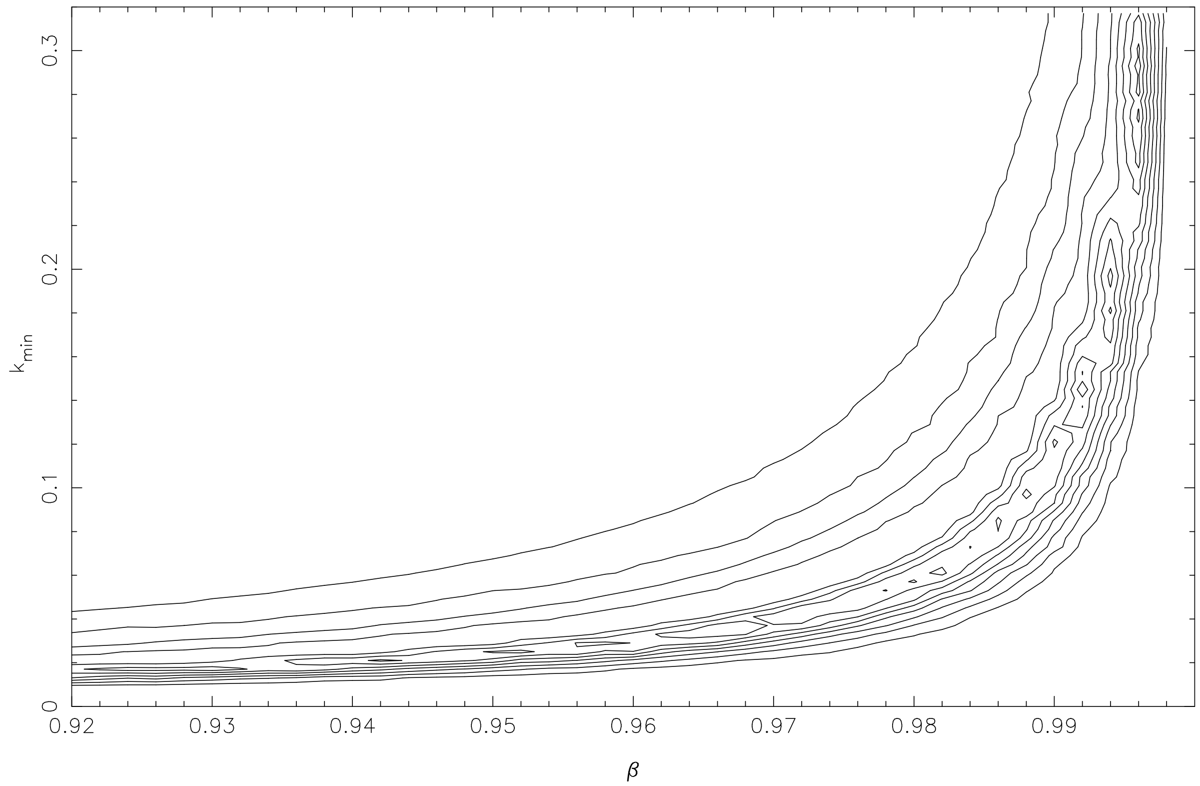

Figure 6.4: Probability contours for core prominence simulations: NLRG with $\theta_{min} = 45°$, $\theta_{max} = 90°$. Contours at $p = 0.05, 0.1, 0.15 \ldots$

- NLRG only. The 22 NLRG have moderately good fits ($p = 0.44$) with $\theta_{min} = 45°$, $\theta_{max} = 90°$; $\beta_c = 0.992$, $k_{min} = 0.145$ (figure 6.4), although the region of parameter space which was best for the combined BLRG-NLRG sample is still comparatively high-probability. This different result and poorer fit is presumably due to the pronounced overlap between the BLRG and NLRG core prominences, and may be an indication that there are still some unidentified broad-line objects in the NLRG sample or that the unification angle should be less than 45°. If θ_{min} is decreased slightly, the fits improve and the numbers converge on those obtained for the combined sample, consistently with this (for $\theta_{min} = 35°$, the highest-probability region has $p = 0.58$, $\beta_c = 0.988$, $k_{min} = 0.085$, though again there is a wide spread of regions with similar probability, including solutions with $\beta_c = 0.995$, $k_{min} \approx 0.2$ and $\beta_c = 0.98$, $k_{min} \approx 0.04$). Too much should not be read into this difference between the NLRG and the whole sample, which depends on a few data points; a larger sample is desirable.

- Low-excitation objects. These 12 objects were not well fitted by highly relativistic core velocities — the best fits ($p = 0.8$) occur around $\beta_c = 0.65$, $k_{min} = 0.02$ for $\theta_{min} = 0°$, $\theta_{max} = 90°$, the angle range suggested by Laing *et al.* (1994). This is because of the small range of core prominences in the low-excitation objects in the sample. Even for $\theta_{min} = 45°$, the best fits occur at $\beta_c \lesssim 0.9$. This could conceivably be a genuine indication of lower velocities in the cores, but given the results of Laing *et al.* (discussed in section 6.6) it may simply be coincidence.

Urry, Padovani and Stickel (1991) suggest that a range of core Lorentz factors (γ_c) is necessary to model the luminosity function of BL Lac objects and FRIs, and Morganti *et al.* (1995) use this approach in their study of core prominences in a complete sample of 2-Jy objects. To allow comparison of my simulations with theirs I ran an alternative set of simulations in which the variables were k_{min} (as above) and $\gamma_{c,min}$; the Lorentz factor for each simulated source was drawn from a power-law distribution ($p(\gamma)d\gamma \propto \gamma^{-\zeta}$) so that

$$\gamma_{c,i} = \left[\left(\gamma_{c,min}^{-(\zeta+1)} - \gamma_{c,max}^{-(\zeta+1)}\right)[0\ldots1] + \gamma_{c,max}^{-(\zeta+1)}\right]^{-1/(\zeta+1)}$$

I chose $\gamma_{c,max} = 36$ and $\zeta = 2$ for comparison with Morganti *et al.* (1995). The results for the NLRG and BLRG are shown in figure 6.5. It can be seen that the introduced scatter in γ_c simply smooths out the probability distribution. The only conclusion that can be drawn from this plot is that $\gamma_c \gtrsim 2$ provides the best fits to the data. A larger sample, perhaps with some better constraints from VLBI measurements, is needed to constrain the beaming in the cores better. The conclusion that the distribution cannot be reproduced without significantly relativistic core velocities and small angles to the line of sight is an important one in view of the other results from modelling, however.

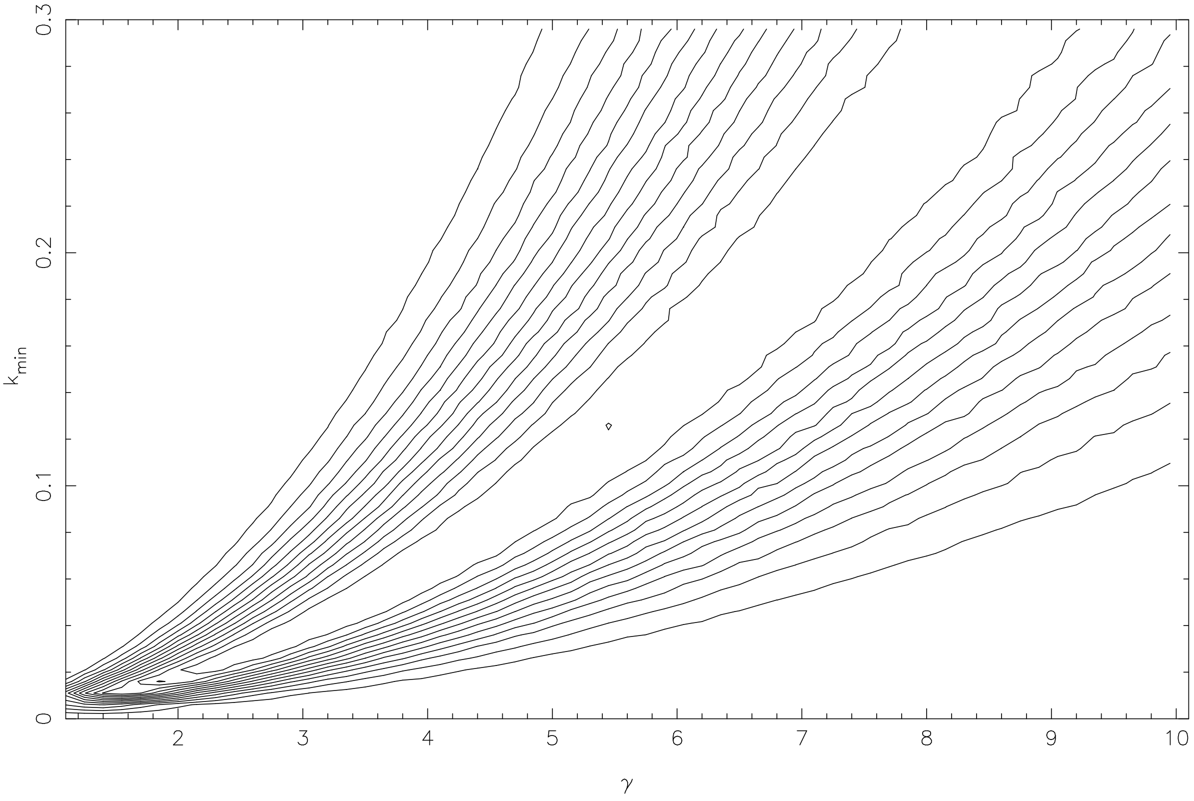

Figure 6.5: Probability contours for core prominence simulations with variable γ_c: BLRG and NLRG with $\theta_{min} = 0°$, $\theta_{max} = 90°$. The x-axis shows $\gamma_{c,min}$. Contours at $p = 0.05, 0.1, 0.15\ldots$

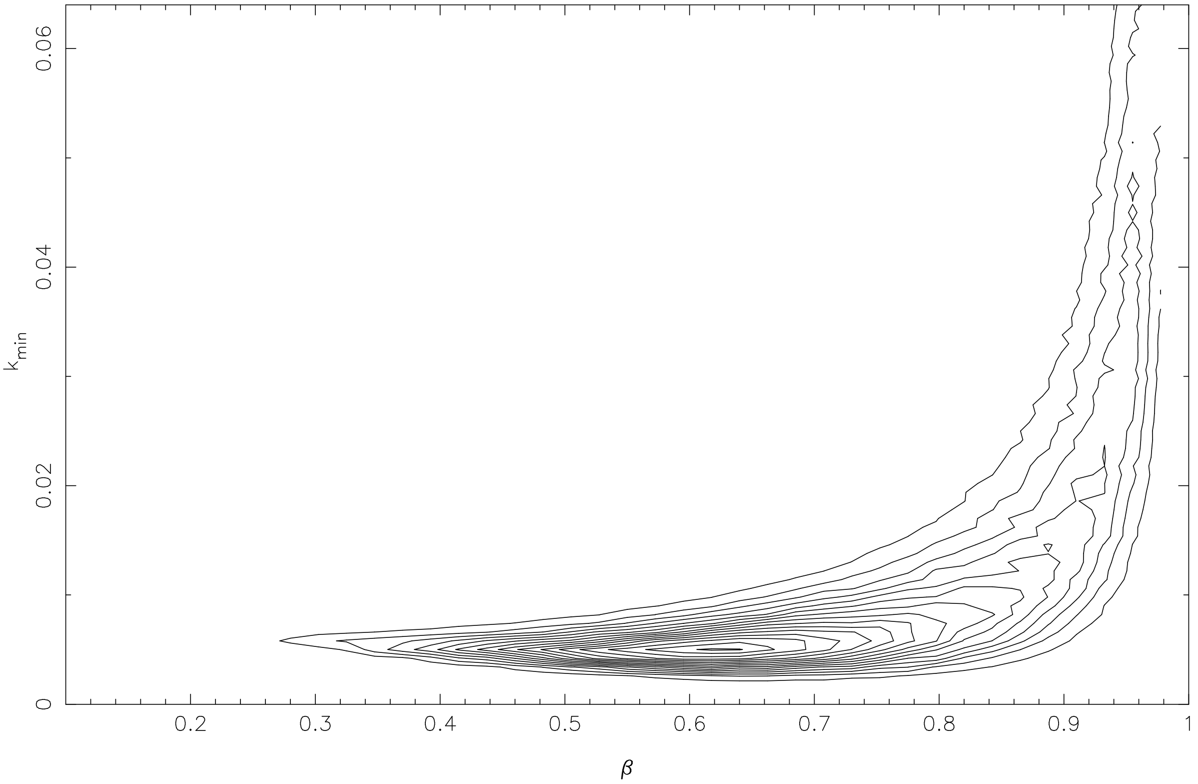

Figure 6.6: Probability contours for jet prominence simulations: BLRG and NLRG with $\theta_{min} = 0°$, $\theta_{max} = 90°$. Contours at $p = 0.05, 0.1, 0.15\ldots$

6.9.3 Jet prominence

The intrinsic flux of the straight jet should be proportional to the total unbeamed source flux, as above. Scatter is introduced into this relationship by the variations in straight jet length and the fact that the extended source flux is not simply determined by the beam power (see above, section 6.2, points 3 and 5) and also by any intrinsic scatter in the efficiency of the straight parts of beams. The simplest possible approach is to treat the straight jet prominence P_j identically to the core prominence, and find the values of 'intrinsic jet prominence' k and relativistic velocity β_j that best fit the data, ignoring these sources of scatter; in other words,

$$P_j = k[\gamma_j(1-\beta_j\cos\theta)]^{-(m+\alpha_j)}$$

with $\alpha_j = 0.8$. The values of k can again be chosen from a top-hat distribution with $k_i = [k_{min}\ldots fk_{min}]$. When this is done with the BLRG and NLRG (see figure 6.25), treating the upper limits on jet promin-

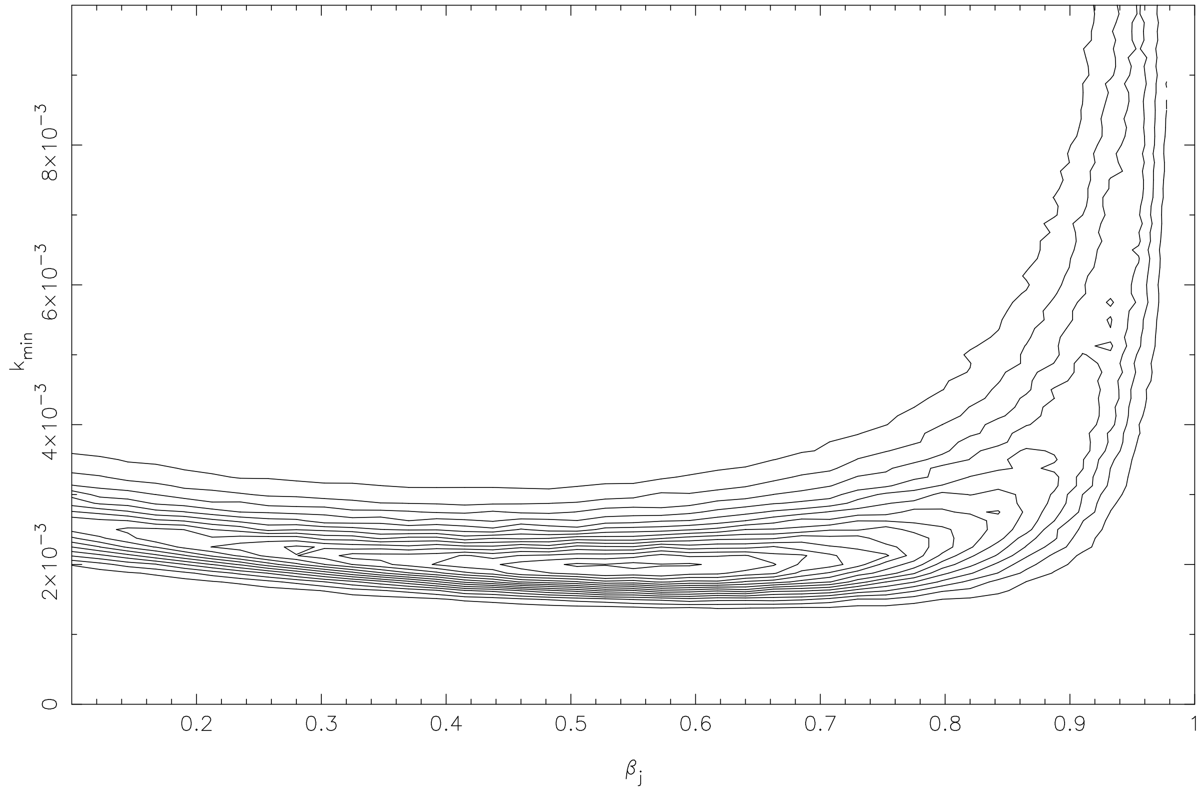

Figure 6.7: Probability contours for jet prominence simulations: BLRG and NLRG with $\theta_{min} = 0°$, $\theta_{max} = 90°$ and $f = 10$. Contours at $p = 0.05, 0.1, 0.15\ldots$

ence as *measurements* and setting $\theta_{min} = 0°$, $\theta_{max} = 90°$, $f = 1.1$, the distribution of probability is as shown in figure 6.6. Again, a wide range of parameters is formally possible, but the probability distribution has a peak at $\beta_j \approx 0.62$, $k_{min} \approx 0.005$ with $p \approx 0.75$. In this case increasing the allowed scatter by introducing larger values of f — reflecting the differing efficiencies and lengths of jets — does marginally improve the fit of the model to the data, at the cost of increasing the spread of the formally allowed values of β_j (since $\beta_j \approx 0$ is a more plausible fit if the spread in intrinsic prominence is larger). Larger values of f also produce smaller best values of β_j. The probability distribution with $f = 10$, which is about the largest f-value to fit the data, is shown in figure 6.7; the best fit β_j is 0.55 and $p = 0.77$, and the mean k implied is again about 0.005.

Estimates of β_j would clearly be increased if the upper limits assigned substantially over-estimate the true straight jet flux, but experiments with lowering the values used for the limits suggest that the effect would not be great (for example, if the objects with upper limits are treated as having straight jet flux equal to five times less than the limit, the best fit $\beta_j \approx 0.65$). This is because of the high rate of jet detection in the sample.

When the NLRG are considered alone, a fit with $\theta_{min} = 45°$, $\theta_{max} = 90°$, $f = 1.1$ gives best-fit values of $\beta_j \approx 0.8$, $k_{min} \approx 0.011$ (figure 6.8) with a reasonable probability for some higher values of β_j; the parameters are clearly less well constrained, and the best-fit value is not consistent with that obtained for the database as a whole. Modelling the NLRG with $\theta_{min} = 30°$, $\theta_{max} = 90°$, $f = 1.1$ gives a best fit of $\beta_j \approx 0.7$ which is more compatible with the fits for the combined BLRG and NLRG sample. The results with $f = 10$ are similar. This effect appears to be due to the presence of a few very prominent jets (e.g. 3C 285) and 'prominent' upper limits (e.g. 3C 284) in the data, but it may suggest that smaller unification angles are needed at this luminosity or that some BLRG are still mis-identified as NLRG.

When this simulation was run on the 11 low-excitation objects with measured jets or upper limits, the best fit values of β_j ($\theta_{min} = 0°$, $\theta_{max} = 90°$) were around 0.8, with considerable scatter but reasonable fits ($p \approx 0.7$). Interpreting this at face value would imply more beaming in the low-excitation objects, but it will be recalled that fits to the sidedness suggested a much lower value of β_j. For this reason this interpretation is suspect.

An approach which reflects the expected contribution to the scatter in jet prominence from the variation in lengths of the jet should allow the scatter in beam efficiencies to be constrained more directly, the other factors inducing scatter being the variation of total source flux with age, which is likely to be small even at this frequency (Kaiser, private communication), any significant scatter in the beaming velocities, and the fact that straight jets do not extend over the whole length of the source. However, there is no obvious analytical fit to the *unprojected* distribution of lengths in the sample (figure 6.12 shows the projected linear sizes). The best distribution function I obtained by trial and error was

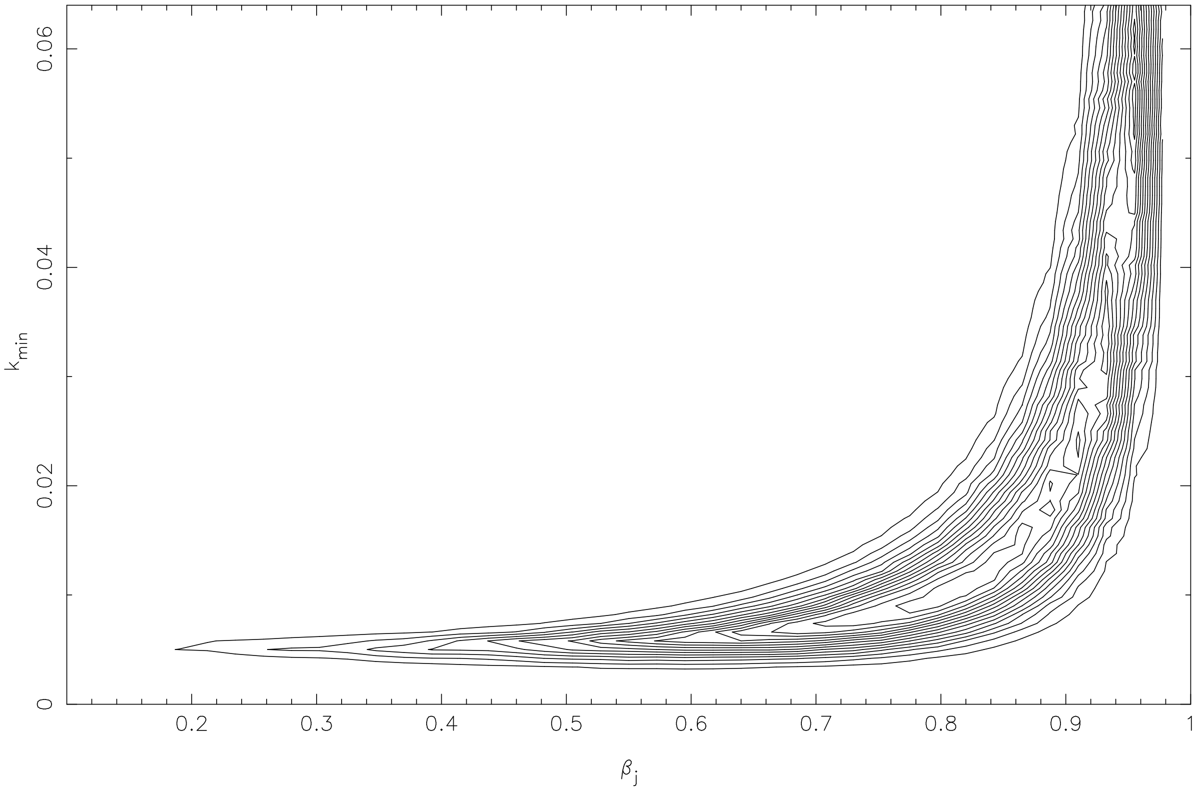

Figure 6.8: Probability contours for jet prominence simulations: NLRG with $\theta_{min} = 45°$, $\theta_{max} = 90°$ and $f = 1.1$. Contours at $p = 0.05, 0.1, 0.15\ldots$

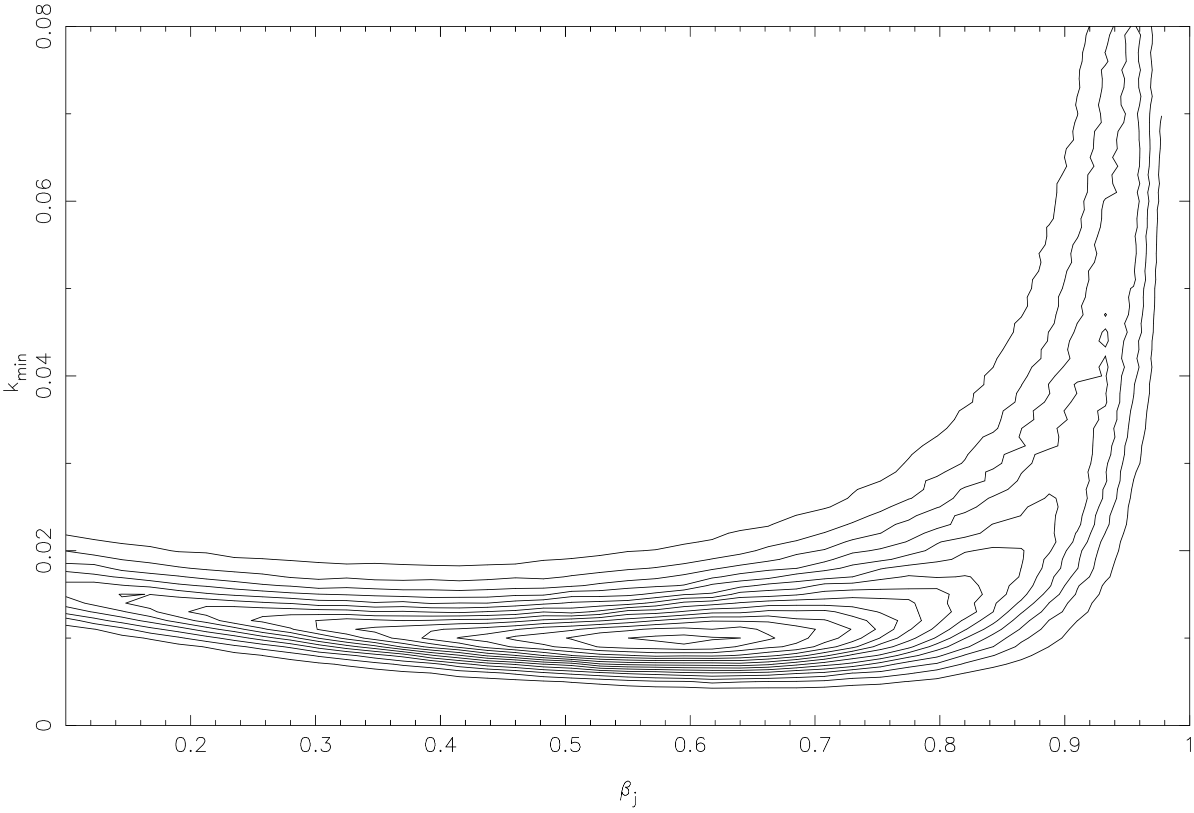

Figure 6.9: Probability contours for jet prominence simulations incorporating the variations in jet length: BLRG and NLRG with $\theta_{min} = 0°$, $\theta_{max} = 90°$ and $f = 1.1$. The y-axis shows $k'_{min} \times 1000$ kpc. Contours at $p = 0.05, 0.1, 0.15\ldots$

$$l_i = l_0 \left\{ \exp\left(-[0\ldots1.75]^2\right) \right\}^{\frac{1}{2}}$$

with $l_0 = 840$ kpc; a simulated distribution of objects with this range of lengths has a typical probability $p \approx 0.7$ (on a K-S test) of being drawn from the same sample as the broad- and narrow-line objects with straight jet measurements when projected at angles $0° < \theta < 90°$ to the line of sight.

I then generated the sample to be compared with the observations by using the same distributions of θ_i and k_i as before, generating a model jet prominence *per unit length* and multiplying by the randomly assigned intrinsic length. The prominence of a given simulated jet $P_{j,i}$ is thus given by

$$P_{j,i} = k'_i l_i [\gamma_j (1 - \beta_j \cos\theta_i)]^{-(m+\alpha_j)}$$

where k'_i now represents the intrinsic jet prominence *per unit length*. (Note that the lengths l_i being used are the lengths of the whole source, while the fits are being made to one-sided jets. The 'unit length' in this case is unit length *of the whole source*, and the actual value of k should be doubled when considering a single jet.) In the model we have been discussing, this should represent the efficiency of the beam only. As before, k' can be drawn from a top-hat distribution to represent the scatter in efficiency, so that $k'_i = [k'_{min} \ldots f k'_{min}]$; fits with $\theta_{min} = 0°$, $\theta_{max} = 90°$ and $f = 1.1$ are shown in figure 6.9. The best fits to the parameters are $\beta_j \approx 0.6$, $k' \approx 1 \times 10^{-5}$ kpc^{-1}; this model is plotted with the data in figure 6.25. Higher factors f again give rise to lower best fit β_j but identical mean k'.

To attempt to constrain the possible degree of scatter in the jet efficiency I next set up simulations that had a fixed mean k' ($\overline{k'} = 10^{-5}$ kpc^{-1}) but allowed the range f to vary; in this case

$$k'_i = \left[\left(\frac{2}{1+f}\right)\overline{k'} \ldots \left(\frac{2f}{1+f}\right)\overline{k'}\right]$$

I ran several thousand iterations of the simulation to ensure convergence. Figure 6.10 shows the results. It will be seen that the best fits are found with small values of f, but that large values are not ruled out by the data. The best interpretation of this is that the true scatter has a distribution with a tail of particularly efficient and/or inefficient sources. The plot allows us to guess at a range for the scatter of an order of magnitude or so, however. It must be borne in mind that the model is not a perfect fit to the data at any point, which (if the model is correct as far as it goes) suggests the presence of additional sources of scatter in the dataset. These may be at least partly due to the poor modelling of the length distribution in the true dataset, but will also include the scatter in extended power introduced by environment and source age and any variation in beaming velocities. When good theoretical models are available for the evolution of source length and high-frequency flux these might provide a better fit to the data.

The best fits found here allow a rough estimate to be made of the typical beam efficiency $\epsilon_j = \mathcal{P}_j/Q$ in this sample (where $\mathcal{P}_j$ is the bolometric power radiated in the kiloparsec-scale jet per unit length). Rawlings and Saunders (1991) suggest a jet power of between 10^{37} and 10^{39} W for the sources in this sample. If the 8-GHz extended flux of a 'typical' source in the sample, at $z = 0.15$, is 0.5 Jy, then its intrinsic jet flux per unit length *of the jet* is 10^{-5} Jy kpc^{-1}; assuming a constant power-law for the spectrum of jets, with $\alpha_j = 0.8$, and integrating between 10 MHz and 100 GHz we find $\mathcal{P}_j$ to be 6×10^{31} W kpc^{-1}; taking Q to be 10^{38} W and dividing by two because there are two jets, $\epsilon_j \approx 10^{-6}$ kpc^{-1} (to within an order of magnitude). Integrated over the lobe length of a normal source, this implies that a typical beam loses considerably less than 1% of its energy in radiation on kiloparsec scales on its way to the hot spots in straight jets. Beams which are dissipative enough that a significant amount of the energy is lost (as suggested for some of the low-excitation sources, e.g. 3C 438) must therefore be two orders of magnitude (or more) less efficient than the norm. It will be noted (1) that the scatter in the efficiency discussed above applies to ϵ_j and (2) that these typical efficiencies are an average over the length of the

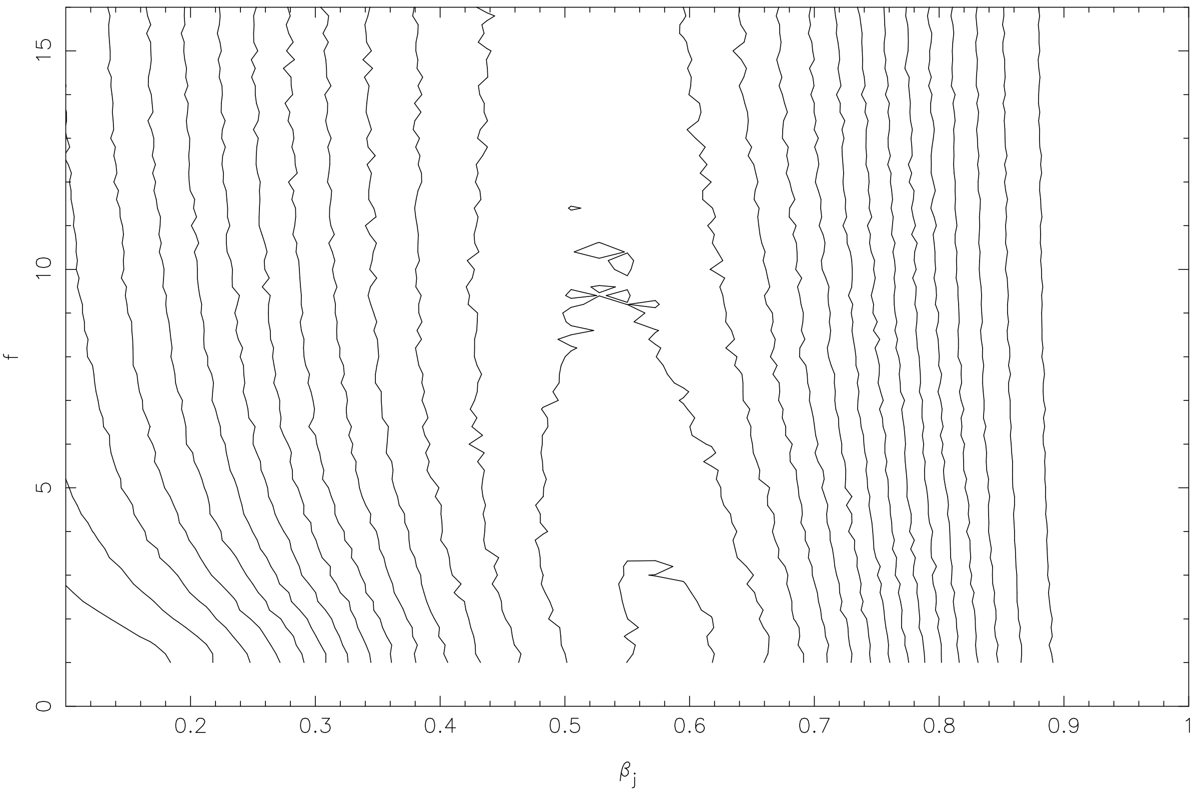

Figure 6.10: Probability contours for jet prominence simulations incorporating the variations in jet length: BLRG and NLRG with $\theta_{min} = 0°$, $\theta_{max} = 90°$, $\overline{k'} = 10^{-5}$ and variable f. Contours at $p = 0.05, 0.1, 0.15\ldots$

source.

6.9.4 Expected correlations

With the best-fit velocities found above, the expected forms of the relationship between straight jet prominence and core prominence (section 6.6) can be calculated. Figure 6.26 shows a plot of this relationship for 250 simulated sources, with $\beta_j = 0.6$, $\beta_c = 0.99$, $\theta_{max} = 90$, $\theta_{min} = 10$, $\overline{k_j} = 0.005$, $\overline{k_c} = 0.08$, $f_j = 10$, $f_c = 5$ (the spreads in the intrinsic prominences f_j, f_c being at the high end of those suggested by model fitting). It can be seen that the plot reproduces a number of the features of figure 6.19, including the overall distribution in the plane, the approximate cutoff point between BLRG and NLRG at $P_c \approx 0.03$, and the fact that the jets in the brightest NLRGs are similar in prominence to those in BLRG. The jet-core prominence relationship is present but relatively weak in this simulated dataset, and it is not surprising that it was not detected in the real data.

Given the relationship between straight jet power and beam power, we may see whether the lack of a correlation in figure 6.21 is consistent with the standard model and the results of Rawlings and Saunders. Figure 6.27 shows the expected form of the beam-jet power relationship for beam powers between 10^{37} and 10^{39} W. In this case $\beta_j = 0.6$, $\varepsilon_j = 10^{-6}$, $f_j = 10$, $\theta_{max} = 90$, $\theta_{min} = 10$, and the effects of a length distribution are included. The simulations reproduce the scatter and general parameter space distribution of figure 6.21 (bearing in mind the empirical result of Rawlings and Saunders that [OIII] power is between 2 and 3 orders of magnitude less than the beam power). However, they predict a stronger correlation than is observed, and suggest that the broad-line objects should be seen to have systematically brighter jets than the narrow-line objects for a given [OIII] power, which is not seen in figure 6.21. Rawlings and Saunders (1991) suggest that there is an order of magnitude scatter in the relationship between narrow line power and beam power, but experiment shows that this is not usually enough to wash out either the correlation or the expected tendency for broad-line objects to have brighter jets. Some form of orientation-dependence of the [OIII] lines is thus probably necessary, as suggested above.

6.10 Interpretation

6.10.1 Velocities and unified schemes

The modelling work described above has shown that the distributions of core and jet prominences in the sample of BLRG and NLRG is consistent with the unified model, with velocities in the jets $\beta_j \approx 0.5$ to 0.6 (found by two complementary methods) and velocities in the cores $\beta_c \gtrsim 0.9$, and random distribution of the angle to the line of sight. Models involving an intrinsic asymmetry as an explanation for jet one-sidedness do not fit the data as well. In this respect my results are similar to those of B94, Hough (1994) and Wardle and Aaron (1996) in a sample of quasars, and to earlier work (Owen and Puschell 1984, Bridle and Perley 1984); but the analysis here has been carried out in a sample which should have few selection effects affecting the orientation or other distributions of the sources. Two puzzles remain. One is the failure of the NLRG alone to reproduce the velocities found for the combined sample; as has been suggested above, this may indicate that the unification angle of 45° is inappropriate in this sample, or that a few BLRG are masquerading as NLRG with prominent jets. The other is the difference between the counterjet detection rates in the radio galaxies and quasars.

The interpretation of the best-fit velocities needs some care. As yet we are not sure what relationship the emitting material has with the beam as a whole (for example, is the emission from a boundary layer, or is it from the entire beam?) so it is quite possible that by assessing velocities from the distributions of prominences in this way we are not saying a great deal about the true bulk velocity of the beam. Indeed, from one point of view, we might hope that this is true, since, if the velocities deduced apply to the whole beam, then, inverting the argument of Bicknell (1994), the inferred deceleration from the core to the jet scales in these objects would suggest that the whole beam was trans-sonic, an inference at odds with the appearances of jets and hot spots. Equally, as B94 have pointed out, it is highly probable that the beam (and therefore, presumably, the emitting part of the beam, whatever that is) should have a distribution of velocities. In this case the velocity measured is a weighted average over the emitting regions of the beam. The results here are therefore not a conclusive proof of beam deceleration between the scales of the cores and the jets, but they are certainly an indication that *something* is different in the two régimes.

It is quite possible that the jet velocity is a function of source luminosity, so that sources with higher power will show more pronounced relativistic effects. Wardle and Aaron's results for the jet velocities in the B94 quasar sample suggest marginally higher values of β_j in those objects. This might help to explain the differences in jet detection between the low- and high-redshift samples studied up until now, as discussed in section 6.5. The present sample is too small to allow any search for a relationship between best-fit velocities and luminosity.

6.10.2 Beam efficiency

The results discussed above have allowed me to constrain the beam efficiency, both in terms of the intrinsic jet prominence and (very roughly) as an estimate of the energy dissipated by the beam on its way to the hot spots. The scatter in beam efficiency is approximately one order of magnitude in normal sources, but I have mentioned above (and will discuss further below) the suggestion that the low-excitation objects with bright jets have particularly dissipative (inefficient) beams.

The question of what *determines* beam efficiency has been left unanswered. A theoretical approach is hampered by the fact that we do not know what part of the beam is responsible for the emission. Are the emitting particles part of the beam, or are they simply advected and excited by it? What process is responsible for the spectra of jets (and what *are* the spectra of jets in FRIIs)? If, as seems likely both from theory and from the highly efficient jets found here, the emission comes from a boundary layer, the efficiency will certainly be strongly influenced by the jet's local environment, but it is hard to say in what way. Sources such as 3C 171 and 3C 438 suggest that beam efficiency is lower when the beam is not propagating through a cocoon (but compare the entire absence of a jet detection in 3C 123). Numerical simulation may be the way forward in this case.

Variation of beam efficiency with source luminosity remains a possibility. In the context of models for the FRI-FRII divide, the beam efficiency clearly varies dramatically with beam power and more weakly with environment, since the beams of FRIs are highly dissipative compared to those of FRIs. If higher-power beams are more efficient, this might again help to explain the lower detection rate of jets in high-redshift galaxies; but, as discussed above, there seems to be little difference in jet detection rates or prominences between the $z < 0.15$ and $0.15 < z < 0.3$ sub-samples studied here.

6.10.3 The low-excitation objects

The low-excitation objects in the models proposed by Laing *et al*. (1994) and others are simply objects whose high-excitation lines are sufficiently weak that we would not expect to see broad lines even if they were present. There is thus no *a priori* reason why they should be different from the narrow-line and broad-line objects in their radio properties.

However, as discussed above, the low-excitation objects are different from the rest of the sample in a number of ways. 3C 15, 3C 401, 3C 424 and 3C 438, possibly with the addition of 3C 388, form a group of objects whose jets and straight jets are 'too bright' for their cores. The jets are more dominant even than those of the quasars, which suggests that their dominance cannot easily be explained by relativistic beaming (certainly not in the case of 3C 438, which is two-sided). Fits of simple relativistic beaming models to their jet and core prominences, described above, give confusing and contradictory results (although the sample is small). The diffuse hot spots in most of these objects are further evidence that their beams are particularly dissipative. In addition, I noted above a tendency for low-excitation objects to be small (first discussed by Black 1992).

Two effects may be working in the same direction in this sample. In section 1.5.3 I noted that strong emission lines were anticorrelated with cluster membership not merely in radio sources but in the elliptical population as a whole. From table 5.2 we can see that the environments of the low-excitation objects are almost all classed as 'cluster' or 'group'. If these objects preferentially lie in dense environments, then their small sizes and dissipative jets are easily explained; for a given beam power and source age, a radio source in a denser environment is expected to be shorter (by the usual ram-pressure balance argument); the material within the lobes will be denser (by conservation of mass) and higher in pressure (if the lobes are in pressure equilibrium with the post-shock material surrounding them) and so a beam propagating through the lobe is likely to be more dissipative and less efficient; it is not necessary for the beam to interact directly with the external medium, although I argued this above for 3C 438. At the same time, as pointed out by Black (1992), objects lying in dense environments would be expected to be brighter for a given beam power than similar sources in isolated galaxies, or, equivalently, to have a lower beam power for a given total luminosity. If a lower beam power implies a lower emission-line luminosity, as argued by Rawlings and Saunders (1991), then we would expect a class of bright small objects with low emission-line power to exist. Thus the weak emission lines in these objects can be explained without reference to the general tendency for all objects in clusters to have weak lines.

The most general result of these arguments, whichever is correct, is that low-excitation objects are selected to lie in dense environments, and so that the relationship between emission line class and size is not surprising. The more specific result is that it is not surprising that the objects with apparently the least efficient beams should lie in this class. However, some of the low-excitation objects appear to have beams of normal efficiency (4C 14.11 and 3C 173.1 are examples of low-excitation objects which are perfectly normal in the radio). As noted above, low-excitation objects have no more detected jets than the other classes; nor is there generally any obvious relationship between environment and jet detection or prominence. The simplest explanation for these facts, and for the problems in fitting models to the low-excitation dataset, is that these objects are not a homogeneous population.

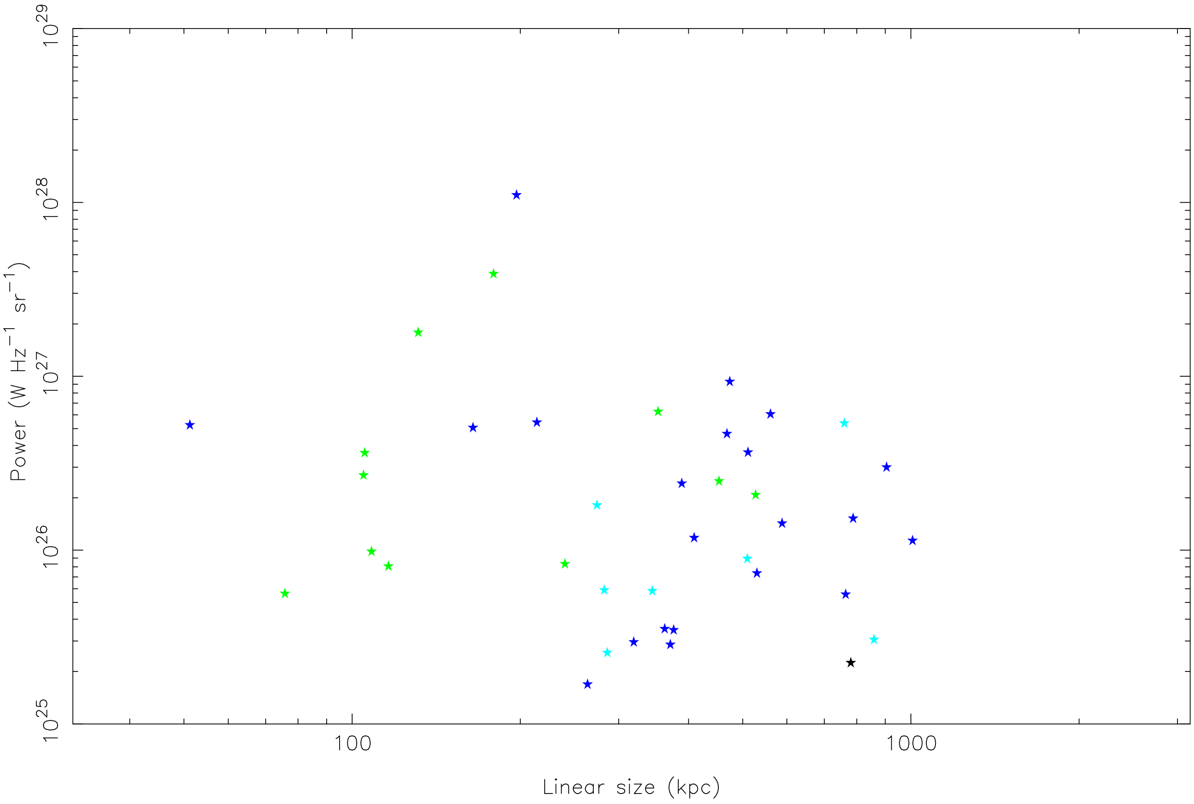

Figure 6.11: The power-linear size diagram for the sample of radio sources.

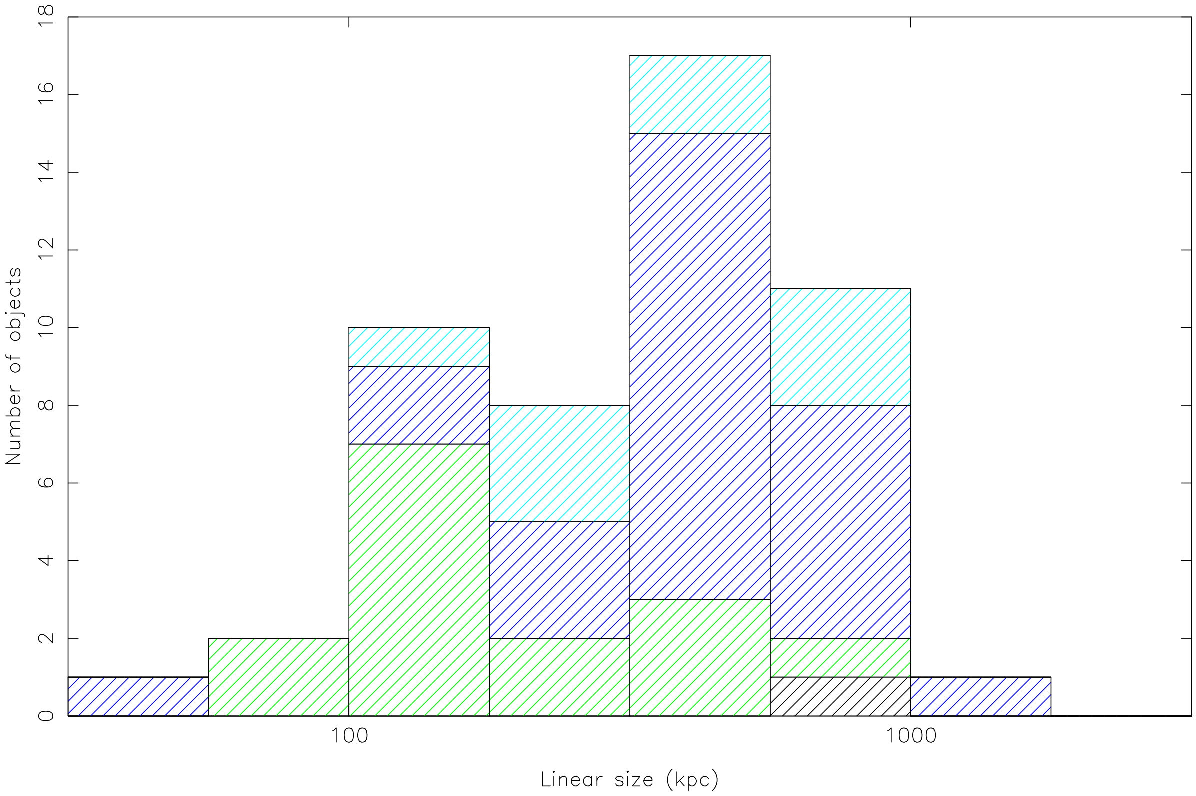

Figure 6.12: Histogram of linear sizes of the sample of radio sources.

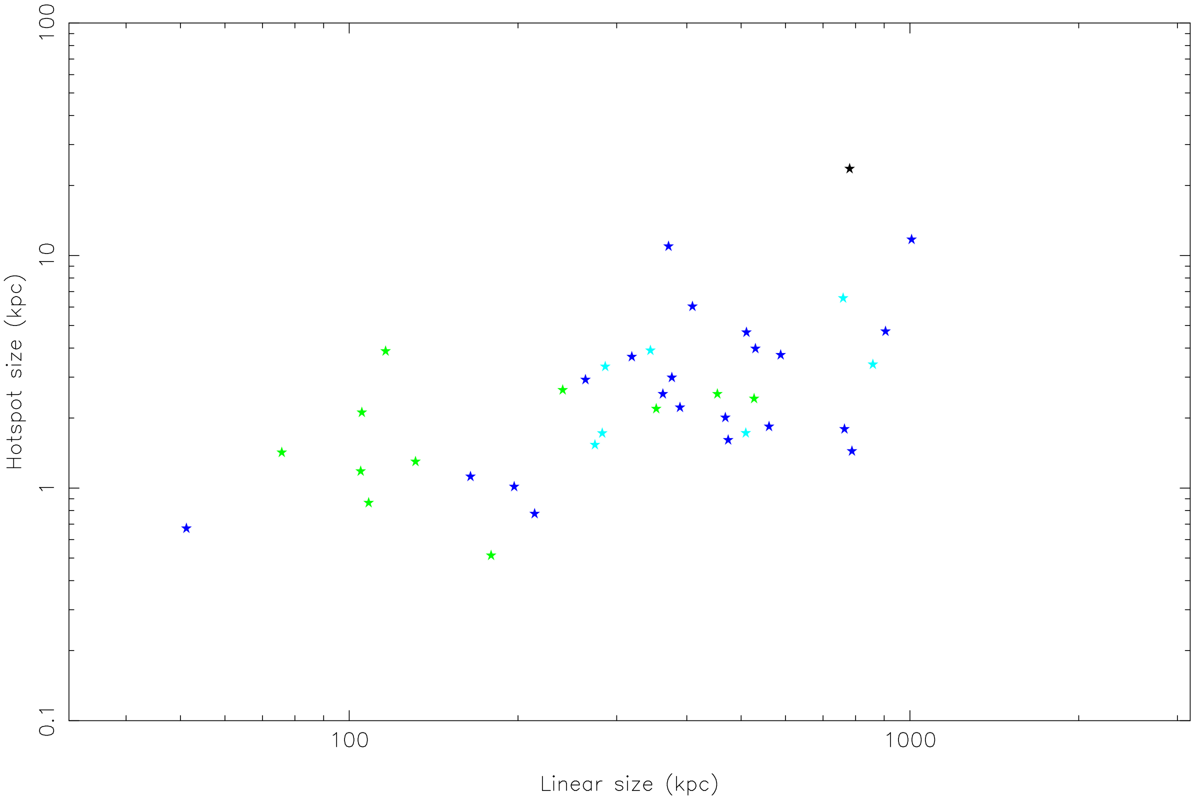

Figure 6.13: Linear sizes of the hot spots of the objects with good measurements against largest linear size.

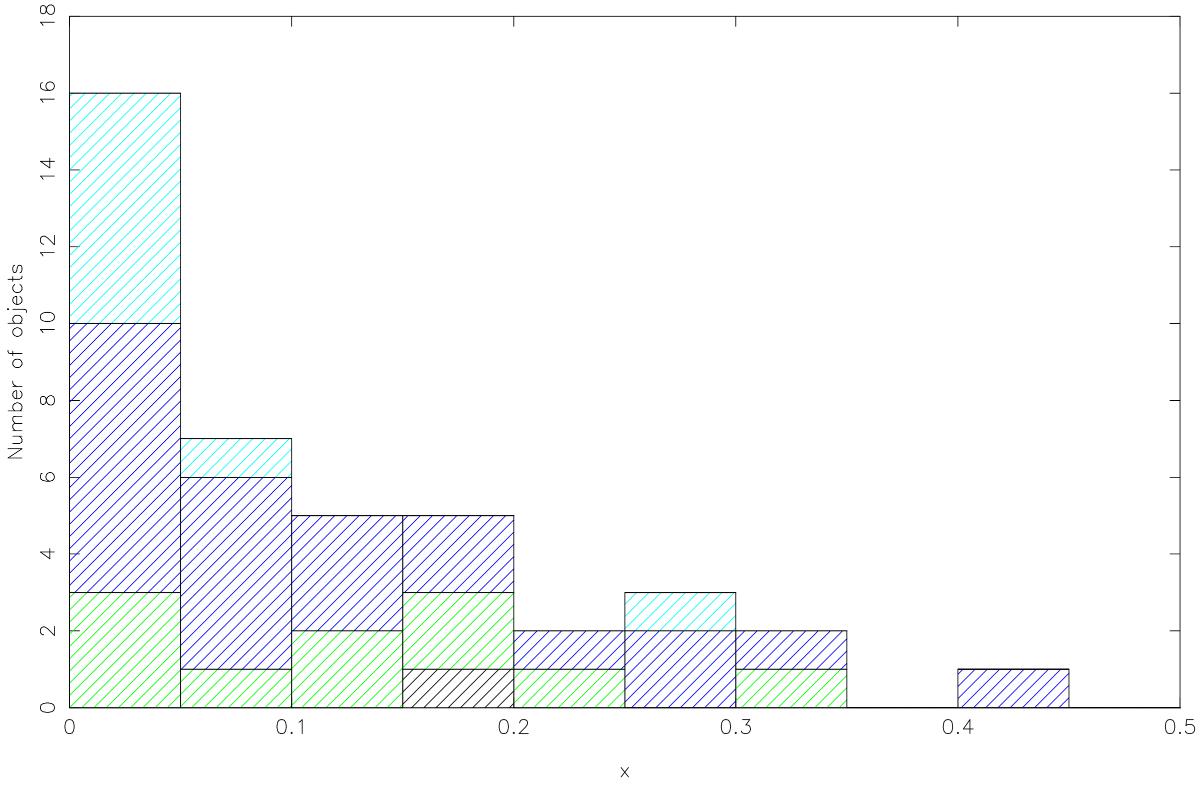

Figure 6.14: Histogram of the parameter x for the sources with measured hot spot positions.

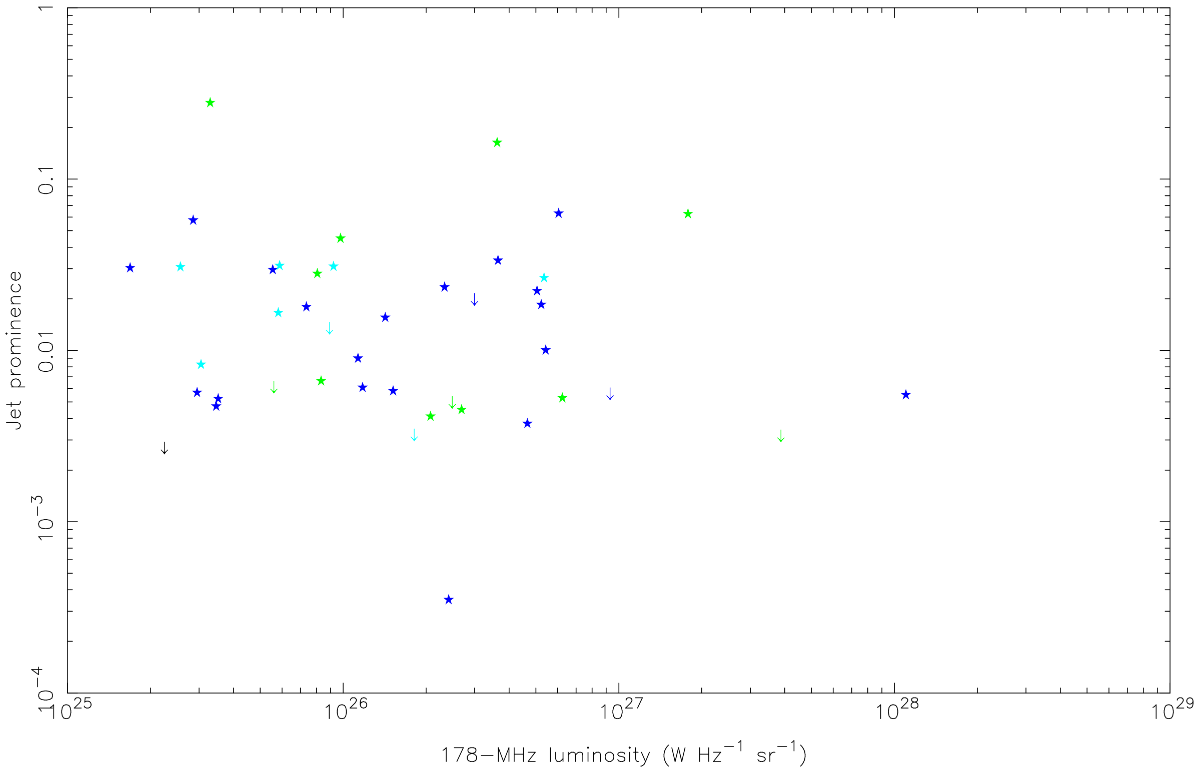

Figure 6.15: (Brightest) jet prominence against total low-frequency luminosity. Upper limits are marked with arrows.

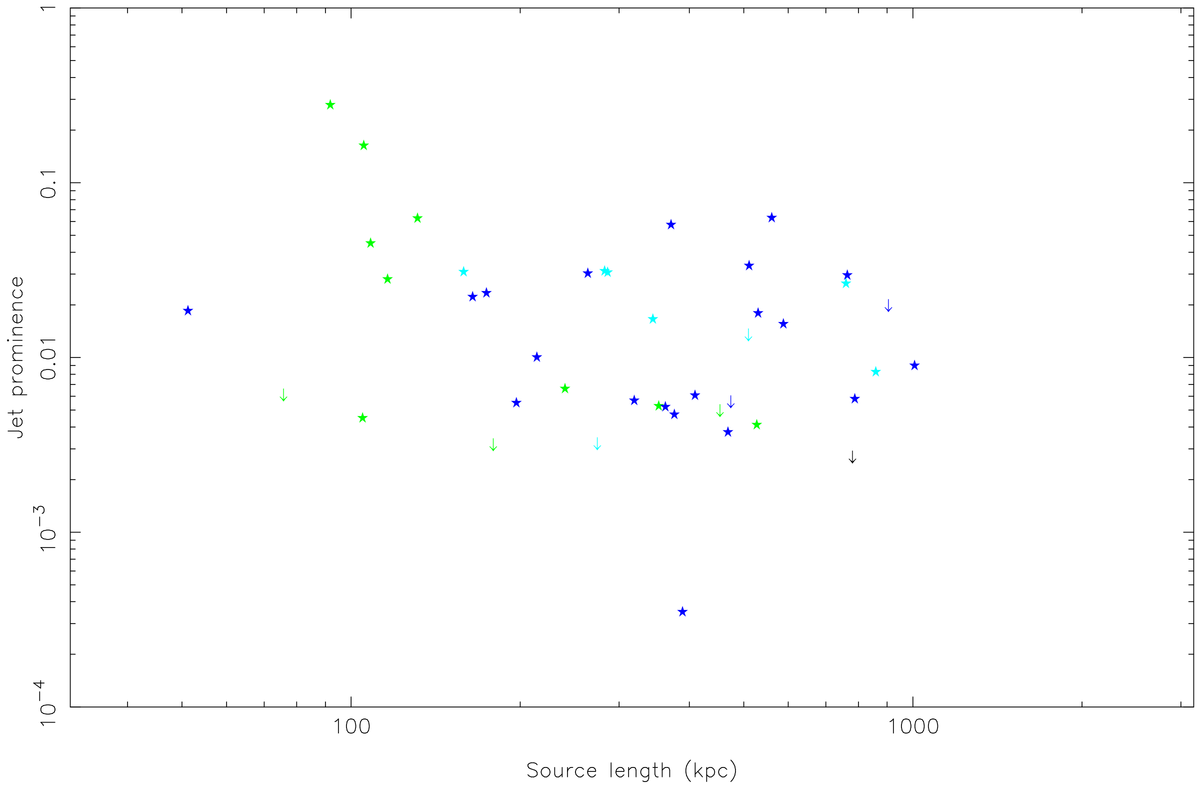

Figure 6.16: (Brightest) jet prominence against linear size. Upper limits are marked with arrows.

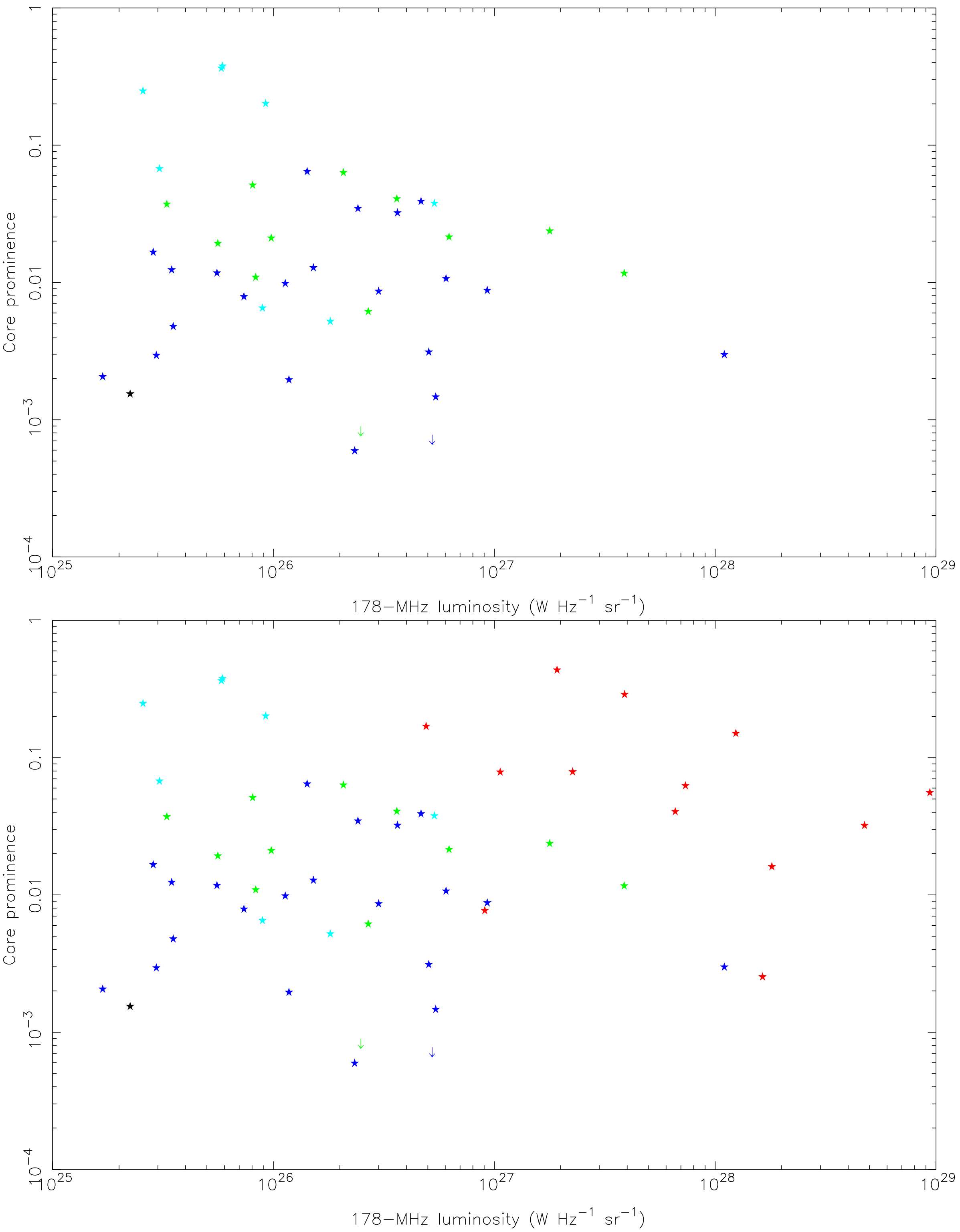

Figure 6.17: Core prominence as a function of luminosity. (a) Above, the radio galaxy sample. (b) Below, the radio galaxies with the B94 quasars.

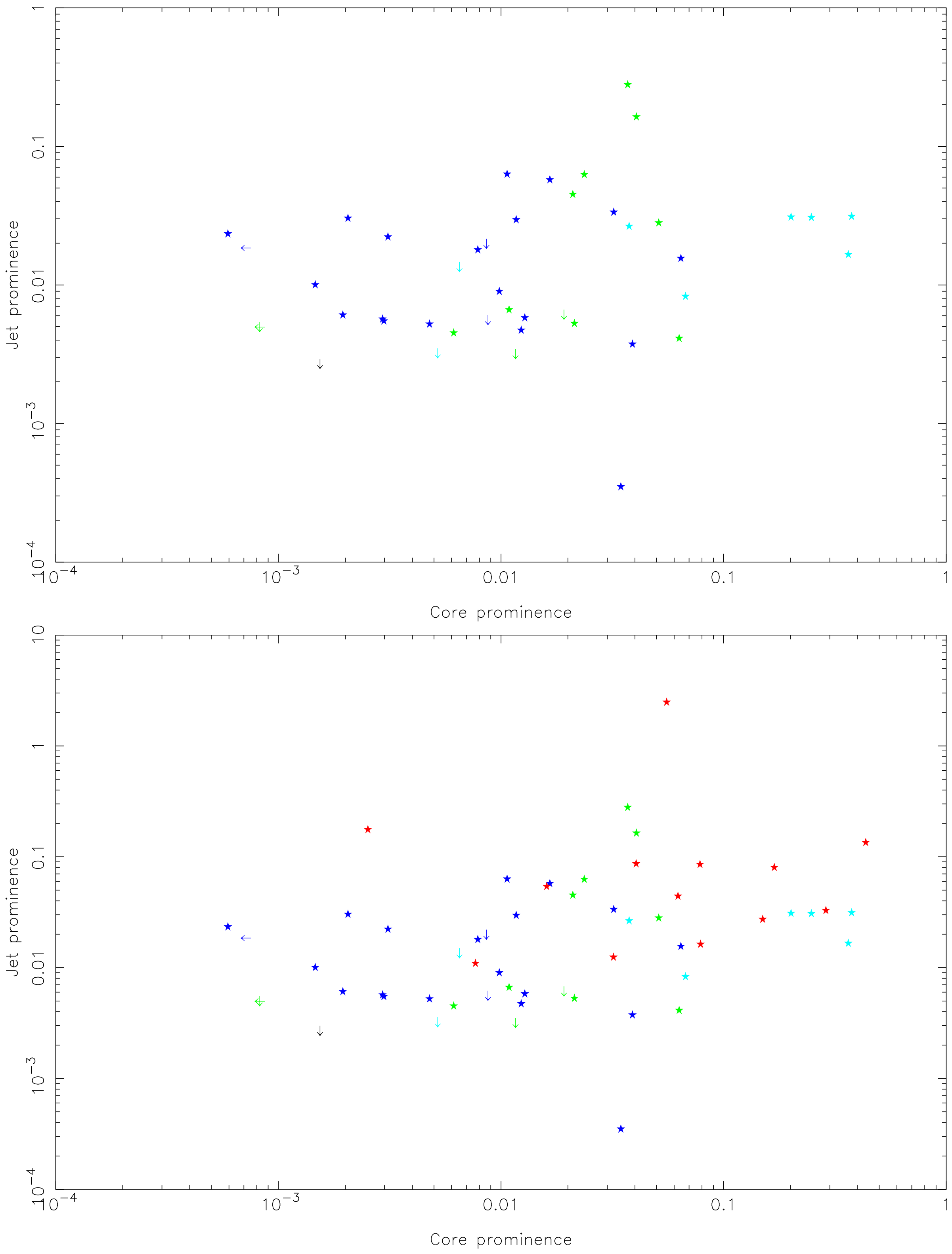

Figure 6.18: (Brightest) jet prominence as a function of core prominence. Upper limits are marked by arrows. (a) Above, the radio galaxy sample. (b) Below, the radio galaxies with the B94 quasars.

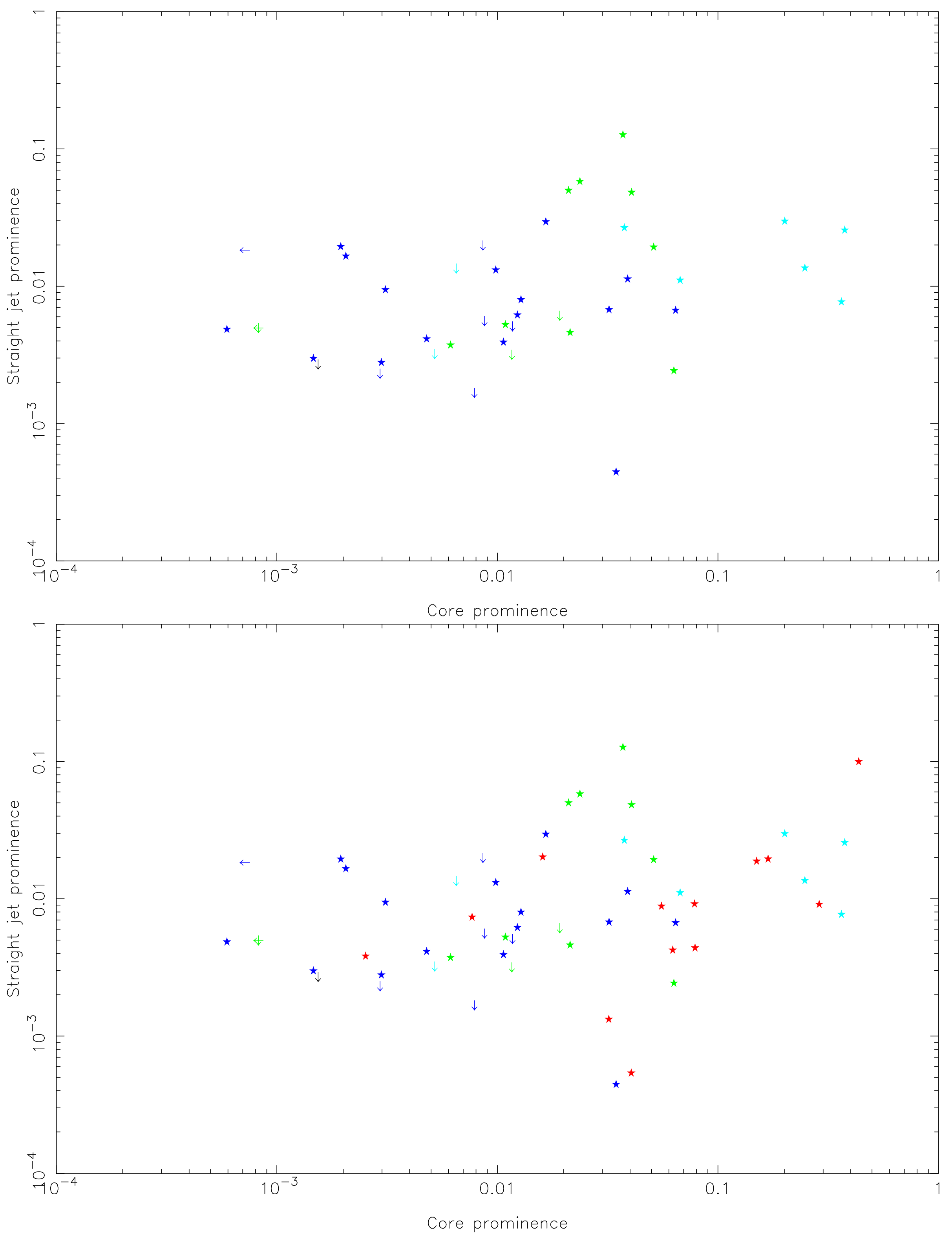

Figure 6.19: (Brightest) straight jet prominence against core prominence. Upper limits are marked by arrows. (a) Above, the radio galaxy sample. (b) Below, the radio galaxies with the B94 quasars.

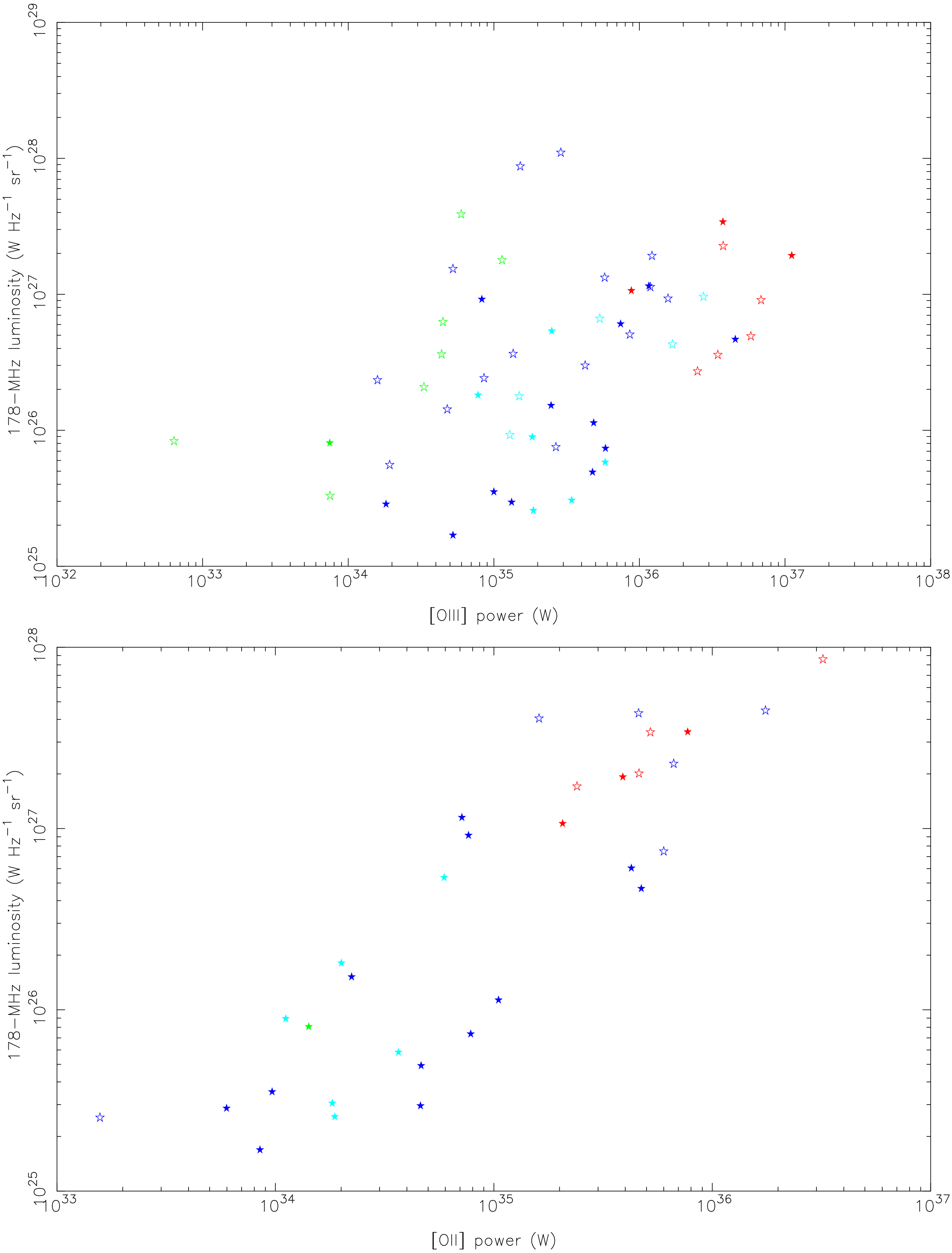

Figure 6.20: Lines and luminosities for an incomplete sample with $z < 0.6$. Above: 178-MHz luminosity against [OIII] power. Below: 178-MHz luminosity against [OII]λ3727 power. Objects appearing on both plots are represented by filled stars; objects appearing on one plot only are open.

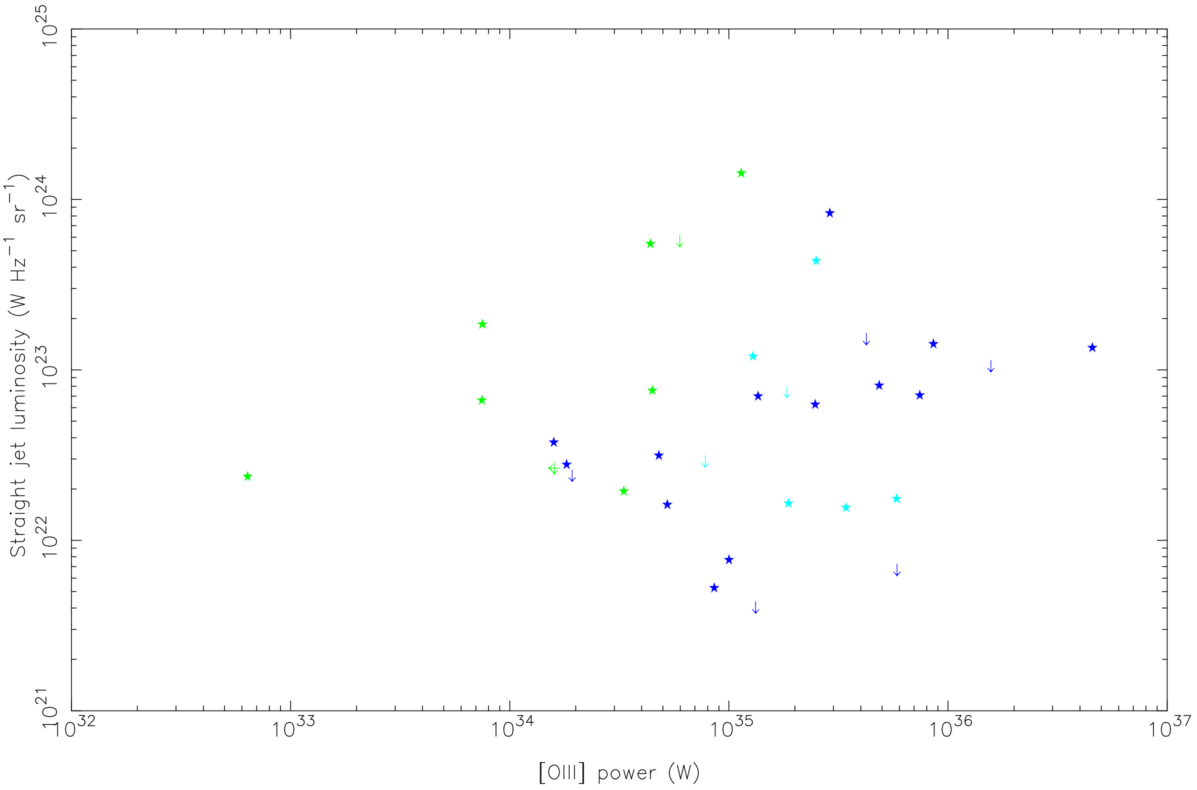

Figure 6.21: Straight jet luminosity against [OIII] power for 34 objects with $z < 0.3$

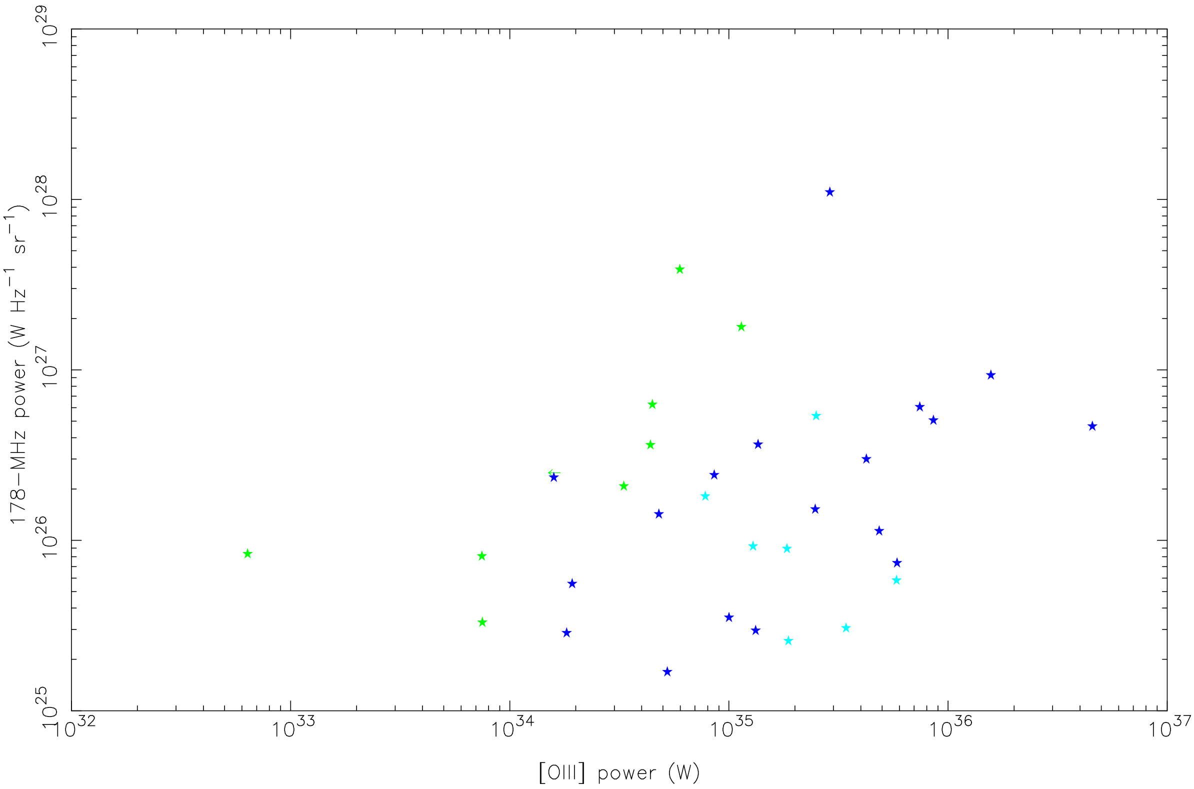

Figure 6.22: Total 178-MHz luminosity against [OIII] power for 34 objects with $z < 0.3$

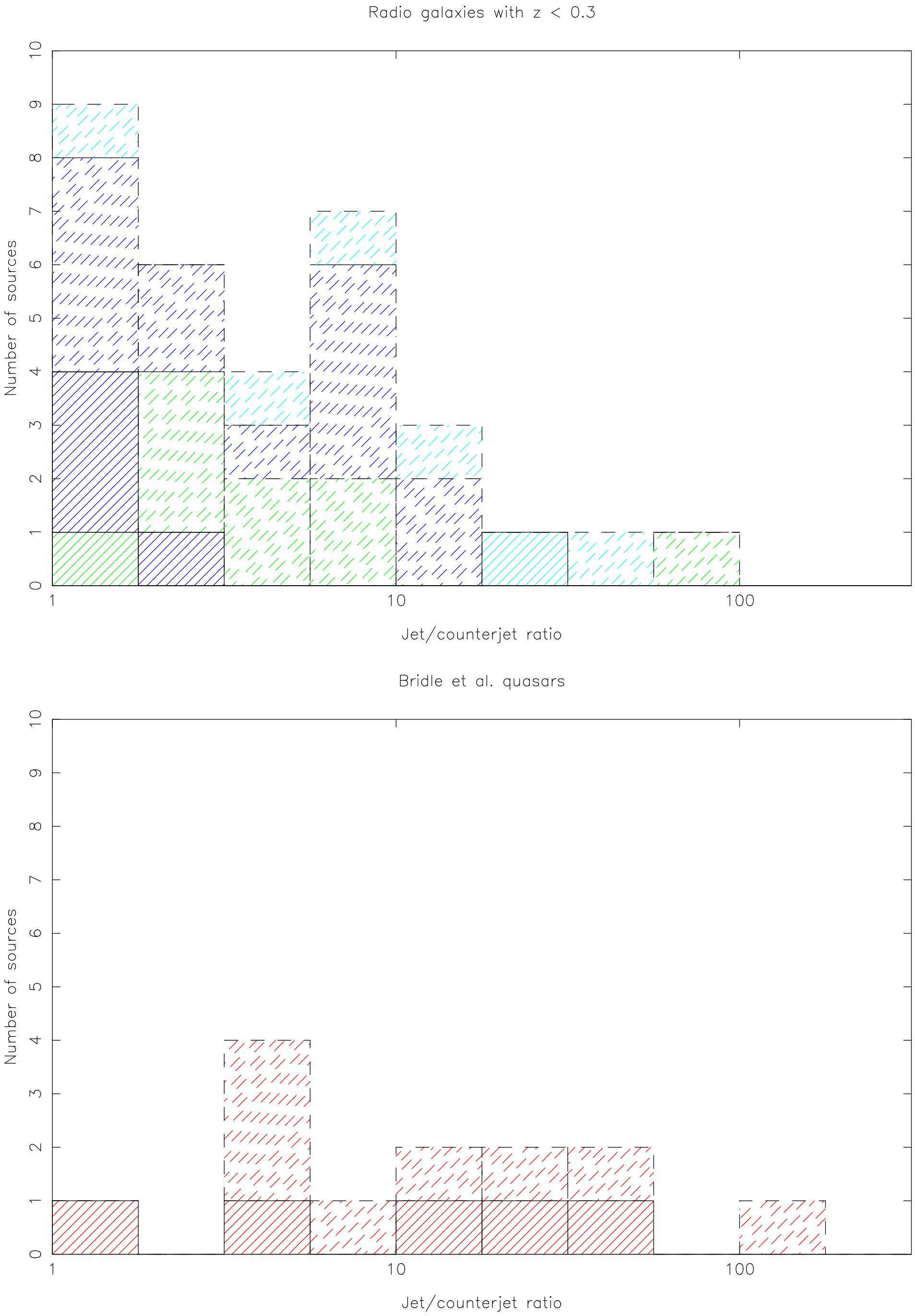

Figure 6.23: Jet sidedness of radio galaxies and quasars. Dashed shading indicates lower limits.

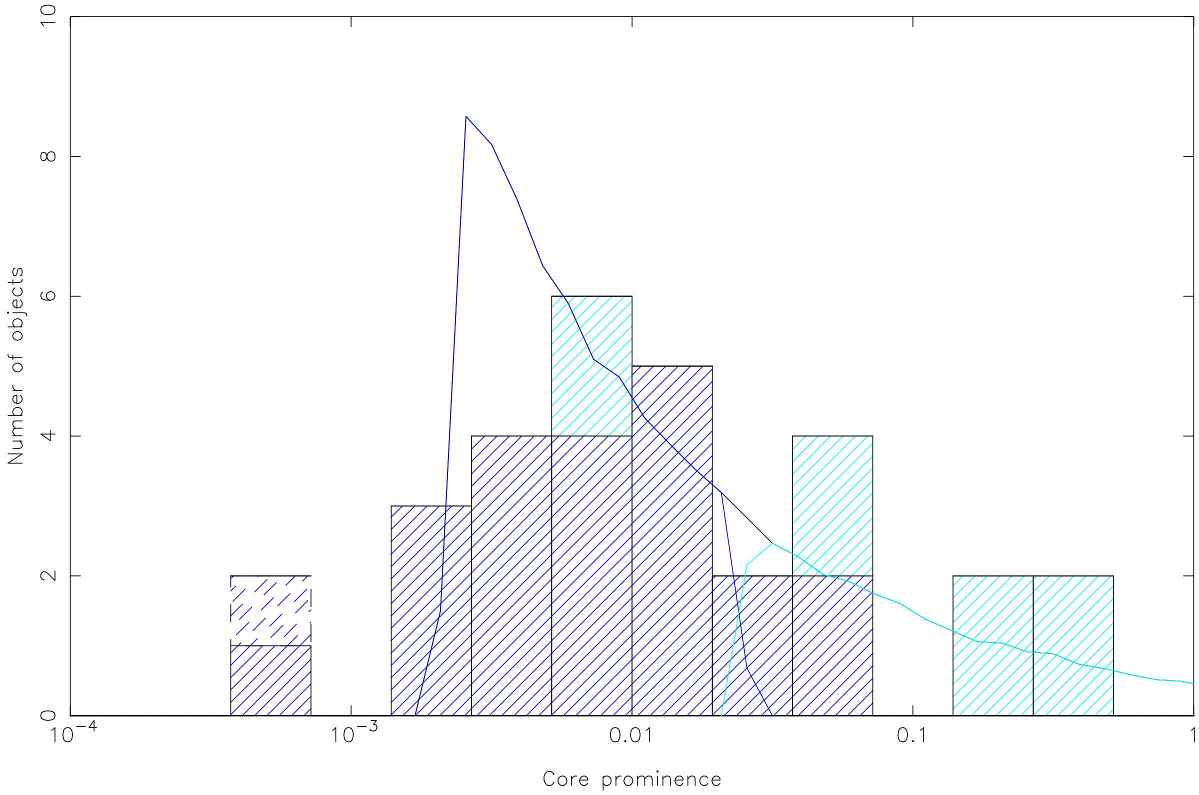

Figure 6.24: Core prominences of NLRG and BLRG. Dashed shading indicates upper limits. The solid line shows the best-fit single-velocity model, with $\beta_c = 0.985$; the dark blue line represents NLRG, the light blue BLRG, with the black showing the sum of the two. Sources treated as BLRG have simulated angle to the line of sight less than 45°.

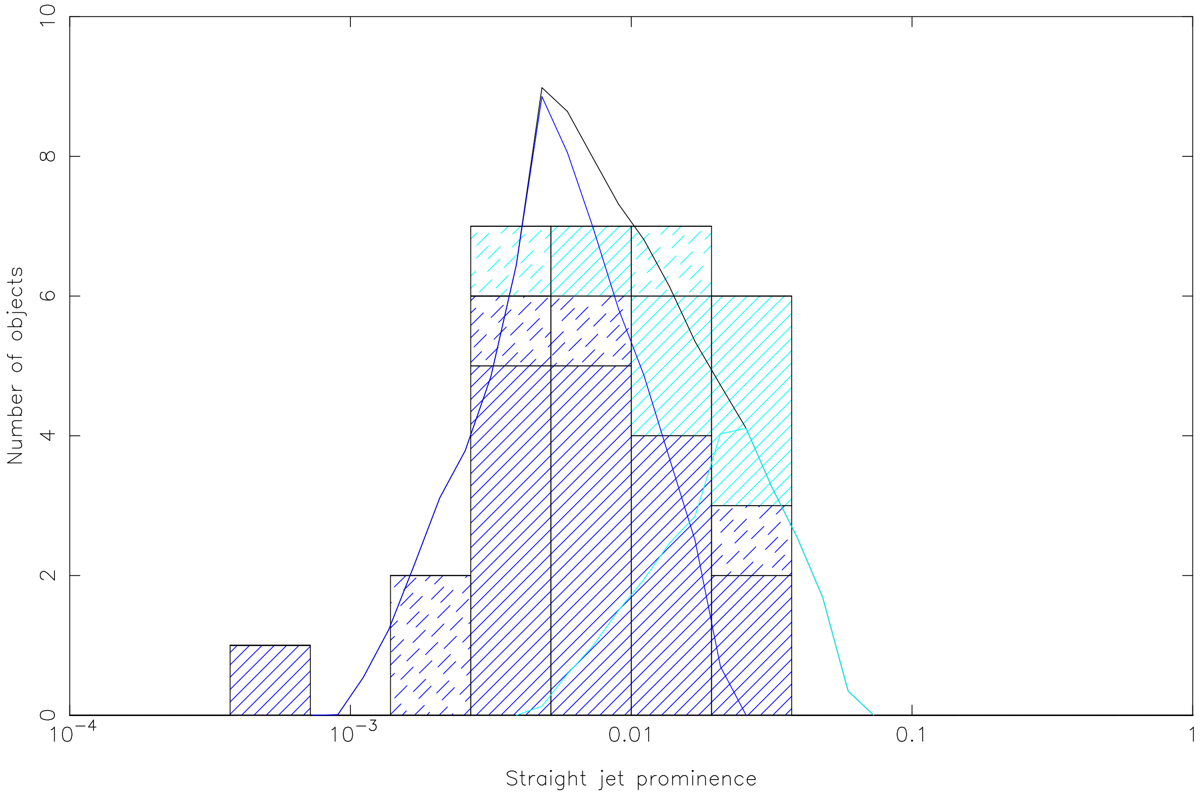

Figure 6.25: Straight jet prominences of NLRG and BLRG. Dashed shading indicates upper limits. The solid line shows the best-fit single-velocity model, with $\beta_j = 0.6$ and a distribution of jet lengths; the dark blue line represents NLRG, the light blue BLRG, with the black showing the sum of the two. Sources treated as BLRG have simulated angle to the line of sight less than 45°.

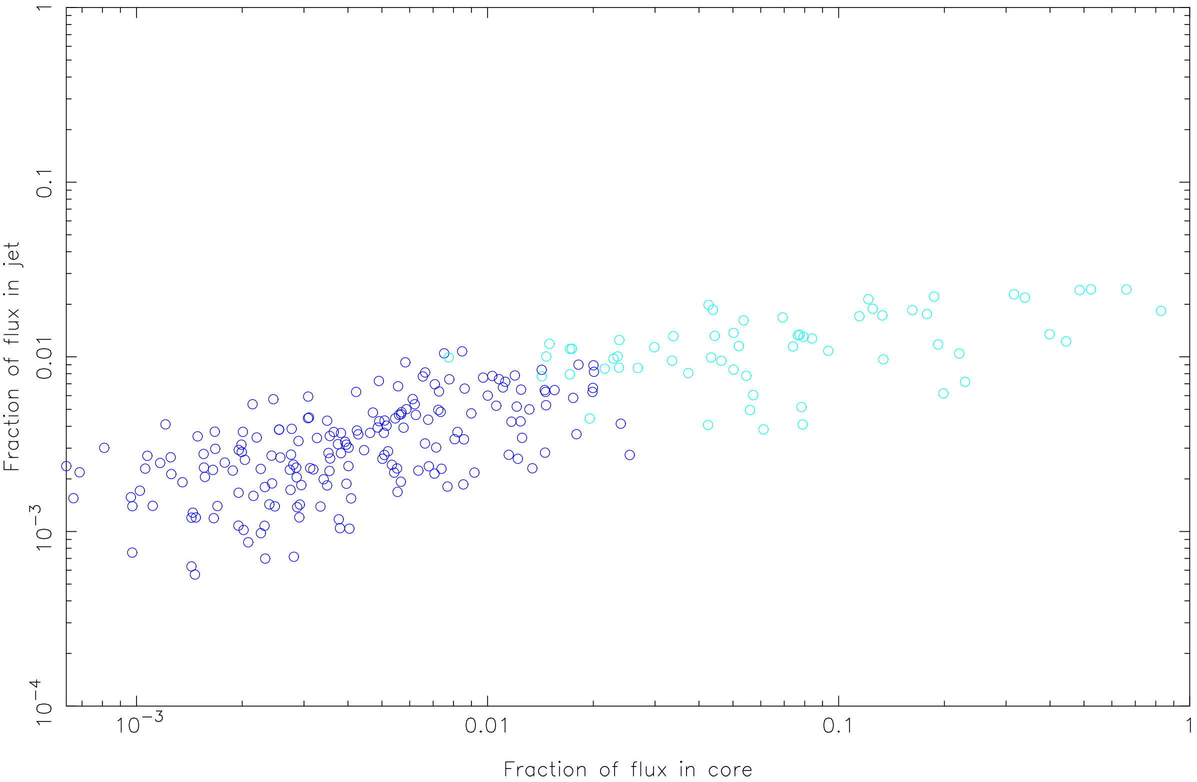

Figure 6.26: Simulations of straight jet prominence against core prominence. Parameters as discussed in the text. Light blue points have simulated angle to the line of sight less than 45°.

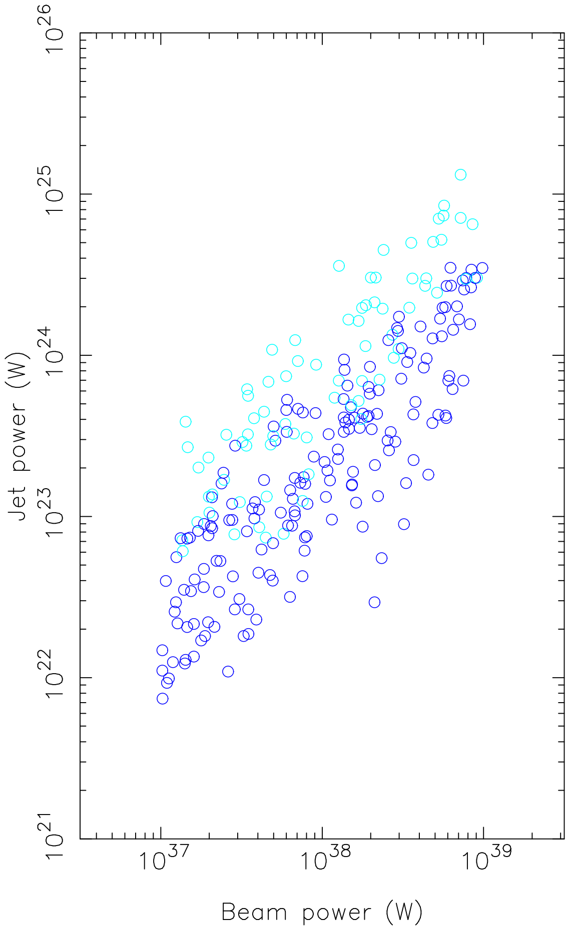

Figure 6.27: Simulations of straight jet power against beam power. Parameters as discussed in the text. Light blue points have simulated angle to the line of sight less than 45°.

Chapter 7

Conclusions

In this chapter I briefly review the main results of the thesis and discuss possible future work.

7.1 Retrospect

In chapter 2 I discussed the techniques necessary to make reliable maps from *uv* datasets containing a wide range of baselines, and the properties and problems of the different deconvolution techniques available. Flexible self-calibration and imaging strategies are necessary in order to get the best from this sort of database at all possible resolutions.

In chapter 3 I presented images of three twin-jet objects and one WAT. The twin-jet objects all show a change in magnetic field direction from a longitudinal to a transverse configuration at some distance from the core; I compared the appearances of the jets in these objects, and others in the literature, to models for the change in field direction and showed that none of them explains it completely. Two of the objects show evidence for a sheath of longitudinal magnetic field surrounding the transverse field at a few kpc from the core. I discussed this as evidence for a shear layer and deceleration in the jet. 3C 296 has a jet-counterjet ratio which is greater in the centre of the jet than at its edges, which supports this model if there are relativistic velocities in the jets; I considered the relativistic beaming model for 3C 66B and 3C 296 and found that the observations were consistent with moderate relativistic velocities and rapid deceleration of the jets. In the case of 3C 66B, which has an optical jet, I showed that the radio-optical spectrum was constant and curved in the inner 5 kpc of the jet, and discussed the necessity for some particle acceleration mechanism in this region in addition to the standard turbulent-entrainment mechanism which is thought to occur on large scales; although the location of such a mechanism is unclear, I suggested that it might be associated with the knotty structure of the 3C 66B jet.

My images of the WAT 3C 130 showed a compact, sub-kpc hot spot and two bright jets with marked bends and longitudinal magnetic field. I suggested that this supports models in which WATs are similar to FRIIs.

In chapter 4 I presented images of 17 FRII radio galaxies, part of a sample of 21 objects with $0.15 < z < 0.3$. These images are in most cases the best so far of the objects in question. I discussed the physics of particular objects in detail. Previously unknown jets were found in four objects; in total, the fraction of objects with definite or possible jet detections is 76%. Double and multiple hot spots were common. The magnetic field in the primary hot spot is generally transverse to the source axis. I suggested that in a number of cases this, together with other features of the sources, suggested that there was ongoing collimated outflow from the primary hot spots feeding the secondaries, but concluded that there is no single mechanism for producing all secondary hot spots.

In chapter 5 I collated radio and other data on a sample of 50 objects with $z < 0.3$, combining my sample of 21 with the 29 objects from B92. High-resolution images were available to me for a total of 43 of the objects, and where possible I measured the fluxes of jets, straight jets, hot spots, cores and lobes. In chapter 6 I investigated the relationships of these quantities in some depth. Results include:

- There is a tendency for the low-excitation objects to be smaller than the high-excitation ones.
- There is a correlation between the linear size of an object and the mean linear size of its hot spots.
- There is no strong relationship in this sample between the jet side and the brighter hot spot or the brighter or longer lobe.
- Jet prominence and detectability is not a function of luminosity; the high jet detection rate in this sample compared to that in previous work is a product of superior imaging techniques.
- Jet detectability is not obviously related to source spectral type, but the most prominent jets in the sample are those of low-excitation objects.
- There is little evidence for a correlation between core and jet prominence, as suggested by B94 for a sample of quasars.
- There is no obvious relationship between the power of the [OIII] line and the straight jet power.
- The objects in the present sample show less of a tendency to be one-sided than the quasars of B94.

I used Monte Carlo simulation to test the fit to this dataset of unified models involving relativistic beaming in the cores and jets. I concluded that the sample was reasonably well fitted by such models, with the velocities in the jets in the range 0.5 – 0.6*c* and the velocities in the cores being greater than 0.9*c*. I deduced an approximate value for the efficiency of a typical beam of 10^{-6} kpc^{-1}. I discussed the interpretation of these results, and suggested that the anomalous behaviour of the low-excitation objects could be explained if they were preferentially in dense environments.

7.2 Lessons and models

The external observer, seeing the beautiful, complicated and disparate images of individual objects now being produced (e.g. 3C 405, see figure 1.1; 3C 353, Swain *et al*. 1996), might wonder why we need more high-resolution, high-sensitivity maps and suggest that the observations have moved far ahead of our understanding of the physics. I hope that the present work has shown this reasoning to be wrong. Excellent work can be done on individual objects, but it is increasingly clear that there is no such thing as a ‘typical’ radio source from which the physics of all the others can be induced. It is only by observing large samples that we can now expect to advance our understanding of the physics from radio work alone.

My work has shown that moderately relativistic velocities in the beams of these objects are plausible on the grounds of their single-frequency radio behaviour alone: the jet sidednesses and polarization structures in the FRI objects, and the distributions of sidednesses, jet prominences and core prominences (supported by other observations) in the FRIIs. This complements work by others on different samples based on modelling of the core or jet prominences and of the luminosity functions, the Laing-Garrington effect in both types of sources, the VLBI observations, and so on. It is increasingly obvious that relativistic beaming is important at some level in all radio sources. Unified models which rely on this are safe; the precise details of unification of broad- and narrow-line radio galaxies are less clear, however.

I have also emphasised the rôle of the efficiency of the beam as a parameter determining source structure. This quantity has been neglected in models to date, partly because it is ‘hidden’ by beaming, partly because — as now appears — its variation can be large even when the effects of beaming are removed. Efficiency is clearly a function of luminosity; a twin-jet FRI converts much of its beam power into radiated jet power (though in the entrainment models the majority of the power will end up as kinetic energy of the cold entrained material; Bicknell 1996) whereas an FRII of the type discussed in chapter 6 loses a small fraction of its power on the way to the hot spots. The basic physics of this dichotomy is well understood; what remains to be made clear is the process by which efficiency is determined in the more powerful sources.

7.3 The future

The projects described here and in earlier work (B92, L96) have provided much observational information on the jets and hot spots in powerful radio sources and have (to some extent) made the physics of these regions clearer. Further advances could now come on several fronts:

- Further observations. In most other scientific disciplines fifty objects would not be considered a large sample; the fact that the present sample can be described as such reflects the difficulty of observing and imaging numbers of objects with the resolution and sensitivity required. The next step from the project of chapter 4 will be comparable observations of a higher-redshift sample; this work is already in progress. Similarly, the models discussed in chapter 3 need to be tested against a large and representative sample of well-imaged FRIs. At the same time, VLBI observations of both types of source are needed to constrain the parsec-scale velocities and jet sidedness; some of this will be done, for FRIs, in the next few years.
- Better modelling. The models against which the observations were compared in chapter 6 were simplistic at best. We are perhaps approaching the stage now where analytical models are detailed enough to be compared with more than just the lengths and powers of radio sources. Such a comparison could take proper account of selection effects, and would allow many more physical quantities to be constrained and related.
- Numerical simulation. The capabilities of simulation are improving rapidly, and simulations have been successful in reproducing much of the physics inferred from the images of hot spots. A couple of particular points where we might hope for an advance deserve mention. First is the perennial problem of visualisation — how to translate the results of a simulation into images comparable with what we observe. We still lack an understanding of where the synchrotron emission comes from. Second, and related, is the necessity (discussed above) for an understanding of where the emission comes from in the jets, and what determines their efficiency. Detailed simulations of the behaviour of jets of different power as they propagate through a realistic medium are necessary.
- Other wavebands. It is remarkable that after a quarter of a century there is still no consensus on the environment of particular sources. Information of this kind is vital if models are ever to be able to reproduce the data, since we know that the environment can affect the behaviour of radio sources on all scales. We are now starting to learn something about the nuclei of 3CR host galaxies from HST observations; also necessary are *reliable* clustering analyses and X-ray observation. These may start to become available in the next few years.

Index of radio sources

References

Akujor C.E., Spencer R.E., Zhiang F.J., Davis R.J., Browne I.W.A., Fanti C., 1991, M.N.R.A.S. **250** 215

Alef W., Wu S.Y., Preuss E., Kellermann K.I., Qiu Y.H., 1996, Astron. Astrophys. **308** 376

Alexander P., 1985, PhD thesis, University of Cambridge

Alexander P., 1987, M.N.R.A.S. **225** 27

Alexander P., Leahy J.P., 1987, M.N.R.A.S. **224** 1

Allington-Smith J.R., Ellis R.S., Zirbel E.L., Oemler A., 1993, Astrophys. J. **404** 521

Antonucci R., 1993, Ann. Rev. Astron. Astrophys. **31** 473

Antonucci R.R.J., 1982, Nature **299** 65

Antonucci R.R.J., 1984, Astrophys. J. **281** 112

Antonucci R.R.J., 1985, Astrophys. J. Suppl. **59** 499

Antonucci R.R.J., Ulvestad J.S., 1985, Astrophys. J. **294** 158

Baars J.W.M., Genzel R., Pauliny-Toth I.I.K., Witzel A., 1977, Astron. Astrophys. **61** 99

Balcells M., Morganti R., Oosterloo T., Pérez-Fournon I., González-Serrano J.I., 1995, Astron. Astrophys. **302** 665

Barthel P.D., 1987, in Zensus J., Pearson T., eds, *Superluminal Radio Sources*, Cambridge University Press, Cambridge, p. 148

Barthel P.D., 1989, Astrophys. J. **336** 606

Barthel P.D., 1994, in Bicknell G.V., Dopita M.A., Quinn P.J., eds, *The First Stromlo Symposium: the Physics of Active Galaxies*, ASP Conference Series vol. 54, San Francisco, p. 175

Baum S.A., Heckman T., 1989a, Astrophys. J. **336** 681

Baum S.A., Heckman T., 1989b, Astrophys. J. **336** 702

Bennett A.S., 1962, Mem. R.A.S. **68** 163

Begelman M.C., Blandford R.D., Rees M.J., 1984, Rev. Mod. Phys. 56 255

Best P.N., Bailer D.M., Longair M.S., Riley J.M., 1995, M.N.R.A.S. **275** 1171

Bicknell G.V., 1986, Astrophys. J. **300** 591

Bicknell G.V., 1994, Astrophys. J. **422** 542

Bicknell G.V., 1996, in Hardee P.E., Bridle A.H., Zensus J.A., eds, *Energy Transport in Radio Galaxies and Quasars*, ASP Conference Series vol. 100, San Francisco, p. 253

Bicknell G.V., De Ruiter H.R., Fanti R., Morganti R., Parma P., 1990, Astrophys. J. **354** 98

Biretta J.A., 1993, in Burgarella D., Livio M., O'Dea C.P., eds, *Astrophysical Jets*, Space Telescope Science Institute Symposium Series 6, Cambridge University Press, Cambridge, p. 263

Biretta J.A., Meisenheimer K., 1993, in Röser H.-J., Meisenheimer K., eds, *Jets in Extragalactic Radio Sources*, Springer-Verlag, Heidelberg, p. 159

Biretta J.A., Stern C.P., Harris D.E., 1991, Astrophys. J. **101** 1632

Biretta J.A., Zhou F., Owen F.N., 1995, Astrophys. J. **447** 582

Birkinshaw M., Laing R., Scheuer P., Simon A., 1978, M.N.R.A.S. **185** 39

Birkinshaw M., Laing R.A., Peacock J.A., 1981, M.N.R.A.S. **197** 253

Birkinshaw M., Worrall D.M., 1996, in Hardee P.E., Bridle A.H., Zensus J.A., eds, *Energy Transport in Radio Galaxies and Quasars*, ASP Conference Series vol. 100, San Francisco, p. 335

Black A.R.S., 1992, PhD thesis, University of Cambridge

Black A.R.S., Baum S.A., Leahy J.P., Perley R.A., Riley J.M., Scheuer P.A.G., 1992, M.N.R.A.S. **256** 186 [B92]

Black A.R.S., 1993, in Röser H.-J., Meisenheimer K., eds, *Jets in Extragalactic Radio Sources*, Springer-Verlag, Heidelberg, p. 15

Blandford R.D., Rees M.J., 1974, M.N.R.A.S. **169** 395

Blandford R., Rees M.J., 1978, in Wolfe A.M., ed., *Pittsburgh Conference on BL Lac Objects*, Univ. Pittsburgh, Pittsburgh, p. 328

Blundell K.M., 1994, PhD thesis, University of Cambridge

Bridle A.H., 1982, in Heeschen, D.S., Wade C.M., eds, *Extragalactic Radio Sources*, IAU Symposium 97, Reidel, Dordrecht, p. 121

Bridle A.H., 1984, Astron. J. **89** 979

Bridle A.H., Fomalont E.B., 1979, Astron. J. **84** 1679

Bridle A.H., Fomalont E.B., Byrd G.G., Valtonen M.J., 1989, Astron. J. **97** 674

Bridle A.H., Hough D.H., Lonsdale C.J., Burns J.O., Laing R.A., 1994a, Astron. J. **108** 766 [B94]

Bridle A.H., Laing R.A., Scheuer P.A.G., Turner S., 1994b, in Bicknell G.V., Dopita M.A., Quinn P.J., eds, *The First Stromlo Symposium: the Physics of Active Galaxies*, ASP Conference Series vol. 54, San Francisco, p. 187

Bridle A.H., Perley R.A., 1984, Ann. Rev. Astron. Astrophys. **22** 319 [BP]

Browne I.W.A., 1983, M.N.R.A.S. **204** 23p

Burch S.F., 1979a, M.N.R.A.S. **186** 293

Burch S.F., 1979b, M.N.R.A.S. **186** 519

Burch S.F., 1979c, M.N.R.A.S. **187** 187

Burn B.J., 1966, M.N.R.A.S. **133** 67

Burns J.O., Basart J.P., de Young D.S., Ghiglia D.C., 1984, Astrophys. J. **283** 515

Burns J.O., Gregory S.A., 1982, Astron. J. **87** 1245

Butcher H.R., van Breugel W., Miley G.K., 1980, Astrophys. J. **235** 749

Caganoff S., Bicknell G., Carter D., 1985, Proc. Astr. Soc. Austr. vol. 6, no. 2, p. 151

Carilli C.L., Dreher J.W., Perley R.A., 1989, in Meisenheimer K., Röser H.-J., eds, *Hotspots in Extragalactic Radio Sources*, Springer-Verlag, Heidelberg, p. 51

Carilli C.L., Harris D.E., 1996, *Cygnus A: Study of a Radio Galaxy*, Cambridge University Press, Cambridge

Carilli C.L., Perley R.A., Harris D.E., 1994, M.N.R.A.S. **270** 173

Chambers K.C., Miley G.K., van Breugel W., 1987, Nature **329** 604

Cimatti A., Di Seregho Alghieri S., Fosbury R.A.E., Salvati M., Taylor D., 1993, M.N.R.A.S. **264** 421

Cimatti A., di Serego Alghieri S., 1995, M.N.R.A.S. **273** L7

Clarke D.A., Bridle A.H., Burns J.O., Perley R.A., Norman M.L., 1992, Astrophys. J. **385** 173

Cohen R.D., Osterbrock D.E., 1981, Astrophys. J. **243** 81

Colina L., Pérez-Fournon I., 1990, Astrophys. J. Suppl. **72** 41

Conway J.E., Cornwell T.J., Wilkinson P.N., 1990, M.N.R.A.S. **246** 490

Cox C.I., 1990, PhD thesis, University of Cambridge

Cox C.I., Gull S.F., Scheuer P.A.G., 1991, M.N.R.A.S. **252** 588

Crane P., 1993, in Röser H.-J., Meisenheimer K., eds, *Jets in Extragalactic Radio Sources*, Springer-Verlag, Heidelberg, p. 223

Crane P., Tyson J.A., Saslaw W.C., 1983, Astrophys. J. **265** 681

de Koff S., Baum S.A., Sparks W.B., Biretta J., Golombek D., Machetto F., McCarthy P., Miley G.K., 1996, Astrophys. J. **,** in press [dK96]

Dreher J.W., 1981, Astron. J. **86** 833

Dunlop J.S., Peacock J.A., 1993, M.N.R.A.S. **263** 936

Eales S.A., 1985a, M.N.R.A.S. **213** 899

Eales S.A., 1985b, PhD thesis, University of Cambridge

Eracleous M., Halpern J.P., 1994, Astrophys. J. Suppl. **90** 1

Fabbiano G., Miller L., Trinchieri G., Longair M., Elvis M., 1984, Astrophys. J. **277** 115

Fanaroff B.L., Riley J.M., 1974, M.N.R.A.S. **167** 31P

Fasano G., Falomo R., Scarpa R., 1996, M.N.R.A.S. **282** 40

Feigelson E.G., Berg C.J., 1983, Astrophys. J. **269** 400

Felten J.E., 1968, Astrophys. J. **151** 861

Feretti L., Gioia I.M., Giovannini G., Gregorini L., Padrielli L., 1984, Astron. Astrophys. **139** 50

Fernini I., Burns J.O., Bridle A.H., Perley R.A., 1993, Astron. J. **105** 1690

Ficarra A., Grueff G., Tomassetti G., 1985, Astron. Astrophys. Suppl. **59** 255

Fleming T.R., O'Fallon J.R., O'Brien P.C., Harrington D.P., 1980, Biometrics **36** 607

Fomalont E.B., Bridle A.H., Willis A.G., Perley R.A., 1980, Astrophys. J. **237** 418

Fraix-Burnet D., 1992, Astron. Astrophys. **259** 445

Fraix-Burnet D., Nieto J.-L., Lelièvre G., Macchetto F.D., Perryman M.A.X., di Serego Alghieri S., 1989a, Astrophys. J. **336** 121

Fraix-Burnet D., Nieto J.-L., Poulain P., 1989b, Astron. Astrophys. **221** L1

Garrington S., Leahy J.P., Conway R.G., Laing R.A., 1988, Nature **331** 147

Garrington S.T., Conway R.G., 1991, M.N.R.A.S. **250** 198

Garrington S.T., Conway R.G., Leahy J.P., 1991, M.N.R.A.S. **250** 171

Giovannini G., Feretti L., Gregorini L., Parma P., 1988, Astron. Astrophys. **199** 73

Giovannini G., Venturi T., Feretti L., Comoretto G., Wehrle A.E., 1993, in Röser H.-J., Meisenheimer K., eds, *Jets in Extragalactic Radio Sources*, Springer-Verlag, Heidelberg, p. 65

Gisler G.R., 1978, M.N.R.A.S. **183** 633

Gower J.F.R., Scott P.F., Wills D., 1967, Mem. R.A.S. **71** 49

Grandi S.C., Osterbrock D.E., 1978, Astrophys. J. **220** 783

Gregorini L., Padrielli L., Parma P., Gilmore G., 1988, Astron. Astrophys. Suppl. **74** 107

Guthrie B.N.G., 1979, M.N.R.A.S. **187** 581

Guthrie B.N.G., 1981, M.N.R.A.S. **194** 261

Hales S.E.G., Baldwin J.E., Warner P.J., 1988, M.N.R.A.S. **234** 919

Hardcastle M.J., Alexander P., Pooley G.G., Riley J.M., 1996, M.N.R.A.S. **278** 273

Hardee P.E., Norman M.L., 1990, Astrophys. J. **365** 134

Hargrave P.J., Ryle M.J., 1974, M.N.R.A.S. **166** 305

Harris D.E., Carilli C.L., Perley R.A., 1994, Nature **367** 713

Harris D.E., Stern C.P., 1987, Astrophys. J. **313** 136

Heavens A.F., Meisenheimer K., 1987, M.N.R.A.S. **225** 335

Heckman T.M., Smith E.P., Baum S.A., van Breugel W.J.M., Miley G.K., Illingworth G.D., Bothun G.D., Balick B., 1986, Astrophys. J. **311** 526

Heckman T.M., van Breugel W.J.M., Miley G.K., 1984, Astrophys. J. **286** 509

Hes R., 1995, PhD thesis, University of Gronigen

Hes R., Barthel P.D., Fosbury R.A.E., 1993, Nature **362** 326

Hewitt A., Burbidge G., 1987, Astrophys. J. Suppl. **63** 1

Hill G.J., Lilly S.J., 1991, Astrophys. J. **367** 1

Hiltner P.R., Meisenheimer K., Röser H.J., Laing R.A., Perley R.A., 1994, Astron. Astrophys. **286** 25

Hine R.G., Longair M.S., 1979, M.N.R.A.S. **188** 111

Higgins S., O'Brien T., Dunlop J., 1996, in Ekers R.D., Fanti C., Padrielli L., eds, *Extragalactic Radio Sources*, IAU Symposium 175, Kluwer, Dordrecht, in press

Hough D.H., 1994, in Zensus J.A., Kellermann K.I., eds, *Compact Extragalactic Radio Sources*, NRAO workshop no. 23, NRAO, Green Bank, West Virginia, p. 169

Hughes P.A., Miller L., 1991, in Hughes P.A., ed., *Beams and Jets in Astrophysics*, Cambridge University Press, Cambridge, p. 1

Hutchings J.B., 1987, Astrophys. J. **320** 122

Hutchings J.B., Johnson I., Pyke R., 1988, Astrophys. J. Suppl. **66** 361

Inoue M., Tabara H., Kato T., Aizu K., 1995, Pub. Astr. Soc. Japan **47** 725

Jägers W.J., 1983, Astron. Astrophys. **125** 172

Jackson N., Browne I.W.A., 1991, M.N.R.A.S. **250** 422

Jackson N., Browne I.W.A., 1990, Nature **343** 43

Jackson N., Sparks W.B., Miley G.K., Macchetto F., 1993, Astron. Astrophys. **269** 128

Jenkins C.J., McEllin M., 1977, M.N.R.A.S. **180** 219

Jenkins C.J., Pooley G.G., Riley J.M., 1977, Mem. R.A.S. **84** 61 [JPR]

Jennison R.C., Das Gupta M.S., 1953, Nature **172** 996

Johnson R.A., Leahy J.P., Garrington S.T., 1995, M.N.R.A.S. **273** 877

Kapahi V.K., Murphy D.W., 1990, in Zensus J.A., Pearson T.J., eds, *Parsec-scale Radio Jets*, Cambridge University Press, Cambridge, p. 313

Keel W.C., 1988, Astrophys. J. **329** 532

Keel W.C., Martini P., 1995, Astron. J. **109** 2305

Kellermann K.I., Pauliny-Toth I.I.K., Williams P.J.S., 1969, Astrophys. J. **157** 1 [KPW]

Killeen N.C.B., Bicknell G.V., Ekers R.D., 1986, Astrophys. J. **302** 306

Kollgaard R.I., Wardle J.F.C., Roberts D.H., Gabuzda D.C., 1992, Astron. J. **104** 1687

Komissarov S.S., Falle S.A.E.G., 1996, in Hardee P.E., Bridle A.H., Zensus J.A., eds, *Energy Transport in Radio Galaxies and Quasars*, ASP Conference Series vol. 100, San Francisco, p. 327

Konigl A., Choudhuri A.R., 1985, Astrophys. J. **289** 173

Kronberg P.P., Strom R.G., 1977, Astrophys. J. **215** 438

Laing R.A., 1980, M.N.R.A.S. **193** 439

Laing R.A., 1981a, Astrophys. J. **248** 87

Laing R.A., 1981b, M.N.R.A.S. **195** 261

Laing R.A., 1982, in Heeschen, D.S., Wade C.M., eds, *Extragalactic Radio Sources*, IAU Symposium 97, Reidel, Dordrecht, p. 161

Laing R.A., 1984, in Bridle A.H., Eilek J.A., eds, *Physics of Energy Transport in Radio Galaxies*, NRAO Workshop no. 9, NRAO, Green Bank, West Virginia, p. 90

Laing R.A., 1988, Nature **331** 149

Laing R.A., 1989, in Meisenheimer K., Röser H.-J., eds, *Hotspots in Extragalactic Radio Sources*, Springer-Verlag, Heidelberg, p. 27

Laing R.A., 1993, in Burgarella D., Livio M., O'Dea C.P., eds, *Astrophysical Jets*, Space Telescope Science Institute Symposium Series 6, Cambridge University Press, Cambridge, p. 95

Laing R.A., 1996, in Hardee P.E., Bridle A.H., Zensus J.A., eds, *Energy Transport in Radio Galaxies and Quasars*, ASP Conference Series vol. 100, San Francisco, p. 241

Laing R.A., Bridle A.H., 1987, M.N.R.A.S. **228** 557

Laing R.A., Jenkins C.R., Wall J.V., Unger S.W., 1994, in Bicknell G.V., Dopita M.A., Quinn P.J., eds, *The First Stromlo Symposium: the Physics of Active Galaxies*, ASP Conference Series vol. 54, San Francisco, p. 201

Laing R.A., Peacock J.A., 1980, M.N.R.A.S. **190** 903

Laing R.A., Riley J.M., Longair M.S., 1983, M.N.R.A.S. **204** 151 [LRL]

Law-Green J.D.B., Leahy J.P., Alexander P., Allington-Smith J.R., van Breugel W.J.M., Eales S.A., Rawlings S.G., Spinrad H., 1995, M.N.R.A.S. **274** 939

Lawrence C.R., Pearson T.J., Readhead A.C.S., Unwin S.C., 1986, Astron. J. **91** 494

Leahy J.P., 1984, M.N.R.A.S. **208** 323

Leahy J.P., 1985, PhD thesis, University of Cambridge

Leahy J.P., 1991, in Hughes P.A., ed., *Beams and Jets in Astrophysics*, Cambridge University Press, Cambridge, p. 100

Leahy J.P., 1993, in Röser H.-J., Meisenheimer K., eds, *Jets in Extragalactic Radio Sources*, Springer-Verlag, Heidelberg, p. 1

Leahy J.P., Jägers W.J., Pooley G.G., 1986, Astron. Astrophys. **156** 234

Leahy J.P., Black A.R.S., Dennett-Thorpe J., Hardcastle M.J., Komissarov S., Perley R.A., Riley J.M., Scheuer P.A.G., 1996, M.N.R.A.S. submitted [L96]

Leahy J.P., Parma P., 1992, in Roland J., Sol H., Pelletier G., *Extragalactic Radio Sources: from Beams to Jets*, Cambridge University Press, Cambridge, p. 307

Leahy J.P., Perley R.A., 1991, Astron. J. **102** 527 [LP]

Leahy J.P., Perley R.A., 1995, M.N.R.A.S. **277** 1097

Leahy J.P., Williams A.G., 1984, M.N.R.A.S. **210** 929

Ledlow M.J., Owen F.N., 1996, in Hardee P.E., Bridle A.H., Zensus J.A., eds, *Energy Transport in Radio Galaxies and Quasars*, ASP Conference Series vol. 100, San Francisco, p. 359

Lilly S.J., Longair M.S., 1984, M.N.R.A.S. **211** 833

Lilly S.J., McLean I.S., Longair M.S., 1984, M.N.R.A.S. **209** 401

Liu R., Pooley G.G., 1991a, M.N.R.A.S. **249** 343

Liu R., Pooley G.G., 1991b, M.N.R.A.S. **253** 669

Liu R., Pooley G.G., Riley J.M., 1992, M.N.R.A.S. **257** 545

Longair M.S., Gunn J.E., 1975, M.N.R.A.S. **170** 121

Longair M.S., Riley J.M., 1979, M.N.R.A.S. **188** 625

Longair M.S., Seldner M., 1979, M.N.R.A.S. **189** 433

Lonsdale C.J., Barthel P.D., 1986, Astron. J. **92** 12

Lonsdale C.J., Morison I., 1983, M.N.R.A.S. **203** 833

Lynden-Bell D., 1969, Nature **223** 690

Maccagni D., Tarenghi M., 1981, Astrophys. J. **243** 42

Macchetto F., Albrecht R., Barbieri C., 1991, Astrophys. J. **373** L55

Mackay C., 1971, M.N.R.A.S. **154** 209

Mackay C., 1973, M.N.R.A.S. **162** 1

Macklin J.T., 1981, M.N.R.A.S. **196** 967

Macklin S.T., 1983, M.N.R.A.S. **203** 147

Matthews T.A., Morgan W.W., Schmidt M., 1964, Astrophys. J. **140** 35

McCarthy P.J., 1988, PhD thesis, University of California at Berkeley

McCarthy P.J., 1993, Ann. Rev. Astron. Astrophys. **31** 639

McCarthy P.J., Spinrad H., van Breugel W., 1995, Astrophys. J. Suppl. **99** 27

McCarthy P.J., van Breugel W., 1989, in Frenk C.S., Ellis R.S., Shanks T., Heavens A.F., Peacock J.A., eds, *The Epoch of Galaxy Formation*, NATO ASI Series, Kluwer, Dordrecht, p. 57

McCarthy P.J., van Breugel W., Kapahi V.K., 1991, Astrophys. J. **371** 478

McCarthy P.J., van Breugel W., Spinrad H., Djorgovski S., 1987, Astrophys. J. **321** L29

Meisenheimer K., Röser H.-J., Hiltner P.R., Yates M.G., Longair M.S., Chini R., Perley R.A., 1989, Astron. Astrophys. **219** 63

Miley G.K., Norman C., Silk J., Fabbiano G., 1983, Astron. Astrophys. **122** 330

Miley G.K., Wade C.M., 1971, Astrophys. J. **8** L11

Miyoshi M., Moran J., Herrnstein J., Greenhill L., Nakai N., Diamond P., Inoue M., 1995, Nature **373** 127

Morganti R., Oosterloo T.A., Fosbury R.A.E., Tadhunter C.N., 1995, M.N.R.A.S. **274** 393

Murphy D.W., Browne I.W.A., Perley R.A., 1993, M.N.R.A.S. **264** 298

Muxlow T.W.B., Garrington S.T., 1991, in Hughes P.A., ed., *Beams and Jets in Astrophysics,* Cambridge University Press, Cambridge, p. 52.

Myers S.T., Spangler S.R., 1985, Astrophys. J. **291** 52

Neff S.G., Roberts L., Hutchings J.B., 1995, Astrophys. J. **99** 349

Norman M.L., Balsara D.S., 1993, in Röser H.-J., Meisenheimer K., eds, *Jets in Extragalactic Radio Sources*, Springer-Verlag, Heidelberg, p. 229

Northover K.J.E., 1973, M.N.R.A.S. **165** 369

O'Dea C.D., Owen F.N., 1986, Astrophys. J. **301** 841

O'Donoghue A.A., Owen F.N., Eilek J.A., 1990, Astrophys. J. Suppl. **72** 75

O'Donoghue A.A., Eilek J., Owen F., 1993, Astrophys. J. **408** 428

Okayasu R., Isiguro M., Tabara H., 1992, Pub. Astr. Soc. Japan **44** 335

Orr M.J.L., Browne I.W.A., 1982, M.N.R.A.S. **200** 1067

Osterbrock D.E., Miller J.S., 1975, Astrophys. J. **197** 535

Owen F.N., Dwarakanath K.S., Smith C.C., Ledlow M.J., Keel W.C., Morrison G.E., Vöges W., Burns J.O., 1996, in Hardee P.E., Bridle A.H., Zensus J.A., eds, *Energy Transport in Radio Galaxies and Quasars*, ASP Conference Series vol. 100, San Francisco, p. 353

Owen F.N., Hardee P.E., Cornwell T.J., 1989, Astrophys. J. **340** 698

Owen F.N., Laing R.A., 1989, M.N.R.A.S. **238** 357

Owen F.N., Ledlow M.J., Keel W.C., 1995, Astron. J. **109** 14

Owen F.N., Puschell J.J., 1984, Astron. J. **89** 932

Owen F.N., White R.A., 1991, M.N.R.A.S. **249** 164

Owen F.N., O'Dea C.P., Inoue M., Eilek J.A., 1985, Astrophys. J. **294** L85

Palimaka J.J., Bridle A.H., Fomalont E.B., Brandie G.W., 1979, Astrophys. J. **231** L7

Parma P., Cameron R.A., De Ruiter H.R., 1991, Astron. J. **102** 1960

Parma P., De Ruiter H.S., Fanti R., 1996, in Ekers R.D., Fanti C., Padrielli L., eds, *Extragalactic Radio Sources*, IAU Symposium 175, Kluwer, Dordrecht, p. 137

Parma P., Fanti C., Fanti R., Morganti R., De Ruiter H.R., 1987, Astron. Astrophys. **181** 244

Parma P., Morganti R., Capetti A., Fanti R., De Ruiter H.R., 1993, Astron. Astrophys. **267** 31

Patnaik A.R., Banhatti D.G., Subrahmanya C.R., 1984, M.N.R.A.S. **211** 775

Peacock J.A., Perryman M.A.C., Longair M.S., Gunn J.E., Westphal J.A., 1981, M.N.R.A.S. **194** 601

Peacock J.A., Wall J.V., 1982, M.N.R.A.S. **198** 843

Pearson T.J., 1996, in Hardee P.E., Bridle A.H., Zensus J.A., eds, *Energy Transport in Radio Galaxies and Quasars*, ASP Conference Series vol. 100, San Francisco, p. 97

Pedelty J.A., Rudnick L., McCarthy P.J., Spinrad H., 1989a, Astron. J. **97** 647

Pedelty J.A., Rudnick L., McCarthy P.J., Spinrad H., 1989b, Astron. J. **98** 1232

Perley R.A., 1989, in Meisenheimer K., Röser H.-J., eds, *Hotspots in Extragalactic Radio Sources*, Springer-Verlag, Heidelberg, p. 1

Perley R.A., Bridle A.H., Willis A.G., 1984, Astrophys. J. Suppl. **54** 291

Perley R.A., Carilli C.L., 1996, in Carilli C.L., Harris D.E., eds, *Cygnus A — Study of a Radio Galaxy*, Cambridge University Press, Cambridge, p. 168

Perley R.A., Dreher J.W., Cowan J.J., 1984, Astrophys. J. **285** L35

Perley R.A., Willis A.G., Scott J.S., 1979, Nature **281** 437

Perlman E.S., Stocke J.T., 1994, Astron. J. **106** 56

Perryman M.A.C., Lilly S.J., Longair M.S., Downes A.J.B., 1984, M.N.R.A.S. **209** 159

Phinney E.S., 1985, in Miller J.S., *Astrophysics of Active Galaxies and Quasi-Stellar Objects*, Oxford University Press, Oxford, p. 453

Pooley G.G., Henbest S.N., 1974, M.N.R.A.S. **169** 477

Press W.H., Flannery B.P., Teulolsky S.A., Vetterling W.T., 1992, *Numerical Recipes: The Art of Scientific Computing*, Cambridge University Press, Cambridge

Prestage R.M., Peacock J.A., 1988, M.N.R.A.S. **230** 131

Preuss E., Alef W., Wu S.Y., Qiu Y.H., Qian Z.H., Kellermann K.I., Matveenko L., Götz M.M.A., 1990, in Zensus J.A., Pearson T.J., eds, *Parsec-scale Radio Jets*, Cambridge University Press, Cambridge, p. 120

Price R., Gower A.C., Hutchings J.B., Talon S., Duncan D., Ross G., 1993, Astrophys. J. Suppl. **86** 365

Prieto M.A., Walsh J.R., Fosbury R.A.E., di Seregho Alghieri S., 1993, M.N.R.A.S. **263** 10

Röser H.-.J., Meisenheimer K., 1991, Astron. Astrophys. **252** 458

Rawlings S., 1987, PhD thesis, University of Cambridge

Rawlings S., Saunders R., 1991, Nature **349** 138

Rawlings S., Saunders R., Eales S.A., Mackay C.D., 1989, M.N.R.A.S. **240** 701

Rees M.J., 1978, Nature **275** 516

Riley J.M., Longair M.S., Gunn J.E., 1980, M.N.R.A.S. **192** 233

Riley J.M., Pooley G.G., 1975, Mem. R.A.S. **80** 105 [RP]

Riley J.M., Pooley G.G., 1978, M.N.R.A.S. **183** 245

Roettiger K., Burns J.O., Clarke D.A., Christiansen W.A., 1994, Astrophys. J. **421** L23

Rossiter D.A., 1987, PhD thesis, University of Cambridge

Rudnick L., 1984, in Bridle A.H., Eilek J.A., eds, *Physics of Energy Transport in Radio Galaxies*, NRAO Workshop no. 9, NRAO, Green Bank, West Virginia, p. 35

Ryle M., Hewish A., 1960, M.N.R.A.S. **120** 220

Ryle M., Longair M.S., 1967, M.N.R.A.S. **136** 123

Sandage A.R., 1973a, Astrophys. J. **180** 687

Sandage A.R., 1973b, Astrophys. J. **183** 711

Sargent W.L.W., 1977, Astrophys. J. **212** L105

Saunders R., Baldwin J.E., Rawlings S., Warner P.J., Miller L., 1989, M.N.R.A.S. **238** 777

Scheuer P.A.G., 1974, M.N.R.A.S. **166** 513

Scheuer P.A.G., 1982, in Heeschen, D.S., Wade C.M., eds, *Extragalactic Radio Sources*, IAU Symposium 97, Reidel, Dordrecht, p. 163

Scheuer P.A.G., 1987, in Zensus J., Pearson T., eds, *Superluminal Radio Sources*, Cambridge University Press, Cambridge, p. 104

Scheuer P.A.G., 1995, M.N.R.A.S. **277** 331

Schmidt M., 1963, Nature **197** 1040

Schmidt M., 1965, Astrophys. J. **141** 1

Simard-Normandin M., Kronberg P.P., Button S., 1981, Astrophys. J. Suppl. **45** 97

Simpson C., Ward M., Clements D.L., Rawlings S., 1996, M.N.R.A.S. **281** 509

Smith E.P., Heckman T.M., 1989, Astrophys. J. **341** 658

Smith E.P., Heckman T.M., 1990, Astrophys. J. **348** 38

Smith H.E., Spinrad H., 1980, Pub. Astr. Soc. Pacific **92** 553

Smith H.E., Spinrad H., Smith E.O., 1976, Pub. Astr. Soc. Pacific **88** 621

Spangler S.R., Myers S.T., Pogge J.J., 1984, Astron. J. **89** 1478

Spencer R.E., Schilizzi R.T., Fanti C., Fanti R., Parma P., van Breugel W.J.M., Venturi T., Muxlow T.W.B., Rendong N., 1991, M.N.R.A.S. **250** 225

Spinrad H., 1978, Astrophys. J. **220** L135

Spinrad H., Djorgovski S., Marr J., Aguilar L., 1985, Pub. Astr. Soc. Pacific **97** 932

Stephens P., 1987, PhD thesis, University of Manchester

Strom R.G., Jägers W.J., 1988, Astron. Astrophys. **194** 79

Stull M.A., 1971, Astron. J. **76** 1

Swain M.R., Bridle A.H., Baum S.A., 1996, in Hardee P.E., Bridle A.H., Zensus J.A., eds, *Energy Transport in Radio Galaxies and Quasars*, ASP Conference Series vol. 100, San Francisco, p. 299

Swarup G., Banhatti D.G., 1980, M.N.R.A.S. **194** 1025

Tadhunter C.N., Morganti R., di Serego Alighieri S., Fosbury R.A.E., Danziger I.J., 1993, M.N.R.A.S. **263** 999

Tadhunter C.N., Scarrott S.M., Draper P., Rolph C., 1992, M.N.R.A.S. **256** 53p

Tanaka Y., Nandra K., Fabian A.C., Inoue H., Otani C., Dotani T., Hayashida K., Iwasawa K., Kii T., Kunieda H., Makino F., Matsuoka M., 1995, Nature **375** 659

Taylor G.B., Dunlop J.S., Hughes D.H., Robson E.I., 1996, M.N.R.A.S. in press

Taylor G.B., Perley R.A., Inoue M., Kato T., Tabara H., Aizu K., 1990, Astrophys. J. **360** 41

Thomasson P., Garrington S.T., Muxlow T.W.B., Leahy J.B., 1994, *MERLIN User Guide*, University of Manchester

Thompson A.R., Moran J.M., Swenson G.W., 1986, *Interferometry and Synthesis in Radio Astronomy*, Wiley, New York

Urry C.M., Padovani P., Stickel M., 1991, Astrophys. J. **382** 501

van Breugel W.J.M., Dey A., 1993, Astrophys. J. **414** 563

van Breugel W.J.M., Jägers W.J., 1982, Astron. Astrophys. Suppl. **49** 529

Venturi T., Feretti L., Giovannini G., Comoretto G., Wehrle A.E., 1993, Astrophys. J. **408** 81

Véron P., 1977, Astron. Astrophys. Suppl. **30** 131

Wardle J.F.C., Aaron S.E., 1996, in Hardee P.E., Bridle A.H., Zensus J.A., eds, *Energy Transport in Radio Galaxies and Quasars*, ASP Conference Series vol. 100, San Francisco, p. 123

Williams A.G., 1991, in Hughes P.A., ed., *Beams and Jets in Astrophysics*, Cambridge University Press, Cambridge, p. 342

Williams A.G., Gull S.F., 1985, Nature **313** 34

Willis A.G., Strom R.G., Bridle A.H., Fomalont E.B., 1981, Astron. Astrophys. **95** 250

Wilson A.S., 1993, in Burgarella D., Livio M., O'Dea C.P., eds, *Astrophysical Jets*, Space Telescope Science Institute Symposium Series 6, Cambridge University Press, Cambridge, p. 122

Wyndham J.D., 1966, Astrophys. J. **144** 459

Yates M.G., Miller L., Peacock J.A., 1989, M.N.R.A.S. **240** 129

Yee H.K.C., Green R.H., 1987, Astrophys. J. **319** 28

Yee H.K.C., Oke J.B., 1978, Astrophys. J. **226** 753

Zirbel E.L., Baum S.A., 1995, Astrophys. J. **448** 521

Zukowski E., 1990, PhD thesis, University of Toronto

‘Had I been present at the Creation, I should have given some useful hints for the better ordering of the Universe.’

— Alfonso the Wise, King of Castile and Léon (1221–84)